Experimental Studies on Phase Transitions and Nucleation-Growth in Liquid Crystals

Vishnu Deo Mishra

Raman Research Institute
Bengaluru

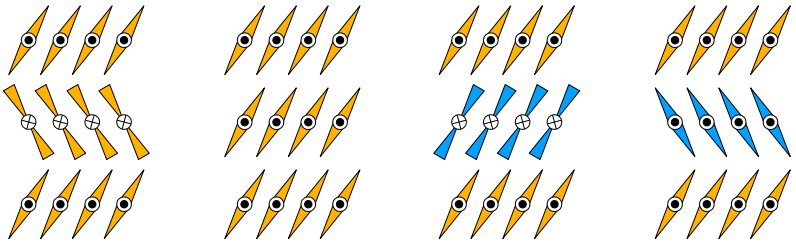

A thesis submitted to
Jawaharlal Nehru University, New Delhi
for the degree of
Doctor of Philosophy

To my parents!

Declaration

I, ***Vishnu Deo Mishra***, hereby declare that the content presented in this thesis entitled ***'Experimental Studies on Phase Transitions and Nucleation-Growth in Liquid Crystals'*** is entirely original. This thesis has been composed independently by me at the ***Raman Research Institute (RRI)*** under the supervision of ***Prof. Arun Roy***. The subject matter presented in this thesis has not previously formed the basis for the award of any degree, diploma, membership, associateship, fellowship, or any other similar title of any other university or institution. I also declare that this thesis has been checked using the DrillBit plagiarism software.

Vishnu Deo Mishra

Prof. Arun Roy
(Thesis supervisor)
Soft Condensed Matter Group
Raman Research Institute,
Bengaluru-560080, India.

Certificate

This is to certify that the thesis entitled ***'Experimental Studies on Phase Transitions and Nucleation-Growth in Liquid Crystals'*** submitted by ***Vishnu Deo Mishra*** for the award of the degree of ***Doctor of Philosophy*** of the Jawaharlal Nehru University, New Delhi, India is his original work. The work presented in the thesis has not been published or submitted elsewhere for the award of any degree or diploma.

Prof. Arun Roy
(Thesis supervisor)
Soft Condensed Matter Group
Raman Research Institute,
Bengaluru-560080, India.

Prof. Tarun Souradeep
Director
Raman Research Institute,
Bengaluru-560080, India.

Synopsis

Liquid crystals are a particular class of materials that exhibit phases between their crystal and isotropic liquid phases. Thus, the liquid crystalline phases have intermediate structures with the combination of the orientational or translational order found in crystals and the fluid nature of liquids. This combination results in a number of phases and unique physical properties of liquid crystals. The liquid crystals are highly sensitive to external stimuli, such as electric or magnetic fields, which have been exploited for various technological applications. When a liquid crystal has ferroelectric behavior, its response to an electric field becomes even more substantial. Based on the symmetry argument, R. B. Meyer first proposed the possibility of liquid crystals displaying ferroelectric behavior. It was demonstrated that the arrangement of molecules with chirality leads to breaking the symmetry of the tilted smectic C phase. This symmetry-breaking results in the formation of long-range polar order in the system. Another breakthrough took place with the discovery of bent-core mesogens, which provided a new method to develop macroscopic polar order. The rotation of the bent-core molecules about their long axes gets hindered due to their bent shape, leading to a parallel alignment of molecular transverse dipole moments. This alignment produces polar smectic layers. Moreover, an intra-layer tilt order of the molecular long axes with respect to the layer normal introduces macroscopic layer chirality in the system. The interplay between polarity and chirality gives rise to a rich variety of phase behavior and unique physical properties. Recent years have witnessed the synthesis and thorough investigation of numerous bent-core molecules by researchers. Nonetheless, the diverse variety of phase ordering, their distinctive physical properties, and possibilities of utilization in potential applications continue to make these studies an exciting field of research.

This thesis deals with experimental investigations on three different compounds comprised of bent-core (BC) banana shaped molecules exhibiting distinct phase behaviors. We also studied the nucleation growth process of a liquid crystalline phase from its isotropic melt for one of the studied compounds. This thesis comprises five chapters. **Chapter 1** introduces a comprehensive overview of liquid crystalline phases comprised of anisotropic molecules of different shapes and various essential topics relevant to the thesis. In **Chapter 2**, we present a brief exploration of the

diverse experimental methodologies employed for the studies. These methods encompass techniques such as Polarising Optical Microscopy (POM), Field Emission Scanning Electron Microscopy (FESEM), X-ray Diffraction (XRD), Dielectric studies, and Custom-built setups for electro-optic studies, among others.

In **Chapter 3**, we present the distinctive phase behavior exhibited by a homologous series of compounds comprised of strongly asymmetric bent-core molecules. We have performed detailed physical characterizations using various experimental techniques on these compounds synthesized in our chemistry laboratory. The general chemical formula of the compounds is *4-((4-(octyloxy) phenoxy) carbonyl)phenyl4′-((4-(n-alkoxy)-3-fluorobenzoyl)oxy)-[1,1′-biphenyl]-3-carboxylate*. The compounds are abbreviated as **8OBFn** in this thesis, where 'n' represents the number of carbon atoms in the aliphatic chain attached to one end of the molecules, and it varies from 8 to 16. This variation in the chain length, along with the dissimilarities in the rigid arms of these BC molecules, introduces a strong asymmetry in the molecular structure. The x-ray diffraction (XRD) studies clearly indicate that the compounds exhibit a tilted smectic phase with a layer undulated structure. In addition to strong peaks corresponding to the lamellar molecular organization, several weak satellite peaks were observed in the small-angle region, indicating a two-dimensional structure. Based on the detailed analysis of the XRD results, we propose a frustrated layer undulated tilted smectic phase, which will be denoted as SmC_{LU} in this thesis.

Conventionally, in the case of lamellar phases exhibited by BC molecules, it has been proposed that sufficiently strong polarization (exceeding one mC/m^2) promotes the splay in the uniform polar order in the direction orthogonal to the molecular long axes in order to minimize the free energy. This results in the formation of stripes of a few tens of nanometers in width consisting of splayed molecules. Defect walls separate these stripes at their edges, giving rise to varying thicknesses of the layer. To incorporate these defects, the layers undulate periodically to form a polarization-modulated smectic phase or so-called B7 phase, which has been observed experimentally. Interestingly, our investigation on the compound 8OBFn revealed a consistent layer undulated structure for all the studied homologs, but evidence of spontaneous layer polarization was not found. A low value of dielectric constant in the SmC_{LU} phase also supports the absence of spontaneous polarization. Despite the absence of layer polarization, we observed an intriguing field-induced irreversible transition arising due to the coupling between the dielectric anisotropy of the system and the applied electric field. Furthermore, the cryogenic FESEM studies on the sample revealed a periodic structure when the sample was quenched from the mesophase by plunging it into liquid nitrogen. The periodicity in the FESEM texture was found to be consistent with the XRD results, confirming the layer undulated structure. Based on our experimental findings, we proposed a model involving

a double-tilted smectic structure with periodic undulation along the layers. The undulation in our experimentally observed SmC_{LU} phase arises due to the "leaning" order of the molecules in the layers. This leaning order can be attributed to the pronounced asymmetric shape of the constituent BC molecules. The model can also be used for layer undulation phenomena arising in other BC molecular systems lacking layer polarization.

Chapter 4 describes the investigation of a thiophene-based liquid crystal comprised of symmetric and achiral BC molecules, which exhibits unique phase behavior. The chemical formula of the compound is *2,5-bis(4′-(octyloxy)-[1,1′-biphenyl]-4-yl)thiophene-3-carbonitrile*, which we denote as **BTCN8**. The compound exhibits the following sequence of enantiotropic mesophases and a glassy state on cooling from its high-temperature isotropic phase:

$$\text{Isotropic} \xrightarrow{517.4\ \text{K}} \text{Nematic} \xrightarrow{514.9\ \text{K}} \text{dSmA} \xrightarrow{402\ \text{K}} \text{SmC} \xrightarrow{271\ \text{K}} \text{Smectic Glass}$$

It has a short temperature range of a nematic phase below the isotropic phase and two smectic phases at lower temperatures. On further lowering the temperature, the compound shows glassy behavior.

In the conventional orthogonal SmA phase, the molecules align on average parallel to the layer normal with layer spacing of the order of molecular length. Across the transition to the SmC phase, the molecules tilt away from the layer normal, giving rise to layer thickness significantly smaller than the molecular length. Thus, a considerably large layer contraction is observed across the orthogonal SmA to SmC phase transition. However, in our sample, the higher temperature SmA phase transforms to the lower temperature SmC phase with minimal layer contraction across the transition. Such SmA phase is known as 'de-Vries smectic A' or dSmA phase. In the dSmA phase, the molecules within a layer are tilted with respect to the layer normal with random azimuthal tilt directions. The random distribution of the tilt directions makes this phase optically uniaxial about the layer normal, akin to the conventional SmA phase. Across the transition from the dSmA to the SmC phase, the already tilted molecules in the layers in the dSmA phase choose a particular azimuthal orientation in the SmC phase. This results in practically no layer contraction during the transition in contrast to the conventional SmA to SmC transition. Our XRD and optical measurements confirmed the de-Vries nature of the higher temperature smectic phase. The layer contraction at 10 K below the dSmA – SmC transition temperature is found to be only about 0.17%. Across the whole range of about 225 K in the dSmA and SmC phases, the layer contraction was found to be about 5%. The optical measurements show that the birefringence is lower in the SmA phase compared to that in the SmC phase, which also supports the de-Vries nature of the higher temperature SmA phase.

In addition, a notable dielectric relaxation mode emerged in the dSmA phase in the MHz range, which persists even in the lower temperature SmC phase with no discernible change across the transition. Intriguingly, the relaxation frequency of this dielectric mode shifted to an unusually low frequency range on decreasing the temperature in the SmC phase. At ambient temperature, the relaxation frequency attains a value in the range of tens of Hertz. The empirical Havriliak-Negami equation was utilized to analyze the measured dielectric relaxation process. The computed fitting parameters indicate that the relaxation process is of the Cole-Cole type, where the width of the dielectric loss spectrum was found to increase with decreasing temperature. The temperature-dependent relaxation frequency followed the Vogel-Fulcher-Tammann (VFT) equation, suggesting the highly fragile glassy nature of the sample. The calorimetry measurements further confirmed the glass transition at a temperature of 271 K of the sample with no considerable dependence on the cooling rate. Based on the molecular organization in the dSmA phase, a mechanism contributing to the relaxation mode was proposed. Notably, this is the first report of a BC liquid crystal exhibiting the de-Vries SmA phase along with the glassy relaxation. The compounds manifesting the dSmA phase are known to be of significant importance for ferroelectric display devices. Furthermore, glass-forming liquid crystals hold unique significance as they retain the qualitative features of the liquid crystal phase and can be exploited in various applications such as holography, wave plates, and optical storage.

Chapter 5 presents the experimental studies performed on a BC compound composed of azo-substituted highly asymmetric bent-core molecules. The chemical formula of the compound is *4-((4-(dodecyloxy)benzoyl)oxy)phenyl 3-(((4-((4-(ndodecyloxy) phenyl)diazenyl)phenyl)imino)methyl) benzoate*, which is abbreviated as **DIBO12** in this thesis. The compound exhibits one enantiotropic liquid crystal phase. The observed mesophase was characterized using a variety of experimental techniques. The XRD measurements confirmed a lamellar molecular organization with the layer spacing significantly smaller than the molecular length. The POM studies showed a complex inhomogeneous texture with a large number of defects for a planar-aligned sample between crossed polarizers. Interestingly, on slow cooling (0.01 K/min) of the sample from the isotropic phase, the mesophase nucleates as small droplets, which subsequently grow by forming distinctive bud-like structures at the interface. As this bud-like structure continues to grow, it exhibits a tendency to curl. Unlike the typical B2 phases usually observed for the BC molecules, the polarization reversal current measurement on the mesophase of our sample did not detect any signature of layer polarization. A low dielectric constant value in the mesophase and quadratic dependence of optical transmittance on the applied electric field further supports the absence of spontaneous polarization. Based on these experimental observations, we speculate that the observed mesophase is a

'general tilted smectic C phase' (SmC_G). This phase might favor spontaneous layer curvature, possibly due to inherent up-down asymmetry within the layers.

We studied the nucleation growth process of the mesophase while thermally quenching the system from its isotropic phase. Usually, the smectic phases grow as batonnet-like structures when cooled from their isotropic phase. This phenomenon is primarily attributed to the more pronounced growth occurring in the direction of the layer normal compared to the layer plane. During this transition, the interfaces between the liquid crystal and the isotropic phase remain smooth in order to minimize surface energy. Interestingly, the nucleation and growth of the mesophase for the compound DIBO12 shows a fractal structure while cooling from the isotropic phase. The fractal interface is usually not expected as the structure's surface area is more extensive, implying a higher surface energy. We quantitatively investigated this unusual fractal growth using video microscopy to understand the underlying mechanism. We found that the fractal dimension of the growth interface does not depend on the experimentally controlled parameters such as quench depth, quench rate, and thickness of the sample. Based on our experimental results, we discuss a plausible mechanism of nucleation and growth, taking into account the asymmetric shape of the constituent molecules and inter-molecular interactions. The steric interaction driven by the shape anisotropy of the BC molecules perhaps leads to relatively faster growth in the direction of the layer plane compared to that along the layer normal. This asymmetric growth, combined with the curling tendency of the layers, perhaps gives rise to the fractal interface between the mesophase and the isotropic phase.

Finally, we conclude in **Chapter 6** with a discussion on the significance of the main results obtained in the thesis and briefly point to the scope for future work.

Vishnu Deo Mishra

Prof. Arun Roy
(Thesis supervisor)
Soft Condensed Matter Group
Raman Research Institute,
Bengaluru-560080, India.

List of publications

1. Glassy relaxation in a de Vries smectic liquid crystal consisting of bent-core molecules; VD Mishra, G Pratap, A Roy; *Phys. Rev. E* 109, 024703 (2024)

2. Leaning induced layer undulated tilted smectic phase of asymmetric bent-core liquid crystals; VD Mishra, HT Srinivasa, A Roy; *J. Chem. Phys.* 158, 074906 (2023)

3. Molecular organization and molecular order of two rod-like smectogens in mesophases; AA Boopathi, NP Lobo, VD Mishra, A Roy, T Narsimhaswamy; *Liquid Crystals* 50, 13-14 (2023)
   This paper is not part of the thesis.

4. Tilted smectic phase with fractal growth morphology of bent-core molecules; VD Mishra, V Prasad, A Roy; *Liquid Crystals* (Under review)

Vishnu Deo Mishra

Prof. Arun Roy
(Thesis supervisor)
Soft Condensed Matter Group
Raman Research Institute,
Bengaluru-560080, India.

Acknowledgement

A number of individuals have played a vital role in ensuring the success of this thesis. I would like to take this opportunity to convey my sincere appreciation to each one of them.

First and foremost, I would like to express my sincere gratitude to Prof. Arun Roy, my *Ph.D. supervisor*, for his tireless support and invaluable guidance throughout my doctoral journey. Working under his mentorship has been an incredible learning experience. His constant encouragement and support significantly contributed to improving the work presented in this thesis. I am also grateful for the freedom he provided and admire his patience and humility.

I thank my collaborators, Prof. T. Narasimhaswamy, Dr. H. T. Srinivasa, and Prof. Veena Prasad, for providing the liquid crystal compounds for the studies during my Ph.D. I am grateful to have had numerous invaluable discussions with Raghu and Madhusudana. The insights and comments they provided proved vital in successfully completing some of my work. I thank Vasudha Ma'am for her help in acquiring DSC and XRD data and Yadu (Yateendran) for SEM imaging of the samples.

Meetings with my $advisory\ committee$ (Yashodan and Sayantan) have helped me get a holistic view of my thesis. Sandeep, Gautam, Ranjini, Pramod, and EEG group members were very kind in allowing me to use their lab facilities whenever required. I am thankful to have my lab seniors, Deepshika and Subhadip, to teach, discuss, and help with various instrumental and conceptual details. I thank Dipak and Arsalan for helping me learn programming languages and various useful software and engaging in numerous scientific or other discussions. I also appreciate Swarnak, Saichand, Susovan, and Neha for being great lab mates.

I thank the $Admin$, $academics$, $SAAC$, including C.S.R. Murthy, Naresh, Sachin, Radha, Vidya, Merissa, Harini, Gayatri, Shailaja for taking care of various aspects of my PhD program; KRK, Amudha, Chaitanya, Raja, Venkatesh, and Murali for helping us with lab management-related activities; $Mechanical\ workshop$ (Ibrahim); $Electrical\ department$ (Muneeshwaran, GB) for helping me with var-

ious electrical issues in the lab and hostel; $IT/Computer\ department$, $Purchase$, $Accounts$, $Library$ (Manju, Nagaraj, etc.); $Hostel\ cooks$ (Mangla ji, Saujanya ji, etc.), and $Canteen$ for helping with various other aspects.

Away from the lab, I enjoyed the company of Arsalan, Nishant, Sebanti, Ashish, Anand, Chandeswar, Sumit, Amar, Satyabhama, Saurabh (Pandey), Krishna, Pankaj, Bhim, Akhilesh, Aditya, Girijesh, Ansuman, Rajkumar, Pradosh, Palak, Raj Prince, Nomaan, Mari, Swamy, Anindya, Irla, Jaggu, Sreyas, Abhishek (Mathur), Chandan, JK, Venu, Asha, Vardhan, Arun, Abhishek (Ghadai), Tiwari, Subodh, Niranjan, Sanjay, Sumanth, Sreeja, Sagar, Maheshwar, DubeyJi, Nancy, Adwaith, Varun, Alka, Vani, SukhVeer, Akhil, Anson, Pooja, Saurabh (Kaushik), Sachi, Hari, Ion, Bapan, Rishab, Ranita, Sanhita, Saikat, Sanchari, Avik, Tanuman, Silpa, Gunjan, Manami, Sukanya, Vaibhav RSP, Vaibhav, Deepak, Makarand, Saumya, Manish, Shashank, Mukesh, Vaibhav, Aman, etc. in a wide variety of activities like running, swimming, cricket, bike rides, chess, badminton, hiking, cooking, and many more in addition to discussing science.

Finally, but most importantly, I thank my parents (Mrs. Gyanti Mishra & Mr. Paras Nath Mishra), my maternal uncle (Mr. Shreedhar Mishra), and all family members for their exceptional support and encouragement in letting me pursue my dreams of career and life in general.

Vishnu

Contents

1 Introduction **1**

1.1 Calamatic liquid crystals . . . 3

1.1.1 Nematic phase . . . 3

1.1.2 Cholesterics . . . 8

1.1.3 Smectics . . . 9

1.1.4 de-Vries smectic A (dSmA) phase . . . 11

1.1.5 Effects of chirality: Ferro– and Antiferroelectric liquid crystals 14

1.2 Discotic liquid crystals . . . 15

1.3 Bent-core liquid crystals (BCLCs) . . . 15

1.3.1 Orthogonal smectic phases of BC molecules . . . 17

1.3.2 Tilted smectic phases of BC molecules . . . 18

1.3.3 Modulated smectic phases of BC molecules . . . 22

1.3.4 Columnar phases of BC molecules . . . 23

1.4 Glass transition in liquid crystals . . . 24

1.5 Nucleation and growth of mesophases . . . 26

2 Experimental techniques **29**

2.1 Differential scanning calorimetry . . . 29

2.2 X-ray diffraction . . . 31

2.3 Construction of liquid crystal cells . . . 32

2.3.1 LC cells for homeotropic alignment . . . 32

2.3.2 LC cells for homogeneous planar alignment . . . 33

2.4 Polarizing Optical Microscopy . . . 34

2.4.1 Birefringence measurement . . . 36

2.4.2 Optical transmittance . . . 38

2.5 Electro-optic setup . . . 38

2.6 Impedance analysis of sample . . . 39

2.6.1 Determination of dielectric constant . . . 42

2.7 Polarization switching current measurement . . . 43

2.8 Field-emission scanning electron microscopy . . . 45

2.8.1 Cryogenic – SEM . . . 46

3 Leaning induced layer undulation in bent-core liquid crystals **47**

3.1 Introduction . . . 47

3.2 Experimental results and discussion . . . 48
3.2.1 Sample details and differential scanning calorimetry studies . 48
3.2.2 POM observations and electric field effects . . . 50
3.2.3 Dielectric studies . . . 56
3.2.4 XRD measurements . . . 58
3.2.5 Cryo-FESEM observation . . . 64
3.2.6 Discussion . . . 65
3.3 Conclusion . . . 69

4 Glassy relaxation in de Vries smectic liquid crystals 71
4.1 Introduction . . . 71
4.2 Results and discussion . . . 73
4.2.1 Phase sequence . . . 73
4.2.2 X-ray diffraction studies . . . 75
4.2.3 POM and electro-optic measurements . . . 77
4.2.4 Dielectric studies . . . 85
4.3 Conclusion . . . 96

5 Unusual nucleation and growth morphology of smectic phase 97
5.1 Introduction . . . 97
5.2 Results . . . 99
5.2.1 Sample and DSC observations . . . 99
5.2.2 XRD studies . . . 100
5.2.3 POM observations . . . 101
5.2.4 Cryo-FESEM observation . . . 106
5.2.5 Electro-optic and dielectric studies . . . 107
5.2.6 Nucleation and growth of SmC_x phase . . . 111
5.3 Discussion . . . 114
5.4 Conclusion . . . 117

6 Conclusion and future outlook 119

Bibliography 123

1 Introduction

Matter encompasses everything around us, from the vast celestial bodies to the tiniest particles invisible to our naked eye. One intriguing aspect of matter is its ability to exist in various phases, commonly known as the state of matter. These phases take distinct forms depending on the movement and spatial arrangement of the constituent molecules. There are three primary states of matter: **solid**, **liquid**, and **gas** [1]. Solids are characterized by their rigidity and give sharp Bragg reflections during diffraction experiments, providing evidence of an ordered arrangement of atoms or molecules. Liquids and gases are fluid, which flow even under minimal shear stress. Further, they produce diffuse rings in diffraction experiments, signifying the absence of any long-range order of constituent molecules. The transition between the different phases is governed by changes in external conditions, such as temperature or pressure. For instance, when heat is applied to ice, it reaches its melting point and transforms into water. If the constituent molecules are sufficiently anisotropic in shape, a crystalline solid may go through one or more intermediate phases before transforming into an isotropic liquid. **Liquid crystals** are an example of such intermediate phases that exhibit anisotropic physical properties of crystals while retaining fluidity like liquid [2]. Liquid crystalline phases are often termed mesophases, and compounds are known as mesomorphic; 'meso' is a Greek word for intermediate. In their crystalline phases, the molecules exhibit long-range positional and orientational order. As the crystalline phase is heated, the positional order may be partially or entirely lost while retaining the orientational order, leading to the formation of various liquid crystalline phases. On further heating, the liquid crystal phases eventually transform into an isotropic liquid phase, where the molecules no longer possess any orientational or positional order. Figure 1.1 represents the schematic organization of rod-like molecules in different phases of liquid crystal depending on temperature. The detailed description of these mesophases will be discussed later.

Liquid crystals were discovered by accident in 1888 when Austrian botanist Friedrich Reinitzer examined cholesteryl benzoate extracted from carrots [3]. Reinitzer noticed two distinct melting points while heating the material. Initially, it transformed into a cloudy fluid and then became a clear liquid upon further heating. The significance of this discovery was later elucidated by Otto Lehmann, who studied cholesteryl benzoate and related materials, revealing that the cloudy fluid possessed

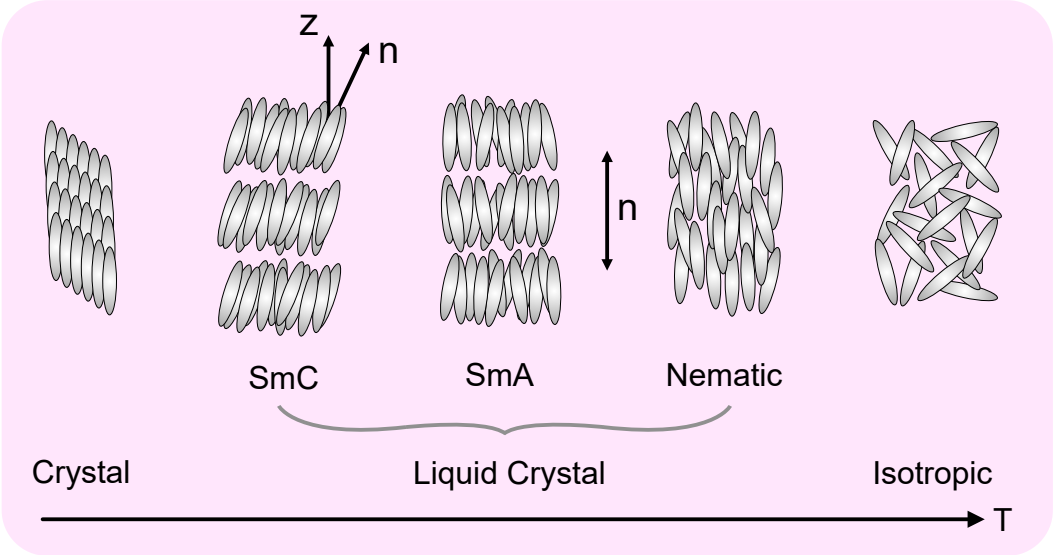

Fig. 1.1: Schematic organization of anisotropic rod-like molecules in different phases of thermotropic liquid crystals.

crystal-like properties while retaining the fluidity of a liquid. Lehmann's paper, '*Über fliessende Krystalle*' (i.e., 'On flowing crystals') established that the cloudy fluid represented a new phase of matter and laid the foundation of the science of liquid crystals [4].

At the beginning of the 20^{th} century, German chemist Daniel Vorländer developed methods to synthesize organic compounds exhibiting liquid crystalline phases [5]. Several thousands of compounds are now known to exhibit liquid crystalline phases. An essential requirement in the formation of liquid crystals is the geometrical anisotropic shape of the constituent molecules, such as **rod-like** (calamatic), **disk shaped** (discotic) or **bent-core banana shaped** molecules. These unique shapes lead to the liquid crystalline phases characterized by long-range orientational order and often partial positional order of the constituent anisotropic molecules. Depending on the intricate structure of the molecules, a compound can exhibit one or more liquid crystalline phases. In addition to being formed by organic compounds, liquid crystals are also found in nature, such as in the shells of beetles, DNA molecules, human bone, and wood cellulose.

The liquid crystals can be broadly divided into two subcategories based on the control parameters that determine the phase transitions: ***lyotropic*** and ***thermotropic*** liquid crystals. In **lyotropic liquid crystals**, the phase behavior and transitions are influenced primarily by the concentration of amphiphilic molecules in the solvent. These molecules have both hydrophilic and hydrophobic regions, and their arrangement in the solvent leads to the formation of distinct mesophases. Among the simplest examples of lyotropic liquid crystals is the mixture of soap and

water. On the other hand, phase transitions in the **thermotropic liquid crystals** are controlled by purely thermal processes. A mesophase is termed *enantiotropic* if it remains stable during both the heating and cooling cycles of the sample. Conversely, a phase is referred to as *monotropic* if it only maintains stability during the cooling process.

The focus of this thesis revolves around experimental studies of **thermotropic liquid crystals**, specifically those composed of bent-core banana-shaped molecules. Before delving into the complexities of bent-core liquid crystals, we shall discuss the typical phases exhibited by **rod-like molecules** and their associated physical properties.

1.1 Calamatic liquid crystals

The calamatic liquid crystals are comprised of elongated rod-like molecules. These molecules typically consist of a rigid rod-like core with terminal aliphatic chains attached to either both or one end of the rigid core. Two well-known examples of rod-like molecules that display a range of liquid crystal phases as a function of temperature are 5CB and 8OCB. Their chemical structures are illustrated in figure 1.2a, highlighting the characteristic elongated shape of these compounds. According to the nomenclature originally proposed by Friedel [6], calamatic liquid crystals can broadly be classified as *nematic*, *cholesteric*, and *smectic* phases.

1.1.1 Nematic phase

The nematic phase is the most fundamental and intriguing liquid crystalline phase. In the nematic phase, the constituent elongated molecules align on average along a common direction, exhibiting a long-range orientational order. This orientational order gives rise to a macroscopically anisotropic state. Despite this ordered orientation, the molecules are free to move past each other, allowing the nematic phase to retain its characteristic fluid-like properties with no long-range translational order. The nematic phase usually appears when a compound comprised of rod-like molecules is cooled from its isotropic phase. The organization of the molecules in the nematic phase is illustrated schematically in figure 1.2(a). The average orientation of molecular long axes is known as the **director**, represented by a unit vector $\hat{n}$. As the molecular organization in the nematic phase is head-tail symmetric, i.e., $\hat{n}$ and -$\hat{n}$ are indistinguishable, the director $\hat{n}$ is apolar in nature. X-ray diffraction studies of the nematic phase reveal only diffuse peaks at both wide and small angles corresponding to weak lateral and longitudinal correlations of molecules.

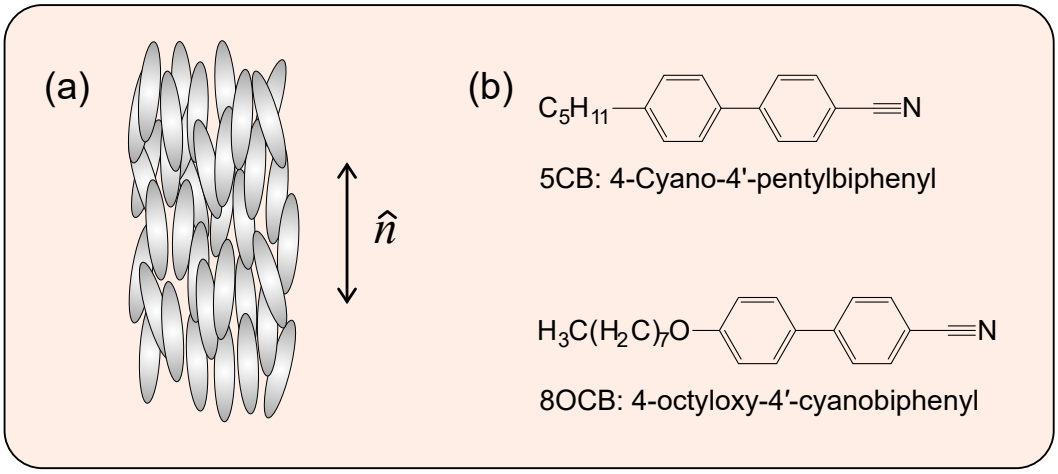

Fig. 1.2: (a) Schematic representation of the molecular organization in the nematic phase. The arrow indicates the mean orientation of molecular long axes and is denoted by director $\hat{n}$. (b) The molecular structures of typical rod-like molecules 5CB and 8OCB, which follow the phase sequence $Isotropic \rightarrow Nematic \rightarrow Crystal$ and $Isotropic \rightarrow Nematic \rightarrow SmA \rightarrow Crystal$, respectively.

The rod-like molecules can often have an asymmetric shape. For example, the molecules of the compounds 5CB and 8OCB, shown in figure 1.2(b), consist of a highly polar cyano group at one end of the molecules. This gives rise to a non-zero dipole moment along the long axis of the individual molecules. However, in the nematic phase, these dipole moments align on average antiparallel to each other, giving rise to zero net polarization in the medium. This satisfies the necessary $\hat{n}$ and -$\hat{n}$ equivalence condition of the nematic phase.

The orientational order parameter

An **order parameter** quantitatively characterizes the order-disorder transition of a physical system. Typically, the order parameter is defined to be **zero** in the higher temperature disordered phase, takes on a non-zero value in the lower temperature ordered phase during the transition, and tends to **one** in a perfectly ordered state. In the context of the uniaxial nematic phase, we make the simple assumption that the constituent molecules behave as rigid rods with cylindrical symmetry [7]. In this phase, the long axes of these rod-like molecules tend to align, on average, about the **director** ($\hat{n}$). Two key aspects are crucial for characterizing the orientation order in the nematic phase: the local preferred director $\hat{n}$ and the distribution of molecular long axes around $\hat{n}$.

To construct an orientational order parameter, we define the unit vector $\hat{u}$ to represent the orientation of the long axis of a molecule at a position $\vec{r}$. Then, we consider the ensemble average of appropriate tensors comprised of $\hat{u}$ over a small but

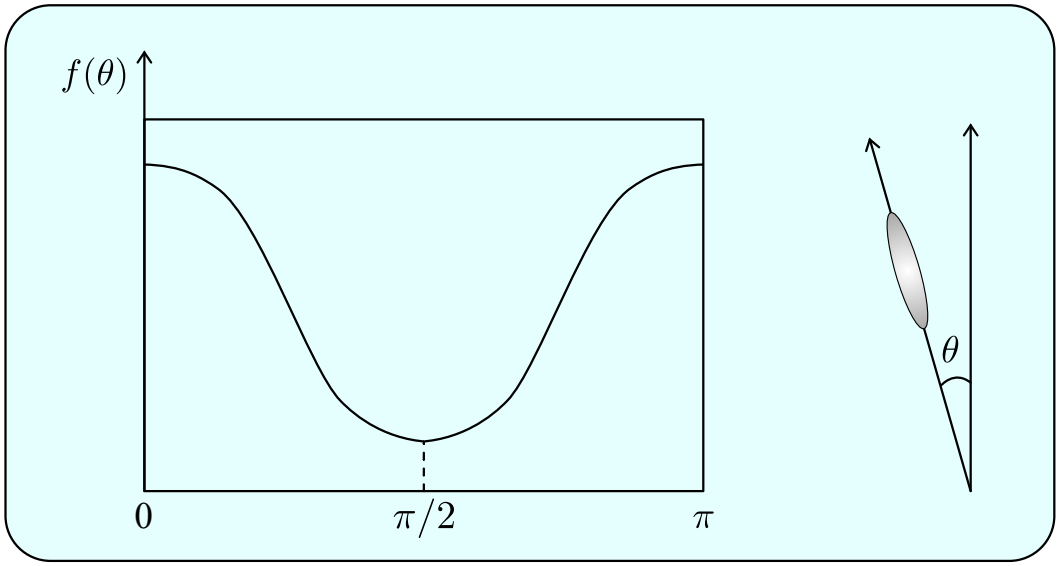

Fig. 1.3: The orientational distribution function $f(\theta)$ of rod-like molecules in the nematic phase. For rod-like molecules, the distribution $f(\theta)$ generally attains a minimum value at $\theta = \pi/2$ and maximum values at $\theta = 0$ and π.

macroscopic volume around the point $\vec{r}$. The scalar order parameter $\langle \hat{u} \cdot \hat{u} \rangle$, i.e., zero rank tensor, is constant and, therefore, will not be suitable. Here, angular brackets denote the ensemble average. Our next choice is a vector order parameter $\langle \hat{u} \rangle$, which is analogous to magnetization in the case of ferromagnets. In this case, however, a non-zero value of $\langle \hat{u} \rangle$ violates the cylindrical symmetry, i.e., the equivalence of $\hat{n}$ and $-\hat{n}$ required in the case of the nematic phase. So, the next possible choice as an order parameter is a second-rank tensor Q. Assuming the director $\hat{n}$ pointing along the z-axis, the elements of Q can be written as [7],

$$Q_{\alpha\beta} = \frac{1}{2}\langle 3u_\alpha u_\beta - \delta_{\alpha\beta} \rangle; \qquad \alpha, \beta = x, y, z \tag{1.1}$$

Here, the additional Kronecker delta term ensures that the order parameter $Q_{\alpha\beta}$ is zero in the isotropic phase as $\langle u_\alpha^2 \rangle = 1/3$. The tensor order parameter Q is symmetric and traceless and, therefore, has five independent elements. Such tensors can be diagonalized by choosing an appropriate coordinate system. If all the diagonal elements are different, the tensor describes a biaxial nematic phase and two equal eigenvalues describe a uniaxial nematic phase. In the case of the uniaxial nematic phase with director $\hat{n}$ denoting the mean orientation of molecular long axes, the most general form of order parameter can be written as [7],

$$Q_{\alpha\beta}(\vec{r}) = S\,[n_\alpha(\vec{r}) n_\beta(\vec{r}) - \frac{1}{3}\delta_{\alpha\beta}] \tag{1.2}$$

where the scalar S is a measure of the degree of alignment of the molecular long axes along $\hat{n}(\vec{r})$. $\hat{n}$ is independent of $\vec{r}$ for a uniformly aligned nematic phase.

Let us now consider a distribution function $f(\theta, \phi)$ of the molecular long axes about the director $\hat{n}$, where θ is the angle made by a molecular long axis with the director, and ϕ is the azimuthal angle. The distribution function $f(\theta, \phi)d\Omega$ gives the probability of finding the molecules in a solid angle $d\Omega = \sin\theta \; d\theta \; d\phi$ about the direction (θ, ϕ). Figure 1.3 shows the distribution function for a rod-like molecular system in the nematic phase. Taking into account, the cylindrical symmetry, i.e., $f(\theta, \phi)$ is independent of ϕ, and $\hat{n}$ and $-\hat{n}$ equivalence, the scalar order parameter S is defined as [2],

$$\boxed{S = \frac{1}{2}(3\langle\cos^2\theta\rangle - 1)} \tag{1.3}$$

For a perfect alignment of the molecules, S = 1, whereas S = 0 corresponds to the isotropic phase. The value of S decreases with increasing temperature in the nematic phase and drops discontinuously to 0 at the nematic to isotropic transition point T_{NI}. The discontinuous jump signifies the first-order nature of the transition.

Anisotropic fluid

The orientational order in the liquid crystalline phases gives rise to anisotropic physical properties of the medium, which are generally represented by second-rank tensorial quantities. With the appropriate choice of the coordinate system, these tensorial quantities can be diagonalized with three eigenvalues. If two of the eigenvalues are equal but distinct from the third one, the medium is said to be uniaxial. The medium is biaxial in nature when all three eigenvalues are distinct. In the Nematic phase, the molecules are free to rotate around their long axes, and the distribution of their long axes about director $\hat{n}$ is azimuthally symmetric. This molecular organization gives rise to $D_{\infty h}$ point symmetry of the nematic phase. The azimuthal symmetry about the director $\hat{n}$ makes this phase uniaxial in nature. Thus, the physical properties of the liquid crystals depend on the direction, resulting in an anisotropic medium.

For example, the electric permittivity in a liquid crystalline medium is anisotropic in nature and can be represented by second-rank tensor ϵ_{ij}. The response of liquid crystals to an external electric field $\vec{E}$ illustrates this anisotropic behavior. When an electric field is applied to a nematic liquid crystal, the induced polarization in the medium can be written as,

$$P_i = \epsilon_0 \, \chi_{ij} \, E_j \tag{1.4}$$

where, ϵ_0 is permittivity of free space and χ_{ij} is electric susceptibility tensor of the material. In the uniaxial nematic phase, the induced dipole moment parallel to the director is different from that perpendicular to it. Hence, the principle value $(\chi_{\parallel})$ of the susceptibility tensor along the director $\hat{n}$ is different from the perpendicular

component $\chi_\perp$. The electric permittivity of the material is closely related to χ_{ij} via $\epsilon_{ij} = \epsilon_0 (\delta_{ij} + \chi_{ij})$. Thus, there is an anisotropy in the electric permittivity given by $\Delta\epsilon = \epsilon_\parallel - \epsilon_\perp$, where $\epsilon_\parallel$ and $\epsilon_\perp$ are the electric permittivities parallel and perpendicular to the director, respectively. The dielectric anisotropy $\Delta\epsilon$ in the nematic medium is generally positive but can also have a negative value in certain materials.

The uniaxial nematic phase also exhibits optical anisotropy, having two principal refractive indices n_o and n_e associated with ordinary and extraordinary rays, respectively. Considering $n_\parallel$ and $n_\perp$ to be refractive indices in the direction parallel and perpendicular to the nematic director $\hat{n}$, it follows that

$$n_0 = n_\perp; \quad n_e = n_\parallel \tag{1.5}$$

The birefringence of the medium is defined by $\Delta n = n_e - n_0$ and is equal to $n_\parallel - n_\perp$ for uniaxial nematic. The birefringence Δn of the liquid crystals can be strong, taking a value up to 0.5, and can easily be controlled by an external electric field. Numerous liquid crystal-based electro-optical devices benefit from the fact that a significant phase change can be achieved with a relatively low applied voltage.

Curvature elasticity

In an ideal nematic medium, the orientation of the director is spatially uniform. However, in a real scenario, limiting factors such as boundary walls or external fields can deform the orientation of the director. This spatially varying director field has higher energy than the spatially uniform ground state. In the limit of long wavelength variation of the director field, the free energy density can be written as a combination of three basic curvature deformations: 'splay,' 'twist,' and 'bend.' The Frank free energy density [2, 7] associated with these curvature deformations is

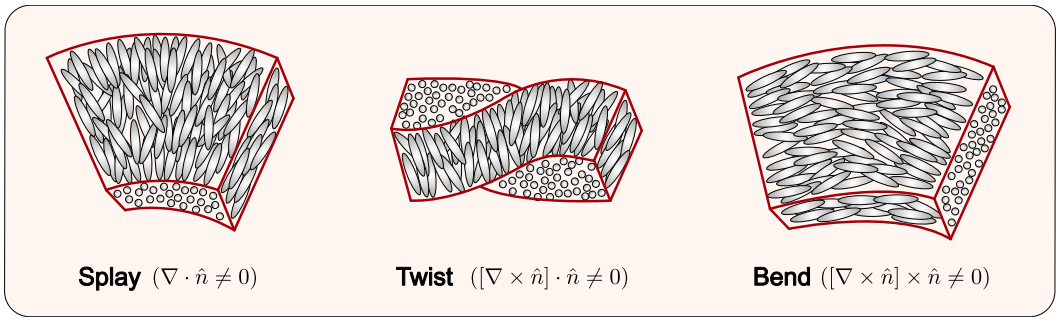

Fig. 1.4: Schematic representation of splay, twist, and bend deformations in the nematic phase.

given by,

$$F_d = \frac{1}{2}K_{11}[\nabla \cdot \hat{n}]^2 + \frac{1}{2}K_{22}[\hat{n} \cdot \nabla \times \hat{n}]^2 + \frac{1}{2}K_{33}[\hat{n} \times \nabla \times \hat{n}]^2 \tag{1.6}$$

where K_{11}, K_{22}, and K_{33} are the splay, twist, and bend elastic constants, respectively. The curvature elastic constants of a nematic medium are assumed to be positive, having typical magnitude $\sim 10^{-12}$ Newton and generally $K_{33} > K_{11} > K_{22}$. A schematic representation of these deformations is shown in figure 1.4.

1.1.2 Cholesterics

The uniform nematic phase becomes unstable to twist deformation when the constituent molecules are chiral, i.e., the molecules possess non-superimposable mirror images. The resulting structure is known as the cholesteric phase. Locally, the cholesteric phase is similar to nematic, but globally, the director $\hat{n}$ spontaneously twists in a direction perpendicular to itself. This gives rise to the formation of a helical structure with a well-defined pitch p as shown in figure 1.5. Cholesteric phases can also be induced by doping a nematic phase with optically active molecules [2]. Considering the helical axis to be along the z-direction, the equilibrium configuration of the director $\hat{n}$ is given by,

$$n_x = \cos(qz + \phi), \quad n_y = \sin(qz + \phi), \quad n_z = 0, \quad q = 2\pi/p, \tag{1.7}$$

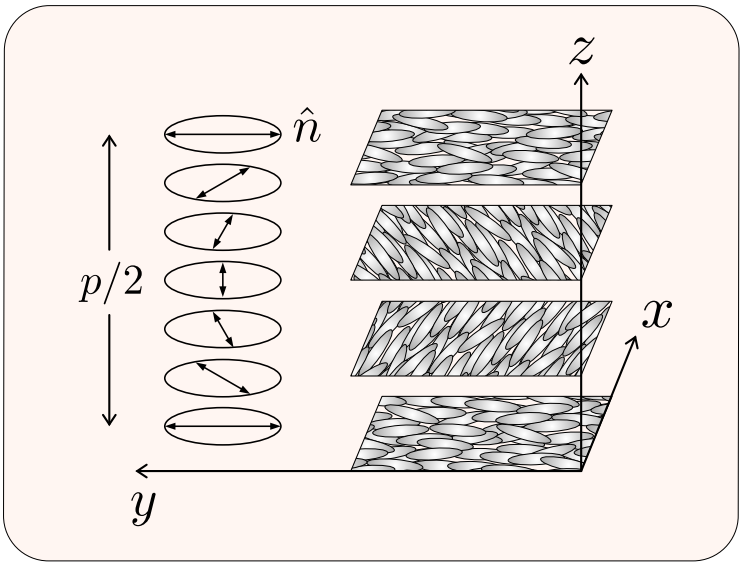

Fig. 1.5: Schematic representation of molecular organization in the cholesteric phase consisting of chiral molecules. The director $\hat{n}$ remains in the xy-plane but rotates about the z-axis, giving rise to a helical structure having pitch p. Note that the spatial periodicity of the structure is $p/2$ because of $\hat{n} \leftrightarrow -\hat{n}$ symmetry.

where p denotes the equilibrium pitch of the cholesteric phase and ϕ is an arbitrary phase angle. Thus, the cholesteric structure is periodic along the z-axis, and because of $\hat{n} = -\hat{n}$ equivalence of the nematic director, this spatial periodicity L is equal to half of the pitch:

$$L = \frac{p}{2} = \frac{\pi}{|q_0|} \tag{1.8}$$

Typical values of L lie in the range of 300 nm, i.e., comparable to optical wavelength.

The cholesteric phase exhibits unique optical properties due to its helical molecular arrangement. The pitch of the helix can generally be controlled by external factors such as temperature. Also, by adjusting the concentrations of the chiral dopants in the nematic phase, the value of the pitch p can be tuned, offering control over the optical properties of the resulting cholesteric structure. Controlling the pitch makes it possible to design photonic materials that can be utilized to manipulate light at specific frequencies. These materials are employed in developing lasers, polarizers, and optical switches [8]. Cholesteric medium displays the selective reflection of circularly polarized light and possesses an extremely large optical rotatory power. These optical characteristics make cholesteric phases of great interest in various applications.

1.1.3 Smectics

Smectic phases have fluid lamellar or layered structures with stacks of layers arranged one on top of the other. Within each layer, the centers of mass of the molecules are randomly distributed, similar to a liquid. Thus, this phase is characterized by a one-dimensional quasi-long range positional order of the centers of mass of the constituent molecules in addition to their orientational order [7]. The periodic layered structure can be described by a one-dimensional density wave along the layer normal. Assuming the layer normal pointing towards the z-axis, the density wave can be written as:

$$\rho = \rho_0[1 + Re\{|\psi|e^{i(qz+\phi)}\}] \tag{1.9}$$

where, ρ_0 is the average density, $|\psi|$ is the amplitude of the density wave, $q(= 2\pi/d)$ is the wave vector; d being the layer thickness, and ϕ is an arbitrary phase. Smectic phases, being more ordered, usually manifest at temperatures below the nematic phase for certain compounds. Based on the orientation of the director $\hat{n}$ with respect to the layer normal, the smectic phase can further be classified into two main types: smectic A (SmA) and smectic C (SmC).

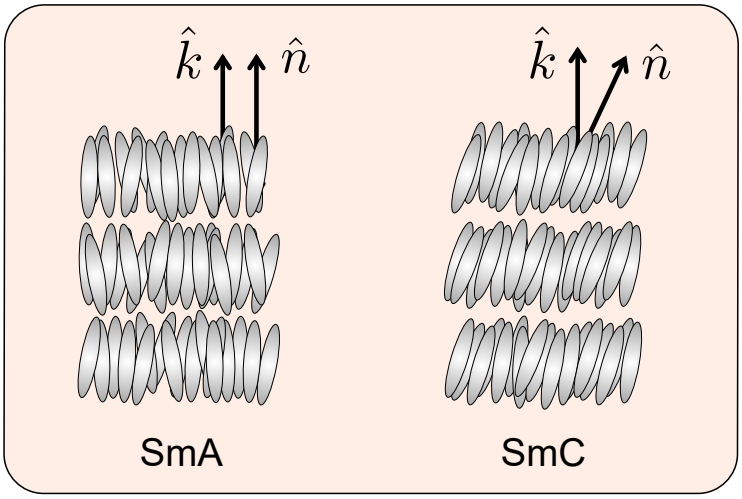

Fig. 1.6: Schematic representation of the molecular organization in fluid lamellar structure in the SmA and SmC phases. The director $\hat{n}$ orient parallel to the layer normal in the case of the SmA phase, whereas it tilts away from the layer normal in the case of the SmC phase.

Smectic A (SmA) phase

In the SmA phase, the director $\hat{n}$ is parallel to the layer normal $\hat{k}$ as shown schematically in figure 1.6(a). The layer thickness (d) is of the order of the molecular length (l). The SmA phase can be easily identified using x-ray diffraction (XRD) measurements. The XRD profile of the SmA phase exhibits a sharp peak, and sometimes its higher order peaks in the small angle region, indicating the layered structure. Additionally, a diffuse peak appears at the wide-angle region, corresponding to a weak positional correlation of the molecules within the layers, which confirms the fluid lamellar structure of the SmA phase. The SmA phase is optically uniaxial with cylindrical point symmetry $D_{\infty h}$. Despite higher viscosity than the nematic phase, the SmA phase retains fluidity along the layers, and low interlayer interactions allow layers to slide over each other.

Smectic C (SmC) phase

In the SmC phase, the director $\hat{n}$ tilts away from the layer normal $\hat{k}$ by a tilt angle (θ), as shown in Figure 1.6(b). This tilt gives rise to a reduced layer thickness $d = l\cos\theta$ compared to the molecular length l. In the conventional SmC phases, the tilt direction remains the same in successive layers, resulting in a so-called **synclinic** structure. Though the molecules in the SmC layers rotate almost freely about their long axes, the tilted molecular configuration gives rise to a small degree of biaxility. This biaxiality arises as the orientational distribution function is sharper in the tilt direction than in the azimuthal direction due to the layered structure. In

XRD measurements, the SmC phase exhibits sharp peaks in the small-angle region corresponding to a lamellar structure with layer thickness d significantly smaller than the molecular length l. In addition, a broad diffuse peak in the wide-angle region suggests an intralayer fluid-like order of the molecules.

1.1.4 de-Vries smectic A (dSmA) phase

In the conventional SmA phase, the director $\hat{n}$ aligns parallel to the layer normal $\hat{k}$. In such a configuration, the layer spacing d is of the order of the molecular length l, as shown in figure 1.7(a). In the SmC phase, on the other hand, the director $\hat{n}$ tilts away from the layer normal $\hat{k}$ by a tilt angle θ having layer spacing d significantly smaller than the molecular length l, as shown in figure 1.7(a). The tilt angle $\theta = \cos^{-1}(d/l)$ is generally found to be temperature-dependent in the SmC phase. Thus, the layer thickness reduces significantly across the transition from the SmA to the SmC phase for a given sample, and the layer contraction is usually about 10%

It was experimentally found that the layer spacing for some compounds didn't change appreciably across the SmA-SmC transition. Moreover, the layer spacing in the SmA phase was found to be much smaller than the molecular length. The first experimental observation of materials showing the SmA phase with layer thickness 5-10% smaller than the molecular length was presented by Diele et al. [9] based on x-ray diffraction experiments. Subsequently, a number of materials were reported showing the existence of the SmA phase with a thickness significantly smaller than the length of the constituent molecules [10–12]. For such SmA phases, the layer thickness across the SmA to the SmC transition was found to be practically constant. Such observations were initially explained by conformational changes of the molecules, giving rise to their smaller length or interdigitation of the molecules between adjacent layers [13]. In 1974, Adriaan de Vries proposed that the smaller layer spacing in the SmA phase compared to molecular length resulted from molecules being tilted similarly to the SmC phases but without long-range correlation between tilt directions. This type of SmA phase with a uniaxial order about the layer normal and a layer thickness significantly smaller than the length of the constituent molecules is known as the 'de Vries SmA phase.' Henceforth, in our discussion, we shall denote the de Vries SmA phase as the 'dSmA' phase. The reduction of correlation in tilt directions gives rise to two types of model for the dSmA phase, namely, the non-correlated layer model and the diffusive cone model. At a macroscopic level, both models can account for the characteristic properties observed experimentally for the dSmA phase.

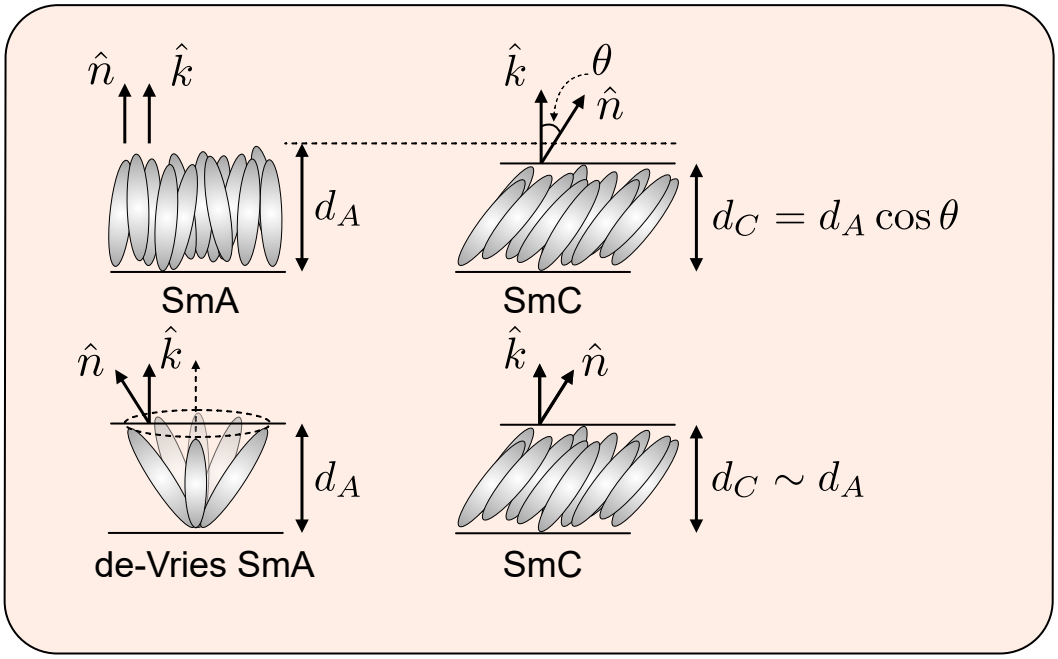

Fig. 1.7: Schematic representation of the molecular arrangement in conventional SmA, SmC, and de-Vries SmA phases comprised of calamitic molecules. In the de Vries SmA phase, the molecules are oriented with a large tilt angle with respect to layer normal having long axes randomly distributed on a cone according to the diffuse cone model proposed by Adrian de Vries. During the transition from the SmA to the SmC phase, a significant layer contraction is observed. In contrast, the dSmA to SmC transition is accompanied by practically no layer contraction.

Non-correlated layer model

In this model [11], it was postulated that the molecules are, on average, tilted in a preferred direction within each layer, but the tilt directions from layer to layer are random. The short-range correlations of the tilt directions between the layers give rise to the macroscopic uniaxial order of the dSmA phase.

Diffusive cone model

In this model [14, 15], the molecules within each layer are, on average, tilted uniformly but with random azimuthal tilt directions. In other words, the long axes of the molecules in a layer are distributed randomly across the surface of a cone, as illustrated in figure 1.7(b). Consequently, there is no long-range tilt correlation of the molecules in each layer. As a result, the average orientation direction of long axes of the molecules within a layer, i.e., the director $\hat{n}$, remains parallel to the layer normal, giving rise to the uniaxial dSmA phase. As the molecules are already tilted in the dSmA phase, the layer spacing across the transition from the dSmA to the SmC phase remains practically constant, as shown in figure 1.7(b).

Across the dSmA to SmC transition, the rotational symmetry about the layer

normal is lost, and the tilt directions become correlated, giving rise to the tilted biaxial order in the SmC phase. This phase transition from the dSmA to the SmC phase is usually found to be second-order or weakly first-order in nature. Therefore, the differential scanning calorimetry studies produce either no peak or a very weak peak associated with this transition.

Moreover, in contrast to the conventional SmA phase, the birefringence of the dSmA phase is smaller than that of the SmC phase. This can be attributed to the azimuthal distribution of molecular long axes in the dSmA phase. The tilt directions get correlated towards one preferred direction in the SmC phase, giving rise to the increased alignment of the molecules and, hence, the increase in birefringence. The temperature variation of the birefringence across the dSmA to SmC transition can be measured experimentally to corroborate the de Vries nature of the SmA phase.

Thus, the dSmA phase can be characterized as follows:

- The layer spacing is smaller than the molecular length, but the optic axis remains parallel to the layer normal.
- There is no significant layer contraction during the deVries SmA to SmC transition, in contrast to the transition from the conventional SmA to SmC phase.
- An increase in birefringence is generally associated with the transition from the deVries SmA to the SmC phase.

Chevron geometry

The conventional SmA phases adopt a molecular arrangement known as the “book-shelf geometry" when confined between two glass substrates, which are treated for homogeneous planar alignments. In this configuration, the smectic layers are approximately perpendicular to the substrates, as depicted in figure 1.8a. The molecules are anchored parallel to the rubbing direction of the confining surfaces, with the smectic layer spacing denoted as d_A (figure 1.8). Across the transition to the tilted SmC phase, the thickness of the layers begins to reduce while the molecules at the surface remain anchored along the rubbing direction. To reconcile both the surface anchoring with thickness d_A and the SmC structure with a reduced layer thickness denoted as $d_C < d_A$, the only plausible solution is the buckling of the layers, forming a chevron geometry [16], illustrated in figure 1.8(b). The chevron geometry allows the layers to adjust their tilt angle and layer spacing, satisfying the requirements of the SmC phase while keeping the molecules anchored along the rubbing direction of the confining surfaces as in the SmA phase. The chevrons of

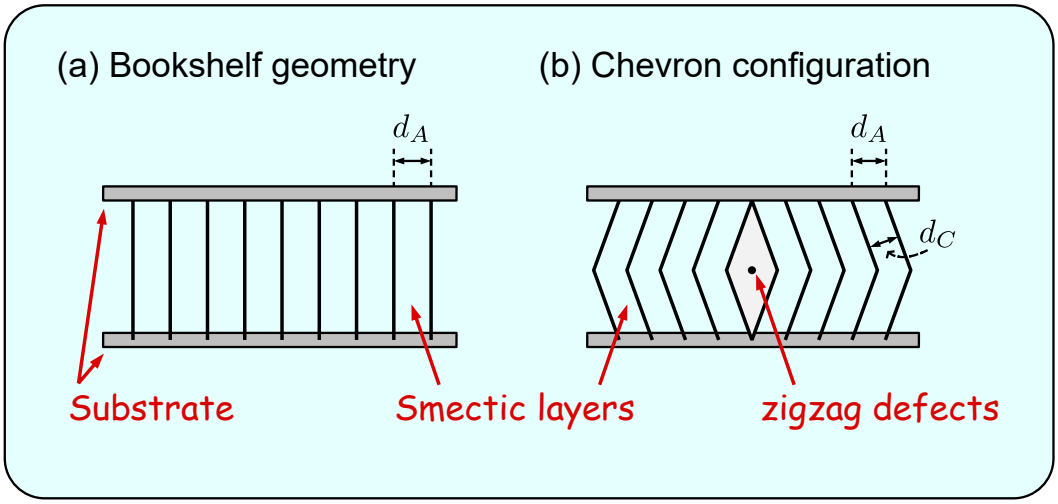

Fig. 1.8: (a) A 'bookshelf geometry' of the homogeneously planar aligned SmA phase with layers perpendicular to the bounding plates. (b) A chevron configuration giving rise to zig-zag defects. It arises due to the buckling of the layers while transitioning from the SmA to the SmC phase.

opposite fold directions, as shown in figure 1.8(b), are separated from each other by so-called zigzag defects. Due to the formation of chevron and zigzag defects, the quality of electro-optic devices based on ferro– and antiferroelectric liquid crystals was found to be degraded. The dSmA phase forming the ferro– or antiferroelectric smectic phase was proven to be a possible solution to this problem. The minimal layer contraction across the dSmA to the SmC phase transition does not produce the chevron structure that is detrimental to the electro-optic devices.

1.1.5 Effects of chirality: Ferro– and Antiferroelectric liquid crystals

The layers in the SmC structure possess C_{2h} point symmetry, i.e., it has a twofold rotation axis orthogonal to the tilt plane and a reflection symmetry parallel to it. This symmetry does not allow a polar order in the smectic layers, and therefore, the SmC phases cannot possess electric polarization. Meyer et al. [17] first conceived the possibility of spontaneous polarization if the constituent molecules are chiral in the SmC phase. The chiral SmC phase is denoted by SmC*. The chirality of the molecules lifts the mirror symmetry of the layers in the SmC phase, giving rise to C_2 point symmetry of the layers. This reduced symmetry of the layers allows a polar order along the two-fold rotation axis (C_2). Thus, the SmC* phase possesses electric polarization within the layers locally along the C_2 direction. Depending on the stacking of the polar order from layer to layer, various possible subphases, such as ferroelectric, antiferroelectric, and ferrielectric phases, have been observed.

1.2 Discotic liquid crystals

Discotic liquid crystals are composed of disk-like molecules, which were initially discovered by Chandrasekhar et al. in 1977 [18]. These disk-like molecules consist of a central aromatic core surrounded by flexible alkyl chains along the periphery and are found to exhibit various discotic liquid crystal phases [19]. Due to this specific geometry, the normals to the disk-like molecules align parallel to each other, and their average orientation is referred to as the director $\hat{n}$.

The disk-like molecules arrange themselves by stacking on top of one another to form columns, and these columnar assemblies can further organize into a two-dimensional lattice structure, leading to a distinct mesophase commonly known as the **columnar phase**. In the columnar phase, the constituent molecules exhibit a fluid-like order along the columns, and the columns organize in a two-dimensional lattice perpendicular to the columnar axes. Depending on the ordering along the columns and the nature of the two-dimensional order, various columnar phases are possible [19]. Moreover, the disk-like molecules can also exhibit pure orientational order, giving rise to a Discotic Nematic (N_D) phase.

1.3 Bent-core liquid crystals (BCLCs)

As discussed above, in the case of chiral smectic phases, molecular chirality reduces the symmetry of the tilted SmC phase sufficiently to allow for the long-range polar order. The discovery of bent-core banana shaped mesogens provided a new route to achieve the macroscopic polar order [20, 21]. A bent-core (BC) banana-shaped molecule is usually made of two rigid rod-like arms of similar lengths joined end to end at an angle of about 120°. This bent or opening angle typically ranges from 90 to 150 degrees. In addition, long flexible aliphatic chains are generally attached at the ends of the molecule to reduce the melting temperature of the compounds and to enhance the smectic ordering. The general molecular structure of a bent-core molecule is depicted in Figure 1.9(a), with two rigid rod-like arms connected to the central bending unit (BU) at a specific opening angle. Two terminal aliphatic chains (R and R′) are attached to each end of the molecule. The central bending unit, lateral rod-like arms, and terminal chains of the molecules significantly influence the properties of mesophases they exhibit. The linking groups in the lateral arms further affect the electron density, flexibility, and partial polarity of the individual molecules.

Figure 1.9(b) shows a schematic model of a symmetric BC molecule viewed

from three different angles. The line joining the two endpoints of the molecule can be considered as the long axis or bow axis of the molecule, and the transverse bent direction of the molecule can be denoted as an arrow axis. For symmetric BC molecules, the long axis is apolar in nature, whereas the molecules have shape polarity along the arrow axis. Thus, the individual molecules possess C_{2v} point symmetry with a 2-fold rotation symmetry about the arrow axis and a mirror plane containing the two rigid arms (figure 1.9(b), center). The presence of the mirror plane symmetry makes the individual molecules achiral in nature. The 90° clockwise and counterclockwise rotated view of the BC molecule at the center is shown at the left and right of figure 1.9(b), respectively. The *cross* and *dot* symbols represent that the arrow axis of the molecules is pointing downward and upward, respectively. The tapering ends of the arms represent that the arm is going away from the viewer. Because of their bent shape, the BC molecules generally possess non-zero dipole moments along the transverse direction, i.e., along the arrow axis. These model structures of the BC molecule will frequently be used in this thesis to represent the molecular organization in their mesophases.

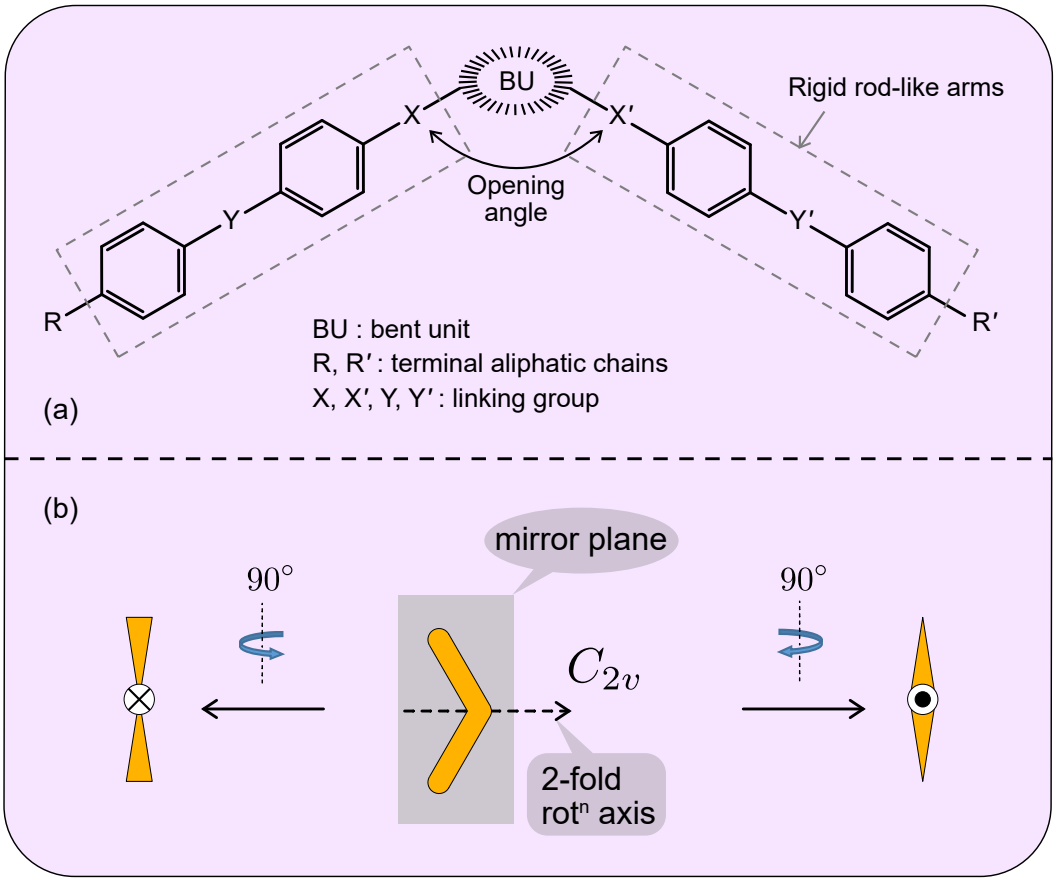

Fig. 1.9: (a) A typical molecular structure of bent-core banana shaped liquid crystal. (b) Schematic representation of a bent-core molecule when viewed from three different directions. The cross and dot symbols represent the arrow axis pointing downward and upward, respectively.

The first bent-core mesogens were synthesized in the early twentieth century by Vorländer, who reported low thermal stability of these compounds compared to its calamatic analogs [22]. The mesophases, however, were not characterized, and the molecules were termed bad rods. The bent-core liquid crystal garnered significant attention in 1996 after Niori et al. [20] reported a breakthrough polar switching behavior in a compound comprised of such achiral molecules. The bent conformation of the BC molecules leads to steric hindrance, stopping the free rotation about their long axes. The BC molecules preferentially align parallel to each other within the smectic layers, with the arrow axes, on average, pointing in a direction orthogonal to the layer normal. This gives rise to *spontaneous polarization* within the layers. The linear coupling of the polarization with the external field makes these materials valuable in fast-switching devices [23]. In addition to the polar order within the layers, when the average orientation of the long axes of the BC molecules, i.e., the director $\hat{n}$ is tilted away from the layer normal in a plane orthogonal to the polar order, the mirror symmetry of the layers is lost. This results in *macroscopic layer chirality* in the system [21], even though the constituent molecules are achiral. Due to the interplay between polarity and chirality, the bent-core liquid crystals exhibit remarkably distinct optical and electro-optical properties and a wide range of phase behavior [23, 24].

1.3.1 Orthogonal smectic phases of BC molecules

In orthogonal smectic phases, the long axes of the BC molecules align on average parallel to the layer normal with layer spacing comparable to the molecular length [23, 25]. In addition, the arrow axes align on average along a direction within the plane of the layer. Such arrangement of the molecules results in a layer with local polarization within the plane of the layer. Thus, the layers exhibit C_{2v} point symmetry and are designated as SmAP configuration, where *P* denotes the layer polarization. Depending on the stacking of such SmAP layers, the following three types of orthogonal smectic phases have been found.

- **$SmAP_F$:** When the polarization direction in the adjacent smectic layers aligns on average parallel to each other (see figure 1.10), the phase is termed as ferroelectric $SmAP_F$, where subscript *F* stands for ferroelectric ordering. Sekine et al. [26] first proposed the existence of orthogonal SmA phase with transverse polar order having C_{2v} symmetry of the layer and later ferroelectric $SmAP_F$ type of order was observed experimentally [27].

- **$SmAP_A$:** If the direction of layer polarization alternates in successive layers (figure 1.10), the phase is denoted as $SmAP_A$, where subscript *A* stands for

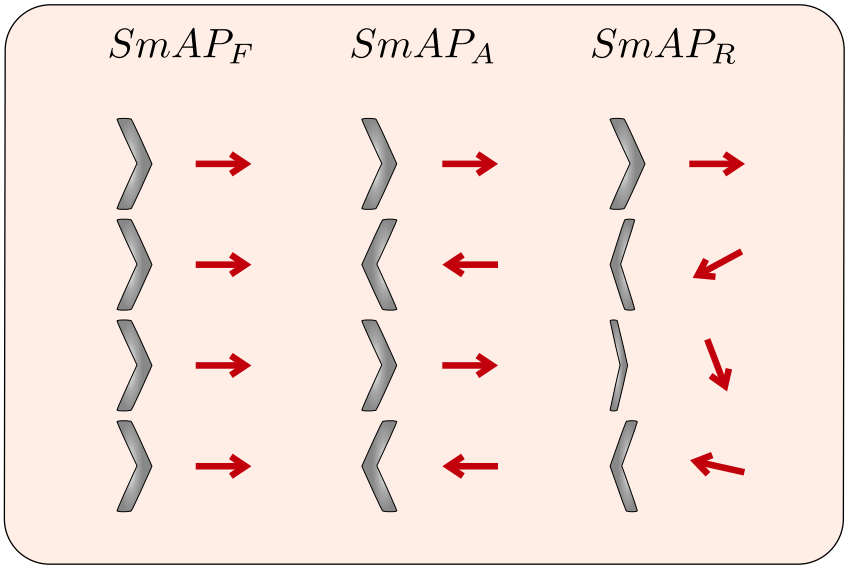

Fig. 1.10: A schematic representation of the arrangement of bent-core molecules in different orthogonal smectic phases.

antiferroelectric ordering between the layers. A compound exhibiting $SmAP_A$ phase has also been found experimentally [28].

- $SmAP_R$: In the $SmAP_R$ phase, the smectic layers are polarized in the plane of the layers, but the relative orientation of the polarization direction is random from layer to layer (see figure 1.10). A few compounds have been found experimentally exhibiting $SmAP_R$ phase [29–31].

1.3.2 Tilted smectic phases of BC molecules

Most of the mesophases exhibited by BC molecules are tilted smectic phases. In the tilted smectic phases, the director $\hat{n}$ tilts away from the layer normal $\hat{k}$ with layer spacing significantly smaller than the molecular length. The molecular configuration in the tilted smectic phase of BC molecules can be characterized by three vectors: director $\hat{n}$, layer normal $\hat{k}$, and polarization $\vec{P}$. Depending on the relative orientation of $\hat{n}$, $\hat{k}$ and $\vec{P}$, the order in the layers of the tilted smectic phase can be classified as follows:

(a) SmCP phases

In 1997, Link et al. [21] published their seminal work on BC compounds under the application of electric field, reporting a tilted antiferroelectric phase. The study identified two key spontaneous symmetry-breaking instabilities: layer polarity and macroscopic chirality induced by achiral molecules due to the tilted molecular

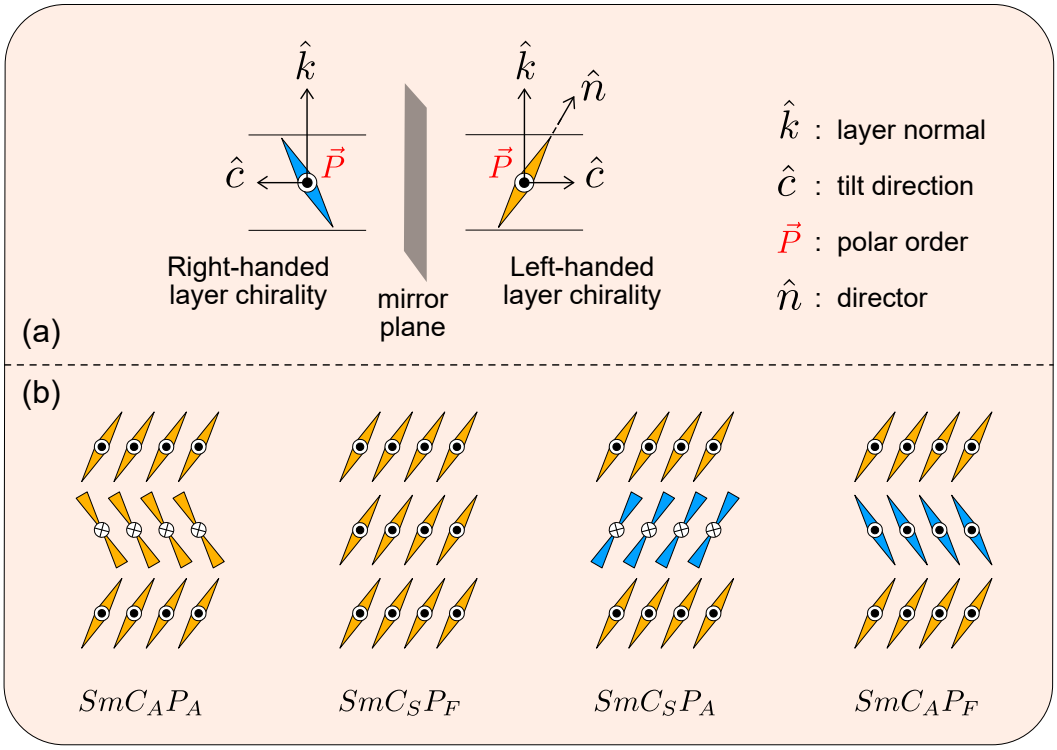

Fig. 1.11: (a) Schematic representation of tilted molecular configuration in a layer. The layer normal ($\hat{k}$), tilt direction ($\hat{c}$), and polar order ($\vec{P}$) are orthogonal to each other, giving rise to a particular handedness of the layers. (b) Schematic representation of the arrangement of bent-core molecules in different tilted smectic phases (B2 phase). Yellow and blue colors represent left-handed and right-handed layer chirality, respectively. The notations used have the following meaning: $C_A \rightarrow$ anticlinic tilt, $C_S \rightarrow$ synclinic tilt, $P_A \rightarrow$ antiferroelectric polar order, and $P_F \rightarrow$ ferroelectric polar order.

organization in the layers. In this SmCP layer order, $\vec{P}$ aligns perpendicular to the tilt plane of the molecules, as shown in figure 1.11(a). In this illustration, the tilt plane lies in the plane of the page, and $\vec{P}$ is oriented out of the page. This configuration of the molecules gives rise to macroscopic layer chirality, exhibiting two-handedness determined by the relative orientations of the polarization and tilt direction with respect to the layer normal, as also depicted in figure 1.11(a). The symbol *C* and *P* in the SmCP order denote the tilt and layer polarization, respectively. The SmCP phase stands out as the first example of spontaneous chiral symmetry breaking occurring in a bulk state of a liquid [23, 32].

The stacking of SmCP layers gives rise to four different types of structures based on the tilt and polarization directions in successive layers (see figure 1.11(b)) and are commonly known as *SmCP* or *B2 phase*. When the tilt direction is the same from layer to layer, the phase is denoted as synclinic and labeled as C_S. Conversely, if the tilt alternates in direction from layer to layer, the phase is termed anticlinic and designated as C_A. Similarly, if the polarization vectors align parallel to each other from layer to layer, the phase is classified as ferroelectric and is denoted by

P_F. In contrast, when the polarization vectors align antiparallel in the adjacent layers, the phase is identified as antiferroelectric (P_A). Consequently, there are four distinct tilted polar smectic phases, namely SmC_AP_A, SmC_SP_F, SmC_SP_A, and SmC_AP_F, as illustrated in figure 1.11(b). Additionally, these phases are termed as *homochiral* and *racemic* depending on whether the layer chirality remains uniform or alters between the successive layers, respectively. Thus, SmC_SP_F and SmC_AP_A are homochiral, and SmC_SP_A and SmC_AP_F are racemic in nature. The homochiral and racemic domains lead to different textural appearances and can clearly be distinguished using polarization optical microscopy. The x-ray diffraction patterns of the SmCP phase are similar to that of smectic phases, i.e., it consists of small-angle sharp peaks in addition to a wide-angle diffusive peak [26].

The SmCP phases typically show antiferroelectric ground states [21]. This is due to the fact that usually, SmCP phases exhibit large layer polarizations (P $>$ 2 mC/m^2), and uniform polarization introduces higher free energy. One way to escape from the uniform polarization is to form alternate polar ordering in the adjacent layers, i.e., the antiferroelectric phase. Under the application of a sufficiently strong electric field, the antiferroelectric state switches to the ferroelectric one. It has been observed experimentally that during electric field-induced switching, the majority of BC compounds exhibiting SmCP phases preserve their chirality where molecules rotate about the layer normal. Nevertheless, for compounds having moderately long terminal chains (12 $<$ n $<$ 16 carbon atoms), the molecules rotate about their long axes under an applied electric field, and the layer chirality changes [24]. In experiments, the ferroelectric and antiferroelectric phase can be distinguished by switching current measurements where a single and double switching current reversal peaks appear [23, 33] under the application of a triangular wave voltage (see section 2.7 for experimental details). In addition to compounds showing ferroelectric and antiferroelectric switching, some BC materials have been found to exhibit multi-state ferrielectric-like switching [24]. However, till now, no ground state ferrielectric phases have been found in BC liquid crystals.

(b) SmTP phases

Another theoretical possibility for an arrangement of BC molecules in the layers is that the polarization $\vec{P}$ remains in the tilt plane. This phase is termed the 'leaning' or 'tipping' phase and is denoted by *SmTP*. Different combinations of tilt and polarization in the adjacent layers give rise to four possible structures, namely SmT_SP_A, SmT_AP_A, SmT_AP_F, and SmT_SP_F, as depicted in figure 1.12. The subscripts are defined in a similar way as in the case of the SmCP phase. In the SmTP configurations, the tilt plane of the molecules acts as a mirror plane, and the symmetry of the layer is C_S. Thus, the presence of mirror plane symmetry

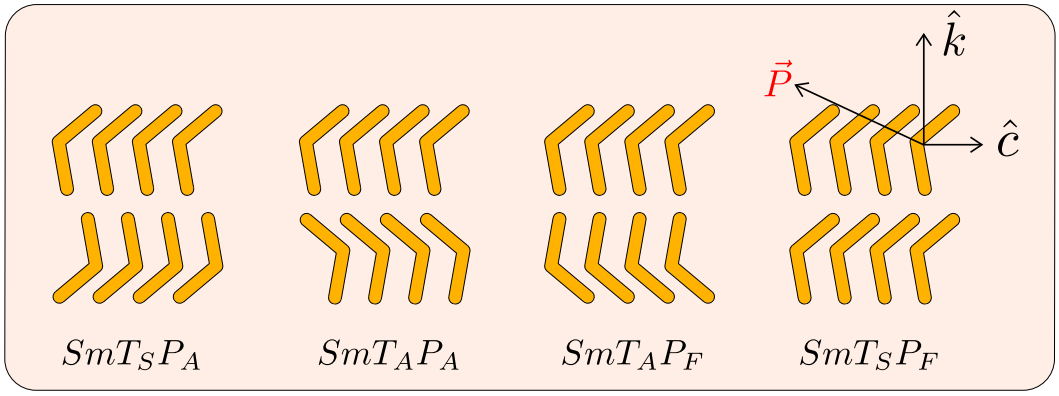

Fig. 1.12: Schematic diagram of the molecular configuration in four possible structures for **leaning phase**. Here, the molecular long axes are leaned (tilted) with respect to the layer normal in a way that the polar order remains in the tilt plane. These structures are achiral in nature.

renders the SmTP phases as achiral in nature. The existence of the SmTP phase was predicted theoretically by Emelyanenko et al. [34], but no experimental evidence has been found for symmetric BC compounds exhibiting SmTP phase. In recent years, a few BC compounds comprised of strongly asymmetric molecules have been found to exhibit SmTP-like ordering [35–37].

(c) SmC_G phase

Finally, the smectic phase of BC molecules can have a more general structure where the polarization $\vec{P}$ is neither parallel nor perpendicular to the tilt plane, i.e., $\vec{P}$ orients at an oblique angle with respect to the plane of $\hat{n}$ and $\hat{k}$. This phase was first predicted by de-Gennes [7] for biaxial molecules and is called the general *SmC_G* phase. In the smectic phase of BC molecules with layer polarization pointing in a general direction, the layer order is termed as *$SmCP_G$*, where the BC molecules acquire both tilted and tipping organization in the layers [24]. The $SmCP_G$ layers possess triclinic C_1 point symmetry [38]. Based on whether the tilt, the tipping, and the polar order remain the same or alternate from layer to layer, there are eight possible structures in the $SmCP_G$ phase. A detailed schematic diagram of these structures in $SmCP_G$ phase can be found in references [39] and [24]. The experimental evidence of $SmCP_G$ phase has been reported in free-standing films [40] as well as in the bulk samples [41–43]. The $SmCP_G$ compounds essentially exhibit ferroelectric structure, though a few examples of antiferroelectric order have also been found [41].

1.3.3 Modulated smectic phases of BC molecules

As we discussed earlier, the macroscopic uniform polarization in the smectic layers introduces higher free energy. If the polarization is large enough in the ferroelectric $SmCP_F$ phases (P_0=1 mC/m^2 [24]), a splay in the polar order is introduced in order to escape from uniform polarization. Since the splayed polar order of a given sign can not extend infinitely in the layer plane, it leads to the formation of stripes of alternate signs of the splayed polar order with reduced packing efficiency. The width of these stripes lies in a few tens of nanometers, and they are separated by defect walls at their edges. To incorporate these defects, the layers undulate periodically to form a *polarization-modulated smectic phase* $SmCP_{mod}$ or so-called *B7* phase [44–46]. In other words, due to the presence of defect walls, the molecular tilt decreases at the edges of the stripes. This results in the variation of the layer thickness locally and drives the undulation of the smectic layers. Based on the combination of the polarization, the slope of layer undulation, and the continuity of layers across the defect walls in neighboring stripes, a number of structures are possible for the B7 phase [46]. One possible structure with the antiferroelectric

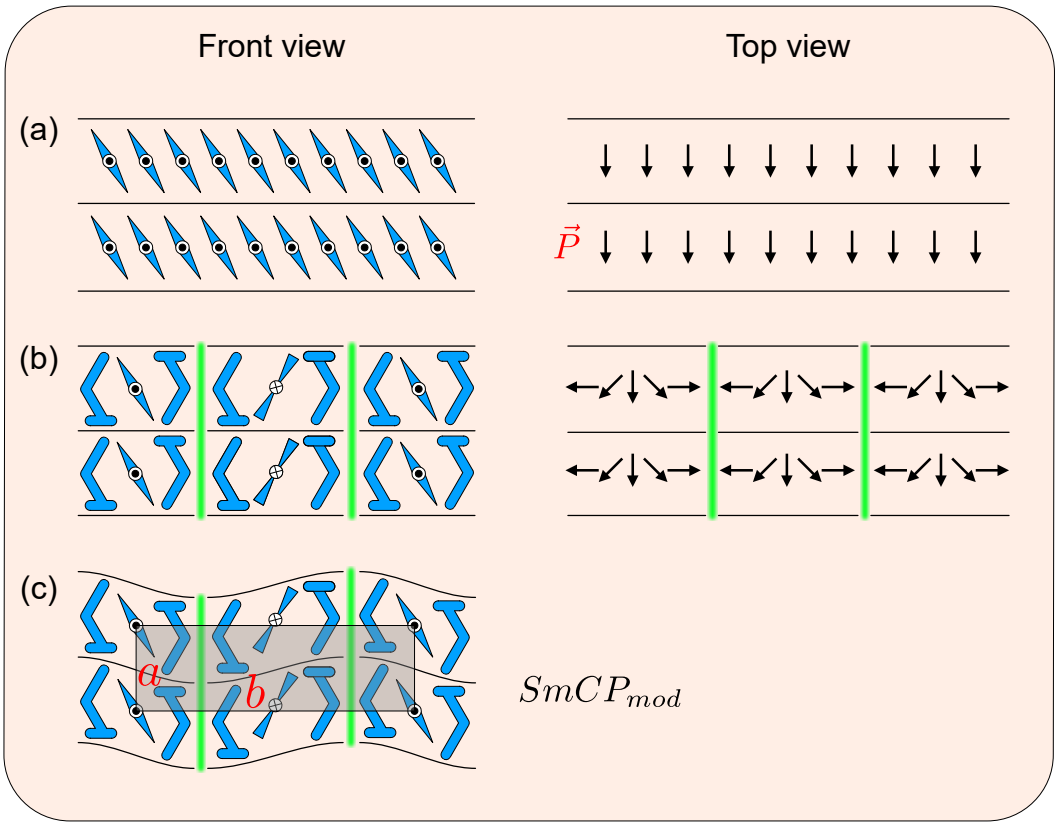

Fig. 1.13: (a) Schematic representation of SmCP layers having uniform polar order. For large polarization, the splay of polar order takes place, resulting in stripes separated by defects (b). To incorporate these defects, the layers undulate at the edges of the stripes and form $SmCP_{mod}$ phase (c). a and b are the lattice parameters corresponding to the rectangular lattice structure.

organization of $SmCP_{mod}$ phase is shown in figure 1.13. For a strong enough applied electric field, the modulated polar order can sometimes be forced to align towards the applied field, resulting in a uniform layer structure, i.e., the $SmCP_{mod}$ phases often undergo a transition to SmCP phase above a threshold field.

The undulated smectic phases exhibit a variety of textures under crossed polarizers such as myelinic, checker-board, banana leaf, ribbons, and screw filaments [47]. In some cases, these textures can be modified into a fan-like texture typically observed for the SmCP phase by applying a high enough electric field. The $SmCP_{mod}$ phases can be distinguished from the SmCP phase based on x-ray diffraction (XRD) studies. The XRD pattern is accompanied by sharp reflection peaks in the small angle region along with a diffuse wide angle peak corresponding to the lamellar structure of $SmCP_{mod}$ phase. In addition, a number of weak satellite peaks are also observed in small-angle regions associated with undulation along the layers. These undulations give rise to two-dimensional lattices and the XRD peaks can often be indexed using rectangular (lattice parameters a and b, and a vertex angle $\gamma = 90°$) [44, 45, 48] or oblique lattices (a, b, and $\gamma \neq 90°$) [49, 50]. The polarization usually increases with decreasing temperature, which results in an increase in splay. Hence, the undulation wavelength in the $SmCP_{mod}$ phase is usually found to increase with decreasing temperature [42]. In addition to XRD studies, the stripe of the $SmCP_{mod}$ phase can also be directly visualized using freeze-fracture transmission electron microscopy (FFTEM) [44]. The width of the stripes found in FFTEM was shown to agree with the undulation wavelength calculated from the XRD studies.

1.3.4 Columnar phases of BC molecules

The columnar mesophases are usually formed by disk-shaped molecules, as discussed earlier 1.2. Interestingly, some bent-core mesogens are also found to exhibit columnar phases. There are broadly two categories of columnar phase composed of bent-core molecules [23]. The first one is a columnar phase formed from a two-dimensional ordering of broken layer fragments, which could be understood by continuing the discussion of the $SmCP_{mod}$ phase. The large polarization in the layers leads to splay order, which results in the formation of finite-size stripes separated by defects at the edges. For the compound usually having short terminal chains [51], the stripes (layer fragments) slide halfway through the layers in order to incorporate the defects. This leads to the formation of a two-dimensional columnar structure as shown in figure 1.14 and also referred to as **B1** phase. The second type of columnar phase is formed by stacking disk-like assemblies comprised of bent-core molecules. It was argued that the splay of polarization is the basic driving mechanism in the formation of layer undulated smectic phase as well as columnar phases comprised

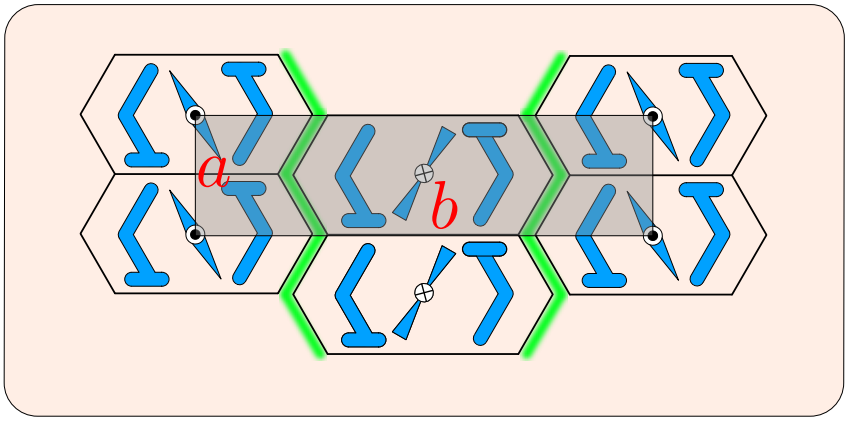

Fig. 1.14: Schematic representation of columnar phase where stripes slide halfway through the layers to exhibit two-dimensional ordering. Along the columns, the molecules have a fluid-like order.

of bent-core molecules [46]. Usually, the B1 phase does not respond to an applied electric field. In some cases, however, the B1 phase is known to exhibit polarization switching at high enough fields (E $>$ 15 V/μm). This reorientation of polarization was explained by models [49, 52, 53] in which the arrow axes of the BC molecules lying perpendicular to the column axis align parallel to the column axis leading to so-called $B1_{rev}$ phase.

The XRD patterns obtained for columnar phases are also indexed by two-dimensional lattices similar to $SmCP_{mod}$ phase. However, the XRD patterns are slightly distinct, as the (1 1) reflection peak in the case of columnar phases is often more substantial. Another distinct property of XRD results in columnar phases is that the lattice parameter b, perpendicular to the average long axes of the molecules, does not vary with temperature, unlike in the case of $SmCP_{mod}$ phase. Depending on the order of polarization and the nature of lattices, a number of columnar phases are possible [23, 24, 26, 54, 55].

1.4 Glass transition in liquid crystals

Glasses are disordered materials that have the liquid-like translational ordering of the constituent molecules but mechanically behave like solids. The formation of a glassy state is often found to occur in various natural phenomena [56–59]. It is also vital for numerous applications, including pharmaceutical [60], food processing [61], polymers [62], and the preservation of insect life under dehydration [63], among others [63–66]. In addition, the glass transition is a long-standing fundamental problem yet to be properly understood [67, 68]. The glass formation can take place by many routes [69], a conventional one of which is rapid enough cooling of a

liquid phase to avoid the nucleation and growth process of crystallization. The liquid appears frozen on the time scale of experimental observation. Although this process of glass formation has been known for centuries, the exact molecular dynamics that lead to this frozen liquid state are still not fully understood. Rapid cooling is required for glass formation in most liquids. However, some organic liquids [70], polymers [69], and liquid crystals [71] can exhibit glass transition at a moderate cooling rate. This is probably because of the relatively longer constituent molecules, which are hard to crystallize.

In the glass-forming liquid crystal, the orientational order can be frozen by preserving the direction of order by some external means (strong anchoring or applied electric/magnetic field) while cooling the system. This allows the formation of partially ordered glasses retaining all the qualitative features of the liquid crystal phase, which could be exploited in possible applications such as wave plates, holography, and optical storage [72]. A large number of studies can be found on glass formation and molecular dynamics studies for calamatic liquid crystals [72–78]. However, there are very few reports on glass-forming bent-core liquid crystals [79]. Recently, it has been pointed out that for some materials while cooling from the high-temperature nematic phase, the lower temperature smectic transition can be frustrated or completely circumvented to produce glasses with tunable liquid crystalline order that can be utilized in organic electronic applications [80, 81].

Glass is usually identified by its high value of viscosity in the range of $10^{12} - 10^{14}$ Pa/sec, as proposed by Angell [69, 82]. The increase in viscosity is associated with the dynamic slowdown of the constituent units. In other words, the relaxation time corresponding to different modes in the system becomes very large. The viscosity or the relaxation time is generally controlled by temperature. The relaxation time is extremely sensitive to temperature in the vicinity of the glass transition. The temperature dependence of relaxation time provides a useful classification of glassformers along a 'strong' to 'fragile' scale [69]. The former shows an Arrhenius dependence of the relaxation time on temperature, whereas the latter deviates from the Arrhenius behavior. The temperature variation of relaxation time for silica follows the Arrhenius dependence [69] given by,

$$\tau = A \exp\left(\frac{E_a}{K_B T}\right) \tag{1.10}$$

where, A is a pre-exponential factor, E_a is temperature independent activation energy and K_B is Boltzmann constant. Many other liquids show deviations from the Arrhenius behavior and exhibit a more pronounced viscous slow-down close to the

glass transition following Vogel–Tammann–Fulcher (VTF) equation [66] given by,

$$\tau = \tau_\infty \exp\left(\frac{D\,T_0}{T - T_0}\right) \tag{1.11}$$

where τ_∞ is a pre-exponential constant, T_0 is Vogel temperature, and D is a constant that determines the deviation of the system away from the Arrhenius behavior, i.e., the fragility of the system. Furthermore, especially in the case of liquid crystalline glassformers, it has been shown [83–85] that the relation

$$\tau = \tau_0 (T - T_x)^{-\gamma} \tag{1.12}$$

can be used to better portray the behavior of relaxation time in accordance with the mode coupling theory (MCT) [86, 87] in comparison with the VFT relation. Here T_x denotes the MCT singular temperature describing a hypothetical crossover from the ergodic to the non-ergodic regime, and the exponent $2 < \gamma < 4$ is a non-universal parameter [86].

The glass transition can sometimes be detected experimentally by differential scanning calorimetry studies. The heat capacity of the glassformers increases at the glass transition, which corresponds to a step change in the heat flow curve observed in calorimetry measurements. Additionally, dielectric measurements provide an excellent tool to measure the relaxation time associated with different molecular dynamics in liquid crystalline systems. The details of a bent-core liquid crystal exhibiting glass transition will be discussed in Chapter 4 of this thesis.

1.5 Nucleation and growth of mesophases

The nucleation and growth of phases in condensed matter systems have been a subject of steady scientific interest to study the phase ordering processes [88]. Nucleation occurs when a small nucleus begins to form from the constituent components in the less ordered phase. This process typically occurs in response to changes in temperature, pressure, or other external factors that drive the system away from its equilibrium state. Following nucleation, the growth process involves the enlargement and organization of the nuclei into larger, well-defined structures. The nuclei with radii greater than a critical size then grow spontaneously as the constituents (atoms or molecules) from the less ordered phase are attached to it and transform into the higher ordered phase. The study of nucleation and growth plays a significant role in determining the characteristics of the structures.

In condensed-matter systems, the growth of a daughter phase can take a

variety of different forms while quenching the system from the higher temperature phase [89]. The growth displays nearly perfect single crystals in the semiconductor industry, spherulitic structures in the crystallization of polymers, and dendritic and fractal structures predominantly observed in soft matter systems such as colloids and polymers [90]. In addition to the wide variety of phases, the nucleation and growth of liquid crystalline phases in its isotropic melt on cooling provides a unique opportunity to study these processes. The conventional smectic phases grow as a so-called *batônnet* structure when cooled from their isotropic phase due to the anisotropic lamellar order of the system [91]. It has been argued that the growth along the layer normal direction is more dominant compared to the growth in the layer plane direction. In other words, the formation of smectic layers is favored over the growth of individual layers. This preference leads to the formation of shape-anisotropic batônnet aggregates with an aspect ratio on the order of 5:1 [91]. These batônnet structures tend to minimize their interfacial energy during their growth process and produce compact domains. Nevertheless, Dierking et al. found that some calamatic [92] and BC liquid crystals [91, 93, 94] exhibit highly irregular domains of mesophases with fractal structure when quenched from their isotropic phase.

The concept of fractal geometry was invented to analyze complex patterns that often emerge in various physical systems, including polymer networks [95], aggregation and growth phenomena [96], Brownian motion [97] and neural networks in brain [98], among others [99]. The fractal dimension of such structures and aggregates provides valuable information about the growth process and the underlying mechanism. A few studies have been carried out on the fractal growth of liquid crystalline phases [92, 93, 100, 101] and compared with the simulated fractal patterns [92] using percolation mechanism [102]. However, the physical relevance of this percolation mechanism for such fractal growth processes in LCs is yet to be understood.

The concept of *fractal (Hausdorff) dimension* plays a crucial role in the study of fractal structures, which can take non-integer values, unlike classical Euclidean dimensions having integer values such as 1, 2, or 3. To define the fractal dimension, let us start with two-dimensional Euclidean shapes. For a circle of radius R, the circumferential length is $2\pi R$, and the area bounded by the disc is πR^2. Based on this, it follows that

$$(length) = \sqrt{4\pi}\,(area)^{1/2} \tag{1.13}$$

The corresponding relation for squares will be

$$(length) = 4\,(area)^{1/2} \tag{1.14}$$

Thus, in two dimensions, the $length$ varies as the square root of $area$. Mandelbrot proposed a relation between $area$ and $length$ for fractal structures [103] in two dimensions given by,

$$(length) \propto (area)^{D_p/2} \tag{1.15}$$

here, D_p is the area-perimeter dimension. For a 2-dimensional Euclidean surface, the D_p value should be 1, whereas $D_p > 1$ indicates the fractal nature of the surface.

Chapter 5 of this thesis presents a discussion on the nucleation and growth of a liquid crystalline phase comprised of BC molecules. We used eqn. 1.15 to compute the area-perimeter dimension D_p of growing smectic domains.

2 Experimental techniques

This chapter aims to provide a comprehensive overview of the experimental methodologies utilized to characterize the mesomorphic behavior of the liquid crystal compounds studied in this thesis.

2.1 Differential scanning calorimetry

Differential scanning calorimetry (DSC) is a widely used technique for thermal analysis of materials. In particular, it measures the heat flow associated with physical transformation, such as phase transitions in a sample as a function of temperature. This technique can be used to observe the first-order phase transitions as well as the glass transitions of the samples. Usually, two types of techniques, namely *Heat-flux* and *power compensating* methods, are used in DSC measurements. The former measures the difference in heat flux between the sample and a reference, whereas the latter monitors the difference in power supplied to the sample and a reference.

In our experiments, a commercially available power-compensating DSC setup was utilized. The instrument consists of two sample holders (aluminium crucibles), one containing the sample of interest and the other kept empty, acting as a reference. Both the sample holders are subjected to identical temperature conditions throughout the experiment. When the sample undergoes a physical transformation such as a first-order phase transition, it will require more heat (for the endothermic process) or less heat (for the exothermic process) than the reference to maintain the same temperature of both the sample and reference. For example, if the sample melts from a crystal to a liquid phase, more heat flow to the sample is required than the reference. The absorption or release of heat by the sample during the endothermic or exothermic processes, respectively, are measured during heating and cooling. The plot of measured heat flow as a function of temperature is termed a DSC thermogram. A typical DSC thermogram while heating and cooling a liquid crystalline sample at a rate of 5 K/min is shown in figure 2.1. The observed peaks correspond to various phase transitions. A phase is termed *monotropic* if it appears only on the cooling cycle. On the other hand, if a phase appears both in the heating and cooling cycle, it is known as the *enantiotropic* phase. Since the experiments are executed under constant pressure conditions, the area under the curve in the DSC thermogram

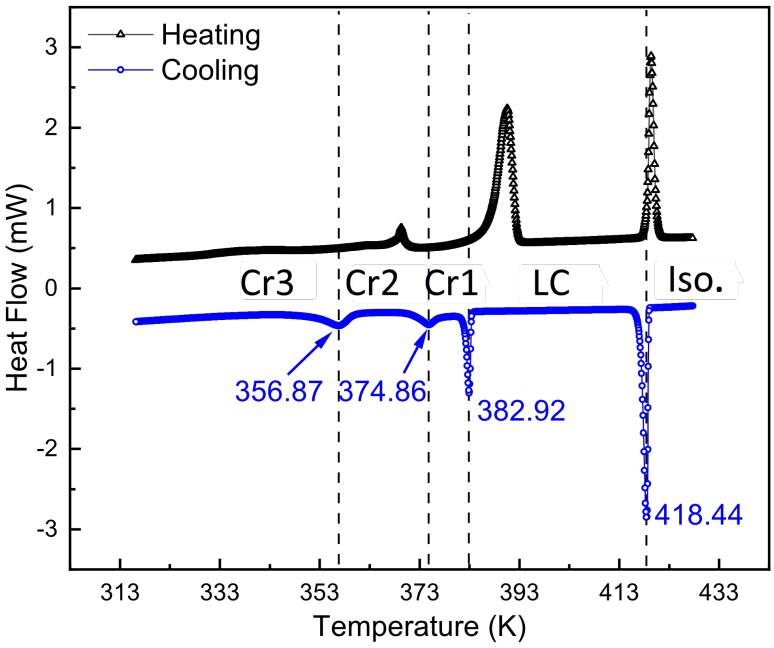

Fig. 2.1: The typical DSC thermogram of a compound 8OBF12 (discussed in chapter 3) while heating and cooling the sample at a rate of 5 K/min. The peaks correspond to various phase transitions.

provides the change in enthalpy corresponding to the first-order phase transitions and is given by,

$$\Delta H = \int_{t_1}^{t_2} \left(\frac{dH}{dT}\right)_p dT = \int_{t_1}^{t_2} \left(\frac{dQ}{dT}\right)_p dT = \Delta Q \tag{2.1}$$

where p denotes the pressure.

The glass transition can also often be detected using DSC. This transition takes place when a liquid is cooled sufficiently fast to avoid crystallization and form a disordered solid. Thus, the glass transition is not a thermodynamic phase transition. During this transition, the heat capacity of the sample changes, and it appears as a step change in the heat flow of the DSC thermogram.

In this thesis, we employed a commercially available DSC setup ($Mettler\ Toledo\ DSC\ 3$) to study the phase transition of our samples. This DSC setup is capable of scanning the samples in a temperature range of 233 K to 873 K with rates varying from 0.01 K/min to 200 K/min. The sample was kept in a small aluminium crucible ($Mettler\ Toledo$) and sealed. The empty and filled crucibles were then weighed and kept in the DSC setup to measure the heat flow, giving rise to the DSC thermogram. The peak or dip positions in the thermogram indicate the transition temperatures with a temperature resolution of about 0.12 K.

2.2 X-ray diffraction

The X-ray diffraction (XRD) technique is a versatile and vital tool for investigating the positional and/or orientational order of molecular organization in crystalline materials. The diffraction takes place when the wavelength of the x-ray is comparable with the spacing between parallel lattice planes in the crystal. The constructive interference occurs when the path difference between the diffracted rays is an integer multiple of λ and is determined by the condition of Bragg's law [104],

$$2d_{hkl}\,\sin\theta = n\lambda \tag{2.2}$$

where d_{hkl} is the separation between the lattice planes having Miller indices (hkl), 2θ is the scattering angle, n is any integer, and λ is the wavelength of the incident x-ray beam. The diffraction pattern obtained experimentally can be analyzed to determine the crystal structure of the sample of interest.

In our experiments, a $DY\ 1042 - Empyrean\ (PANalytical)$ diffractometer with CuK$_\alpha$ radiation of wavelength 1.54 Å was utilized to acquire the x-ray intensity profile of the samples. The diffractometer was equipped with a $PIXcel$ 3D detector. In their liquid state, samples were filled in Lindemann capillary tubes with an outer diameter of 1.0 mm, which were then flame-sealed for the XRD measurements. A hot stage and a temperature controller ($Linkam$-T95) were used to maintain the temperature of the samples during the measurements with a temperature resolution of 0.1 K. The samples were initially heated to the isotropic phase, and the XRD

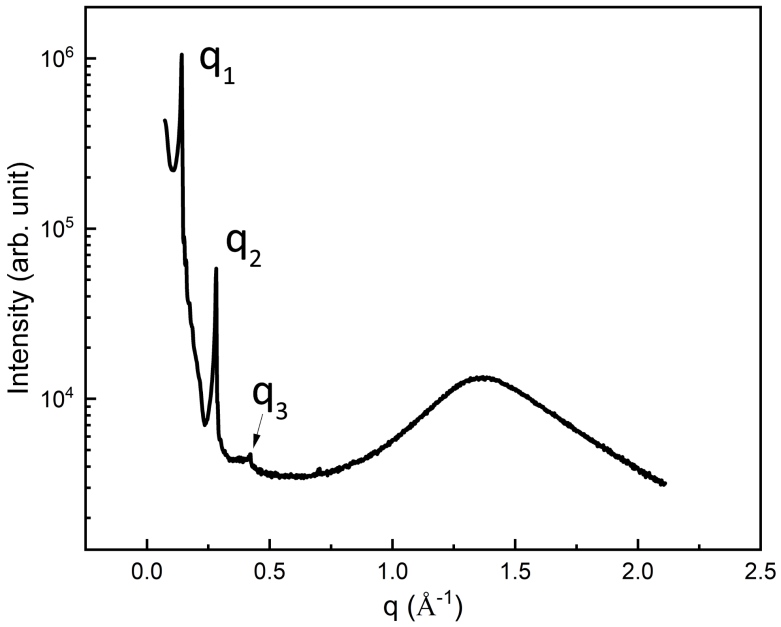

Fig. 2.2: A typical XRD intensity profile characteristic of a smectic phase.

intensity profiles were acquired by subsequently cooling the sample to the desired temperatures. The sample was exposed to incident x-rays for sufficiently long duration of time (about 45 minutes) to minimize the error in the intensity profile. The peak positions in the intensity profiles were determined from the angular position of the detector. The angular resolution of the instrument is 0.026°.

A typical XRD intensity profile as a function of wave vector observed for a smectic phase of a liquid crystalline sample is shown in figure 2.2. The sharp peaks in the small angle region with scattering vector q in the ratio of 1:2:3 indicate a lamellar configuration of the molecules. A diffuse peak in the wide-angle region corresponds to a weak lateral correlation of the molecules and suggests an intralayer fluid-like order.

2.3 Construction of liquid crystal cells

In general, without any special care, the orientation of the director $\hat{n}$ of liquid crystalline samples usually varies gradually in space depending on the boundary conditions. In order to study the physical properties of the liquid crystalline sample, it is often useful to have uniformly aligned director $\hat{n}$ in a preferred direction. This preferred direction of the director can be achieved in liquid crystal cells made of two parallel glass plates separated by a distance. We employed commercially available as well as custom-made LC cells for our experimental studies. In most experimental studies, two types of liquid crystal cells were used based on specific types of alignments, namely *homogeneous planar* and *homeotropic* alignment.

2.3.1 LC cells for homeotropic alignment

In the homeotropic alignment, the director $\hat{n}$ of the liquid crystalline phase aligns perpendicular to the glass substrates, as shown in figure 2.3. Indium-tin-oxide (ITO) coated glass plates with a thickness of 0.5 mm were utilized to construct cells facilitating homeotropic alignment of the anisotropic molecules. The ITO coating facilitates the application of an electric field while maintaining the optical transparency of the glass plates. A thin coating of long-chain molecules such as octadecyl triethoxy silane (ODSE) is generally used for homeotropic alignment. These long-chain molecules are amphiphilic in nature, i.e., the constituent molecules are comprised of a polar head group with a long aliphatic chain attached to it. The polar silane head group of ODSE gets attached to the glass substrate, and the aliphatic tail interacts with the alkyl chain of the liquid crystal molecules. This results in a perpendicular alignment of director $\hat{n}$ with respect to the glass plates.

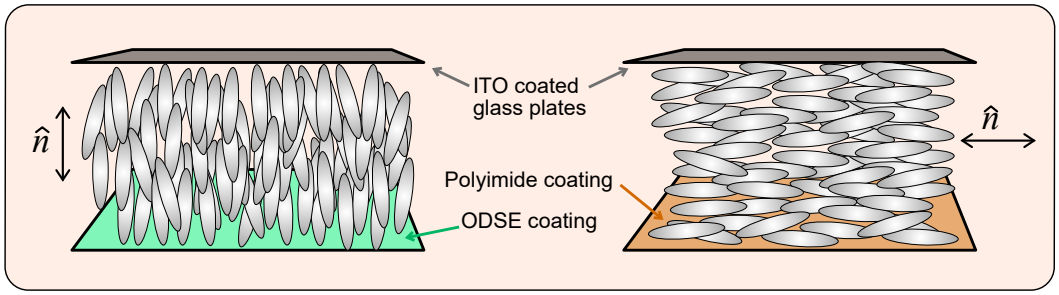

Fig. 2.3: Schematic representation of homeotropic (left) and homogeneous planar (right) alignment of director $\hat{n}$.

The rectangular (or circular) ITO electrode pattern is usually etched on the plates, creating a known active electrode area. These ITO glass plates were then coated with 0.1% solution of ODSE in toluene and then cured at 423 K for an hour. Subsequently, the glass plates were cut to the required size to make the LC cells. The plates were assembled on top of each other, ensuring that the active electrode areas overlap and the ITO coated electrodes are on the inner surface of the cells. The separation between glass plates was maintained using mylar spacers of known thickness or glass beads mixed with epoxy glue at the edges, followed by curing at 423 K for 45-60 minutes.

2.3.2 LC cells for homogeneous planar alignment

In homogeneous planar alignment, the director $\hat{n}$ aligns parallel to the glass substrates along a preferred direction, as shown in figure 2.3. A thin coating of Polyimide (PI) on glass plates is generally utilized to achieve homogeneous planar alignment. A 0.1% solution of the imide monomers of Polyimide was prepared in N-Methyl-2-pyrrolidone or methyl carbitol solvent. A thin uniform coating of this solution on the glass plates was formed using a spin coater or by dragging with a clean cylindrical glass rod. The PI coated plates were then baked at 531-553 K for an hour, which polymerized the monomers to form the PI coating. Subsequently, the coated surface was rubbed unidirectionally for homogeneous planar alignment of the anisotropic molecules. It is believed that the rubbing action produces micro-grooves, which favors the homogeneous planar alignment of the molecules.

The separation between the glass plates of the LC cells can be accurately measured using an interferometric spectroscopic technique. A fiber optic spectrometer (*Ocean Optics* S-2000) was utilized for sample thickness measurement.

The polarizing optical microscope textures of a sample in the homeotropic and planar alignment taken between crossed polarizers are shown in figure 2.4a and 2.4b, respectively. The texture appears completely dark for the homeotropic

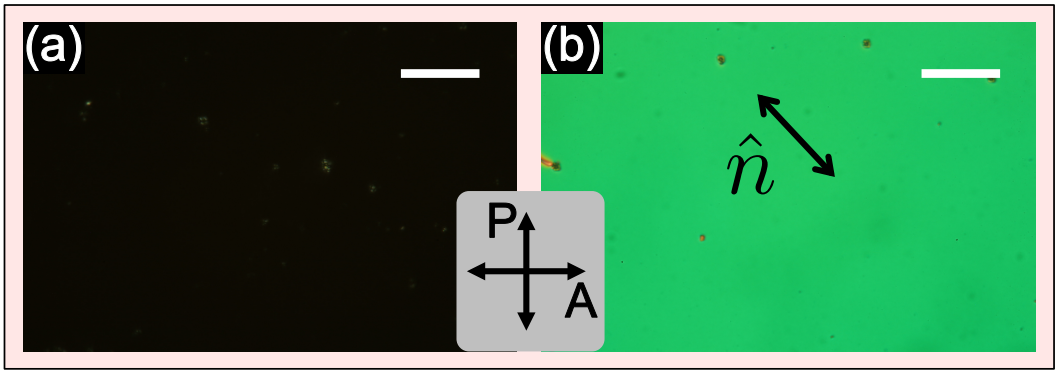

Fig. 2.4: The typical POM texture of a thin sample in the nematic phase in (a) homeotropic alignment and (b) homogeneous planar alignment. Crossed arrows represent the orientation of crossed polarizers. The double arrow in (b) shows the orientation of the director, which is similar to the rubbing direction of the LC cell. Scale bar: 50 μm.

aligned sample, as expected due to the perpendicular orientation of the director $\hat{n}$ with respect to the glass substrate. In a planar-aligned sample, the texture shows a uniform birefringent color when the director $\hat{n}$ is oriented at an angle with respect to the polarizer.

2.4 Polarizing Optical Microscopy

Polarizing optical microscopy (POM) is a widely employed technique for investigating birefringent samples. A polarizing optical microscope is an extension of a simple optical microscope with a polarizer positioned before the condenser and an analyzer placed after the objective lens, as schematically shown in figure 2.5. The rotatable polarizer and analyzer are usually kept in crossed conditions, i.e., at an angle of 90° from each other, and the specimen of interest is kept between them. The birefringent specimens generally appear bright between crossed polarizers, while optically isotropic samples appear dark. Our POM studies were performed using a polarizing optical microscope ($Olympus\ BX50$) equipped with a digital camera ($Canon\ 80D$). The temperature of the samples was monitored using a microscope hot stage ($Linkam\ LTS420E$) and a temperature controller ($Linkam$-T95).

The principle of operation of the polarizing optical microscope can be described as follows. The refractive indices of a birefringent sample can be represented by an ellipsoid surface known as the *optical indicatrix ellipsoid*. The cross-section of this indicatrix, perpendicular to the light propagation direction, essentially determines the birefringence of the samples. In the case of optically isotropic samples, all the principal indices are identical; therefore, the indicatrix cross-section is always circular. This gives rise to zero effective birefringence. Consequently, light passing

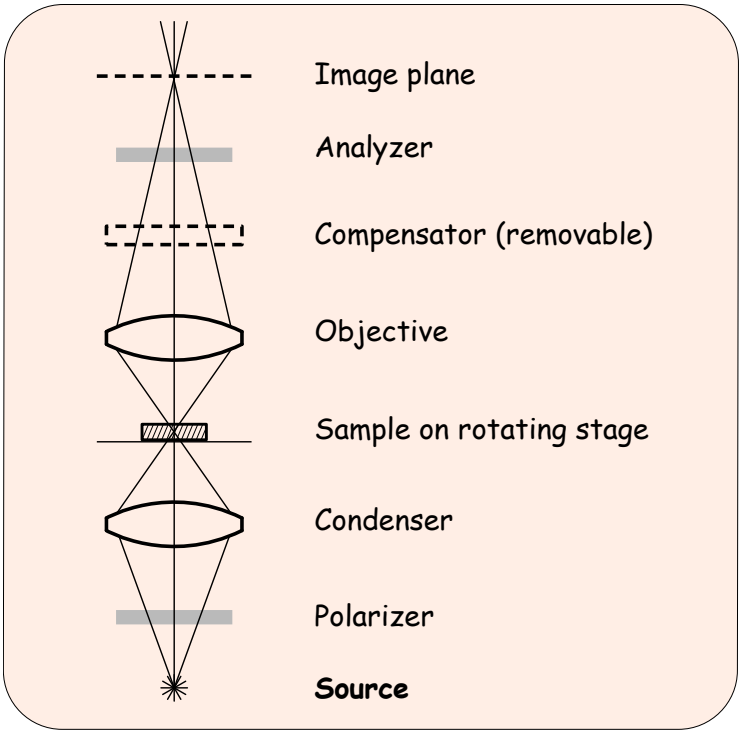

Fig. 2.5: Schematic representation of optical components in a polarizing microscope.

through isotropic samples retains its polarization state, causing such systems to appear dark between crossed polarizers.

In optically anisotropic samples, on the other hand, the cross-section of the indicatrix perpendicular to the light propagation direction is generally elliptical in shape. As a result, its polarization state generally changes when passing through the sample, and the sample appears bright between the crossed polarizers. The changes in the state of polarization depend on the optical path difference encountered by the light while passing through the sample.

For a homogeneous planar aligned liquid crystalline sample kept between crossed polarizers, the transmitted light intensity for a given wavelength can be written as [7, 105],

$$\boxed{I = \frac{I_0}{2} \sin^2 2\psi(1 - \cos\Delta\Phi) + I_d} \tag{2.3}$$

where I_0 is the intensity of the incident light, ψ is the angle between the local optic axis and the polarizer, I_d is the dark current measured under crossed polarizer condition in the absence of sample, and the phase difference is given by,

$$\Delta\Phi = \frac{2\pi\,\Delta n\,d}{\lambda} \tag{2.4}$$

Here, d is the sample thickness, λ is the wavelength of the incident light, and Δn

is the effective birefringence of the uniaxial sample. It can be seen from the eqn. 2.3 that when the optic axis of the uniaxial medium aligns with the polarizer (ψ = 0 or $\pi/2$), the sample appears dark. Consequently, four extinction positions are possible during a complete 360° rotation of the sample. The maximum brightness is achieved when the optic axis of the medium is oriented at ±45° with respect to the polarizer.

In white light illumination, the sample appears generally colored depending on the effective phase retardation introduced by the samples. This birefringence color arises due to the interference effect between the ordinary and extraordinary components of the light introduced by the sample. The variation in interference color, corresponding to changes in optical path difference, is visually represented in the Michel-Lévy chart [106]. This chart provides a graphical depiction of the relationship between interference color and the optical characteristics of specimens when illuminated with white light.

2.4.1 Birefringence measurement

The birefringence of a uniaxial medium is characterized by the difference in refractive index for light polarized parallel or perpendicular to the director:

$$\Delta n = n_{\parallel} - n_{\perp} \tag{2.5}$$

The experimental determination of the birefringence of the planar-aligned samples as a function of temperature can be performed by monitoring the average intensity passing through the sample kept between crossed polarizers [105, 107, 108] and utilizing eqn. 2.3 & 2.4. During the experiments, the planar-aligned sample is positioned on a microscope stage with its local optic axis at an angle of $\psi = 45°$ with respect to the polarizer direction to achieve maximum intensity. Consiquently, eqn. 2.3 becomes,

$$I = \frac{I_0}{2}\left(1 - \cos\Delta\Phi\right) + I_d. \tag{2.6}$$

The intensity now will be maximum and minimum at $\Delta\phi = \pi$ and $\Delta\phi = 0$, respectively. Thus, the maximum and minimum intensities is given by,

$$I_{max} = I_0 + I_d \tag{2.7}$$

$$I_{min} = I_d \tag{2.8}$$

In the experiments, the I_{min} is the measured intensity under crossed polarizer

condition in the absence of the sample and I_{max} is measured intensity in the presence of the sample in its isotropic phase under completely uncrossed polarizers condition. The I_0 value can be determined using above equations and is given by,

$$I_0 = I_{max} - I_{min} \tag{2.9}$$

The value of absolute phase difference $\Delta\phi$ and birefringence Δn can be calculated by substituting the value of I_0 in eqn. 2.6 and is given by,

$$\Delta\phi = \cos^{-1}\left[1 - 2\left(\frac{I - I_{min}}{I_{max} - I_{min}}\right)\right], \tag{2.10}$$

and

$$\Delta n = \frac{\Delta\phi\,\lambda}{2\pi d}. \tag{2.11}$$

During the measurement, a red high-pass filter with a cut-on wavelength of about 600 nm was introduced in the light path of the microscope. The POM images were taken as a function of temperature using a microscope hot stage (*Linkam* LTS420E) and a temperature controller (*Linkam*-T95). The average transmitted intensity was computed from the POM images using `MATLAB` software. A region of interest with homogeneous texture was selected from the series of images, and the mean intensity was determined by averaging the grayscale values of all the pixels in that region. The averaging of this intensity over a suitably large number of pixels reduces the error in the intensity measurement to a very low value. Hence, the error bars in the birefringence measurements are smaller than the size of the symbols and have not been included. Substituting these measured intensities in eqn. 2.10, the temperature variation of phase difference $\Delta\Phi$ introduced by the sample can be determined. Subsequently, the birefringence Δn of the sample can be determined from the calculated values of phase deference $\Delta\Phi$ using eqn. 2.11.

It is important to note that the transmitted intensity is an oscillatory function of $\Delta\Phi$, as described by eqn. 2.3. Consequently, $\Delta\Phi$ can only be determined modulo 2π, and the order of absolute phase difference is generally not known. For nematic samples with positive dielectric anisotropy, the absolute phase difference can be determined by the application of a high electric field. At a given temperature in the nematic phase, the phase difference tends to zero at high fields due to Fréedericksz transition [109]. Then, when the field is lowered slowly, the transmitted intensity through the sample between crossed polarizers exhibits an oscillatory dependence on the field. The order of the absolute phase difference can then be determined by counting the number of maxima and minima in the intensity profile. For samples that do not show Fréedericksz transition, the order of the absolute phase difference

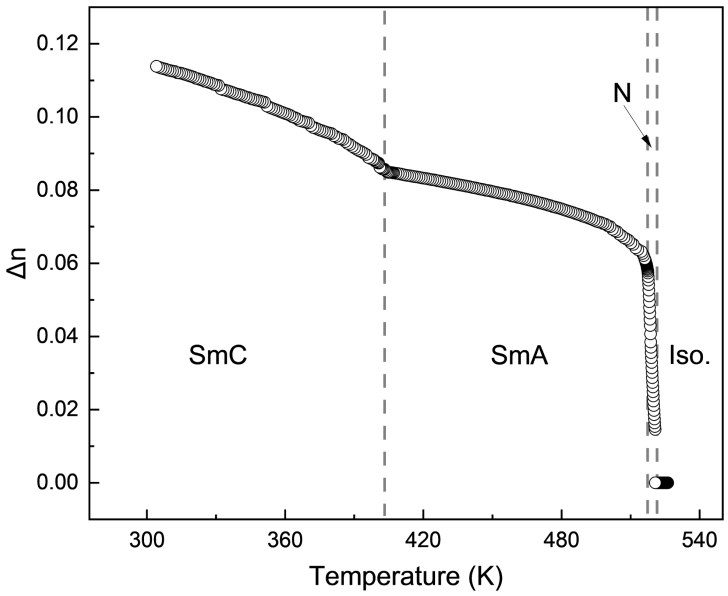

Fig. 2.6: The variation of effective birefringence as a function of temperature for the compound BTCN8 discussed in chapter 4.

can be estimated from the interference color using the Michel-Lévy chart.

2.4.2 Optical transmittance

The optical transmittance through the samples between crossed polarizers often provides useful insights into their physical properties. For an optical transmittance measurement, a He-Ne laser ($\lambda = 632.9\ nm$) was allowed to pass through the sample. The sample was placed at an orientation of maximum transmittance, i.e., the local director oriented at 45° from the polarizer direction. A low noise high gain photodiode connected to a mixed signal oscilloscope ($Agilent\ Technologies$ MSO6012A) was employed to record the transmitted intensity from the sample. A typical steady-state optical transmittance profile as a function time through an aligned liquid crystal sample along with the applied triangular wave voltage is shown in figure 2.7. The $2f$ dependence of the optical signal with respect to the applied field indicates the quadratic coupling between the applied field and dielectric anisotropy of the sample. This quadratic coupling dominates due to the apolar nature of the orientational order in liquid crystalline phases.

2.5 Electro-optic setup

An experimental setup was built for the simultaneous measurement of the optical transmittance of the samples and their dielectric constant with varying

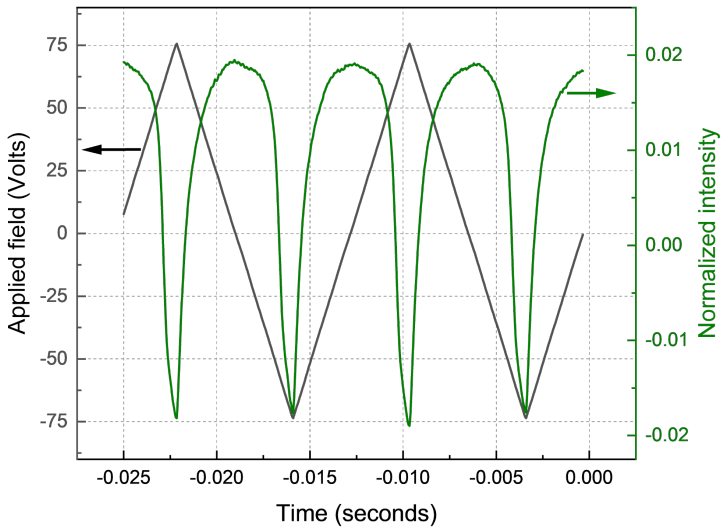

Fig. 2.7: The temporal variation of the steady state optical transmittance along with the applied field for compound BTCN8 discussed in chapter 4.

experimental parameters such as temperature and electric field. The schematic of the setup is shown in figure 2.8. A He-Ne laser of wavelength $\lambda = 632.8$ nm was passed through a polarizer and then divided into two parallel beams using a beam splitter. A dual-frequency light chopper ($Perkin\ Elmer$, model 198 A) was used to chop the two light beams at two different frequencies in the ratio of 11:18. One beam was directly sent to the photodiode, and it acts as a reference. Another beam was allowed to pass through the sample, which was kept between crossed polarizers and fell to the same photodiode. The photodiode output was monitored using a dual-channel lock-in amplifier ($Perkin\ Elmer$ model 7265A). The ratio of beam intensity from the sample to that of the reference beam ensures the removal of any external intensity fluctuations. This ratio was used for further analysis to determine the optical properties of the sample. In order to measure the dielectric constant and conductivity of the samples, a sinusoidal AC voltage was applied to the sample cell, and a resistance $R_m = 1$ kΩ connected in series. A lock-in amplifier ($Stanford\ Research$ SR830) was utilized to measure the amplitude and phase of the voltage drop across R_m. The impedance analysis was used to determine the capacitance of the LC cell with and without the sample. The ratio of these measured capacitances gives the effective dielectric constant of the sample. The capacitance of the cell can be determined by impedance analysis as follows.

2.6 Impedance analysis of sample

Liquid crystalline materials are usually dielectric in nature and have relatively high resistivity. Therefore, one can consider an LC cell filled with the sample to be

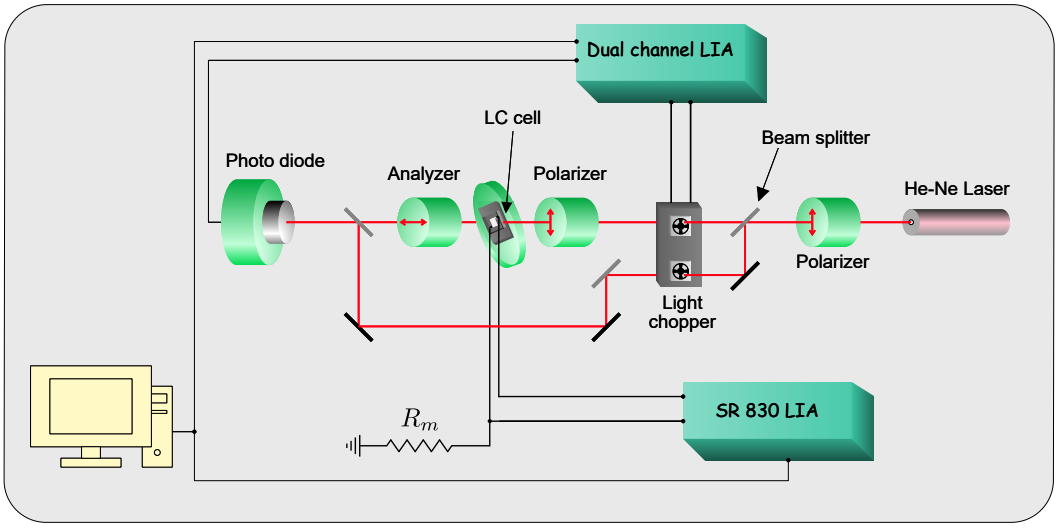

Fig. 2.8: Schematic diagram of electro-optical setup

equivalent to a parallel plate capacitor C_s and a resistor R_s in parallel combination, as shown in figure 2.9. For dielectric measurements, a known resistance $R_m = 1$ kΩ was connected in series with the LC cell, and the electrical circuit diagram is also shown in figure 2.9. An AC voltage was applied using a lock-in amplifier, and the amplitude and phase of the voltage dropped across R_m locked at the same frequency as the input voltage, which was measured using the same lock-in amplifier.

Using the electric circuit shown in figure 2.9, the impedance of the LC cell can be calculated as,

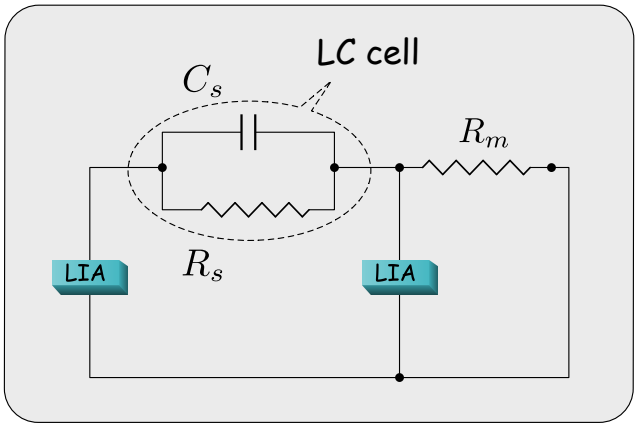

Fig. 2.9: Schematic diagram of the electrical circuit of RC equivalent of LC cell used in the dielectric measurements.

$$
\begin{aligned}
Z_c &= R_s||C_s \ (Z_s = 1/j\omega C_s) \\
&= \frac{R_s}{1 + j\omega C_s R_s} \\
&= \frac{R_s(1 - j\omega C_s R_s)}{(1 + \omega^2 C_s^2 R_s^2)}
\end{aligned}
$$

where $\omega = 2\pi f$, f is the frequency of the applied voltage, and $j = \sqrt{-1}$. The total impedance Z_T of the circuit (Z_c and R_m are connected in series) is given by,

$$
\begin{aligned}
Z_T &= \frac{R_s(1 - j\omega C_s R_s)}{(1 + \omega^2 C_s^2 R_s^2)} + R_m \\
&= \frac{R_s(1 - j\omega C_s R_s) + R_m + \omega^2 C_s^2 R_s^2 R_m}{(1 + \omega^2 C_s^2 R_s^2)}
\end{aligned}
\tag{2.12}
$$

Let the applied input voltage be $V_i = V_0 e^{j(\omega t + \phi_0)}$; where V_0 and ϕ_0 are the amplitude and phase of the applied voltage, respectively. The total current I_T passing through the circuit is given by,

$$
\begin{aligned}
I_T &= \frac{V_0 e^{j(\omega t + \phi_0)}}{Z_T} \\
&= \frac{V_0 e^{j(\omega t + \phi_0)}(1 + \omega^2 C_s^2 R_s^2)}{R_s(1 - j\omega C_s R_s) + R_m + \omega^2 C_s^2 R_s^2 R_m}
\end{aligned}
\tag{2.13}
$$

Now, the voltage drop across the known resistance R_m can be written as,

$$
\begin{aligned}
V_m e^{j(\omega t + \phi_m)} &= I_T \, R_m \\
&= \frac{V_0 e^{j(\omega t + \phi_0)} \, R_m \, (1 + \omega^2 C_s^2 R_s^2)}{R_s + R_m + \omega^2 C_s^2 R_s^2 R_m - j\omega C_s R_s^2}
\end{aligned}
\tag{2.14}
$$

where V_m and ϕ_m are the amplitude and phase of the measured voltage. Comparing the real part of the above equation, we get,

$$
\begin{aligned}
V_m \cos(\omega \, t + \phi_m) = \frac{V_0 R_m [\cos(\omega t + \phi_0)\{R_s + R_m + \omega^2 C_s^2 R_s^2 R_m\}}{} \\
\frac{- \omega C_s R_s^2 \sin(\omega t + \phi_0)]}{(R_s + R_m)^2 + \omega^2 C_s^2 R_s^2 R_m^2}
\end{aligned}
\tag{2.15}
$$

In a similar way, comparing the imaginary part of the eqn. 2.14 results,

$$V_m \sin(\omega t + \phi_m) = \frac{\begin{array}{c} V_0 R_m[\omega C_s R_s^2 \cos(\omega t + \phi_0) \\ + \{R_s + R_m + \omega^2 C_s^2 R_s^2 R_m\} \sin(\omega t + \phi_0)] \end{array}}{(R_s + R_m)^2 + \omega^2 C_s^2 R_s^2 R_m^2} \tag{2.16}$$

Solving equations 2.15 and 2.16 we get two unknown quantities C_s and R_s corresponding to the liquid crystal cell given by,

$$\boxed{R_s = R_m \left[\frac{V_m^2 - V_0^2}{V_m\{V_m - V_0 \cos(\phi_m - \phi_0)\}} - 2 \right]} \tag{2.17}$$

$$\boxed{C_s = \frac{V_m V_0 \sin(\phi_m - \phi_0)}{\omega R_m\{V_m^2 + V_0^2 - 2V_m V_0 \cos(\phi_m - \phi_0)\}}} \tag{2.18}$$

The amplitude V_m and the phase difference $\phi_m - \phi_0$ corresponding to the voltage drop across the resistance R_m are measured experimentally using a lock-in amplifier (SR830). The setup is automated using a Labview program with a computer, and the capacitance C_s and resistance R_s corresponding to liquid crystal cell can be computed using eqn. 2.18 and eqn. 2.17, respectively.

2.6.1 Determination of dielectric constant

In order to measure the dielectric constant of the samples, firstly, the capacitance of the empty LC cells was measured before filling the sample and is given by,

$$C_0 = \frac{\epsilon_0 A}{d} \tag{2.19}$$

where ϵ_0 is permittivity of free space, A is the effective area of the electrode, and d is the thickness of the cell. This relation is valid when the sample thickness d is smaller than the electrode diameter. Subsequently, the sample is introduced into the LC cell by capillary action in its high-temperature isotropic phase using a hot plate. After filling the sample, the cell capacitance can be written as,

$$C_s = \frac{\epsilon_0 \epsilon_r A}{d} \tag{2.20}$$

where ϵ_r is the dielectric constant of the sample. The filled cell capacitance C_s and empty cell capacitance C_0 is obtained experimentally using eqn. 2.18 and the ϵ_r can

be determined by taking the ratio of the eqn. 2.19 to the eqn. 2.20 given by,

$$\boxed{\epsilon_r = \frac{C_s}{C_0}} \tag{2.21}$$

Furthermore, experimentally observed sample resistance R_s (eqn. 2.17) can be utilized to calculate the conductivity of the sample using,

$$\boxed{\sigma = \frac{d}{R_s A}} \tag{2.22}$$

2.7 Polarization switching current measurement

The triangular wave technique [33] is a simple and ingenious way to study the ferro- or antiferroelectric behavior of liquid crystal samples. A schematic diagram of the experimental setup used for the polarization current measurements is shown in figure 2.10a. The temperature of the liquid crystalline samples is monitored using a temperature controller (*Linkam* T95HS) connected to a hot stage LTS 420E. The sample can simultaneously be observed by a polarizing optical microscope (*Olympus* BX50). A function generator (*Agilent* 33220A) is employed to provide a triangular wave voltage of desired frequency and amplitude, which is then amplified by a high voltage amplifier *Trek* (Model 601B-3) having an amplification gain of 100. The amplified voltage is subsequently applied across the sample cell connected in series to a known resistance $R = 1$ kΩ. The voltage drop across the known resistance R is monitored by an oscilloscope (*Agilent* MSO6012A). The output voltage drop was measured by averaging over a suitably large number of cycles of the applied triangular wave voltage to minimize the error to a low value. The current response of the sample can be calculated by dividing the measured voltage by the resistance R.

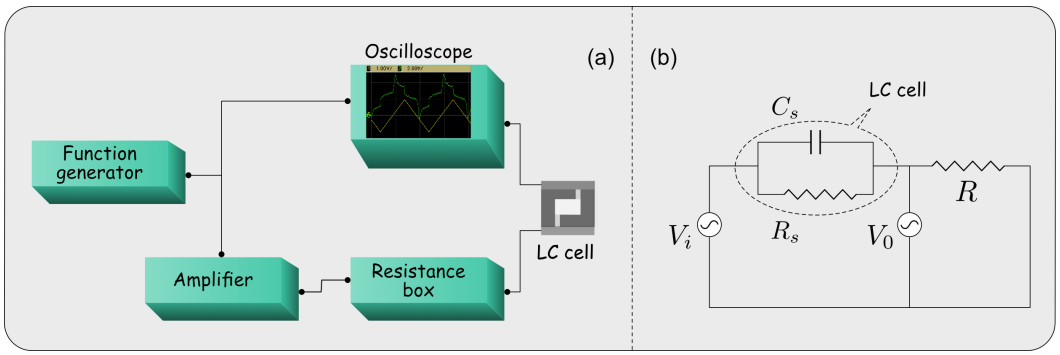

Fig. 2.10: (a) Schematic diagram of the experimental setup for polarization reversal current measurements. (b) Schematics of the corresponding electrical circuit with the RC equivalent of LC cell.

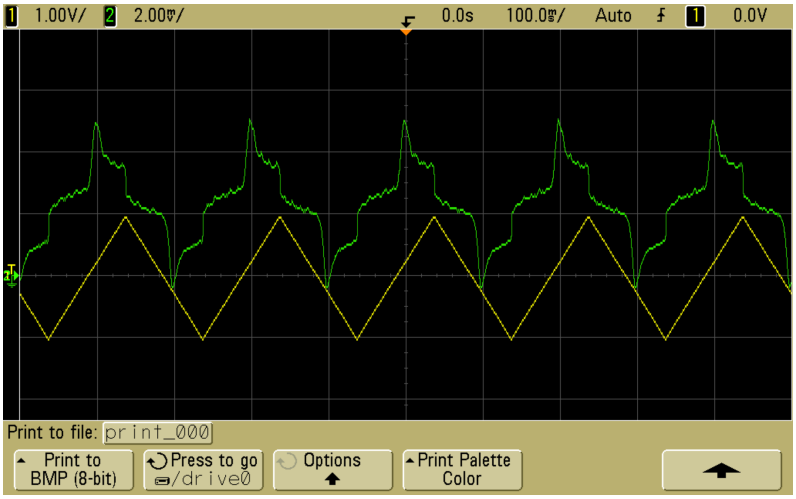

Fig. 2.11: Typical signal showing a polarization reversal current response under the application of a triangular wave voltage.

The switching current measurements were performed over a suitably large number of cycles of the applied triangular wave voltage to minimize the error to a low value.

The current I through the samples generally has three contributions: charge accumulation to the capacitor I_c, realignment of polarization I_p, and ionic current I_i. Thus, we can write [33],

$$I = I_c + I_p + I_i = C\frac{dV}{dt} + \frac{dP}{dt} + \frac{V}{R_s} \tag{2.23}$$

where P is the polarization of the medium, and C is the capacitance of the LC cell. The ionic contribution to the current I_i is assumed to be ohmic in nature with effective resistance R_s of the sample. For an applied triangular wave voltage, it is clear from the eqn.2.23 that the ohmic response follows the applied voltage and a square wave response will be produced due to capacitive current [33]. Now, if the sample exhibits spontaneous polarization, extra peaks appear above a threshold voltage corresponding to the switching of the polarization in each half cycle of the applied field. Figure 2.11 shows the typically observed signal under the application of a triangular wave voltage. The appearance of a single peak in each half-cycle of the current response is suggestive of the ferroelectric behavior of the LC samples. However, two peaks appear in each half-cycle of the current response when the sample exhibits antiferroelectric polarization. Also, there is a possibility of more than two peaks appearing in a half cycle of the applied field, which is suggestive of ferrielectric behavior.

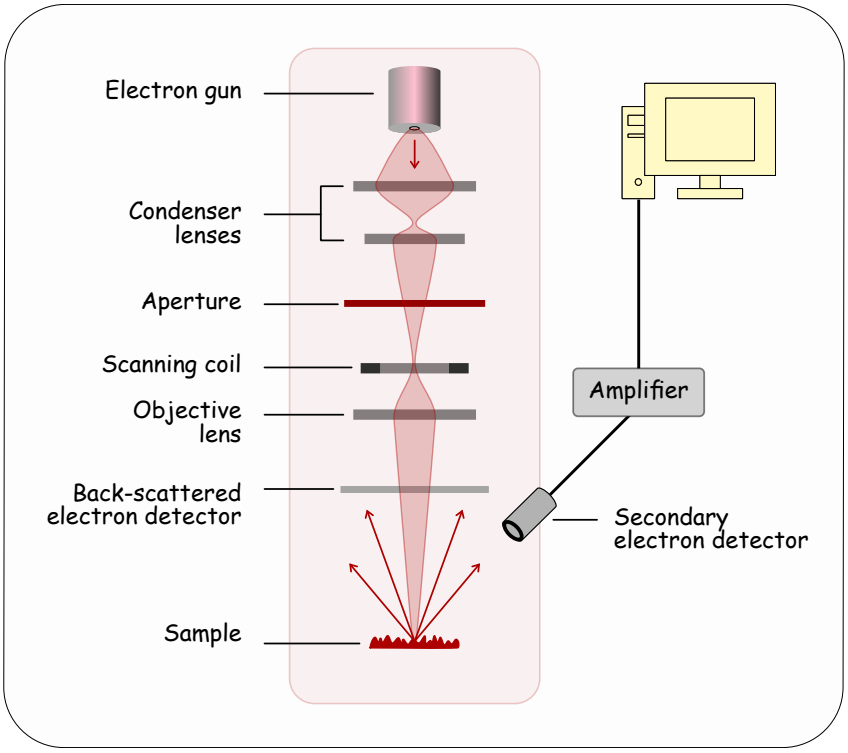

Fig. 2.12: Schematic representation of components in a scanning electron microscope.

2.8 Field-emission scanning electron microscopy

Field-emission scanning electron microscopy (FESEM) is used to probe the high-resolution topography of the sample by using a focused electron beam as a source of illumination. Because of the smaller de Broglie wavelength associated with the electrons, the resolution of electron microscopes is in the nanometer range. In our experiments, we used a *Carl Zeiss* (Ultra Plus model) scanning electron microscope for imaging. It uses the *field emission* electron gun as a source. The field emission source utilizes two anode plates: the first is kept at high voltage to draw electrons from the source, and the second one determines the velocity of outgoing electrons. The beam passes through the final lens, which raster or scans the focused electron beam over the specimen, hence the name, scanning electron microscope. The schematic block diagram of the scanning electron microscope showing its working principle is shown in figure 2.12.

Sample preparation is also an important aspect of scanning electron microscopy (SEM) imaging, especially for samples that are electrically non-conductive. During SEM imaging, the sample absorbs the primary electron beam. There should be a conducting path from the point of beam incidence through the sample, sample mount, and finally, sample stage. Otherwise, charges start accumulating at the sample, and this makes imaging difficult. All the samples used for this thesis work

are non-conductive. Therefore, in our experiments, the surface of the samples was sputter coated with platinum of about 5 nm thickness in order to make a conductive specimen. Subsequently, a silver paste was used to make an electrical connection between the sample surface and the stage so that the sample surface remains electrically neutral during imaging. The bombardment of the electron beam on this conducting surface of the samples yields secondary electrons, which are detected by the detector and produce the image of the sample surface.

2.8.1 Cryogenic – SEM

In order to probe the morphology of fluid phases, the sample kept in a holder was quenched by plunging it into liquid nitrogen at a temperature of about 83 K. Then the frozen sample was transferred to a cryo-chamber ($Quorum$ PP3000T) in a vacuum with pressure in the range between 10^{-4} and 10^{-5} mbar and at a temperature of about 83 K. After transferring the sample into the chamber, it was heated to 183 K. The sample was subsequently cut by a knife to expose a clean surface and sublimated for 15 min at 183 K to remove any ice formed on the surface. Then, the surface was coated with a thin layer of platinum of thickness about 5 nm. Afterward, the sample temperature was brought back to 83 K and transferred to the microscope stage for imaging. The temperature of the microscope stage was maintained at 83 K by the circulation of liquid nitrogen. The pressure in the sample chamber was kept at about 10^{-6} mbar during SEM imaging.

3 Leaning induced layer undulation in bent-core liquid crystals

3.1 Introduction

The polar packing of bent-core (BC) molecules in their smectic phases is well established [20, 23, 24, 47]. In some cases, the macroscopic uniform polarization in a medium introduces higher free energy, and the molecules rearrange themselves in three major ways to escape from the uniform polarization. (a) The polar ordering alternates in adjacent layers to form the antiferroelectric smectic ($SmCP_A$) phase [21]. This is the reason why most of the compounds comprised of BC molecules usually exhibit $SmCP_A$ phase in the absence of an electric field. (b) The uniform polarization gets splayed in ferroelectric smectic ($SmCP_F$) phases having large polarization (> 1 mC/m^2) to reduce the energy. The splayed polar order in the layers leads to the formation of stripes of a few tens of nanometers in width separated by defect walls at the edges of the stripes [23]. To incorporate these defects, the layers undulate periodically to form a polarization-modulated smectic phase or so-called B7 phase [44–46]. Based on the combination of the polarization, the slope of layer undulation, and the continuity of layers across the defect walls in neighboring stripes, a number of structures are possible for the B7 phase [46]. The layer undulation wavelength increases upon lowering the temperature and often undergoes a weak first-order transition to the B2 phase on further cooling. An unusual B7′ phase with linear bistable electro-optical switching has also been reported where polarization reversal current was not observed up to a field of 40 V/μm [110]. A few phenomenological models for the B7 phase have been proposed [111–113]. For strongly asymmetric BC molecules, such a splayed polar layer undulated smectic phase with SmTP type order within the layers have also been reported [35, 36, 114, 115]. (c) Another way to incorporate the defects is the complete fragmentation of the smectic layers to form a variety of two-dimensionally arranged columns [116–119], known as B1 phase. Usually, the B1 phase does not respond to an applied electric field. In some cases, however, the B1 phase is known to exhibit polarization switching at high fields (E $>$ 15 V/μm). This reorientation of polarization was explained by models [49, 52, 53] in which the arrow axes of the BC molecules lying perpendicular to the column axis align parallel to the column axis leading to so-called $B1_{rev}$ phase.

In this chapter, we report the experimental investigations on the phase behavior of a homologous series of compounds comprised of strongly asymmetric BC banana-shaped molecules. Our experimental studies using calorimetry, X-ray diffraction, polarising optical microscopy, cryogenic field emission scanning electron microscopy (Cryo-FESEM), dielectric, and electro-optic studies suggest the existence of a layer undulated liquid crystal phase for these compounds. The X-ray diffraction studies reveal that the layer undulation in this phase produces a two-dimensional rectangular lattice. In contrast to the layer undulated B7 phases, we found no polarization switching current response in this liquid crystal phase. However, an irreversible reorientation of the molecules in the layer was observed at high electric fields in polarised optical microscopy studies. We propose a possible model with a double-tilted smectic structure with periodic undulation along the layers to account for the experimental observations.

3.2 Experimental results and discussion

3.2.1 Sample details and differential scanning calorimetry studies

The experiments were performed on a homologous series of compounds with general formula 4-((4-(octyloxy)phenoxy)carbonyl)phenyl 4′-((4-(n-alkoxy)-3-fluorobenzoyl)oxy)-[1,1′-biphenyl]-3-carboxylate (**8OBFn**) and the molecular structure is shown in figure 3.1(a). The rigid arms, as well as the lengths of terminal aliphatic chains of these BC banana-shaped molecules, are different, introducing strong asymmetry in the molecular structure. The homologs differ by the length of the aliphatic chain attached to one end of the molecule (C_nH_{2n+1}; n= 8 to 16), while the length of the chain attached to the other end remained fixed. Due to the presence of fluorine at one arm, the net dipole moment of the individual molecules orient at an angle away from the molecular long axes. The net molecular dipole moment calculated from the energy-minimized structure of compound 8OBF8 is about 3.14 Debye. The detailed synthetic root and chemical characterization of the compounds can be found in reference [37].

The differential scanning calorimetry (DSC) studies were performed on samples at a heating and cooling rate of 5 K/min. The DSC thermograms of the compound 8OBF12 for the heating and cooling cycle are shown in figure 3.1(b), which detects the transitions between different phases. The compound exhibits one enantiotropic liquid crystal phase below the isotropic liquid phase and different crystal phases at lower temperatures. This was confirmed by x-ray diffraction studies discussed later

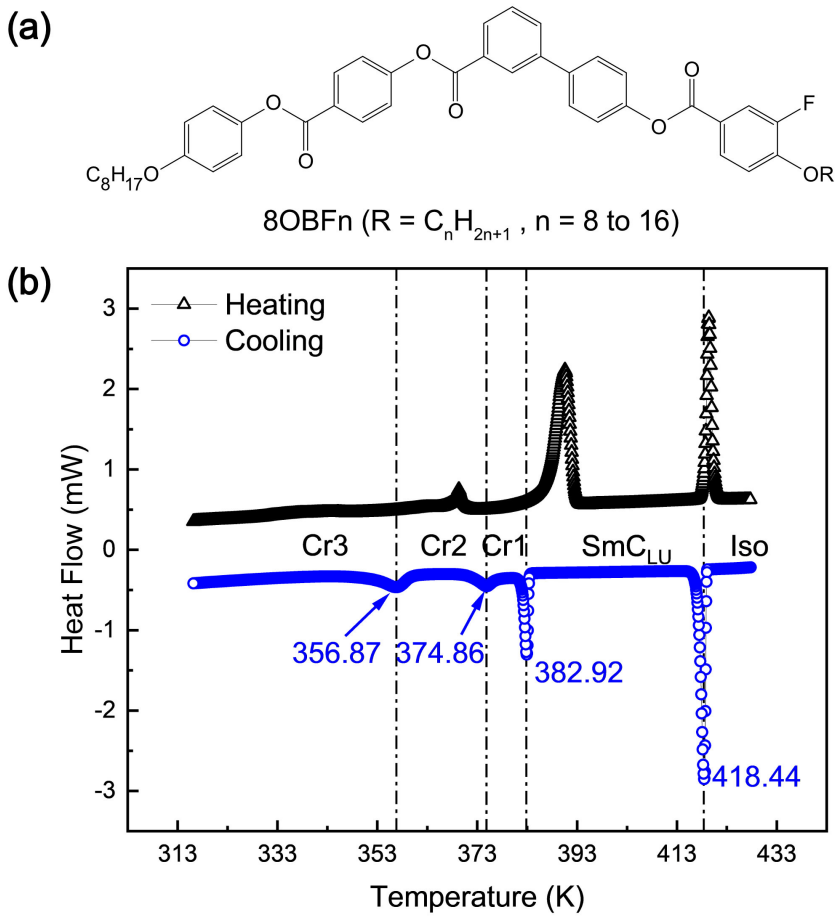

Fig. 3.1: (a) Molecular structure of the homologous series of compounds 8OBFn with varying chain length **n** attached to one end of the BC molecule. (b) DSC thermograms of the compound 8OBF12 with a heating and cooling rate of 5 K/min. Only one enantiotropic liquid crystalline phase was observed below the isotropic phase. All other transitions correspond to crystal to crystal transitions.

in the text. In this chapter, we denote this liquid crystal phase as layer undulated smectic C or SmC_{LU} phase as characterized by our experimental studies performed on these compounds described below. A similar phase sequence of different phases is also observed for the other homologous series of compounds studied. Figure 3.2 shows the plot of transition temperatures observed on cooling the sample from its isotropic phase as a function of the chain length of the homologs. Interestingly, the odd-even effect of the alkyl chain length on the transition temperatures is not observed for these compounds. The phase sequence, transition temperatures, and associated enthalpy changes across the transitions for all the compounds are listed in table 3.1.

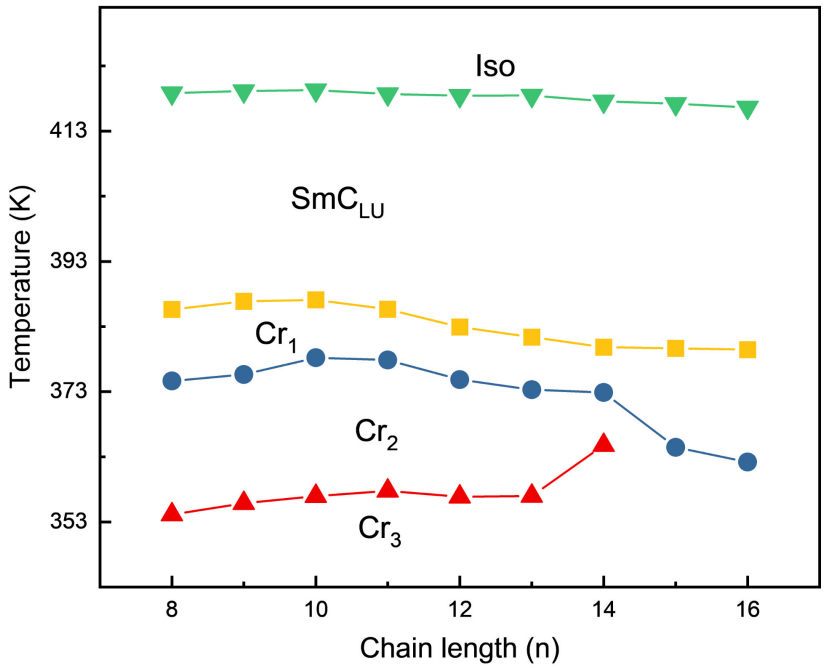

Fig. 3.2: Cooling scan transition temperatures as a function of alkyl chain length **n** attached to one end of the molecule. All the homologs exhibit one enantiotropic liquid crystal phase without any odd-even effect.

3.2.2 POM observations and electric field effects

The polarizing optical microscopy (POM) observations were carried out on samples of thickness 5 μm kept between the crossed polarizers. The commercially available LC cells (Instec Inc.) treated for planar alignment with ITO-coated electrodes were used to apply an electric field across the sample and POM studies. The temperature of the sample was controlled by using a microscope hot stage (Linkam LTS420E) equipped with a temperature controller. A smooth fan texture with extinction brushes parallel to the polarisers was observed on cooling the samples from the isotropic phase to the SmC_{LU} phase at a rate of 0.1 K/min. Figure 3.3(a) shows the POM texture of the SmC_{LU} phase for the compound 8OBF12. The pinkish color of the fans corresponds to a birefringence of 0.07 obtained from the Michel-Levy interference color chart. The fan texture is indicative of the layer undulated structure of the SmC_{LU} phase [44], which is also confirmed by the x-ray diffraction studies discussed later. The familiar circular fan texture suggests that the layer normal is oriented radially along the fans. The extinction brushes appear parallel to the polarizer or analyzer when layer normal is made parallel to them, indicating that the optic axis in the SmC_{LU} phase is along the layer normal. The textural appearance depends on the rate of cooling of the sample from the higher temperature isotropic phase. The smooth fan texture does not appear if the cooling rate is high. At a higher cooling rate of 3 K/min, a fragmented fan texture is observed with the extinction

Tab. 3.1: Transition temperatures and the phase sequence along with the associated changes in enthalpy across the transitions while heating and cooling the sample at a rate of 5 K/min for the homologs 8OBFn; n = 8-16 obtained from the DSC studies. The transition temperatures are in K, and the corresponding enthalpy changes in J/g are shown in the brackets.

Compound	R(n)	Heating scan	Cooling scan
8OBF8	8	Cr 393.89 (27.80) SmC_{LU} 420.34 (12.13) Iso	Iso 418.99 (-22.71) SmC_{LU} 385.78 (-5.11) Cr1 374.79 (-1.12) Cr2 354.29 (-1.99) Cr3
8OBF9	9	Cr 362.29 (7.87) Cr1 392.47 (24.27) SmC_{LU} 420.31 (12.13) Iso	Iso 419.29 (-11.86) SmC_{LU} 387.01 (-5.11) Cr1 375.78 (-0.76) Cr2 356.03 (-0.55) Cr3
8OBF10	10	Cr 391.18 (27.32) SmC_{LU} 420.61 (12.87) Iso	Iso 419.44 (-12.46) SmC_{LU} 387.24 (-5.78) Cr1 378.36 (-0.76) Cr2 357.12 (-2.90) Cr3
8OBF11	11	Cr 370.84 (10.65) Cr1 390.68 (22.46) SmC_{LU} 419.60 (11.46) Iso	Iso 418.85 (-11.56) SmC_{LU} 385.80 (-3.83) Cr1 378.01 (-0.83) Cr2 357.93 (-1.65) Cr3
8OBF12	12	Cr 369.52 (2.40) Cr1 390.75 (30.79) SmC_{LU} 419.54 (14.94) Iso	Iso 418.59 (-15.03) SmC_{LU} 383.07 (-4.51) Cr1 375.01 (-1.37) Cr2 357.02 (-3.83) Cr3
8OBF13	13	Cr 378.17 (12.64) Cr1 390.26 (22.73) SmC_{LU} 419.67 (10.95) Iso	Iso 418.62 (-10.78) SmC_{LU} 381.53 (-3.01) Cr1 373.47 (-1.50) Cr2 357.13 (-2.78) Cr3
8OBF14	14	Cr 374.65 (5.65) Cr1 389.39 (22.60) SmC_{LU} 418.63 (10.44) Iso	Iso 417.74 (-10.25) SmC_{LU} 379.98 (-2.99) Cr1 373.02 (-2.18) Cr2 364.94 (-13.71) Cr3
8OBF15	15	Cr 381.25 (7.49) Cr1 389.23 (23.26) SmC_{LU} 418.16 (10.97) Iso	Iso 417.35 (-10.84) SmC_{LU} 379.80 (-3.24) Cr1 364.61 (-24.86) Cr2
8OBF16	16	Cr 377.52 (2.66) Cr1 388.21 (27.35) SmC_{LU} 417.6 (11.15) Iso	Iso 416.80 (-10.86) SmC_{LU} 379.61 (-3.11) Cr1 362.34 (-23.09) Cr2

brushes aligning along the crossed polarizers, as shown in figure 3.3(b).

The switching current measurements were performed using a triangular [33] and a square wave voltage to determine the presence of electric polarization in the SmC_{LU} phase. The AC voltage of amplitude 100 V was applied across a 5 μm thick planar-aligned sample. The measured current response of the sample did not show any peak due to polarization reversal, as shown in figure 3.5. This indicates that the observed SmC_{LU} phase does not possess spontaneous polarization. In spite of the absence of polarization, an irreversible field-induced transition was observed with the application of an AC electric field of amplitude greater than 15 V/μm. The birefringence color of the texture started to change gradually from pink to blue (see figure 3.4(b)) beyond this field. The field-induced transformation occurs

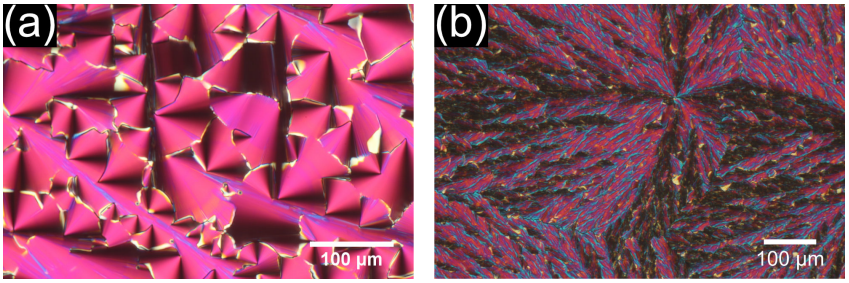

Fig. 3.3: The POM texture of a 5 μm thick planar aligned sample of the compound 8OBF12 between crossed polarizers at 413 K while cooling the sample from the isotropic phase at a rate of (a) 0.01 K/min, and (b) 3 K/min.

with the coexistence of these two colored regions, indicating a first-order transition. The transformation was completed by a further increase of the voltage at about 20 V/μm as shown in figure 3.4(c). This change in the color indicates a field-induced transition to a higher birefringent texture of birefringence $\Delta n \approx 0.12$ estimated from the Michel-Levy interference color chart. The fan texture, as well as the black brush patterns parallel to the polarizers, remained unaltered across this field-induced transition. This indicates a local reorientation of the molecules, producing an increase in the birefringence of the sample without any rotation of the optic axis. It was found that this field-induced transformation can only be observed at small frequencies as the threshold field increases sharply with increasing frequency of the applied electric field. A small change in the color occurs after turning off the field, but the texture does not revert back to the initial zero field one. The field-induced

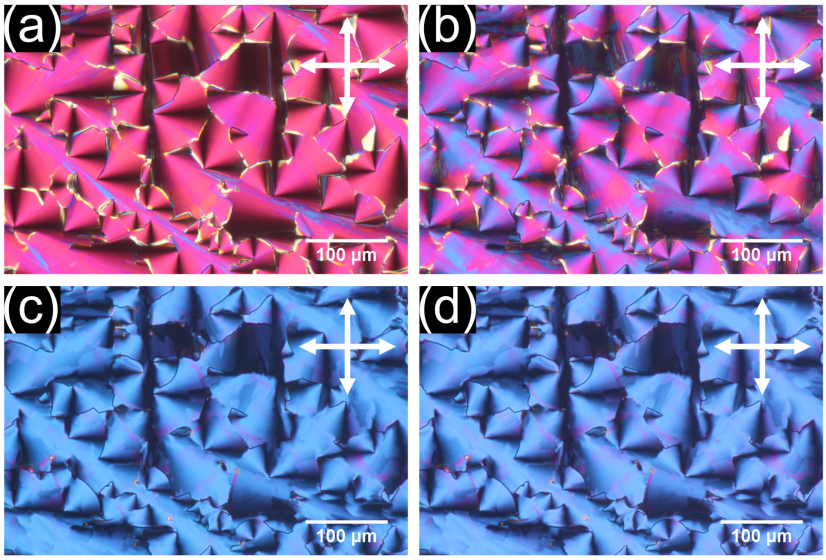

Fig. 3.4: The POM textures of the compound 8OBF12 in a planar aligned LC cell of sample thickness 5 μm between the crossed polarisers at 413 K with (a) no applied field, (b) ac field of 15 V/μm, (c) ac field of 20 V/μm, and (d) after turning off the field. The changes in the birefringence color show the irreversible field-induced transition from the SmC_{LU} phase as a consequence of the dielectric anisotropy.

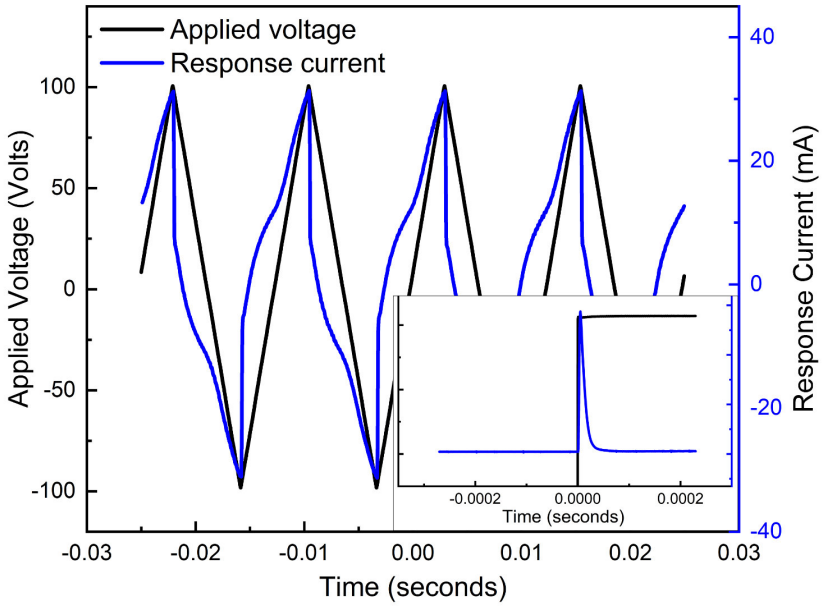

Fig. 3.5: The switching current response of the compound 8OFB12 for a planar aligned sample of thickness 5 μm under the application of a triangular wave voltage. No peak corresponding to polarization reversal was observed, indicating the apolar nature of the SmC_{LU} phase. The inset shows the current response under the application of a square wave voltage. A single exponentially dropping peak was observed associated with the capacitive response of the LC cell, confirming the absence of layer polarization in the SmC_{LU} phase.

state persists even after several days. This shows the irreversible nature of the field-induced transition (see figure 3.4(d)). Even in the field-induced state of the sample, the switching current measurements show the absence of polarization. On heating the sample from the field-induced blue texture, the initial zero field pink color texture tends to be partially restored close to the transition to the isotropic phase. However, the zero field texture could only be retrieved completely by heating the sample to the isotropic phase and cooling it subsequently to the SmC_{LU} phase. Similar changes were observed under the application of a DC field across the sample.

A small current peak at a high field is observed due to the ionic impurities in the sample, as shown in figure 3.6. Due to the ionic impurities, this peak increases with temperature, persists even in the isotropic phase, and disappears at frequencies higher than 150 Hz. A single exponentially decaying current response (see inset of figure 3.6) associated with the capacitance of the sample was observed under the application of square wave voltage. An additional peak with a relatively slow response is expected in the case of polar response, which was found to be absent in the SmC_{LU} phase. Thus, the application of square wave voltage further confirms the apolar nature of the SmC_{LU} phase.

We were unable to align the sample homeotropically even when the sample

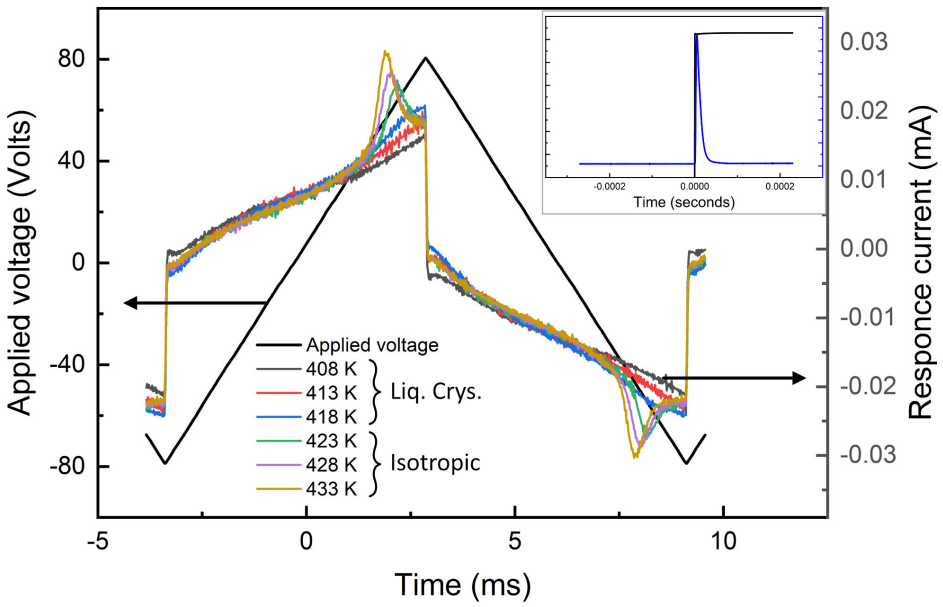

Fig. 3.6: The switching current response of the compound 8OFB12 for a planar aligned sample of thickness 5 μm under the application of a triangular wave voltage at a lower frequency. No peak corresponding to polarization reversal was observed, indicating the apolar nature of the SmC_{LU} phase. The inset shows the current response under the application of a square wave voltage. A single exponentially dropping peak was observed associated with the capacitive response of the LC cell, confirming the absence of layer polarization in the SmC_{LU} phase.

was filled in an LC cell for homeotropic alignment. A smooth fan texture very similar to the texture found in the planar-aligned LC cell was observed with a slightly different birefringent color, as shown in figure 3.7(a). The sample was cooled from the isotropic phase at a slow cooling rate of 0.01 K/min. Also, a thin sample kept between a clean glass plate and a cover slip tends to acquire a planar alignment, as shown in figure 3.7(b), with a cooling rate of 3 K/min. Even in these cells, the texture with relatively larger fans appears only at a very slow cooling rate. Thus, the samples always produce a quasi-planar alignment irrespective of the surface treatment of the bounding glass plates.

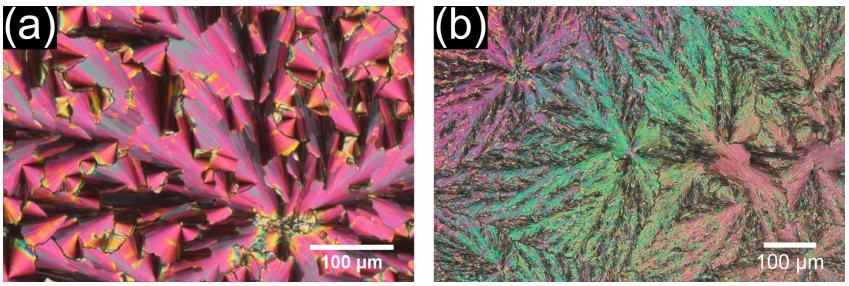

Fig. 3.7: The POM texture of (a) a homeotropically aligned sample of thickness 9 μm, and (b) a thin sample sandwiched between a clean glass plate and a cover slip placed between crossed polarizers.

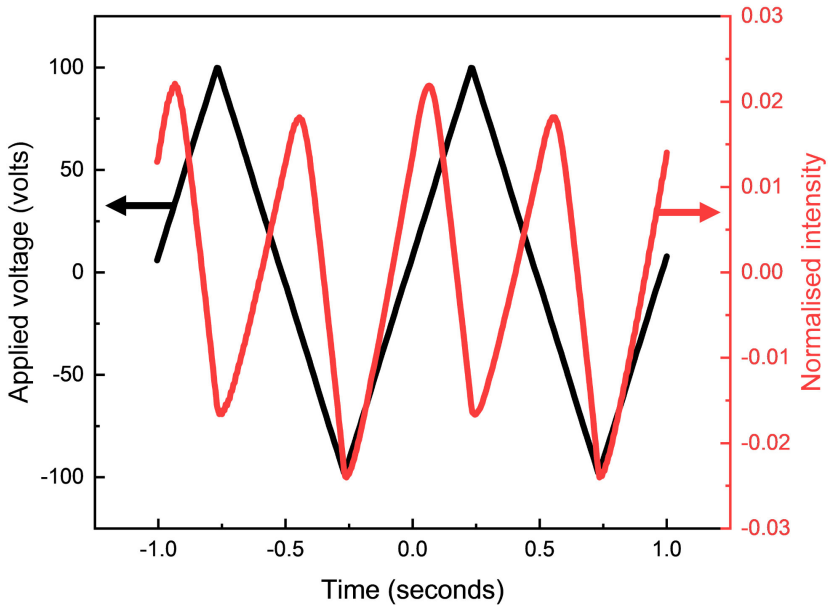

Fig. 3.8: The optical response of a planar aligned sample of thickness 5 μm in the SmC_{LU} phase under the application of a triangular wave voltage. The $2f$ response in the optical signal indicates a quadratic coupling between the electric field and the dielectric anisotropy of the sample.

The optical transmittance through the field-induced state of the sample between crossed polarisers was measured under the application of an AC triangular wave voltage. In this experiment, a He-Ne laser of wavelength 632.9 nm was passed through the sample, and the transmitted intensity was recorded using a high-gain photodiode connected with a mixed signal oscilloscope ($Agilent\ Technologies$ MSO6012A). The details of the experimental setup are discussed in Chapter 2. Figure 3.8 shows the time-dependent normalized optical response along with the applied voltage across the sample. The normalized intensity was calculated using $I_{nor} = (I - I_{ave})/I_{ave}$, where I is the measured transmitted intensity through the sample and I_{ave} is the average value of the transmitted intensity. The optical response clearly varies at twice the frequency of the applied field, indicating that it originates due to quadratic coupling between the electric field and the dielectric anisotropy of the sample. The transmitted intensity is maximum at zero fields, and it decreases with increasing magnitude of the field. The increasing magnitude of the field induces a slight increase in the effective birefringence of the sample with respect to its value in the absence of the field, which is estimated to be 0.12 using POM studies. As this zero field birefringence of the sample produces an optical phase difference between π and 2π for the 5 μm LC cell used in this experiment, the transmitted intensity decreases with the increasing magnitude of the field. This experiment clearly demonstrates the absence of net polarization in the field-induced state of the SmC_{LU} phase.

The POM studies discussed above are found to be similar for all the homologs. The salient features of the studied homologous series of compounds are as follows:

- A similar smooth fan textures under crossed polarizers were observed while cooling the planar aligned samples from their isotropic phase at a slow cooling rate. Figure 3.9(a) and 3.9(c) shows the POM texture of 5 μm thick samples of the compounds 8OBF16 and 8OBF8, respectively, between the crossed polarizers.

- The polarization reversal current peak was found to be absent for all the homologs.

- The irreversible field-induced transformation was observed above a threshold voltage for all the homologs, where only the birefringence of the sample was increased while the textural features were retained. Figure 3.9(b) and 3.9(d) represent the field-induced textures for the compounds 8OBF16 and 8OBF8, respectively, between the crossed polarizers.

Despite the common features exhibited by all the homologs, the shortest chain length homolog 8OBF8 shows slightly different behavior. The smooth fan texture of the 8OBF8 compound was found to have striations along the radial direction (see figure 3.9c). Additionally, a relatively higher electric field of about 30 V/μm was required to induce the textural transformation.

3.2.3 Dielectric studies

The temperature variation of the dielectric constant of the compounds was measured for planar aligned samples of thickness 5 μm in a custom homemade set-up with a frequency range of 1 Hz to 100 kHz while cooling the samples from the isotropic phase. The temperature of the sample was monitored by a microscope hot stage equipped with a temperature controller (INSTEC Inc.). The details of the dielectric setup have been discussed in Chapter 2. In this setup, a sinusoidal AC voltage of rms amplitude 0.5 Volts and frequency 5641 Hz was applied to a series combination of the sample cell and a resistance of 1 kΩ. A lock-in amplifier (Stanford Research SR830) was utilized to measure the amplitude and phase of the voltage drop across the 1 kΩ resistance. The impedance analysis was used to determine the capacitance of the LC cell with and without the sample. The ratio of these measured capacitances gives the real part of the effective dielectric constant of the sample.

The variation of the dielectric constant for the compound 8OBF12 as a function

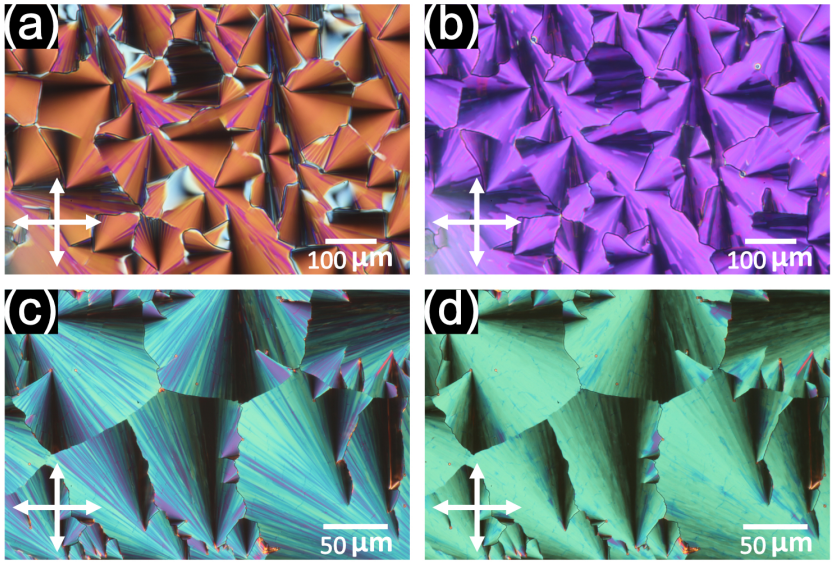

Fig. 3.9: The POM textures of 5 μm thick sample kept between crossed polarizers of the compounds (a) 8OBF16 and (c) 8OBF8 at a temperature of 408 K in the SmCLU phase. The corresponding field-induced textures of compounds (b) 8OBF16 and (d) 8OBF8. The field required to obtain the complete transformation of the SmCLU phase for the compounds 8OBF16 and 8OBF8 was about 20 V/μm and 30 V/μm, respectively.

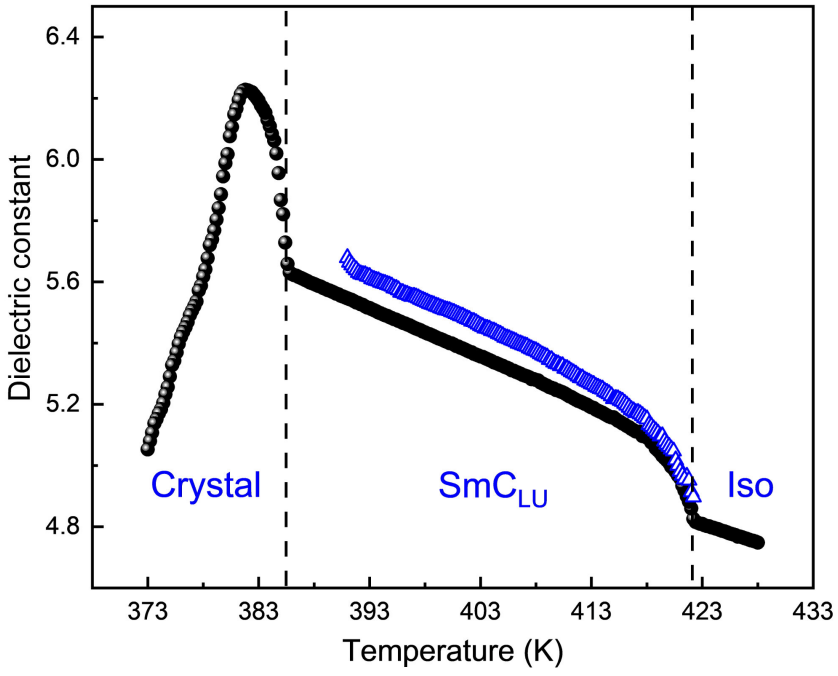

Fig. 3.10: The variation of the effective dielectric constant of the compound 8OBF12 in a planar aligned LC cell of sample thickness 5 μm as a function of temperature. The filled circle symbols show the variation of the dielectric constant on cooling the sample from its isotropic phase, clearly detecting the range of stability of the SmC_{LU} phase. The open triangular symbols show the variation of the dielectric constant on heating the sample from the field-induced state of the SmC_{LU} phase.

of temperature is shown in figure 3.10. The dielectric constant of the sample varies slowly in the isotropic phase, and it increases abruptly at the transition to the SmC_{LU} phase at 421 K. This transition temperature agrees with the DSC measurement. The enhancement of the dielectric constant for the planar aligned sample in the SmC_{LU} phase compared to that in the isotropic phase perhaps indicates negative dielectric anisotropy in the SmC_{LU} phase. The dielectric constant increases slowly on further cooling of the sample and again varies sharply at the transition from the SmC_{LU} phase to the crystal phase. Thus, the dielectric measurements clearly detect the temperature range of stability of the SmC_{LU} phase in these compounds. The measured dielectric constant has a relatively low value in the SmC_{LU} phase suggesting the absence of spontaneous polarization.

The dielectric measurement was also performed on the sample while heating it from the field-induced state of the SmC_{LU} phase. The variation of the measured dielectric constant with temperature is also shown in figure 3.10. The dielectric constant in the field-induced state of the SmC_{LU} phase is slightly higher than that of the zero field state. The difference between these dielectric constant values decreases as the transition temperature to the isotropic phase is approached. This variation is consistent with POM observation that the zero-field texture tends to be partially restored close to the clearing temperature.

3.2.4 XRD measurements

X-ray diffraction (XRD) studies were carried out using a DY 1042-Empyrean (PANalytical) diffractometer with CuK_α radiation of wavelength 1.54 Å equipped with a PIXcel 3D detector. The unaligned powder samples were filled in Lindemann capillary tubes of outer diameter 1 mm to perform the measurements. The samples were initially heated to the isotropic phase and then cooled to the desired temperatures to record the XRD intensity profiles. The XRD intensity profile as a function of the wave vector q for the compound 8OBF12 at 417 K is shown in figure 3.11. A few strong peaks were observed in the small angle region with scattering vectors in the ratio of 1:2:3, indicating a lamellar molecular organization. A diffused broad peak in the wide-angle region suggests a weak lateral correlation between the molecules, indicating liquid-like order within the layers in this SmC_{LU} phase. In addition to the strong peaks, high-resolution measurements focusing on the small angle region revealed several weak satellite peaks, as shown in figure 3.12, indicating some additional order beyond the simple one-dimensional stacking of layers.

The simplest structure that can be invoked to index the observed XRD peaks is a two-dimensional (2D) rectangular lattice. Considering the strong harmonic

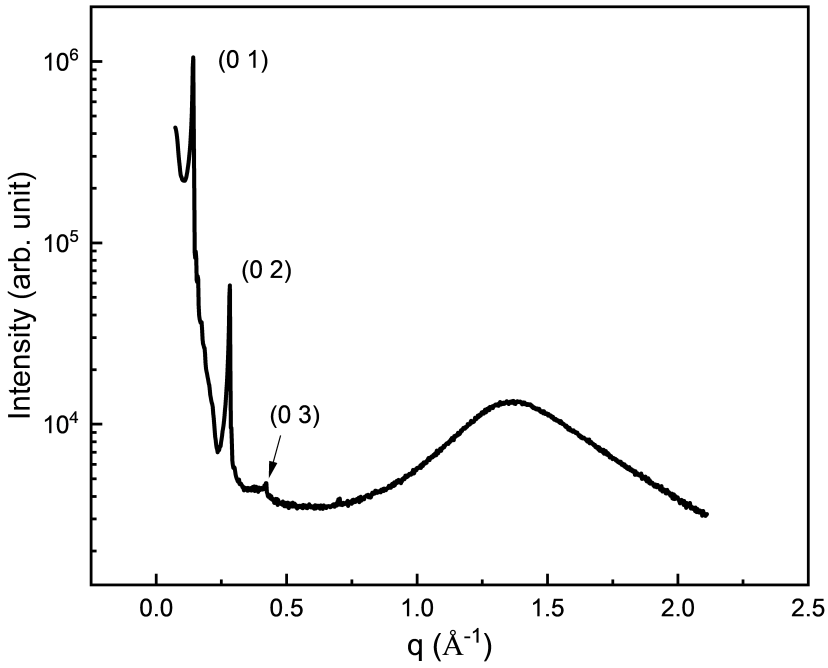

Fig. 3.11: The XRD intensity profile of the compound 8OBF12 at 417 K as a function of wave vector q in the SmC_{LU} phase. The sharp peaks in the small angle region indicate the lamellar order of the molecules in this phase. The broad diffused peak in the wide-angle region indicates a liquid-like order along the layers.

reflections as (0 k), k = 1, 2, 3 corresponding to the layer reflections, the additional weak peaks in the small angle region can be indexed well with a layer undulated structure of the SmC_{LU} phase forming a 2D rectangular lattice. The lattice parameters calculated from the XRD results for the compound 8OBF12 are d = 45 Å and $a \approx$ 600 Å, where d corresponds to the layer thickness and a corresponds to the layer undulation wavelength. The inset of figure 3.12 shows the schematic representation of the reciprocal lattice corresponding to this structure. The calculated peak positions using this model show excellent agreement with the experimentally observed peak positions (see table3.2). Since the lattice parameter a is large compared to layer thickness d, some of the (h 1) peaks are found to be too close to the intense lamellar peaks to be resolved in the XRD intensity profile. We also considered fitting the peaks with centered rectangular and oblique lattices. However, it was found that the 2D rectangular lattice structure gives the best fit to the observed XRD peaks.

We were able to fit the XRD peaks observed for all the homologues (8OBFn, n = 8-16) with a similar 2D rectangular lattice confirming the lattice structure assignment. Figure 3.13 represents the high-resolution XRD intensity profiles of some of the homologs as a function of wave vector q focusing in the small angle region. All the homologs show a similar XRD profile with strong sharp peaks associated with the layer spacing and several weak satellite peaks corresponding to the periodic undulation along the layers. The wave vectors q corresponding to the

Tab. 3.2: XRD results and the lattice parameters for the homologous series of compounds 8OBFn. The calculated scattering vectors were found to be in excellent agreement with that of the experimentally observed values. Due to the relatively large value of lattice parameter a, some of the satellite peaks are too close to be resolved experimentally.

Homologues	$q_{expt.}$	Miller indices			$q_{calc.}$			Lattice parameters
8OBF16	0.1304	(0 1)	(1 1)	(2 1)	0.1304	0.1311	0.1333	
	0.1412	(3 1)	(4 1)		0.1370	0.1419		d = 48.18 Å
	0.1474	(5 1)	(6 1)		0.1479	0.1551		a = 449 Å
	0.1627	(7 1)			0.1631			
	0.1709	(8 1)			0.1718			
8OBF15	0.1329	(0 1)	(1 1)	(2 1)	0.1329	0.1336	0.1358	
	0.1436	(3 1)	(4 1)		0.1394	0.1442		d = 47.28 Å
	0.1496	(5 1)	(6 1)		0.1502	0.1572		a = 449 Å
	0.1646	(7 1)			0.1650			
	0.1735	(8 1)			0.1738			
8OBF14	0.1353	(0 1)	(1 1)	(2 1)	0.1353	0.1360	0.1382	
	0.1457	(3 1)	(4 1)		0.1417	0.1464		d = 46.44 Å
	0.1516	(5 1)	(6 1)		0.1523	0.1592		a = 449 Å
	0.1661	(7 1)			0.1670			
	0.1751	(8 1)			0.1756			
8OBF13	0.1375	(0 1)	(1 1)	(2 1)	0.1375	0.1381	0.1401	
	0.1470	(3 1)	(4 1)		0.1433	0.1477		d = 45.70 Å
	0.1537	(5 1)	(6 1)		0.1532	0.1596		a = 465 Å
	0.1663	(7 1)			0.1669			
	0.1767	(8 1)	(9 1)		0.1749	0.1835		
	0.1933	(10 1)			0.1927			
8OBF12	0.1397	(0 1)	(1 1)	(2 1)	0.1397	0.1401	0.1412	
	0.1428	(3 1)	(4 1)		0.1431	0.1456		
	0.1489	(5 1)			0.1489			d = 44.98 Å
	0.1564	(6 1)	(7 1)		0.1527	0.1572		a = 610 Å
	0.1681	(8 1)	(9 1)		0.1622	0.1677		
	0.1783	(10 1)	(11 1)		0.1736	0.1799		
	0.1939	(13 1)			0.1935			
8OBF10	0.147	(0 1)	(1 1)	(2 1)	0.1470	0.1474	0.1485	
	-	(3 1)	(4 1)		0.1503	0.1528		
	0.156	(5 1)	(6 1)		0.1559	0.1597		d = 42.74 Å
	0.164	(7 1)	(8 1)		0.1641	0.1689		a = 604 Å
	0.178	(9 1)	(10 1)		0.1743	0.1800		
	0.188	(11 1)			0.1863			
8OBF9	0.1488	(0 1)	(1 1)	(2 1)	0.1488	1493	0.1507	
	-	(3 1)	(4 1)		0.1530	0.1563		
	0.1603	(5 1)			0.1604			d = 42.23 Å
	0.1649	(6 1)	(7 1)		0.1653	0.1708		a = 524 Å
	0.1826	(8 1)	(9 1)		0.1770	0.1838		
	0.1897	(10 1)			0.1910			
8OBF8	0.1468	(9 0)			0.1528			
	0.1525	(0 1)	(1 1)	(2 1)	0.1525	0.1534	0.1562	d = 41.20 Å
	0.1668	(4 1)			0.1669			a = 370 Å
	-	(5 1)	(6 1)		0.1745	0.1834		
	0.1924	(7 1)			0.1934			
	-	(8 1)	(9 1)		0.2042	0.2159		
	0.2254	(10 1)			0.2282			
	0.2896	(15 1)			0.2968			

observed XRD peaks are also depicted in figure 3.13. The lattice parameters obtained from the experimental data fitting for all the homologs are given in table 3.2. The scattering vectors calculated using these lattice parameters can very well account for all the experimentally observed peaks. The calculated and the experimentally obtained scattering vectors, along with associated Miller indices, are also listed in table 3.2. The XRD profile for the smallest chain length homolog 8OBF8 is found to be slightly different from that of the other homologs as the satellite peaks corresponding to the periodic undulation along the layers were found to be relatively sharp (see figure 3.13(f)). This is probably due to the tendency of the compound to form a columnar phase because of the smaller chain length, as discussed later in the text.

It should be pointed out that a 2D rectangular lattice structure can also correspond to a columnar phase [118]. However, the dominating sharp XRD peaks corresponding to a layered structure and the presence of many weak (h 1) satellite peaks indicate that the layer undulated structure for the SmC_{LU} phase is more plausible. In addition, studies on the temperature dependence of the lattice parameters were also performed. Figure 3.14 shows the change in lattice parameter a for the compound 8OBF13 as a function of temperature along with the linear fit to the

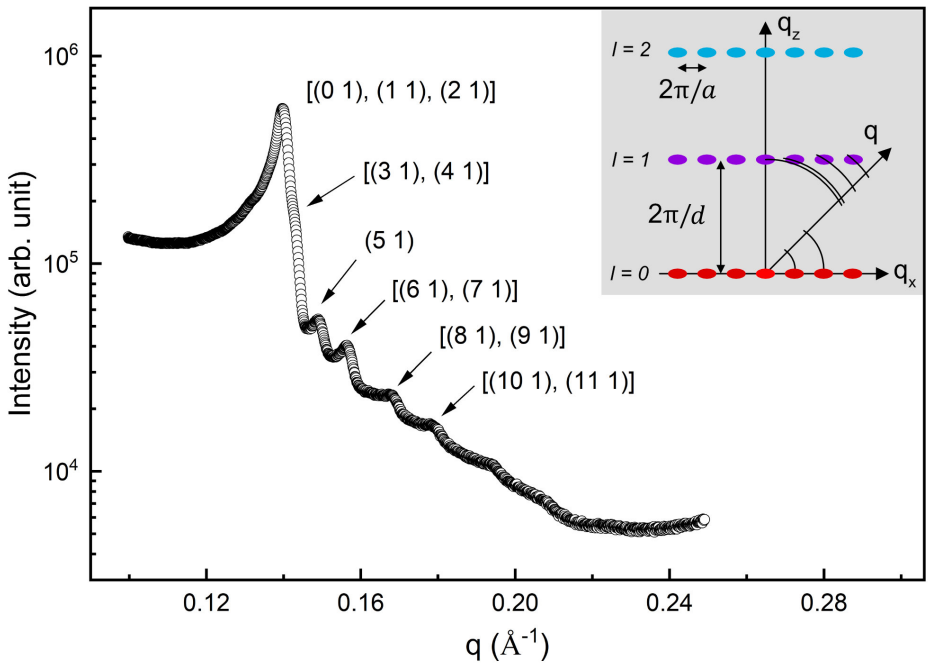

Fig. 3.12: A high-resolution XRD measurement of the compound 8OBF12 focused only in the small angle region shows several weak satellite peaks corresponding to undulation perpendicular to the layer normal, which can be fitted to a 2D rectangular lattice with lattice parameters d and a depicted in the inset. The ordered pairs in the square bracket indicate the Miller indices corresponding to these peaks. Some of the peaks associated with these Miller indices overlap due to a relatively large value of a ($\approx$ 600 Å) and can not be resolved experimentally.

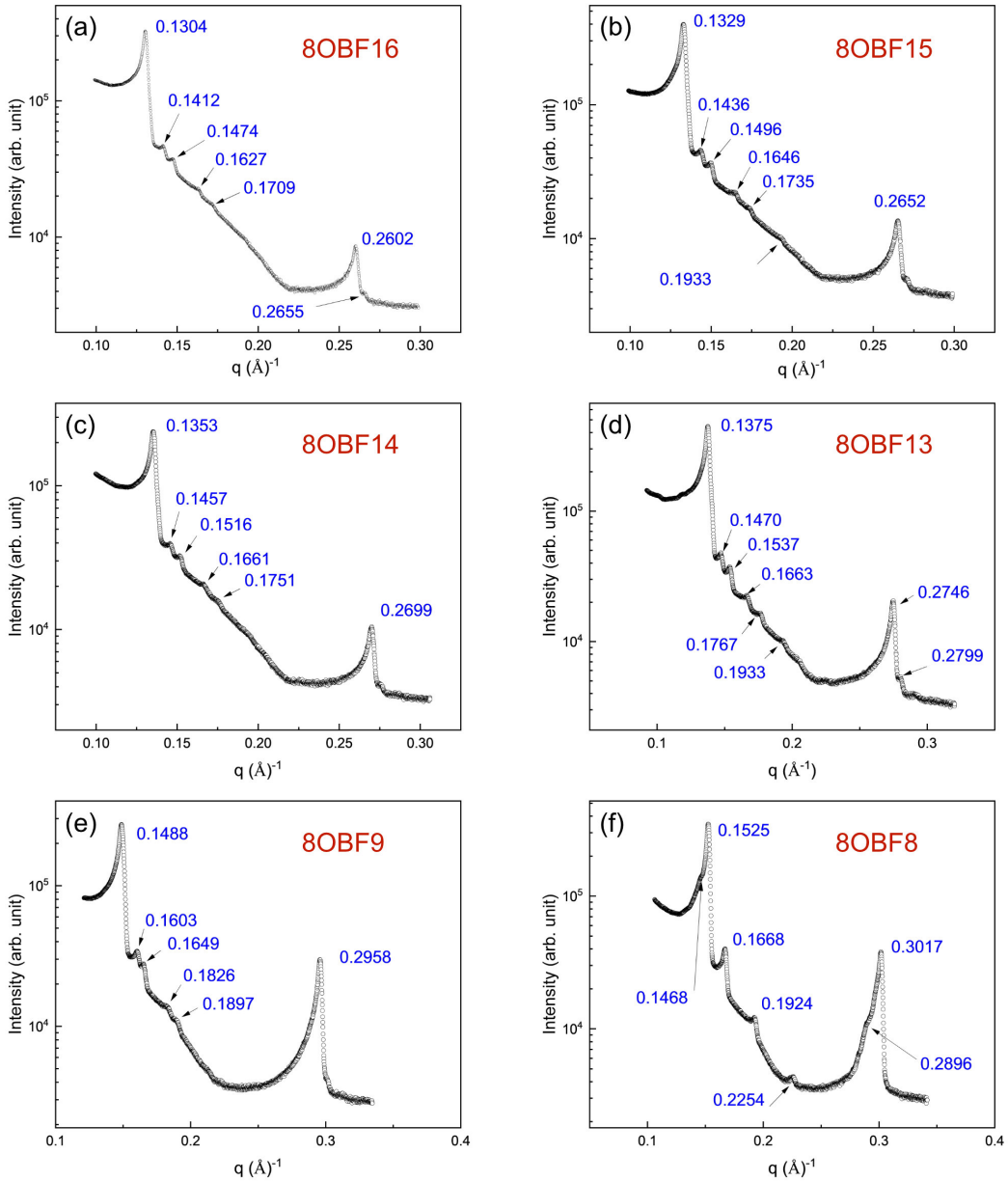

Fig. 3.13: A high-resolution XRD intensity profile measured in the small angle region for the homologs 8OBFn as denoted in each figure. The numbers represent the scattering vector associated with each peak. All the presented XRD profiles were taken at a temperature of 408 K. Strong sharp peaks corresponding to the layer spacing are consistent for the homologs. In addition, numerous weak satellite peaks associated with the layer undulation along the layer were observed. All the peaks can be well-fitted with a 2D rectangular lattice. The XRD profile of the compound 8OBF8 is slightly different from others as the observed satellite peaks were relatively prominent. See the text for a detailed discussion.

experimental data (intercept = 1367.8 ± 51.5, slope = − 6.5 ± 0.4). It is found that the lattice parameter d did not change appreciably with temperature throughout the stability range of the SmC_{LU} phase. On the other hand, the lattice parameter a increases linearly on decreasing the temperature. Such significant increases in the layer undulation wavelength with decreasing temperature have also been observed

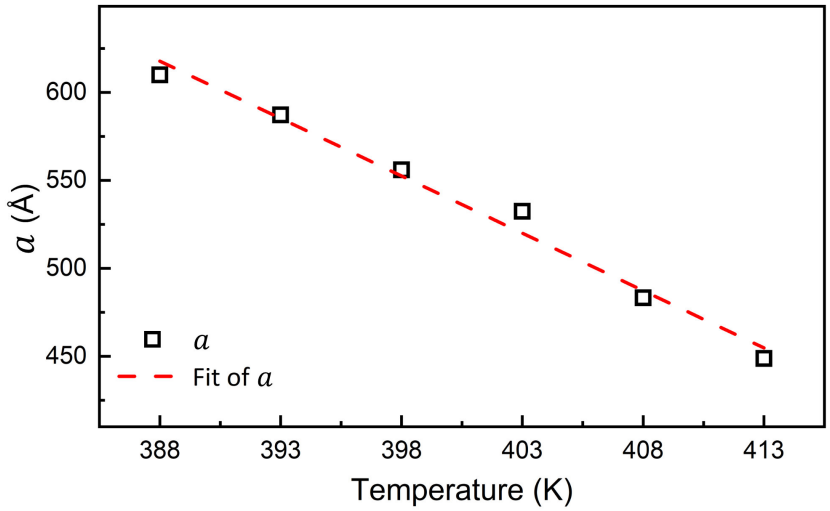

Fig. 3.14: The variation of the layer undulation wavelength a with temperature for the compound 8OBF13. The dashed line shows the linear fit to the data.

for other layer undulated phases reported in the literature [24, 42, 44, 54, 120] and corroborates the proposed structure of the SmC_{LU} phase for our compounds. The increase in the lattice parameter a with decreasing temperature perhaps can be explained by the increase in the elastic constant associated with the bending of the layers.

The molecular length ($l \approx 50$ Å) for the compound 8OBF12 estimated from the molecular structure was found to be larger than the layer thickness d, indicating that the molecules are tilted within the layer at an angle of about 25°. This observation holds true for all the studied homologs, and the corresponding tilt angle θ as a

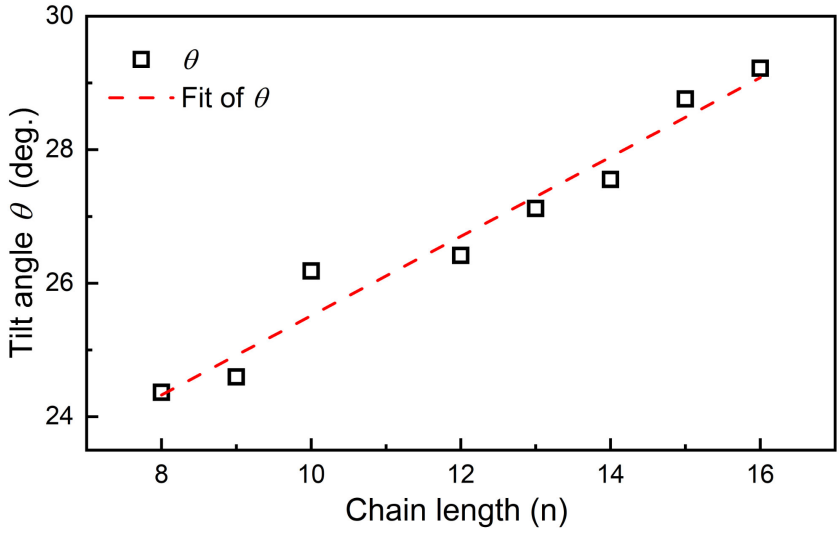

Fig. 3.15: The tilt angle θ as a function of chain length n attached to one end of the molecule for the homologs 8OBFn; n = 8 to 16.

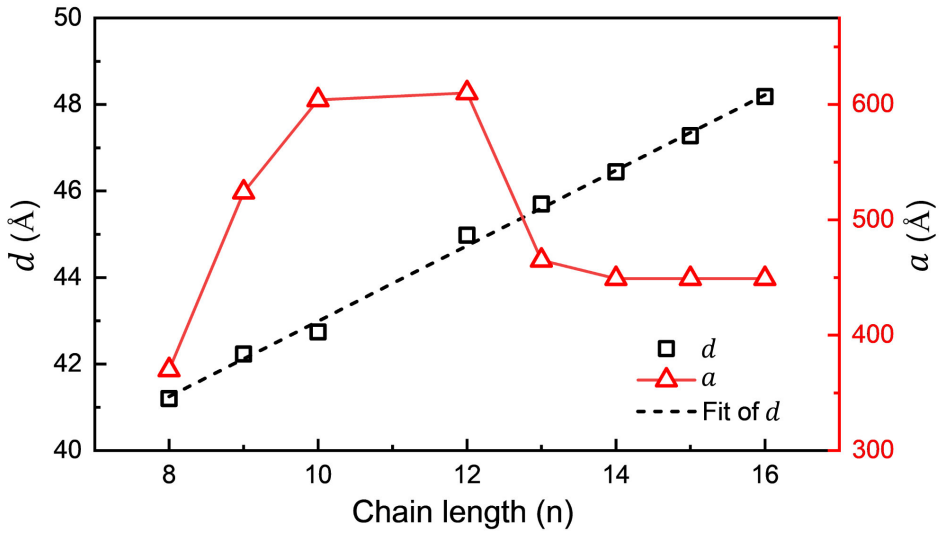

Fig. 3.16: The variation of the lattice parameters d and a as a function of chain length n at temperature 408 K for the homologs 8OBFn; n = 8 to 16.

function of n is shown in figure 3.15. The tilt angle θ increases linearly with chain length n, where the dashed line shows the fit to the data with slope 0.59 $\pm$ 0.04 and intercept 19.5 $\pm$ 0.6. It is interesting to observe that the linear increase in θ implies that the change of l is relatively faster than that of d with increasing n. It should also be noted that, for a given homolog, the layer spacing and, therefore, the θ does not change considerably with temperature within the stability range of SmC_{LU} phase. Figure 3.16 shows the variation of the layer thickness d and layer undulation wavelength a of the SmC_{LU} phase as a function of the chain length n of the homologs. The layer thickness d increases linearly with the chain length n as expected.The dashed line in figure 3.16 shows the linear fit to the data with slope 0.87 $\pm$ 0.02 and intercept 34.3 $\pm$ 0.3. On the other hand, the layer undulation wavelength a associated with the layer undulation periodicity varies non-monotonically with chain length n. The layer undulation wavelength a is almost constant at about 449 Å for the higher homologs, increases to about 610 Å below $n = 13$, and decreases again to a low value of about 370 Å for $n = 8$. The sharp decrease in the value of a for the lowest homolog (8OBF8) may be due to the tendency of this compound to form a columnar structure, as discussed later in the text.

3.2.5 Cryo-FESEM observation

The morphology of the SmC_{LU} phase at higher resolution is probed using the Cryogenic Field Emission Scanning Electron Microscopy (Cryo-FESEM). The Cryo-FESEM studies were carried out by using a Carl Zeiss (model - Ultra Plus) system with an electron beam of strength 5 kV. The sample was initially heated to the isotropic phase, cooled to a desired temperature in the SmC_{LU} phase, and

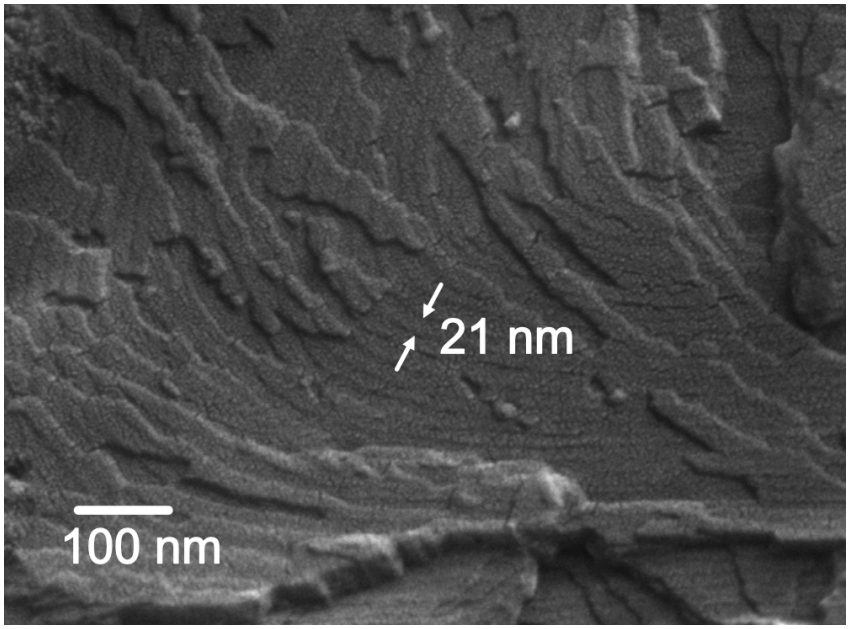

Fig. 3.17: The cryo-FESEM texture of the SmC_{LU} phase for the compound 8OBF15 showing the periodic stripes having periodicity consistent with the XRD measurements.

quenched by plunging it into the liquid nitrogen at about 83 K. The quenching arrests the structure of the liquid crystal phase even at lower temperatures. The sample was transferred to the cryo-chamber (Quorum PP3000T) in vacuum conditions, which was already kept at 83 K. The sample was subsequently cut using a knife and sublimated for 15 minutes at 183 K to remove the ice from the surface. The sample was coated with a thin layer of platinum of approximately 5 nm thickness. Back-scattered secondary electrons were monitored to produce the images of the sample.

Cryo-FESEM observations were performed to probe the morphology of the SmC_{LU} phase in high resolution for the homolog 8OBF15. Figure 3.17 shows the cryo-FESEM texture of the sample in the SmC_{LU} phase. A clear periodic structure was observed, having a period of about 21 nm. The undulation wavelength estimated from the XRD studies for the same compound 8OBF15 was about 450 Å as can be seen in the table 3.2. The observed periodicity in the FESEM texture is nearly half of the undulation wavelength, i.e., the width of the stripes in the model structure discussed below. Thus, the FESEM texture is qualitatively consistent with the XRD results and confirms the undulated structure of the SmC_{LU} phase.

3.2.6 Discussion

Our experimental results clearly indicate the layer undulated structure of the SmC_{LU} phase. But the SmC_{LU} phase was found to have distinct physical properties

from the layer undulated B7 phases reported earlier [24, 42, 44, 46, 121]. The B7 phases are consistently found to exhibit strong ferroelectric polarization within the layers, leading to a polarization splay, which is the basic driving force for undulation along the layers. The B7 phase is often switchable above a threshold electric field. Above this field, the polarization tends to align along the field, expelling the polarization modulation, and a transition from B7 to SmCP phase is induced [23]. The unique feature of the SmC_{LU} phase for the compounds studied here is that beyond a threshold voltage, the birefringence of the sample increases irreversibly without any textural change (see fig. 3.4) and there was no evidence of spontaneous polarization even at a field as high as 30 V/μm. The dielectric measurements discussed above show that the samples have a relatively low dielectric constant in the SmC_{LU} phase, indicating the absence of spontaneous polarization. The electro-optic studies in the SmC_{LU} phase discussed above clearly establish a quadratic coupling between dielectric anisotropy and the applied electric field, again indicating the absence of net polarization. These studies exclude the possibility of the usual polarization modulated layer undulated structure or B7-like configuration for the SmC_{LU} phase observed in our samples. The smooth fan texture, irreversible field-induced transition, and lack of net spontaneous polarization have been observed in some columnar phases [118, 119]. But the temperature variation of the layer undulation wavelength a along the layers and lack of polarization even in the field-induced state of SmC_{LU} phase excludes the possibility of columnar phase.

Based on the experimental results, we propose a possible double-tilted smectic structure with layer undulation for the SmC_{LU} phase as shown in figure 3.18(a). The layers are undulated with the asymmetric BC molecules, having a general tilted configuration with non-zero parallel and perpendicular components of polarization, which vary along the direction of layer undulation. The molecules adopt the SmTP configuration in the regions with large curvature of the layers, whereas in regions with zero curvature, they take the SmCP configuration. This type of organization of the molecules leads to defects separating stripes of continuously modulated regions (see figure 3.18). In the middle of the stripes, the molecules acquire an SmCP configuration with polarization in the plane of the layer, and as we move away from the center, the molecules lean such that the polarization has a non-zero component along the layer normal, i.e., SmCg configuration. At the edges of the stripes, the molecules acquire an SmTP configuration with the polarization vector in the tilt plane. It has been pointed out [38, 122] that the BC molecules having asymmetric structure (e.g., attaching a bulky group at one end of the molecules [36]) lead to the leaning of molecules in the layers. Therefore, the leaning order of the molecules in the layer can be attributed to the asymmetric structure of the BC molecules of our compounds. With the leaning order in the layer, one arm of the BC molecule is tilted more with respect to the layer normal than the other arm, which necessitates excess

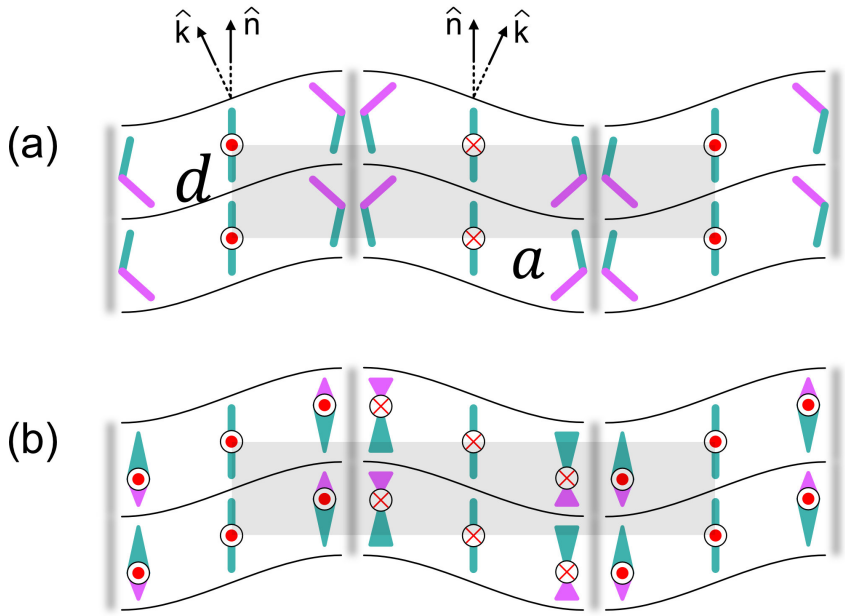

Fig. 3.18: (a) Illustration of undulated layer structure having double tilted organization of BC molecules in the SmC_{LU} phase. The defect walls are shown as gray regions in the layers. Two different colors have been used to indicate the molecular asymmetry. (b) The field-induced metastable state of the structure shown in (a) with the local reorientation of the molecules in the layers, which accounts for the irreversible field-induced transition observed experimentally. The stacking of these undulated layers produces a 2D rectangular lattice with no net polarization.

excluded volume for the former. It leads to the bending of the layers to compensate for the excess excluded volume. The modulation of polarization along the layers takes place in order to construct a continuous layered structure. The regions with high and low curvature of the layers have mainly the splay of the longitudinal and transverse components of the polarization, respectively. The modulated SmC_{LU} phase has net zero polarization over a period of the undulation, although the polarization is nonzero locally. The absence of polarization reversal current response can be attributed to the following reasons,

- The effective transverse component of polarization in the layer plane, which is responsible for the polarization reversal current response, is reduced due to the leaning of the molecules.

- The layer undulation wavelength and the polarization modulation period are in the nanometer scale, leading to zero net polarization macroscopically despite having a nonzero local polarization.

- A strong coupling between the layer undulation and the polarization modulation prevents its realignment along the field and flattening of the layers.

The applied field, perhaps, was not strong enough to induce polarization switching. Rather, the molecules reorient locally as a consequence of dielectric anisotropy of the system to acquire a configuration shown in figure 3.18(b), which can account for the increase in the birefringence of the sample without any change in the overall texture as observed in POM studies. The configuration shown in figure 3.18(b) perhaps is a metastable state that accounts for the irreversible field-induced transition observed experimentally.

It should be pointed out that although all the homologs show the layer undulated structure with similar physical properties, the lowest homolog (8OBF8) exhibits slightly different behavior. Firstly, the fan texture of 8OBF8 is found to be broken (see figure 3.9) in the absence of a field, and the irreversible field-induced transition occurs above a relatively higher threshold field of about 30 V/μm. Secondly, the satellite peaks in the XRD profile corresponding to layer undulation are relatively stronger compared to other homologs. As the polarizability of the aromatic core moiety of the mesogens is much larger than that of the aliphatic terminal chain, the stronger core-core and chain-chain interactions between the molecules tend to segregate these two moieties favouring lamellar phases. Therefore, homologs with larger chain lengths usually form layered structures separating the core and chain moieties. This has been observed experimentally for rod-like as well as bent-core molecules. The bent-core molecules with intermediate chain length tend to form a B1 phase with a columnar structure. Both the above results for the homolog 8OBF8 could be explained by the fact that the lower chain length tends to form a more segregated structure with smaller lattice parameter a, i.e., it has the tendency to form a columnar structure, and it becomes relatively hard to reorient the molecules by an external field. The lattice parameter a as a function of the chain length n is shown in figure 3.16. For the higher homologs (8OBFn, $n = 9 - 16$), the value of a is between 450 to 600 Å, and it decreases sharply to about 370 Å for the compound 8OBF8.

It was found that all the homologs studied show a quasi-planar alignment between glass plates irrespective of the treatment of the glass plates for planar or homeotropic alignment. A typical smooth fan texture (see figure 3.4) in the SmC_{LU} phase was observed between crossed polarizers for all the compounds. This alignment tendency can be attributed to the layer undulated structure of the SmC_{LU} phase as it would lead to excess excluded volume close to the boundary for homeotropic alignment, and this excluded volume effect tends to induce a bookshelf geometry of the layers.

3.3 Conclusion

In conclusion, we experimentally studied the phase behavior of a homologous series of compounds with asymmetric bent-core banana shaped molecules. The compounds exhibit a layer undulated SmC_{LU} phase with a 2D rectangular lattice structure. Unlike the usual B7 phases, the SmC_{LU} phase does not exhibit polarization current response despite showing an irreversible field-induced transition due to the coupling of dielectric anisotropy of the system. The undulation in the SmC_{LU} phase arises due to the leaning of the molecules in the layers. We also propose a model structure of the SmC_{LU} phase to account for the experimental observations.

4 Glassy relaxation in de Vries smectic liquid crystals

4.1 Introduction

Across the transition from the conventional smectic A (SmA) to the smectic C (SmC) phase, there is usually a significant reduction of the layer spacing, as depicted in figure 4.1(a). This is due to the fact that, in the SmA phase, the director $\hat{n}$ is parallel to the layer normal $\hat{k}$ with the layer spacing d similar to the molecular length l. On the other hand, in the SmC phase, the director $\hat{n}$ tilts away from the layer normal $\hat{k}$ by a tilt angle θ with a layer spacing d significantly less than the molecular length l. As discussed in section 1.1.4, across the SmA-SmC transition, the reduction of layer spacing in bookshelf geometry leads to the buckling of layers, resulting in the so-called chevron structure [16]. The chevron structure originates due to a mismatch between the smectic layer spacing in bulk and at the surface [16, 123]. The chevron formation causes various types of defects, such as zig-zag defects, which have been a challenging problem for surface stabilized ferroelectric LC displays [13, 16, 124]. This issue can be addressed using materials with no layer contraction across the SmA−SmC transition, as depicted by figure 4.1(b). Such a SmA phase is known as the "de Vries smectic A" phase, which we shall denote as 'dSmA phase' in our discussion. In the dSmA phase, molecules in a layer are tilted with respect to the layer normal but with random azimuthal tilt directions. The random distribution of the tilt direction makes this phase optically uniaxial about the layer normal, which is a characteristic feature of the SmA phase. This model structure is termed as diffuse cone model of dSmA phase [14, 15]. Across the transition from the dSmA to the SmC phase, the already tilted molecules in the layers in the dSmA phase choose a particular azimuthal orientation in the SmC phase with practically no layer contraction as shown in figure 4.1. A large number of materials consisting of calamatic (rod-like) molecules have been reported to exhibit the dSmA phase [13, 125–128]. But only a few bent-core banana shaped molecules are found to exhibit dSmA phase [129–133].

In addition to liquid crystalline phases, the anisotropic molecules sometimes exhibit a glassy state when cooling. A number of studies have been carried out on molecular dynamics and glass formation of calamatic liquid crystals [72–78], but

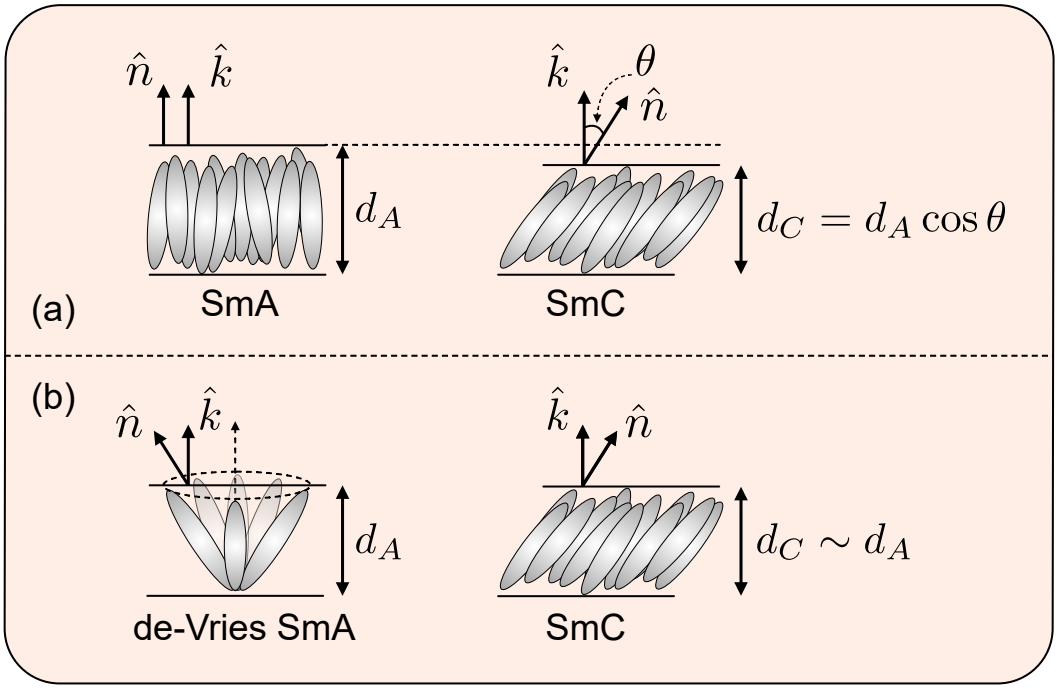

Fig. 4.1: Schematic representation of the molecular arrangement in conventional SmA, SmC, and de Vries SmA phases comprised of calamitic molecules. In the dSmA phase, the molecules are, on average, tilted away from the layer normal by a significantly large angle with their long axes randomly distributed on a cone according to the diffuse cone model proposed by Adriaan de Vries [15].

glass forming bent-core liquid crystals are rarely reported [79].

In this chapter, we investigate the physical properties of liquid crystalline phases of an achiral thiophene-based bent-core liquid crystal using various experimental techniques. The compound exhibits a high temperature short range nematic phase followed by two long range smectic phases. We report two key findings from our experimental studies. Firstly, we find that the higher temperature smectic phase is the dSmA phase, which transits to the SmC phase on decreasing temperature with practically no layer contraction. Unlike the typical BC liquid crystals, both the smectic phases are non-polar with calamatic type phase behavior. Secondly, both the smectic phases show a dielectric relaxation mode whose relaxation frequency decreases sharply when the temperature is lowered, suggesting a glassy behavior. The dielectric relaxation of the mode is of Cole-Cole type, and the temperature variation of relaxation frequency follows the empirical Vogel-Fulcher-Tammann (VFT) equation. This suggests the *fragile* nature of the glass for our sample with fragility parameter $D \approx 3$ [69]. The calorimetric studies further confirmed the glass transition at a temperature of about 271 K, which qualitatively agrees with the dielectric studies. We propose a simple model structure for the dSmA phase to account for the experimental observations. To our knowledge, this is the first study of a bent-core liquid crystal exhibiting a dSmA phase and showing glassy behavior.

4.2 Results and discussion

4.2.1 Phase sequence

The molecular formula of the compound used for our experimental studies is *2,5-bis(4′-(octyloxy)-[1,1′-biphenyl]-4-yl)thiophene-3-carbonitrile* and will be denoted as **BTCN8** in further discussion. The chemical characterization and preliminary studies on this compound can be found in reference [134]. The molecule has a bent-core banana shape with a central thiophene ring, as depicted in Figure 4.2(a). The opening angle and the molecular length, calculated from the energy minimized molecular structure, are about 143° and 43.5 Å, respectively. A strongly polar carbonitrile group attached to the central thiophene ring enhances the net dipole moment of the molecule at an angle to the long axis [134].

The differential scanning calorimetry (DSC) studies were carried out using $Mettler\ Toledo\ DSC\ 3$. The sample with a weight of about 2.56 mg was kept in an aluminum crucible, and another empty aluminum crucible was utilized as a reference. The DSC thermogram was recorded at different rates in both the heating and cooling cycles.

Differential Scanning Calorimetry (DSC) studies were performed on the sample to detect the various phase transitions in heating and cooling cycles at a rate of 5 K/min. The DSC thermogram revealed that the sample melts while heating at 365 K, which, on further heating, showed two transition peaks at 515.9 K and 518.6 K and goes to the isotropic phase. On cooling from the isotropic phase, two transitions were observed at 517.4 K and 514.9 K, and no other transitions were observed on further cooling the sample to room temperature. The inset in figure 4.2(b) shows the expanded view of the two closely spaced transitions. There is a small hysteretic shift in the transition temperatures between heating and cooling for both isotropic to nematic and nematic to SmA transitions, as expected for the first-order transition. Thus, the DSC thermogram clearly indicates the existence of two mesophases for the compound BTCN8 below its isotropic phase. However, detailed polarizing optical microscopy (POM) studies detect another transition at 402 K while cooling the sample. In POM studies, the optical transmittance through a planar aligned 5 μm thick sample kept between crossed polarizers was measured while cooling from the isotropic phase. The rubbing direction of the sample cell was kept at an angle of 45° from the polarizer direction for maximum transmittance. Figure 4.2(c) displays the normalized transmitted intensity as a function of temperature, which clearly detects all the phase transitions. The inset of figure 4.2(c) shows the existence of the short-range nematic phase. The discontinuous change in the slope of the transmitted

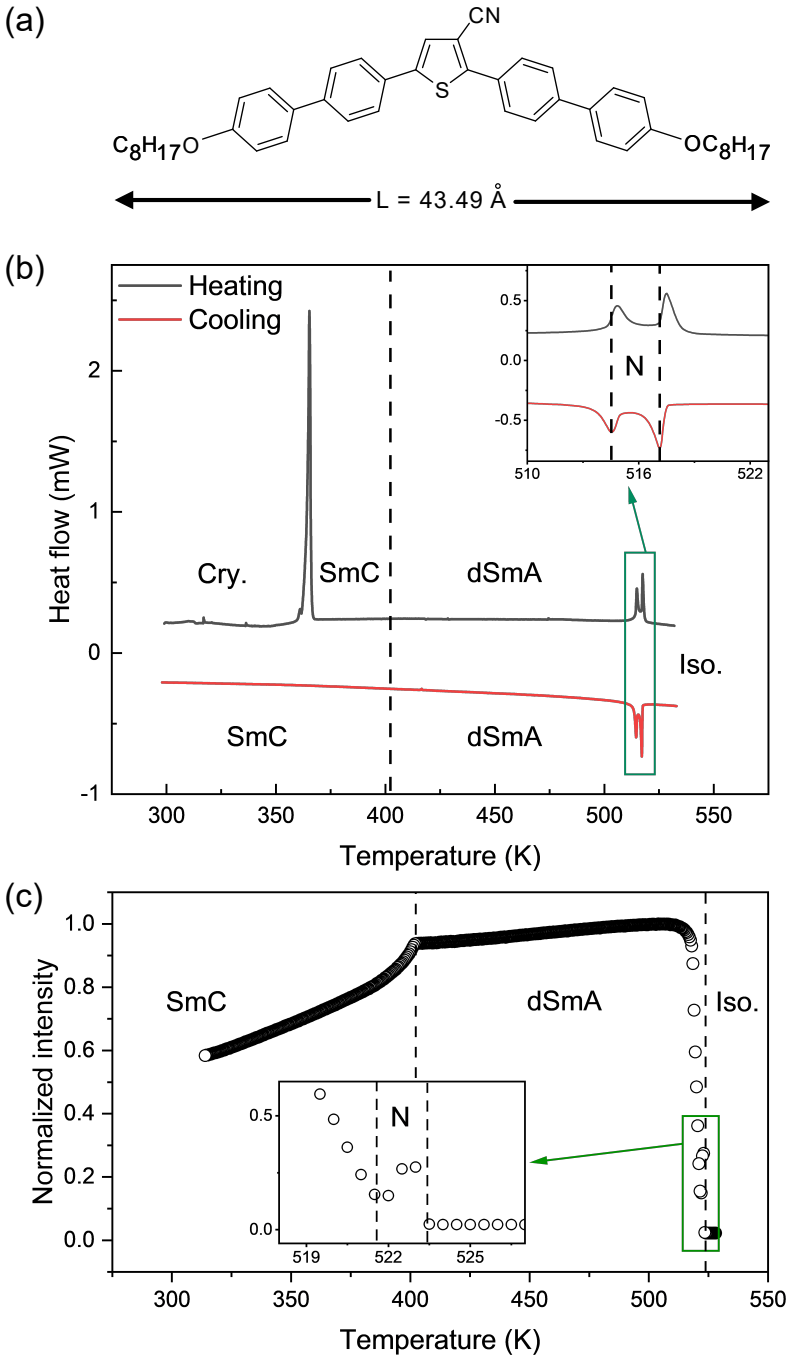

Fig. 4.2: (a) The molecular structure of the compound BTCN8. (b) DSC thermogram of the compound BTCN8 with heating and cooling rate of 5 K/min. The inset demonstrates the existence of a small range nematic phase. The sample does not crystallize on cooling till room temperature. The mesomorphic properties of the sample were retained for several weeks, and the melting transition was observed only on the first heating. (c) The temperature variation of the optical transmittance through a planar aligned sample of thickness 5 μm kept between crossed polarizers while cooling from the isotropic phase. The optical transmittance clearly detects the following phase transition sequence: Isotropic (523.5 K) N (521.5 K) dSmA (402 K) SmC. The inset reveals the existence of a nematic phase with a small range of temperature. All the observed phases are enantiotropic.

intensity curve at 402 K corresponds to an additional phase transition. Based on the experimental studies, we identify the following phase sequence for the compound BTCN8 on cooling till room temperature:

$$\text{Isotropic} \xrightarrow{517.4\ \text{K}} \text{N} \xrightarrow{514.9\ \text{K}} \text{de Vries SmA} \xrightarrow{402\ \text{K}} \text{SmC}$$

All the observed mesophases are found to be enantiotropic. The absence of a DSC peak across the dSmA to SmC phase transition indicates the second-order nature of this transition. The SmC phase became increasingly viscous on lowering the temperature while retaining the fluidity till room temperature. The sample did not crystallize on cooling. Instead, a glass transition was observed at 271 K, which will be discussed later in this chapter.

4.2.2 X-ray diffraction studies

Variable temperature x-ray diffraction (XRD) measurements were conducted using a DY 1042-Empyrean ($PANalytical$) diffractometer with CuK_α radiation of wavelength 1.54 Å and a $PIXcel$ 3D detector. The samples were filled in Lindemann capillary tubes with an outer diameter of 1 mm. The XRD intensity profiles were measured at different temperatures when cooling the sample from its isotropic phase.

The variable temperature XRD studies were carried out at various temperatures to investigate the molecular organization in the observed liquid crystalline phases. In the highest temperature short range nematic phase, a single diffuse peak was observed in the wide angle region with no sharp peak at the small angle region, which is characteristic of the Nematic phase. In the dSmA and SmC phases, the XRD intensity profiles as a function of the scattering vector q are shown in figure 4.3(a). In both of these phases, two sharp peaks were observed in the small angle region at q values in the ratio of 1:2. In addition, a diffused broad peak was observed in the wide angle region centered about $q = 1.36$ Å^{-1} and $q = 1.43$ Å^{-1} in the dSmA and SmC phases, respectively. The shifting of the maximum of the wide angle diffuse peak towards higher values of q on cooling is due to increased molecular packing density. The XRD results indicate a lamellar molecular organization with liquid-like order within the layers. The layer spacings calculated from the XRD data in the dSmA and SmC phases are 38.39 Å and 38.29 Å, respectively, which do not vary appreciably with temperature. The molecular length l of the compound BTCN8 is 43.5 Å, which is significantly larger than the observed layer spacing d in both the smectic phases. This indicates that the molecules are tilted within the layers. The tilt angle with respect to the layer normal can be estimated using $\theta = \cos^{-1}(d/l)$. The

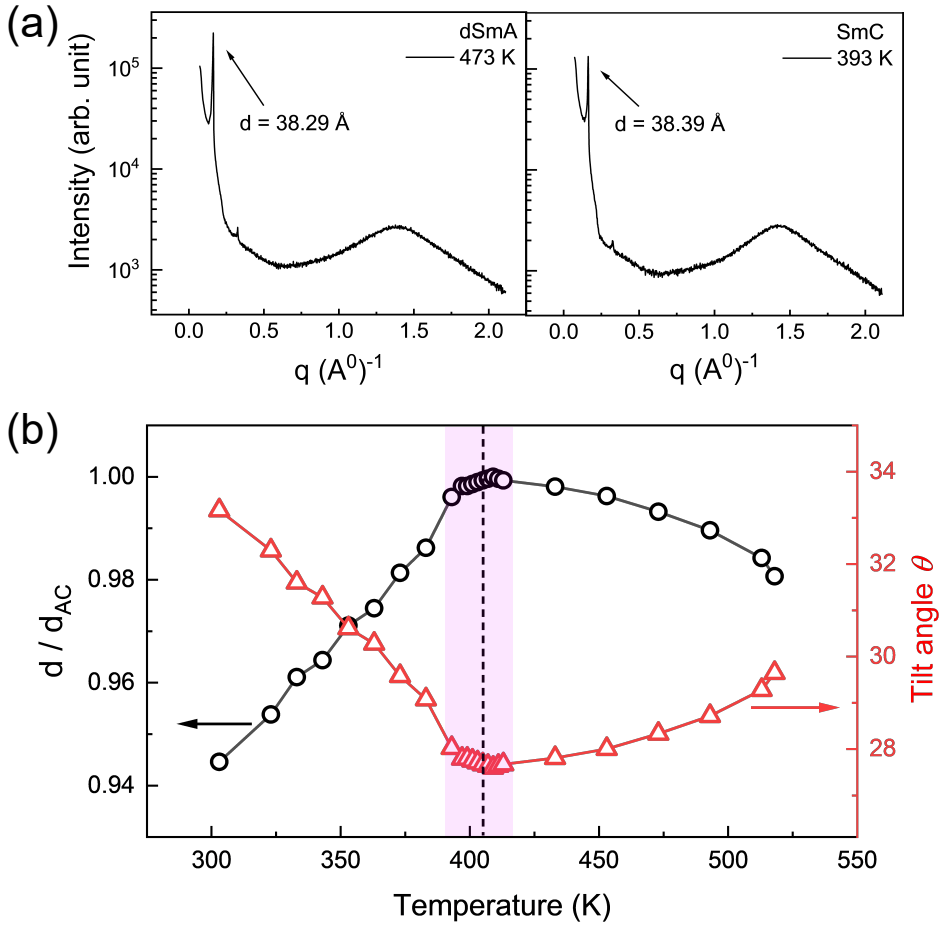

Fig. 4.3: (a) The XRD intensity profile for the compound BTCN8 in dSmA and SmC phases at temperatures 473 K and 393 K, respectively. (b) The temperature variation of the ratio d/d_{AC} and tilt angle θ were obtained from the XRD data and estimated molecular length. The layer thickness remains almost unchanged across the dSmA-SmC transition, showing the de Vries nature of the SmA phase. The vertical dotted line indicates the dSmA to the SmC transition temperature. Across the transition depicted by the pink-shaded region, the layer contraction is only about 0.17%. The error bars are smaller than the size of the symbols.

temperature variation of the tilt angle θ is shown in figure 4.3(b). The tilt angle θ varies slightly across the whole temperature range and attains a shallow minimum value of about 28° near the dSmA to SmC transition. Figure 4.3(b) also shows the temperature variation of the normalized layer spacing d/d_{AC}, where d_{AC} is the maximum value of layer spacing in the dSmA phase close to the transition. It is clear from figure 4.3(b) that the layer spacing does not change appreciably across the transition from the dSmA to the SmC phase. The layer contraction in the SmC phase at 10 K below the dSmA-SmC transition temperature is only about 0.17%. These observations confirm that the higher temperature smectic phase is a de Vries-type SmA phase. In the dSmA phase, the molecules are tilted within the layers, having a uniform azimuthal distribution of their tilt directions, giving rise to optically uniaxial texture about the layer normal. In contrast to the conventional SmA phase, the layer

spacing in the dSmA phase is significantly less than the molecular length. The large opening angle of the bent structure of the BTCN8 molecules and a strong dipole moment due to the polar cyano group projecting in the lateral direction perhaps favor the tilted non-polar molecular organization in the layers [135].

Across the transition from the dSmA to the SmC phase, the random directions of the already tilted molecules get correlated, giving rise to a uniformly tilted configuration with no considerable change in the layer thickness. It can be seen from figure 4.3(b) that the layer spacing is maximum near the dSmA-SmC transition and decreases slightly from this value in the dSmA phase at higher temperatures and in the SmC phase at lower temperatures. The slight increase in the layer thickness in the dSmA phase with decreasing temperature can be attributed to the stretching of the alkyl chain with increasing packing density. This trend of negative thermal expansion of the layer spacing in the dSmA phase has also been observed in other materials exhibiting de Vries-type SmA phases [126, 128]. In our sample, a slight decrease in layer spacing was observed in the SmC phase at lower temperatures. However, the observed layer contraction in the whole temperature range of about 225 K in the dSmA and the SmC phases is only about 5%. The POM studies discussed in the following section further confirmed the de Vries nature of the SmA phase.

4.2.3 POM and electro-optic measurements

Polarized Optical Microscopy (POM) investigations of the sample were conducted using an Olympus BX 50 microscope equipped with a hot stage ($Linkam$ LTS420E) and a digital camera ($Canon$ EOS 80D). For homeotropic alignment of the molecules, a thin sample was sandwiched between a clean glass slide and a glass cover slip. In addition, commercially available LC cells from ($INSTEC\ Inc.$) were employed for the planar and homeotropic alignment of the sample. The thickness of these cells was chosen to be 5 μm and 9 μm. The LC cells contain indium tin oxide (ITO) coated glass plates serving as electrodes for electro-optic and dielectric studies. The sample was introduced into the LC cell by capillary action in its isotropic phase using a hot plate.

The POM observations were carried out on different samples to further characterize the different phases. The POM textures were observed between crossed polarizers while cooling the sample from the isotropic phase. For our compound, the sample sandwiched between a clean glass plate and a cover slip tends to align homeotropically. In this preparation, the sample thickness was not controlled. The nematic phase below the isotropic phase exhibits a characteristic schlieren texture as shown in figure 4.4(a). The quasi-planar alignment of the molecules in the nematic

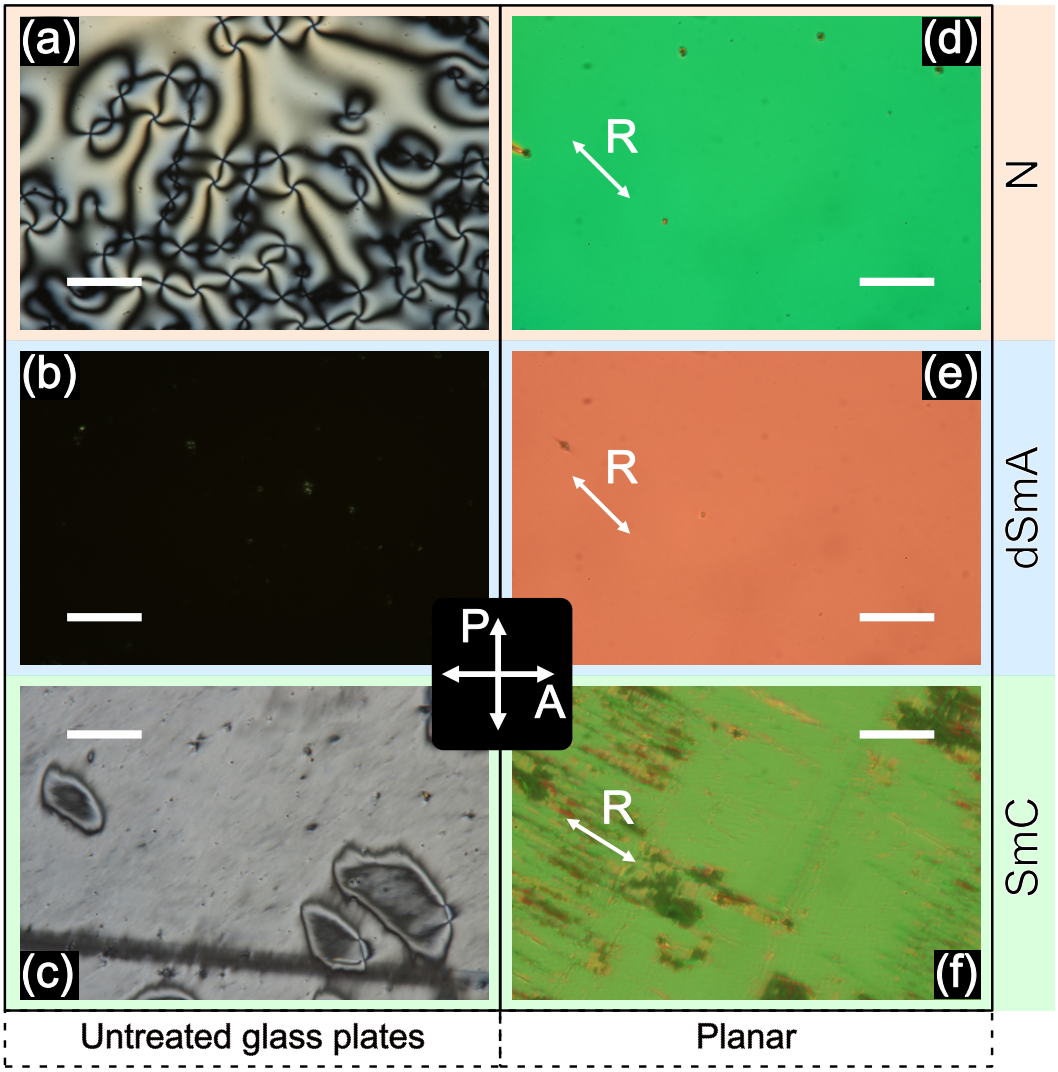

Fig. 4.4: POM texture of homeotropically aligned thin sample kept between a clean glass plate and a cover slip at (a) 522 K, (b) 518 K, and (c) 388 K; and that of the planar aligned sample of thickness 5 μm at (d) 522 K, (e) 508 K, and (f) 333 K. The POM textures were taken under crossed polarizers conditions while cooling the samples from their isotropic phase. ***R*** indicates the rubbing direction, and the crossed arrows denote the positions of the polarizers. The scale bar represents a length of 50 μm.

phase gives rise to the Schlieren texture. Upon cooling to the dSmA phase, the molecules align homeotropically, and the texture appears completely dark, as shown in figure 4.4(b). The dark texture remains invariant when rotating the sample on the microscope stage, confirming the uniaxial nature of the dSmA phase. In the dSmA phase, the layers prefer to orient parallel to the substrate, giving rise to the homeotropic alignment of the molecules. This observation and the intralayer molecular tilt observed in the XRD studies discussed earlier confirm the de Vries nature of the SmA phase. On further cooling, a birefringent schlieren texture was observed in the lower temperature SmC phase as shown in figure 4.4(c). The birefringent schlieren texture in this homeotropic geometry and the layer spacing less than the

molecular length observed in XRD studies suggest the tilted smectic order. Only unit strength defects were observed in the schlieren texture of this SmC phase, indicating the synclinic organization of the molecules in the layers.

In a planar aligned LC cell, the sample aligns homogeneously along the rubbing direction in the nematic and dSmA phase. The textures in the nematic and the dSmA phase are brightest when the rubbing direction is kept at 45° with respect to the polarizer, as shown in figure 4.4(d) and 4.4(e), respectively. In the dSmA phase, the layers are perpendicular to the glass plates, adopting a so-called bookshelf geometry with an optic axis along the layer normal. The smooth texture of the dSmA phase breaks down into two types of domains as shown in figure 4.4(f) in the lower temperature SmC phase. The degeneracy in the azimuthal tilt orientations of the molecules in the dSmA phase is lifted during the transition to the SmC phase. It leads to the formation of two surface stabilized regions with symmetrically opposite optical tilt, as shown in figure 4.5.

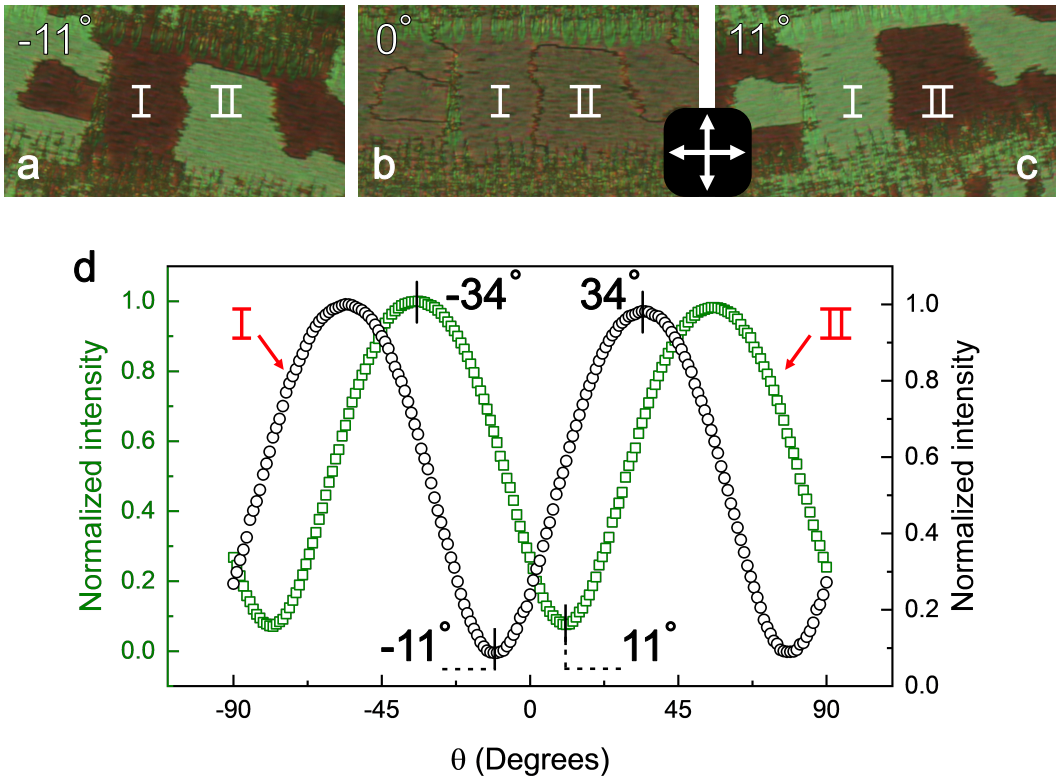

Fig. 4.5: The POM textures of a planar aligned sample of compound BTCN8 in the SmC phase at 373 K for three orientations (a) $-11°$, (b) $0°$, and (c) $11°$ of rubbing direction of the sample cell with respect to the analyzer. Two oppositely tilted domains indicated by i and ii were observed which appears identical at $0°$. The brightness of the domains i and ii interchange on rotating the sample clockwise and counterclockwise. (d) The variation of the normalized intensity of the domain i and domain ii as a function of the rotation angle θ of the rubbing direction of the LC cell with respect to the analyzer. The minima at $\mp 11\circ$ corresponds to the optical tilt angle in the domain i and ii, respectively.

The optical tilt θ_{opt} in the SmC phase of compound BTCN8 is the angle between the optic axis and the layer normal. In the SmC phase, two oppositely tilted domains were observed for a planar aligned sample of thickness 5 μm in POM between crossed polarizers. These domains appear optically identical when the rubbing direction of the LC cell is parallel, i.e., 0° to the analyzer as shown in figure 4.5(b). On rotating the sample stage clockwise (anticlockwise), domain i (domain ii) becomes darkest when the rubbing direction makes an angle of about $\mp 11^\circ$ with respect to the analyzer as shown in figure 4.5(a) (4.5(c)). A domain appears darkest when the local optic axis aligns with the analyzer, and the corresponding rotation angle gives the optical tilt angle θ_{opt}. Figure 4.5(d) shows the detailed variation of normalized intensity as a function of the rotation angle in domains i and ii. The two domains appear optically identical at angles -90°, -45°, 0°, 45°, and 90° due to the symmetric optical tilt in opposite directions in the two domains. The minima of the curves near 0° give the θ_{opt}, and the brightest positions occur at an angle of 45° from the darkest positions in the respective domains.

Though the layer thickness and, hence, the molecular tilt does not change appreciably across the dSmA to SmC transition, the increasing correlation of the molecular tilt direction in the SmC phase gives rise to an optic axis away from the layer normal. The θ_{opt} of a given domain of a 5 μm thick planar aligned sample in the SmC phase was measured using POM as a function of temperature. Figure 4.6(a) shows the variation of θ_{opt} as a function of $(T_{AC} - T)$, where T_{AC} is the dSmA to SmC transition temperature and T is the measured temperature. The inset of figure 4.6(a) depicts the POM texture of two opposite tilted domains under crossed polarizers at 287 K. The rotation angle between dark states in domains of opposite tilt orientations is $2\theta_{opt}$. As can be seen from the figure 4.6(a), the value of θ_{opt} increases continuously from zero and tends to saturate at lower temperatures. This increase in the θ_{opt} at (T_{AC}) is suggestive of a second-order transition from the dSmA to the SmC phase. This can be verified by fitting the temperature variation of the θ_{opt} to the power law:

$$\theta_{opt}(T) = \theta_0(T_{AC} - T)^{\beta}, \tag{4.1}$$

where β is an exponent, which can be related to the nature of the phase transition. The generalized Landau theory predicts $\beta = 0.5$ for second-order transition, whereas $\beta = 0.25$ for a tricritical point corresponding to crossover from second- to first-order transition [136]. The solid line in figure 4.6a shows the fit to the experimental data using eqn. 4.1 with exponent $\beta = 0.255 \pm 0.009$ for our sample. The obtained β value suggests that the dSmA to SmC transition in our sample is close to the tricritical point. The absence of a DSC peak associated with this transition in our sample also suggests that the transition is of second order in nature. Similar values of the exponent β have also been reported for other materials exhibiting dSmA to SmC phase transition [136, 137].

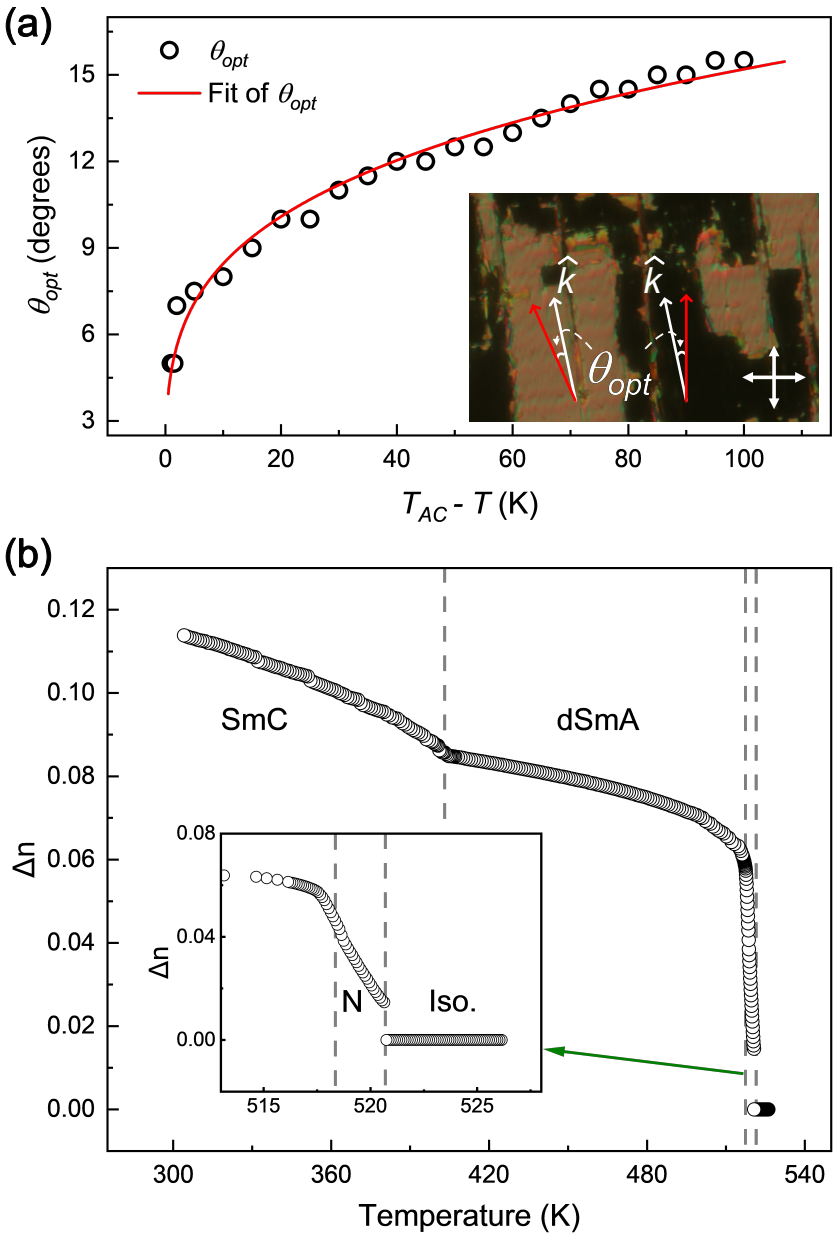

Fig. 4.6: (a) The variation of optical tilt angle θ_{opt} as a function of $(T_{AC} - T)$ in the SmC phase. The solid line shows the fit to the experimental data using eqn. 4.1. The inset of (a) shows the oppositely tilted domains in the SmC phase with the layer normal denoted by unit vector $\hat{k}$. In both the domains, $\hat{k}$ are parallel, but the optic axes are tilted on the opposite side of $\hat{k}$, giving rise to the optical contrast between crossed polarizers. The white and red arrows represent the direction of the layer normal $\hat{k}$ and the optic axis, respectively, in the two domains. (b) Temperature variation of the effective birefringence (Δn) of a planar aligned sample while cooling from the isotropic phase. The inset of (b) shows the magnified view of the data in the short temperature range of the nematic phase.

We also measured the effective birefringence of a planar aligned sample of thickness 5 μm as a function of temperature in the liquid crystalline phases. To evaluate the effective birefringence of a planar aligned sample, we measured the variation of average intensity transmitted through the sample as a function of

temperature. The planar aligned sample was kept on the microscope stage at an angle of maximum transmittance between crossed polarizers, and images were taken with varying temperatures by introducing a red filter of wavelength 700 nm in the light path. The average transmitted intensity was computed from the POM images using MATLAB.

The birefringence was measured by monitoring the transmitted intensity through the sample between crossed polarizers using POM. The transmitted intensity through the sample can be written as [7],

$$I = \frac{I_0}{2} \sin^2(2\Psi)(1 - \cos \Delta\Phi) \tag{4.2}$$

where I_0 is the intensity of the incident light, Ψ is the angle between the local optic axis and the polarizer, and $\Delta\Phi = (2\pi\Delta n d)/\lambda$ is the phase difference introduced by the sample between the ordinary and extraordinary rays. Here, d is the sample thickness, λ is the wavelength of the incident light, and Δn is the effective birefringence of the sample. In our experiments, the angle Ψ was set to 45° for maximum transmittance. The effective birefringence Δn was calculated using eqn. 4.2. The variation of Δn as a function of temperature is shown in figure 4.6(b). While cooling from the isotropic phase, a discontinuous jump in the Δn was observed at the Isotropic-N transition temperature. The value of Δn continued to increase in the N phase, and a slope change at the N-dSmA transition temperature was observed. The Δn value increases slightly with decreasing temperature and tends to saturate at lower temperatures in the dSmA phase. The Δn again started to increase with decreasing temperature from the dSmA to SmC transition temperature. The low value of the birefringence in the dSmA phase ($\Delta n \approx 0.08$) compared to that of the SmC phase supports the de Vries nature of the SmA phase [13].

Though the transition from the dSmA to the SmC phase is not detected in the DSC measurements, a clear textural change was observed in the homeotropic as well as planar-aligned LC cells at about 402 K. In addition, the temperature variation of the optical tilt angle and the birefringence of the sample also show a clear phase transition at 402 K. These observations confirm the existence of phase transition at 402 K and can not be explained by other effects, such as surface-induced changes. The second order nature of this transition accounts for the absence of DSC peak.

The spontaneous electric polarization of the sample in the dSmA and SmC phase was investigated using a triangular wave voltage technique [33] with varying amplitudes and frequencies for planar as well as homeotropically aligned samples. The current response of the sample was measured by monitoring the voltage drop across a 1 kΩ resistor connected in series with the sample cell. A voltage of amplitude

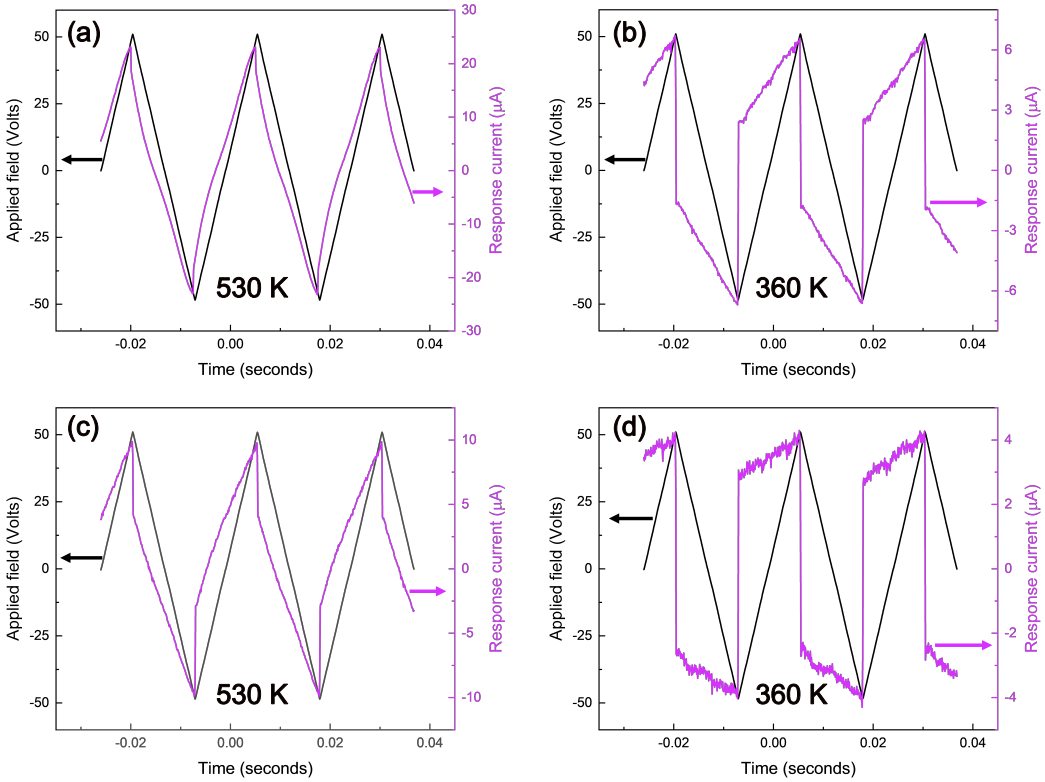

Fig. 4.7: Time evolution of current response when the sample was subjected to a triangular AC voltage of amplitude 50 V and frequency 40 Hz for planar alignment in (a) dSmA and (b) SmC phase, and homeotropic alignment in (c) dSmA and (d) SmC phase, respectively. The absence of a current peak due to polarization reversal indicates that both the smectic phases are apolar in nature.

50 V at frequency 40 Hz was applied across the planar aligned sample of thickness 5 μm. The current response of a 5 μm thick planar-aligned sample in the dSmA and SmC phase are shown in figure 4.7(a) and 4.7(b), respectively. The absence of peaks corresponding to polarization reversal current in both phases confirms that the layers do not possess spontaneous polarization. Similar experiments were performed on a 9 μm thick homeotropically aligned sample. The current response for this alignment in the dSmA and SmC phase are shown in figure 4.7(c) and 4.7(d), respectively. No polarization reversal current was observed again, confirming that the layers in both the smectic phases do not possess spontaneous polarization. Despite the absence of polarization, a clear reversible field-induced change in the texture was observed in the SmC phase for a planar aligned sample.

The texture in the dSmA phase does not change appreciably with the applied field, even at an amplitude of about 10 V/μm. On the other hand, the color of the texture changes slightly in the lower temperature SmC phase even at a small field of about 2 V/μm as shown in figure 4.8(a) and 4.8(b). The changes in the color indicate a slight increase in the birefringence of the sample, which arises due to more localized molecular distribution on the tilt cone, which will be discussed later

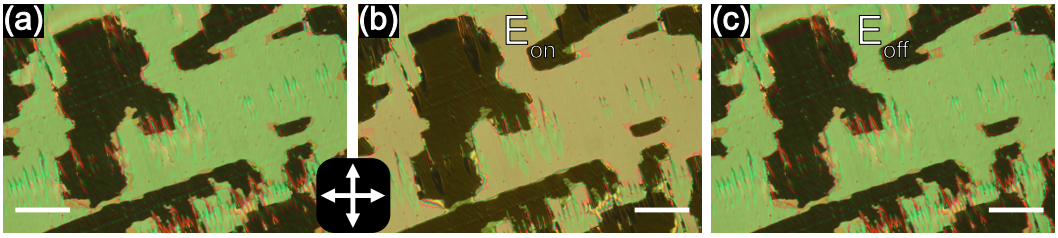

Fig. 4.8: The field induced changes in the POM textures of a planar aligned sample in the SmC phase at 360 K between crossed polarizers. The texture (a) at initial zero fields, (b) with a triangular field of amplitude 2 V/μm and frequency f, and (c) after removing the field. The length of the bar shows a scale of 50 μm.

in the text. This field-induced transformation is reversible in nature as the original texture can be retrieved after removing the field, as shown in figure 4.8(c).

The steady state field induced electro-optical response of a planar aligned sample was measured using a He-Ne laser with the application of a triangular AC voltage. The sample was kept between crossed polarizers at an orientation of maximum transmittance, and the transmitted intensity was recorded using a low-noise high gain photodiode connected to a mixed signal oscilloscope (*Agilent Technologies* MSO6012A). The intensity was normalized using $I_{nor} = (I - \bar{I})/\bar{I}$, where I is the measured transmitted intensity through the sample, and $\bar{I}$ is the mean value of the transmitted intensity.

The time trace of the applied triangular wave voltage, along with the normal-

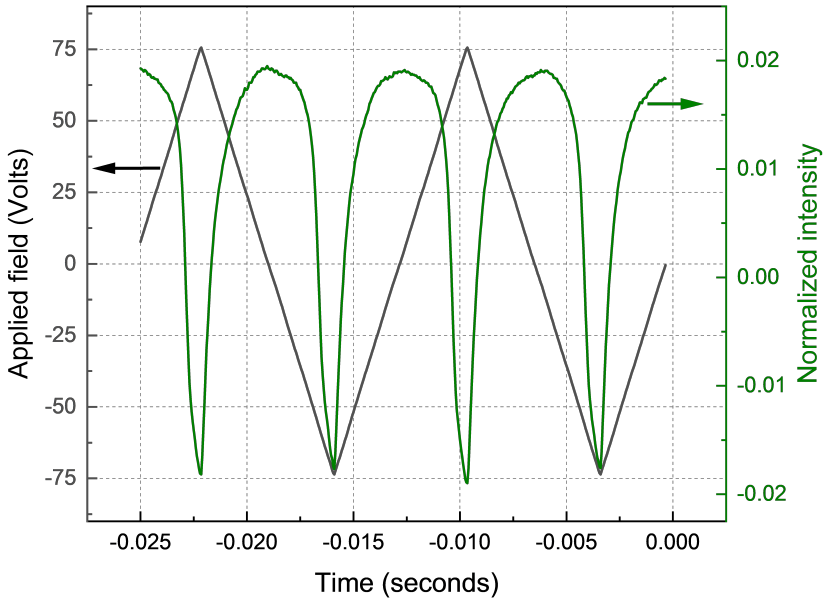

Fig. 4.9: The normalized optical transmittance along with the applied AC voltage as a function of time through a planar aligned sample of thickness 5 μm kept between crossed polarizers at 393 K.

ized optical transmittance through a planar aligned sample kept between crossed polarizers at 393 K is shown in figure 4.9. The observed optical response was found to be at twice the frequency of applied voltage, suggesting a quadratic coupling between the field and the dielectric anisotropy of the sample. This result also indicates the absence of polarization in the SmC phase. As seen from figure 4.9, the transmitted intensity is maximum at zero fields and decreases with increasing magnitude of the field. This is due to the optical phase difference ($\Delta\phi$) lying between π and 2π for our 5 μm thick sample. No such optical response was found in the dSmA phase with an applied field as high as 20 V/μm.

4.2.4 Dielectric studies

Dielectric measurements were performed on the sample filled in commercially available LC cell using a high-performance impedance analyzer ($Novocontrol$ Alpha-A) in the frequency range of 1 Hz to 10 MHz. The measurements were limited to 1 Hz due to the dominating charge current contribution at lower frequencies. A sinusoidal AC voltage with an rms amplitude of 0.5 Volts was used during the dielectric measurement without applying a bias voltage. The temperature of the sample was monitored using a homemade temperature controller with a temperature stability of 0.1 K. However, the maximum temperature that can be attained using this setup is 423 K. Therefore, to study the variation of the dielectric constant of the sample in the higher temperature range, a complimentary custom-made dielectric setup with a frequency range of 1 Hz to 100 kHz was employed. The temperature of the sample was monitored by a microscope hot stage and a controller ($Instec\ Inc.$). In this setup, a sinusoidal AC voltage of rms amplitude 0.5 Volts was applied to the sample cell, and a resistance of 1 kΩ connected in series. A lock-in amplifier ($Stanford\ Research$ SR830) was utilized to measure the amplitude and phase of the voltage drop across the 1 kΩ resistance. The impedance analysis was used to determine the capacitance of the LC cell with and without the sample. The ratio of these measured capacitances gives the effective dielectric constant of the sample.

The dielectric properties of the samples were investigated using the LC cells for planar alignment. The effective dielectric constant (ϵ_{eff}) was measured by applying a sinusoidal AC voltage of rms amplitude 0.5 V and frequency 5641 Hz while cooling the sample from its isotropic phase. Figure 4.10 shows the temperature variation of ϵ_{eff} of the sample, which clearly detects the transitions between the observed phases. The transition temperatures agree with the DSC and POM measurements. The increase of ϵ_{eff} in the planar aligned nematic phase while cooling from the isotropic phase suggests negative dielectric anisotropy of the sample. The ϵ_{eff} continued to increase on further decreasing the temperature till 333 K and sharply

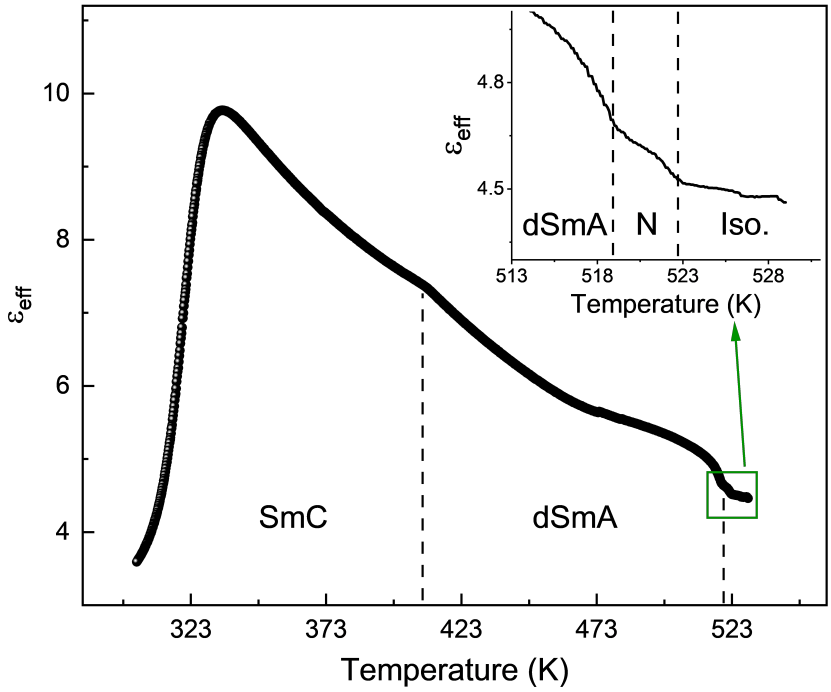

Fig. 4.10: The variation of the effective dielectric constant (ϵ_{eff}) of the compound BTCN8 in a planar aligned LC cell of sample thickness 5 μm as a function of temperature. The data clearly detects the various phase transitions and is in agreement with the DSC and POM observations. The dielectric constant's low value indicates the absence of spontaneous polarization in the sample. The inset shows the magnified view of the marked region.

decreased below it. This sharp decrease does not correspond to a phase transition. Rather, it occurs due to dielectric relaxation, as discussed later in the text.

To study the dielectric relaxation behavior of the samples, the dielectric permittivity was measured as a function of frequency in the range of 1 Hz to 10 MHz at different temperatures for planar aligned samples. The frequency dependent complex dielectric permittivity of the sample can be written as,

$$\epsilon^*(f) = \epsilon'(f) + i\epsilon''(f) \tag{4.3}$$

where ϵ' and ϵ'' are real and imaginary parts of the complex dielectric permittivity, respectively, and f being the frequency of the applied field.

The frequency dependence of $\epsilon''(f)$ at different temperatures in the dSmA and SmC phases are shown in figure 4.11. The observed peaks in $\epsilon''(f)$ curve correspond to the relaxation frequency of different dielectric modes of the sample. Figure 4.11(a) illustrates the frequency dependence of $\epsilon''(f)$ in the high temperature range from 423 K to 393 K with a temperature step of 4 K. The sample is in the dSmA phase at 423 K, and the transition to the SmC phase occurs at about 403 K. The relaxation

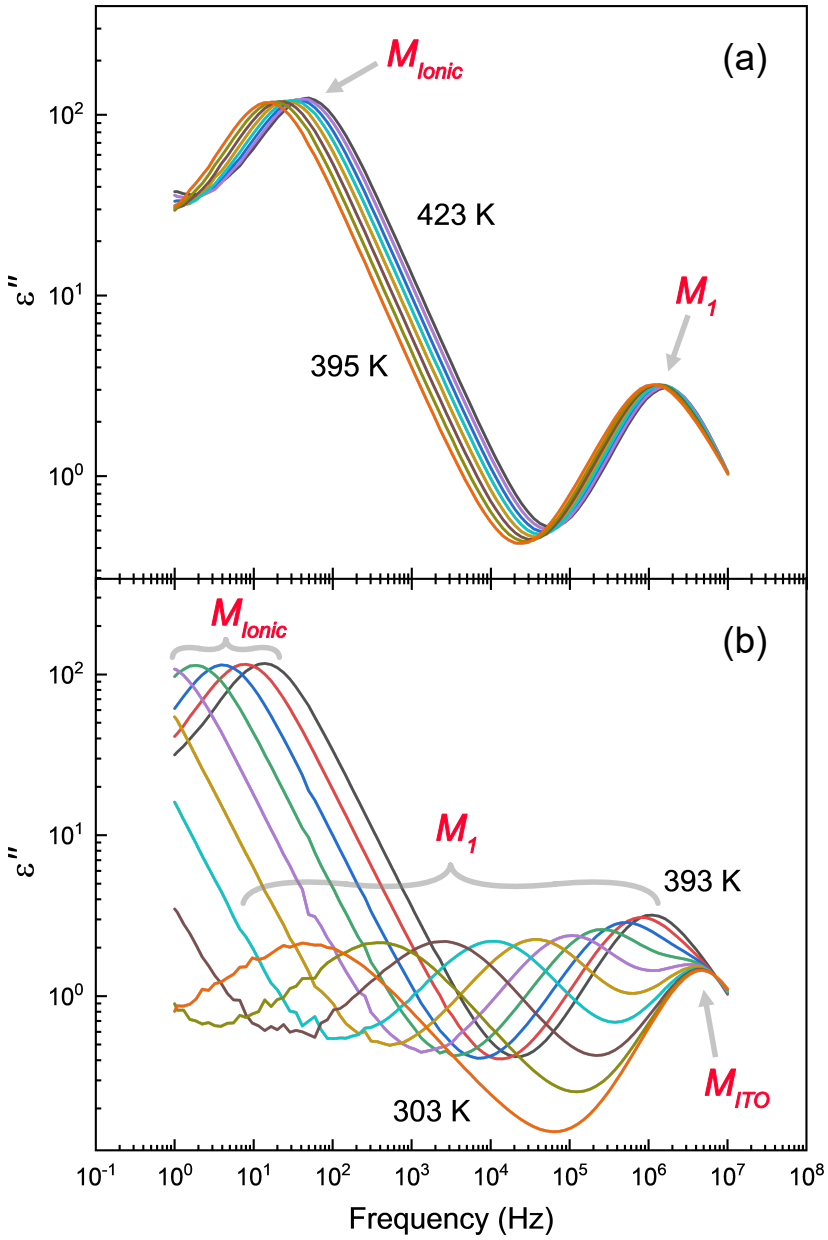

Fig. 4.11: The variation of the imaginary part of the dielectric constant (ϵ'') as a function of frequency at different temperatures. (a) In high temperature range from 423 K to 395 K with a temperature step of 4 K. (b) In the low temperature range from 393 K to 303 K with a temperature step of 10 K. The peaks in the data represent various dielectric relaxation processes.

peaks in the small frequency range below 100 Hz with relatively high dielectric strength are arising due to the ionic effects in the sample and will be ignored in further discussions. Another mode with the relaxation frequency in the MHz range was found in this temperature range, which is denoted as M_1 in the figure 4.11(a). The intensity of these relaxation peaks remained almost constant, and the peak frequency gradually decreased upon lowering the temperature. The M_1 mode was found to exist in both dSmA and SmC phases and does not vary appreciably across

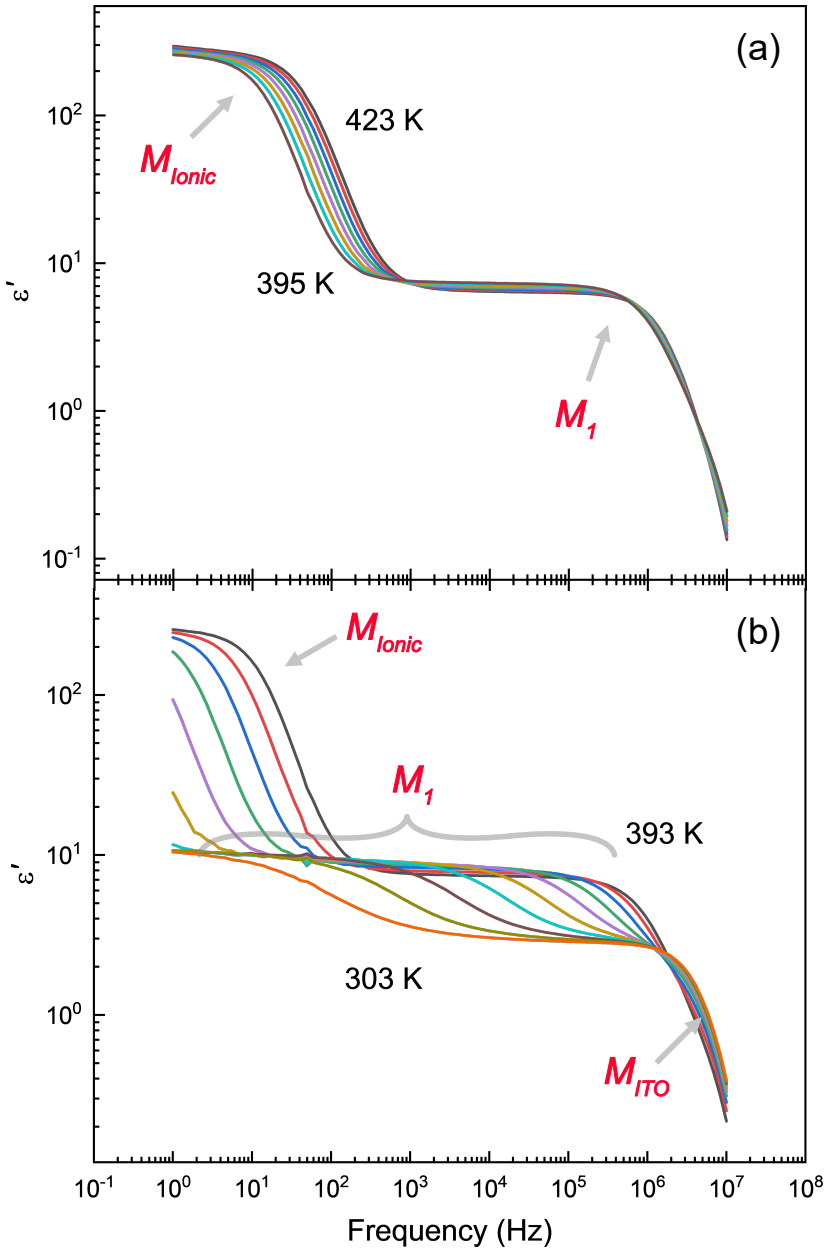

Fig. 4.12: The variation of the real part of the dielectric constant (ϵ') as a function of frequency at various temperatures. (a) In high temperature range from 423 K to 395 K with a temperature step of 4 K. (b) In the lower temperature range from 393 K to 303 K with a temperature step of 10 K. The step change in the data represent various dielectric relaxation processes.

the transition, as can be seen from figure 4.11(a). The frequency dependence of $\epsilon''(f)$ in the lower temperature range from 393 K to 303 K with a temperature step of 10 K is shown in figure 4.11(b). At lower temperatures, the relaxation frequency of mode M_1 started to decrease rapidly with decreasing temperature and attained a value of about 50 Hz at ambient temperature. In this lower temperature range, another weak relaxation peak at about 5 MHz was clearly visible, which did not vary with temperature as shown in figure 4.11(b). This peak, denoted as M_{ITO},

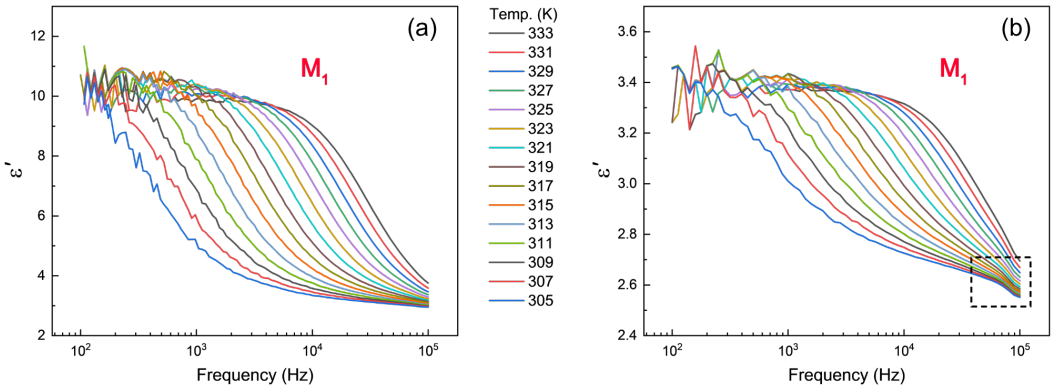

Fig. 4.13: Frequency dependence of the real part of dielectric constant ϵ' for (a) planar aligned sample and (b) homeotropically aligned sample at different temperatures. The noisy data in the lower frequency domain is due to experimental artifacts. The temperature depicted in the legend applies to both graphs. A slight change in the data enclosed by the dotted rectangle is not a sample property. Rather, it occurs due to the LC cell, as it was found to exist in the measurements with empty cells, too.

arises due to the finite sheet resistance of the ITO coating used in the LC cell and is masked by the M_1 mode in the higher temperature range. Figure 4.12 shows the temperature dependence of the corresponding real part of the dielectric constant (ϵ') as a function of frequency. The drop or step change in the ϵ' corresponds to the relaxation frequency of different dielectric modes of the sample.

Similar experiments were carried out on a homeotropically aligned sample, where the real part of the dielectric constant was measured in the homemade custom setup as a function of frequency for planar as well as homeotropic aligned samples at various temperatures. For the planar aligned sample, the dielectric relaxation shown in figure 4.13(a) agrees very well with the measurements performed using a commercially available setup (Novocontrol Alpha A). This further confirms that the relaxation process arises from the sample. In commercially available homeotropic LC

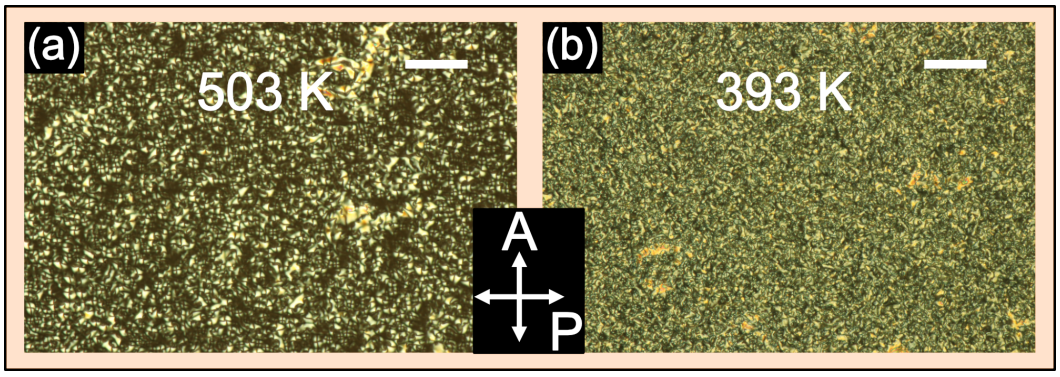

Fig. 4.14: The POM texture of the sample in a homeotropic LC cell of thickness 9 μm under crossed polarizers in (a) the dSmA phase and (b) the SmC phase. The scale bar indicates 100 μm.

cells of thickness 9 μm, the molecular alignment is found to be quasi-homeotropic with a large number of bright spots in the POM texture (non-uniform dark texture) between crossed polarizers, as shown in figure 4.14(a). In the SmC phase at lower temperatures, the sample acquires an inhomogeneous grainy texture, as shown in figure 4.14(b), instead of an expected schlieren texture. This non-uniform alignment is probably due to the incompatibility of the strong homeotropic anchoring and the diffuse cone structure of the dSmA phase. The presence of mode M_1 in the homeotropic cell can be attributed to the quasi-homeotropic alignment of the molecules. Thus, the sample exhibits one dielectric relaxation mode M_1 present in both alignments. The dielectric strength in the homeotropic aligned sample is significantly lower compared to that in the planar cells (see figure 4.13(b)), indicating that the mesophases possess negative dielectric anisotropy.

In order to analyze the measured dielectric relaxation processes, the dielectric spectra were fitted using the Havriliak-Negami (HN) equation [138, 139]. This empirical equation expresses the frequency-dependent complex permittivity ϵ^* in terms of the various relaxation processes given by,

$$\epsilon^*(f) - \epsilon_\infty = -\frac{i\sigma_0}{\epsilon_0 \omega^s} + \sum_{j=1}^{n} \frac{\Delta\epsilon_j}{\{1 + (i\omega\tau_j)^{\alpha_j}\}^{\beta_j}} \tag{4.4}$$

In this equation, $\Delta\epsilon_j$ represents the dielectric strength of the jth relaxation process, τ_j represents the corresponding relaxation time, ϵ_∞ represents the high-frequency limit of permittivity, and α_j, β_j are known as shape parameters. These parameters α_j and β_j describe the broadness and asymmetry of the dielectric loss spectra, respectively, and satisfy the conditions $0 < \alpha_j < 1$ and $0 < \alpha_j\beta_j < 1$. The term $i\sigma_0/\epsilon_0\omega^s$ is related to the conductivity, where σ_0 is the direct current (DC) conductivity, ϵ_0 is the permittivity of free space and s is a fitting parameter that determines the slope of the conductivity. In the case of pure Ohmic conductivity, $s = 1$, while $s < 1$ could be observed in the case of additional influence due to electrode polarization [67]. The HN equation reduces to the Cole-Davidson equation [140] when $\alpha = 1$, and to the Cole-Cole equation [141] when $\beta = 1$. The relaxation process under discussion is termed Debye relaxation for both α and β equal to unity.

The dielectric spectra for our sample could be fitted well using eqn. 4.4. Figure 4.15(a) shows the variation of $\epsilon''(f)$ as a function of frequency at 333 K along with the fitted curve. The fitting parameters obtained for some temperatures are listed in table 4.1. The asymmetry parameter $\beta = 1$ for our sample remains almost constant at varying temperatures. This implies that the shape of the dielectric loss peak is symmetric, and the relaxation process is of the Cole-Cole type. The Cole-Cole parameter α was found to be close to 0.68 at lower temperatures and

tends to decrease slightly with increasing temperature. This indicates that the width of the dielectric loss spectrum tends to increase with decreasing temperature, as can also be seen from figure 4.11(b). The deviation of experimental data from the fitted curve at higher frequencies in figure 4.15(a) is due to the overlap of the relaxation peak with the additional peak at about 5 MHz arising from the ITO coating of the LC cell. We have also carried out the dielectric measurements on a 9 μm LC cell. The relaxation frequency of the observed mode M_1 was found to be independent of the sample thickness.

The temperature dependence of relaxation frequency provides a useful classification of glassformers along a 'strong' to 'fragile' scale [66, 69]. The former shows an Arrhenius dependence, whereas the latter deviates from the Arrhenius behavior. The glass transition is associated with several previtreous phenomena occurring well above the glass transition temperature [85, 142]. To describe the previtreous behavior, numerous model relations have been developed [67, 68]. The empirical Vogel-Fulcher-Tammann (VFT) equation remains the most popular one among them and is nowadays used in the following form [67],

$$f = f_\infty \exp\left(-\frac{D\,T_0}{T - T_0}\right) \tag{4.5}$$

where f_∞ is the pre-exponential constant, extrapolated Vogel temperature T_0 is usually located below the glass transition temperature T_g, and D is a constant denoting the fragility of the system and describes the degree of deviation away from the basic Arrhenius behavior. The measured relaxation frequency as a function of temperature along with its fit to eqn. 4.5 is shown in Figure 4.15(b). The fitting parameters are $T_0 = 253.15 \pm 0.004$ K, $\log_{10} f_\infty = 8.49 \pm 0.19$, and $D = 3.19 \pm 0.39$. Such a large D value indicates the highly fragile glassy nature of our sample. These fragile glasses have also been found for some polymeric systems [82]. The deviation of VFT fit from the experimental data in the higher temperature range is further analyzed as discussed below. It has also been reported that a poorer fit to the

Tab. 4.1: The shape parameters α and β, and dielectric strength $\Delta\epsilon$ value obtained from fitting the experimental data with eqn. 4.4 at different temperatures.

T [K]	α	β	$\Delta\epsilon$
303	0.65 ± 0.02	1 ± 0.08	6.69 ± 0.17
308	0.68 ± 0.01	1 ± 0.06	6.50 ± 0.16
313	0.74 ± 0.02	0.95 ± 0.03	6.44 ± 0.21
318	0.67 ± 0.01	0.99 ± 0.06	7.33 ± 0.07
323	0.68 ± 0.01	1 ± 0.06	7.23 ± 0.06
328	0.67 ± 0.02	1 ± 0.08	7.23 ± 0.07
333	0.68 ± 0.02	1 ± 0.09	7.12 ± 0.08
338	0.69 ± 0.02	1 ± 0.12	7.06 ± 0.11

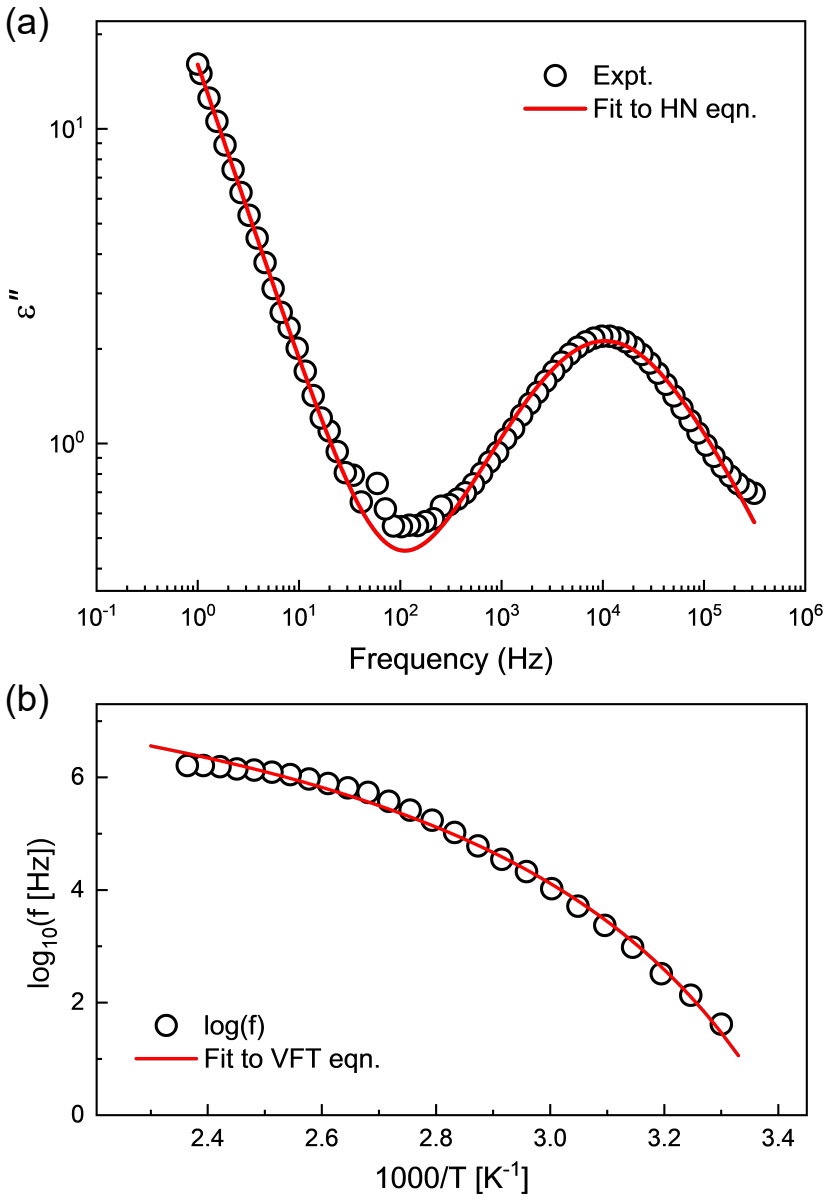

Fig. 4.15: (a) Frequency variation of ϵ'' at 333 K along with fitted curve (solid line) using eqn. 4.4. The deviation of the fitted curve in the higher frequency region is due to the overlap of the relaxation peak in the MHz range associated with ITO coating. (b) Relaxation frequency of mode M_1 as a function of inverse temperature. The solid curve represents the fit to the experimental data using VFT eqn. 4.5, indicating the non-Arrhenius behavior of the liquid.

experimental data is expected for more fragile liquid [69].

The linearized derivative-based analysis, first proposed by Stickel et al. [143], was performed to emphasize subtle changes in the dependence of relaxation time τ on temperature. It has been shown that the plot of $T\ [d(\ln\tau)/d(1/T)]^{-1/2}$ vs T should give rise to a linear dependence in the region where the VFT equation is valid [142]. For our sample, linear temperature dependence with two different slopes

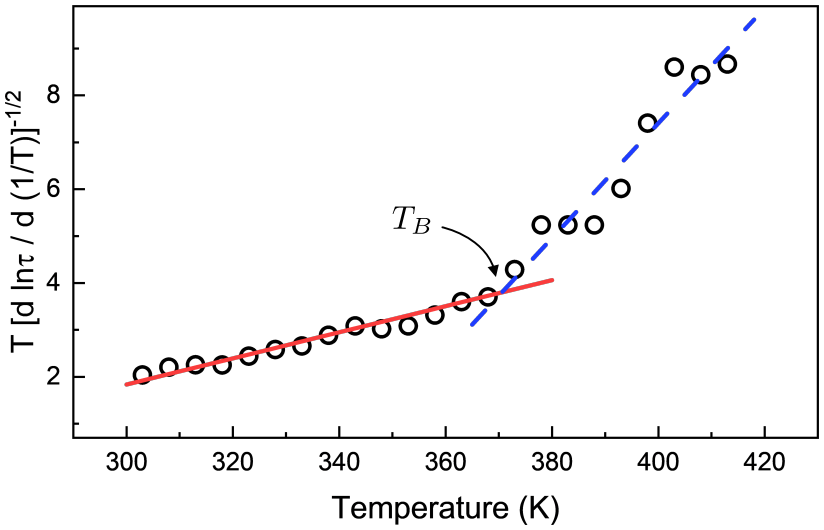

Fig. 4.16: The linear variation of $T\ [d(\ln\tau)/d(1/T)]^{-1/2}$ as a function of temperature showing two dynamical regimes separated by the crossover temperature $T_B = 370\ K$. The slope and ordinate of the linear fit in the lower (higher) temperature region are 0.028 and -6.51 (0.123 and -41.65), respectively.

was found in the low and high-temperature regions, as shown in figure 4.16. The crossover temperature T_B was found to be at about 370 K, which separates the two dynamical regimes. This analysis shows that the VFT relation is more appropriate for describing the temperature variation of the relaxation frequency for our sample.

It has been shown in many cases of liquid crystalline glassformers [83–85] that $\tau = \tau_0(T - T_x)^{-\gamma}$ can be used to portray the behavior of relaxation in accordance with the mode coupling theory (MCT) [86, 87]. Here T_x denotes the MCT singular temperature describing a hypothetical crossover from the ergodic to the non-ergodic regime, and the exponent $2 < \gamma < 4$ is a non-universal parameter [86]. However, for our sample, we found that the temperature variation of the relaxation frequency can be fitted best with the VFT relation given by eqn. 4.5.

The DSC measurements were carried out to measure the possible glass transition in the cooling and heating cycle of the sample at different rates. The observed DSC thermograms are shown in figure 4.17. A step change in the DSC thermogram corresponding to the glass transition was detected on both the cooling and heating cycles. The vitrification temperature (T_g) on cooling at a rate of 20 K/min was 271 K, and the corresponding glass softening temperature on heating was 268 K. These temperatures were determined from the inflection point of the DSC thermogram corresponding to the half height of the step in the heat flow curve. The difference between calorimetric glass transition temperature T_g and Vogel temperature T_0 is about 18 K for our sample, which is considered to be low as expected for highly fragile glassy systems [69]. This difference tends to zero for magnetic relaxation in

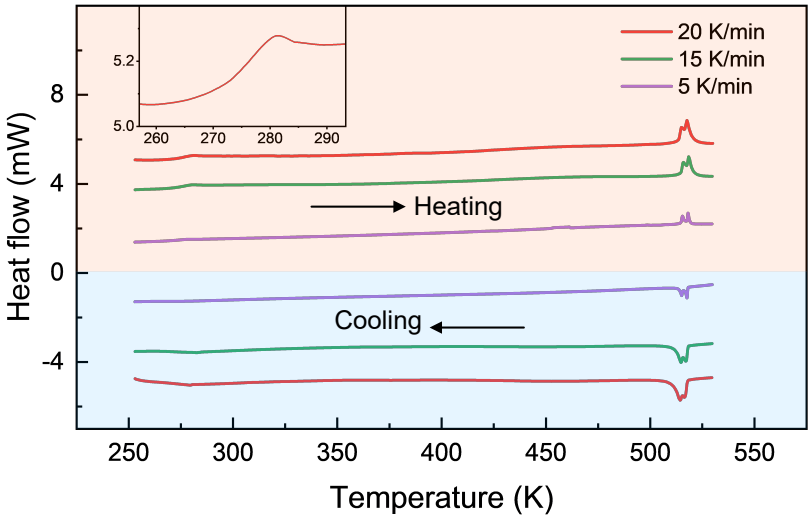

Fig. 4.17: The DSC thermogram of the compound BTCN8 at different rates while cooling from the isotropic phase and subsequent heating. A step change in the curve at a temperature of 271 K is indicative of glass transition. The sample does not crystallize over a few weeks.

spin glasses [144].

Now, we discuss the possible origin of the observed M_1 mode in our sample. The dielectric relaxation processes can be divided broadly into two categories: non-collective and collective dynamics of the molecules. When the rotational dynamics of the individual molecules are not correlated, the liquid crystal molecules themselves can exhibit two dielectric relaxation mechanisms linked to the rotation of the molecules about their long and short axes. The former generally occurs in the GHz frequency range, while the latter occurs at relatively lower frequencies. Particularly when dealing with BC molecules, the relaxation mode associated with molecular rotation about the short axis lies in the range of tens of kHz [145, 146]. Moreover, a number of distinguishable dispersions have been observed for BC compound, the origins of which are not yet clear [145]. For the glass forming system, the relaxation frequencies associated with these dispersions are expected to decrease rapidly near the glass transition. However, in the case of our compound, only one relaxation mode M_1 was observed. This observation suggests that the M_1 mode can possibly arise either due to the non-collective rotation of the molecules about their short axes or due to some collective molecular movement.

Although the BTCN8 molecules have non-zero dipole moments, our experimental studies confirmed the absence of spontaneous polarization in the observed smectic phases. Furthermore, we didn't find experimental evidence of Langevin-type ordering of the dipole moments in the smectic layers [131]. Therefore, mode M_1 is not associated with the collective polar ordering of the molecules in our sample.

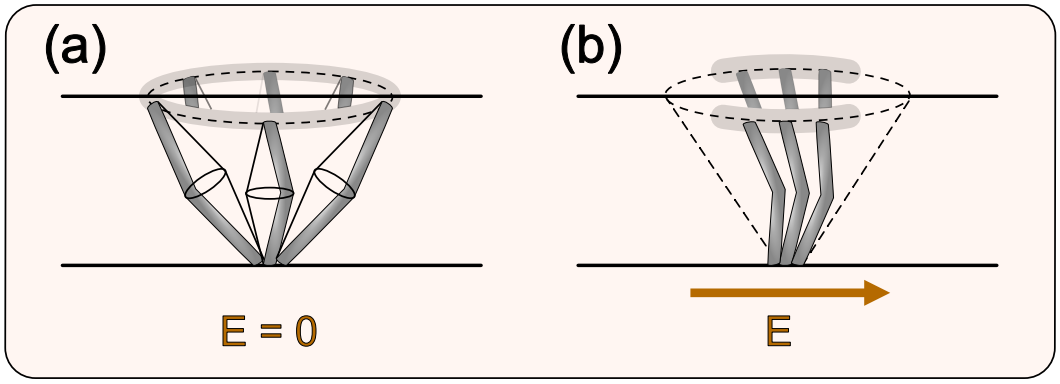

Fig. 4.18: Schematic representation for the arrangement of bent-core molecules in a layer of the dSmA phase (a) without electric field, and (b) in the presence of the field applied parallel to the smectic layer. The change in the molecular distribution on the application of field gives rise to collective mode M_1 observed in our sample.

Based on the molecular configuration in the dSmA and the SmC phases, we propose the following mechanism that gives rise to the M_1 mode. In the dSmA phase, the long axes of the molecules are distributed uniformly on a cone about the layer normal (see figure 4.18(a)). Under the application of a small electric field in the plane of the smectic layers, the molecules reorient azimuthally on the cone, resulting in a weak biaxiality in the system. Due to the strong transverse component of the dipole moment of the molecules, the sample has negative dielectric anisotropy, and the field tends to redistribute the molecules on the cone along the directions perpendicular to the applied field as shown in figure 4.18(b). The observed relaxation mode M_1 in our sample can be attributed to this collective redistribution of the molecules on the cone. In the SmC phase, the molecular distribution around the cone is peaked at a preferred azimuthal angle, giving rise to a nonzero optical tilt. The optical tilt increases with decreasing temperature in the SmC phase. However, the molecules still have a broad distribution along the azimuthal direction. This is also supported by the fact that the optical tilt angle in the SmC phase is about 15° at ambient temperature, which is significantly smaller than the corresponding intralayer molecular tilt measured from XRD studies ($\sim$ 33°). Hence, a similar molecular redistribution confining them in the plane perpendicular to the applied field is expected to occur in the planar aligned SmC phase. Thus, the relaxation frequency of the mode M_1 varies continuously across the transition from the dSmA to the SmC phase and persists throughout the SmC phase. The relaxation frequency of mode M_1 decreases gradually with decreasing temperature, indicating that this molecular redistribution about the cone tends to be frozen. The relaxation frequency starts to decline rapidly in the lower temperature region of the SmC phase because of the experimentally confirmed glassy behavior of our sample.

The broad molecular distribution on the tilt cone also explains the increase in birefringence of the SmC phase under the application of a relatively higher field

of about 2 V/μm, as observed in POM studies (see figure 4.8). The applied field confines the molecules in the plane of the LC cell. This results in the increased order parameters and, hence, the birefringence of the sample. This field induced change is reversible as the molecules relax back to their original distribution after removal of the field. Further detailed experimental studies are required to confirm the exact mechanism giving rise to the observed mode M_1.

The constituent molecules of the compound BTCN8 have a central thiophene ring, which gives rise to an opening angle of about 143°, which is larger than 120° typically found for bent-core molecules. This perhaps can be attributed to the absence of net polarization in the observed smectic phases. We do not see any sign of the B2 phase typically exhibited by bent-core molecules. Rather, the observed phases are calamatic phases generally observed for rod-like molecules.

4.3 Conclusion

We report the experimental studies on a compound consisting of bent-core banana shaped molecules, which exhibits the following enantiotropic liquid crystalline phases on cooling: *Isotropic* $\rightarrow$ *Nematic* $\rightarrow$ *dSmA* $\rightarrow$ *SmC* $\rightarrow$ *Smectic Glass*. The XRD studies show the minimal layer contraction across the dSmA to the SmC transition, and the POM studies further confirmed the 'de Vries' nature of the SmA phase. The switching current measurements indicate the absence of spontaneous polarization in both the smectic phases. A dielectric relaxation mode was observed due to the reorientation of the molecules on the tilt cone in the dSmA phase, and it persists in the lower temperature SmC phase. The relaxation frequency of this mode decreases rapidly with decreasing temperature following the VFT equation, indicating a fragile glassy behavior of our sample. The DSC measurements confirmed the glass transition at about 271 K, which does not depend significantly on the cooling rate. We have proposed a model for the observed dielectric mode in the dSmA phase to account for experimental results. Interestingly, the studied bent-core compound has the unique property of exhibiting a de Vries SmA phase along with the glassy behavior.

5 Unusual nucleation and growth morphology of smectic phase

5.1 Introduction

The tilted smectic phases of BC molecules can be characterized by the mutual orientation of three unit vectors corresponding to the layer normal $\hat{k}$, the projection of director on the layer plane $\hat{c}$, and $\hat{p}$ along the layer polarization. The schematic organization of BC molecules in a layer in four different smectic phases, proposed theoretically [147, 148], are shown in figure 5.1. (i) In the orthogonal **SmAP** phase (figure 5.1(a)), the director $\hat{n}$ orient parallel to the layer normal $\hat{k}$ with transverse polar order, and the layers possess C_{2v} point symmetry. This phase was first proposed by Sekine et al. [26], and later experimental evidence of it was found with antiferroelectric $SmAP_A$ [28] and ferroelectric $SmAP_F$ [27, 149, 150] order in successive layers. (ii) A 'leaning' or 'tipping' phase **SmTP** has tilted molecular organization in the layer, with the molecular planes lying on average in the tilt plane. The polar order has components both in and out of the plane of the layers (figure 5.1(b)). The layers in the SmTP phase have achiral C_S point symmetry. A few compounds made of *asymmetric* BC molecules have been found to exhibit leaning type structure in bulk [35, 37] and in free-standing films [151]. Based on the excluded volume, dispersion, and dipolar interactions, it has been argued that the leaning order in the layers can be attributed to a low dipole moment and relatively large bend angle of the molecules [152]. (iii) A tilted polar **SmCP** phase is formed when the layer polarization is perpendicular to the tilt plane as shown in figure 5.1(c). The polar order, tilt direction, and layer normal are mutually orthogonal to each other in the SmCP phase, giving rise to spontaneous breaking of chiral symmetry of the layers [21, 153]. This is the most common mesophase exhibited by BC molecules and is also known as the B2 phase [23, 24]. The layers in this phase have a chiral C_2 point symmetry. (iv) In a more general double-tilted **$SmCP_G$** phase (figure 5.1(d)), the polar order neither remains in the tilt plane nor orthogonal to it. The layers in the $SmCP_G$ phase of BC molecules possess C_1 point symmetry, resulting in the least symmetric fluid phase. Indirect evidence of the $SmCP_G$ phase in bulk samples has been reported based on x-ray diffraction measurements [154] and optical microscopy with an applied electric field [41, 155]. In free-standing films of the samples, more direct evidence of a triclinic smectic structure has been

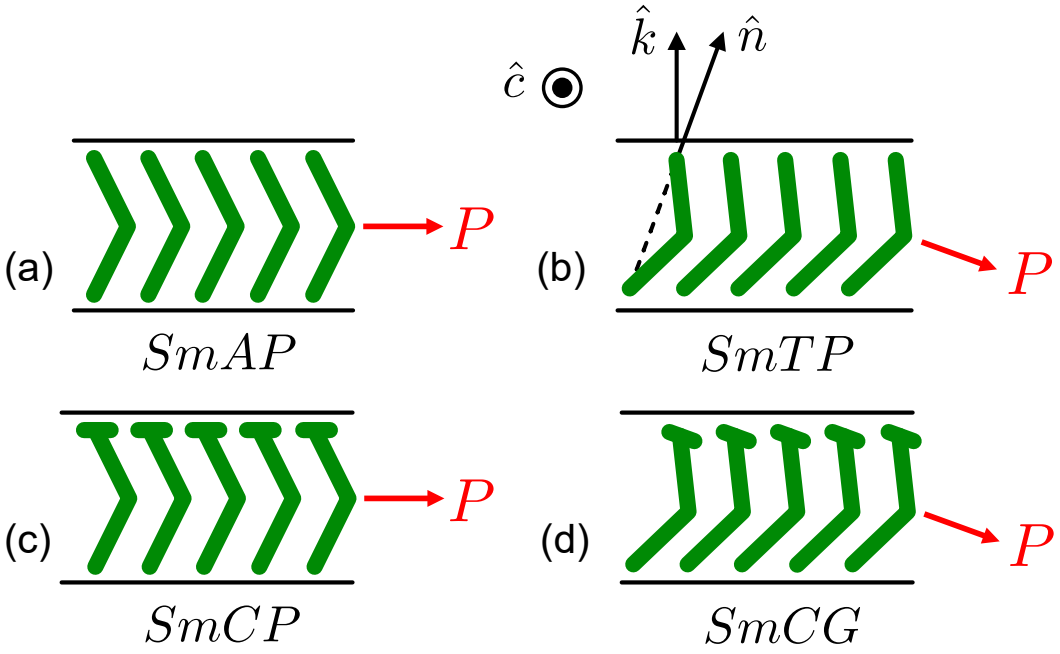

Fig. 5.1: Schematic representation of molecular organization in a layer for different possible smectic phases of BC molecules. The vector P indicates the direction of layer polarization. The unit vectors $\hat{k}$, $\hat{n}$, and $\hat{c}$ show the orientation of layer normal, the director, and projection of $\hat{n}$ on the layer plane, respectively.

reported based on the depolarised reflected light microscopy [40, 156]. This type of smectic phase was first proposed as a "far fetched possibility" by de Gennes for biaxial smectic layers and named SmC_G where G stands for generalized [157]. The SmC_G phases are of particular importance due to their low symmetry, which allows one to study the wide variety of coupling between different orders.

The nucleation and growth of phases in condensed matter systems has been a subject of steady scientific interest to study the phase ordering processes [88]. In addition to the wide variety of phases, the nucleation and growth of liquid crystalline phases in its isotropic melt on cooling provides a unique opportunity to study these processes. The conventional smectic phases grow as a so-called batônnet structure when cooled from their isotropic phase due to the anisotropic lamellar order of the system [91]. These batônnet structures tend to minimize their interfacial energy during their growth process and produce compact domains. Nevertheless, Dierking et al. found that some calamatic [92] and BC liquid crystals [91, 93, 94] exhibit highly irregular domains of mesophases with fractal structure when quenched from their isotropic phase.

In this chapter, we present the experimental studies on the liquid crystalline phase of a compound consisting of BC molecules. The x-ray diffraction and polarizing optical microscopy clearly evidenced a tilted smectic phase. The sample in a planar-

aligned LC cell shows a complex inhomogeneous texture between crossed polarizers, which transforms irreversibly into a smooth fan texture on the application of a sufficiently high electric field. Based on our experimental observations, we propose a tilted smectic phase having polar order modulating along the layers along with a long wavelength layer undulation. We also report the nucleation-growth dynamics of the mesophase on quenching the sample from its isotropic phase. We observe an unusual fractal growth of the smectic domains. The area-perimeter fractal analysis was carried out, and the measured fractal dimension was independent of quench rate and depth.

5.2 Results

5.2.1 Sample and DSC observations

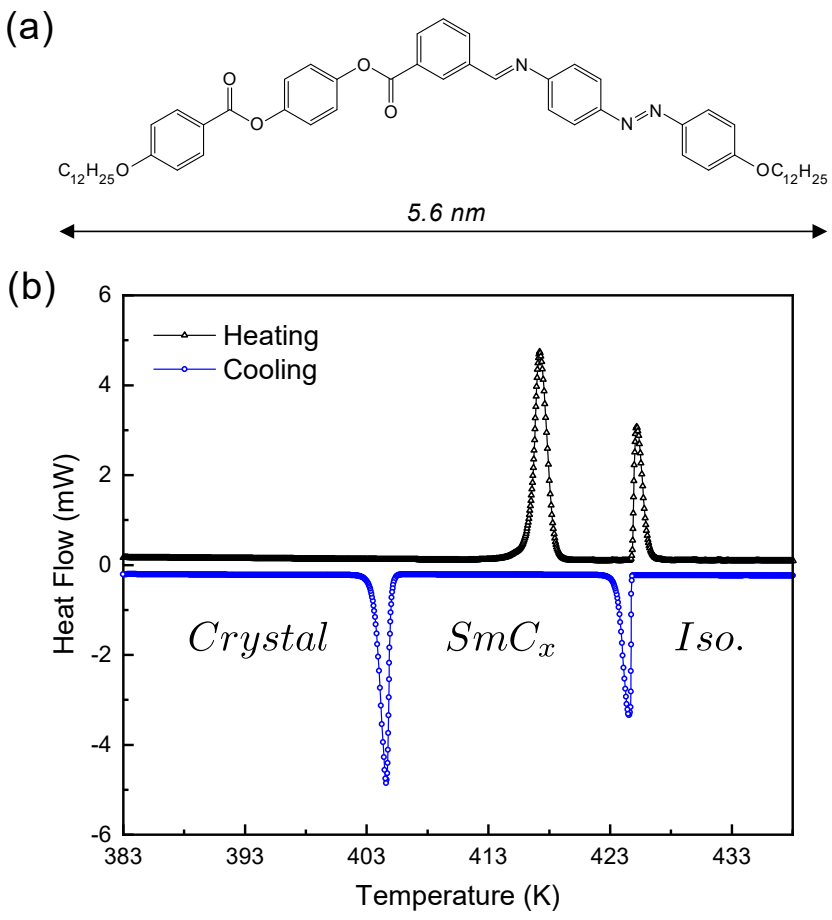

Fig. 5.2: (a) Molecular structure of the compound DIBO12 with asymmetric arms and identical aliphatic chains attached to each end of the BC molecule. (b) DSC thermograms of the sample with a heating and cooling rate of 3 K/min showing the presence of only one mesophase of the compound.

The experimental investigations were performed on the compound *4-((4-*

(dodecyloxy)benzoyl)oxy) phenyl 3-(((4-((4-(n-dodecyloxy)phenyl)diazenyl)phenyl) imino)methyl) benzoate, which will be abbreviated as **DIBO12** in the discussions. The molecular structure of the compound is shown in figure 5.2(a). The molecule has a bent shape with two rigid rod-like arms joined end to end at an angle of about 120°. The different linking groups in the two arms introduce a strong longitudinal molecular asymmetry. Long flexible aliphatic chains are attached to both ends of the molecule to reduce the melting temperature of the compound as well as to stabilize the smectic phase. The compound exhibits only one liquid crystalline phase enantiotropically, following a phase sequence: $Isotropic \longleftrightarrow SmC_x \longleftrightarrow Crystal$. Based on our experimental observations discussed in the later part, we denote this phase as SmC_x.

In order to detect the phase transitions, differential scanning calorimetry (DSC) measurements were performed on the sample at a heating and cooling rate of 3 K/min. Figure 5.2(b) shows the DSC thermograph of the sample, which clearly detects the existence of one enantiotropic liquid crystal phase between the isotropic liquid and crystal phase. The sample undergoes a transition from the isotropic to the SmC_x phase at about 424.68 K on cooling with an enthalpy change of -22.83 J/g. The SmC_x phase transforms to a crystal phase on further cooling at 404.75 K with an enthalpy change of -38.12 J/g. There is a slight hysteresis from the isotropic to SmC_x phase transition, whereas a large hysteresis was observed during the SmC_x to crystal transition. It is interesting to note that the clearing enthalpy for the DIBO12 compound is larger than that observed for typical isotropic to B2 phase transition [158], indicating a strong first-order phase transition.

5.2.2 XRD studies

Temperature-dependent x-ray diffraction (XRD) studies were performed using a DY 1042-Empyrean (PANalytical) diffractometer with CuK_α radiation of wavelength 1.54 Å equipped with a PIXcel 3D detector. The samples were filled in Lindemann capillary tubes with an outer diameter of 1 mm. The sample mounted in the XRD setup was initially heated to the isotropic phase and subsequently cooled to the desired temperatures to record the diffraction patterns. The temperature of the sample was controlled using a hot stage and a temperature controller (Linkam T95) with a temperature stability of 0.1 K.

Figure 5.3 shows the XRD intensity profile as a function of the wave vector in the SmC_x phase at temperature 421 K. Three sharp peaks were observed at small angles with their wave vectors q in the ratio of 1:2:3 corresponding to the first, second, and third order diffraction. This observation confirms the lamellar order of

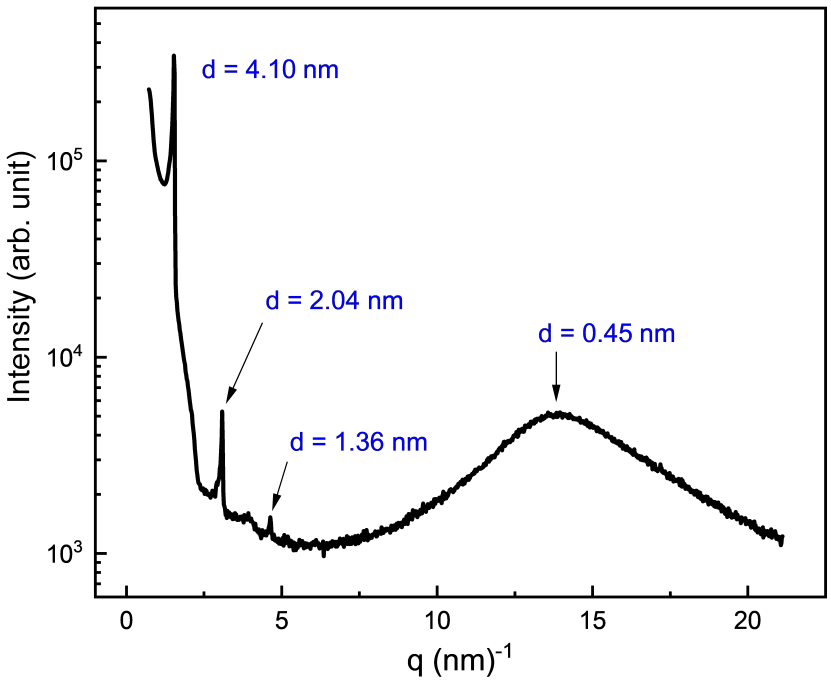

Fig. 5.3: The XRD intensity profile of the compound DIBO12 at 421 K as a function of wave vector q in the SmC$_x$ phase. The sharp peaks in the small angle region reveal the lamellar molecular order in this phase. A diffuse peak in the wide angle region indicates a liquid-like order along the layers.

the molecules in the SmC$_x$ phase with effective layer spacing of 4.10 nm calculated from the wave vectors associated with the peaks. A diffuse peak at the wide-angle region indicates an intralayer fluid-like order. The molecular length estimated from the molecular structure is found to be about 5.61 nm. The layer spacing d being significantly smaller than the molecular length l suggests that the molecules are tilted within the layers. The tilt angle with respect to the layer normal can be calculated using $\theta = \cos^{-1}(d/l)$, which is found to be about 42.8° in the SmC$_x$ phase. The layer thickness and, hence, the tilt angle remained unaltered throughout the temperature stability of the SmC$_x$ phase. A slight increase in the q-value corresponding to wide angle diffuse peak was observed with decreasing the temperature. This can be attributed to the increasing molecular density with decreasing temperature.

5.2.3 POM observations

Polarized Optical Microscopy (POM) investigations of the sample were conducted using a microscope (Olympus BX50) equipped with a digital camera (Canon EOS 80D). A hot stage (Linkam LTS420E) and a temperature controller were utilized to monitor the temperature of the sample with a temperature stability of 0.1 K. The POM studies were carried out on samples sandwiched between a clean glass plate and a cover slip and in commercially available LC cells (Instec Inc.). The LC cells are

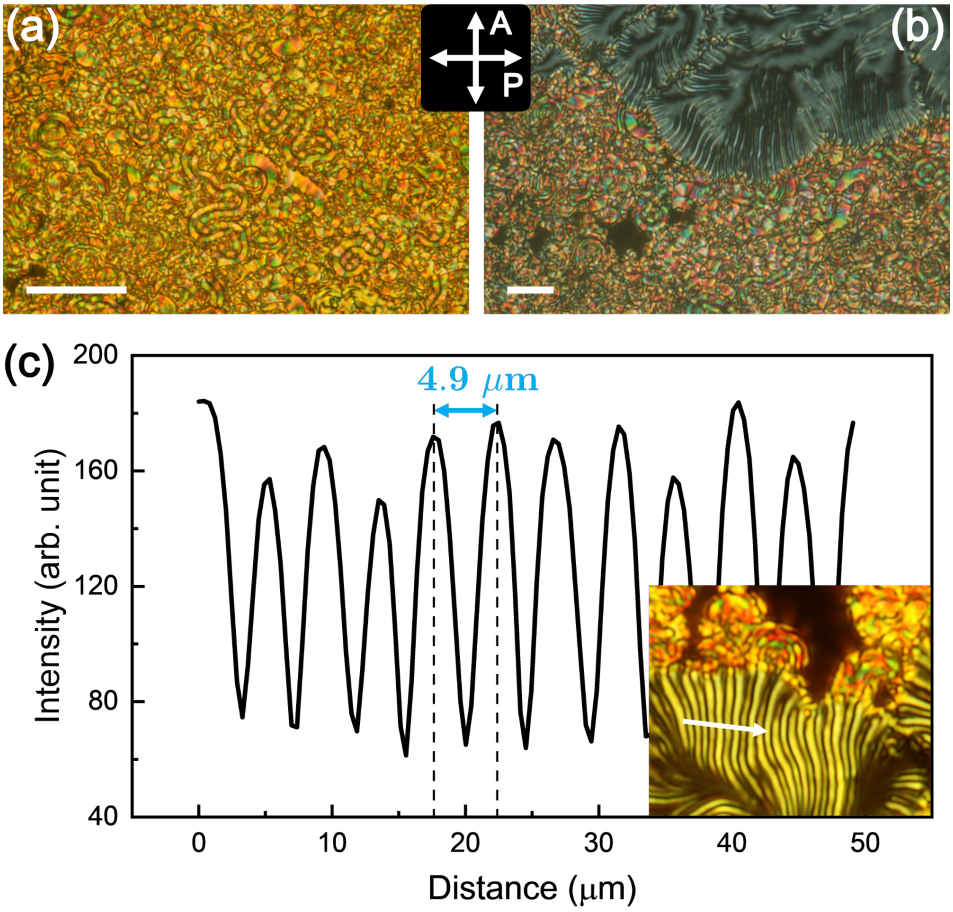

Fig. 5.4: The POM texture of the compound DIBO12 between crossed polarizers kept (a) in a planar aligned LC cell of thickness 5 μm, and (b) between a glass plate and cover slip. The texture in (b) exhibits both planar and homeotropic domains coexisting in the field of view. The schlieren texture in the homeotropic region of the sample showed a periodic undulation. (c) The intensity profile along the white arrow drawn on the undulated texture, which is shown in the inset. Scale bar = 40 μm.

made of indium tin oxide (ITO) coated glass plates, which serve as electrodes for electro-optic and dielectric studies. The sample was introduced into the LC cell by capillary action in its isotropic phase using a hot plate.

Figure 5.4(a) shows the POM texture of a 5 μm thick sample in a planar aligned LC cell between crossed polarizers. An inhomogeneous grainy texture was observed in the SmC_x phase. In this texture, sometimes small circular domains and curved strips with relatively smoother regions were observed. In these domains, the birefringence color was found to vary along the azimuthal direction in the circular domains and along the length of the strips (see figure 5.4(a)). The sample sandwiched between a clean glass plate and a cover slip showed two different textures coexisting in the SmC_x phase, as shown in figure 5.4(b). One of these textures is similar to that found in the planar aligned LC cell (figure 5.4(a)), whereas the other is a schlieren texture with relatively low birefringence. The dark schlieren

texture can be attributed to the homeotropic alignment of the molecules with the layers in the plane of the glass plates. This texture in the homeotropic region clearly indicates the tilted molecular organization in the smectic layers. In addition, dark and bright banded patterns appear in the homeotropic region, indicating a periodic undulation of the layers. The inset of figure 5.4(c) shows a similar periodic undulation. The spatial variation of the intensity of this banded pattern measured along the line A to B is shown in figure 5.4(c), indicating an undulation period of about 4.9 μm. A number of banded patterns were analyzed, and the undulation period was found to lie in the range of 4 to 7 μm. It should be noted here that both POM textures shown in figure 5.4(a) and 5.4(b) are obtained while cooling the samples from its isotropic phase at a slow cooling rate of 0.5 K/min. The POM textures become even more inhomogeneous at a faster cooling rate.

Although the SmC_x phase shows a complex inhomogeneous texture in the planar-aligned LC cells, a few circular domains were found to form in the vicinity of the isotropic to SmC_x phase transition as shown in figure 5.5(a). These small circular domains have relatively smoother textures, and four extinction brushes between crossed polarizers can sometimes be observed. These extinction brushes were found to align parallel as well as at an angle from the crossed polarizers in different domains. These observations indicate the coexistence of *synclinic* and

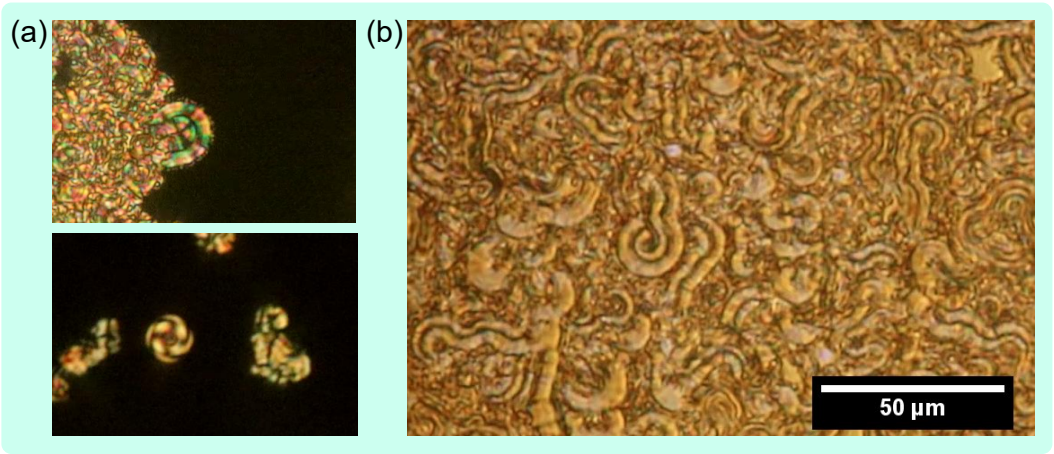

Fig. 5.5: (a) The POM textures containing circular domains of the SmC_x phase for the compound DIBO12 between crossed polarizers. These rarely observed circular domains have extinction brushes oriented at an angle of about 43° in some of them (image at top) and parallel to the crossed polarizers in others (image at bottom). This observation indicates the existence of synclinic as well as anticlinic interlayer molecular configuration. The synclinic structures appear significantly more often than the anticlinic ones. (b) The POM texture of a 5 μm thick planar aligned sample in the SmC_x phase after removing one of the polarizers from the light path while cooling the sample at a rate of 0.1 K/min from its isotropic phase. This enables the visualization of the numerous defects lines in the texture more clearly. The curved defect lines demonstrate the spontaneous bending of the layers, as discussed in detail in the main text.

anticlinic molecular configurations in successive layers. The synclinic configuration was found to be significantly more probable than the anticlinic configuration.

The defect lines in the POM texture can clearly be visualized by removing one of the polarizers from the light path. Figure 5.5(b) represents one such POM texture of a 5 μm thick planar aligned sample while cooling from its isotropic phase at a rate of 0.1 K/min. These large number of defect lines produce the textural inhomogeneity of the sample. Careful observation during the transition from isotropic to SmC_x phase revealed that initially, the SmC_x phase nucleates and grows as circular domains. Then, a bud-like structure forms randomly at the circumference of the circular domain, which tends to grow further and bends spontaneously (see supplementary video). This bending of the growing strips gives rise to coil-like structures (see figure 5.5(b)), which do not follow any preferred handedness, i.e., clockwise and counterclockwise bending are equally probable. This texture in the SmC_x phase (figure 5.5(b)) clearly shows the spontaneous curvature of the defect lines. The curved defect lines are the result of unique nucleation and growth of the SmC_x phase while cooling from the isotropic phase.

In order to quantitatively analyze these curved structures, we consider them to be a part of the circle. The circular Hough transform technique in MATLAB was used to compute the radius of curvature of the circular or curved lines. Figure 5.6 illustrates the grayscale image of the POM texture shown in figure 5.5(b) along

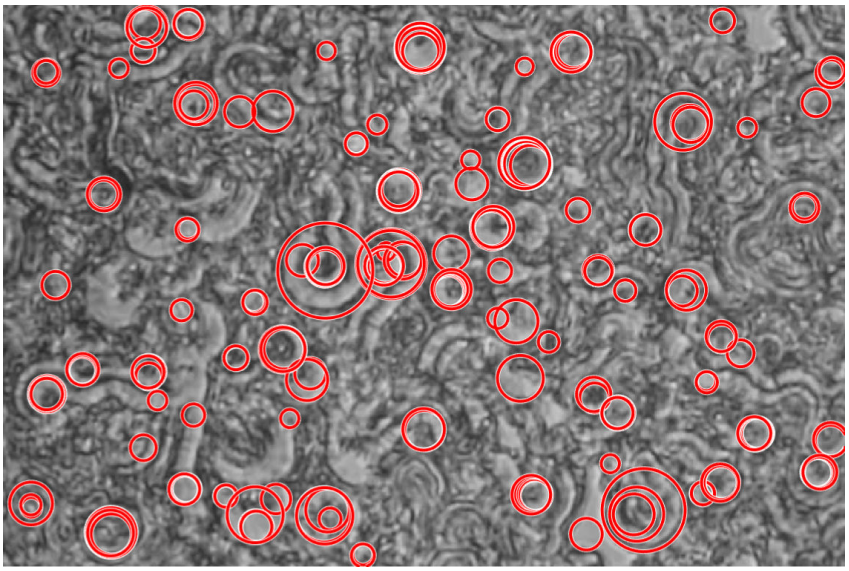

Fig. 5.6: A grayscale image of the POM texture shown in figure 5.5(b) featuring numerous curved defect lines. These curved defect lines are fitted with red circles to calculate the corresponding radii of the curvature within the computational error. The curved defect lines were treated as part of circles, and the radius of curvature for each curved line was computed using the circular Hough transform technique in MATLAB.

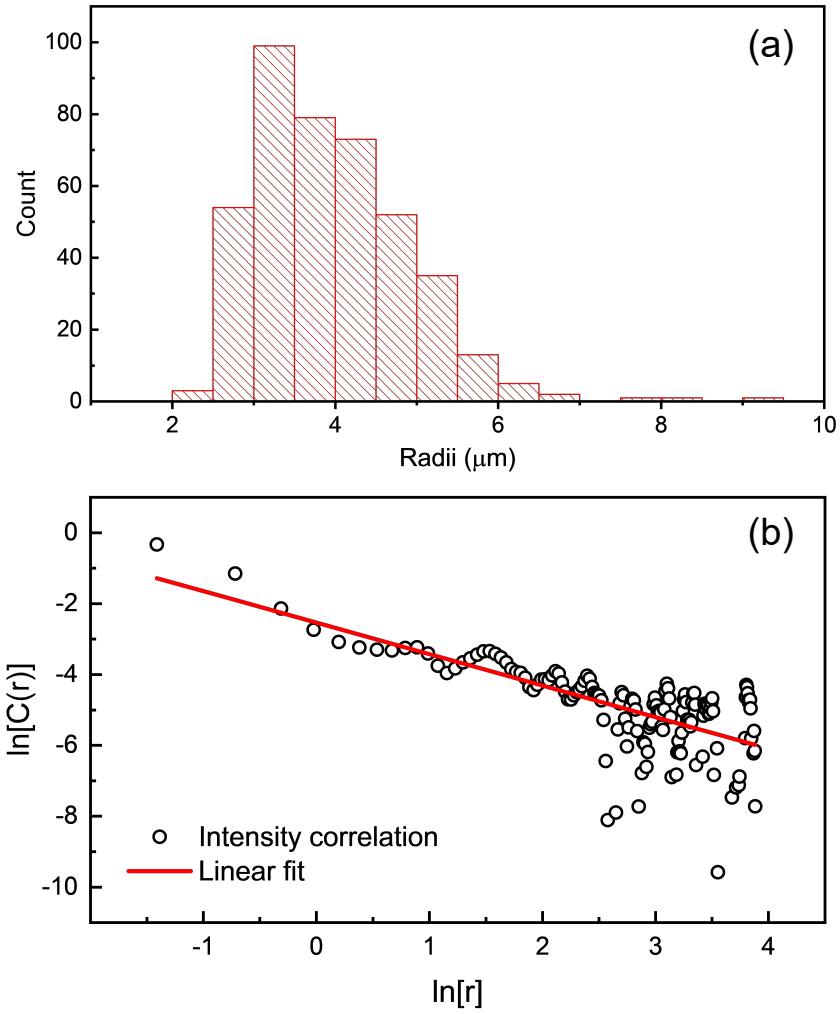

Fig. 5.7: (a) Histogram of preferred radii of curvature of defect lines observed in POM texture after removing one of the polarizers from the light path. (b) The log-log plot of intensity-intensity correlation $C(r)$ as a function of distance r calculated from a POM texture of a 5 μm thick planar aligned sample.

with the fitted red circles. These circles were computed to calculate the radii of curvature corresponding to the curved defect lines observed in the POM textures. The histogram of the computed radii of curvature is shown in figure 5.7(a). The average radius of curvature of the coiled structures is found to be about 4 μm, which is consistent with the undulation period observed in the homeotropic POM texture (figure 5.4(c)).

In order to quantitatively study the inhomogeneity of the POM textures discussed above, we compute the spatial intensity-intensity correlation function $C(r)$ of the POM texture shown in figure 5.4(a), where r is the relative distance between the points in the texture. We employed grey level co-occurrence matrix (GLCM) [159] using Python to calculate the correlation function $C(r)$. The variation of $C(r)$ as a function of distance r in a log-log plot is shown in figure 5.7(b). The linear fit to this

data gives rise to a power law variation of $C(r) = C_0 r^{-\beta}$, with the exponent $\beta = 0.9$. This power law decay of $C(r)$ indicates a scale-free variation of intensity-intensity correlation in the POM texture, which perhaps arises due to the lamellar structure of the mesophase. The lamellar order introduces spatial connectivity within the sample, giving rise to a power law decay of the $C(r)$.

5.2.4 Cryo-FESEM observation

Cryogenic Field Emission Scanning Electron Microscopy (Cryo-FESEM) experiments were performed to visualize the morphology of the SmC_x phase at higher resolutions. A Carl Zeiss (model - Ultra Plus) system with an electron beam of strength 5 kV was employed for these observations. The sample was initially heated to its isotropic phase, cooled to a desired temperature in the SmC_x phase, and subsequently quenched by plunging it into liquid nitrogen. The sample was then transferred into a vacuum chamber at 100 K (PP3000T Quorum technology). The sample was cryo-fractured using an in-built knife and sublimated at a temperature of 183 K for 15 minutes to remove the water content at the upper surface. Finally, the sample's surface was coated with a thin layer of platinum of thickness about 5 nm for enhanced contrast during imaging. Back-scattered secondary electrons were utilized to produce the surface images of the sample.

The FESEM micrographs (figure 5.8) of the sample in the SmC_x phase reveal the lamellar structure exhibiting spontaneous bending. The undulation of the layers and circular domains formed by them can be seen in figure 5.8(a) and 5.8(b), respectively. These observations are consistent with the POM studies. It should be pointed out that the wavelength of the undulated structure perhaps depends on the size of the lamellar assembly and, therefore, varies over a wide range. This also

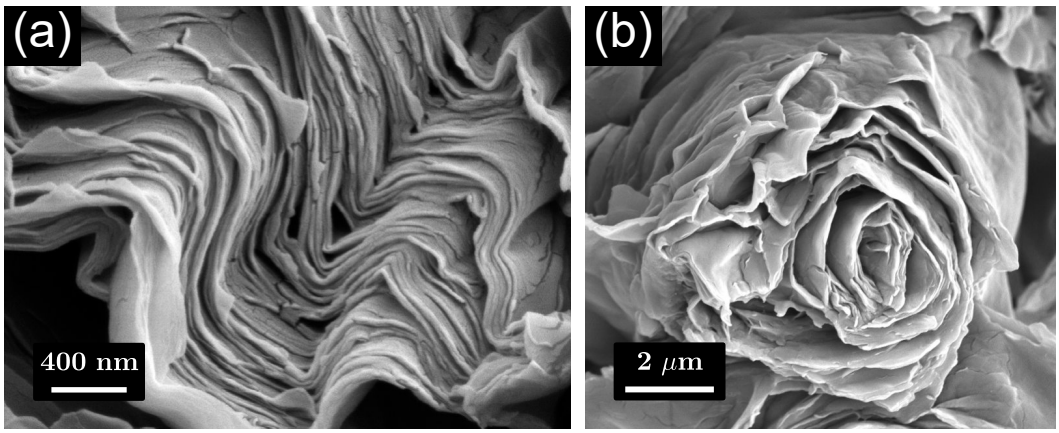

Fig. 5.8: The cryo-FESEM texture of the SmC_x phase showing (a) the undulated layers and (b) the layers forming circular domains.

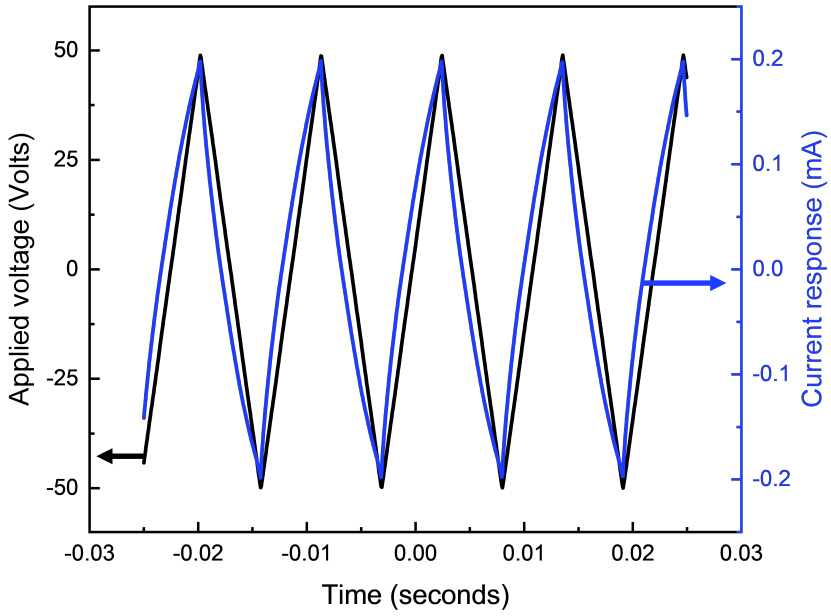

Fig. 5.9: The current response for a planar aligned sample of thickness 5 μm in the SmC$_x$ phase at 408 K under the application of a triangular wave voltage (50 V, 1 kHz).

explains the wide range of values of the radius of curvature shown in figure 5.7(a).

5.2.5 Electro-optic and dielectric studies

The current response under the application of a triangular wave voltage was measured to detect the existence of layer polarization in the SmC$_x$ phase [33]. The sample was connected in series with a 1 kΩ resistor, and a voltage was applied to this series combination. The voltage drop across the 1 kΩ resistor was monitored to determine the current response at a given temperature. An LC cell of thickness 5 μm treated for planar alignment was utilized in the experiment. If the sample exhibits ferroelectric (antiferroelectric) property, one (two) polarization reversal current peaks are expected in each half cycle of the current response. Figure 5.9

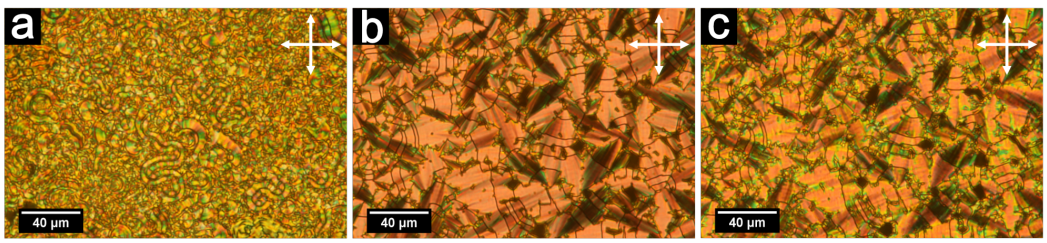

Fig. 5.10: The POM textures of a 5 μm thick sample in planar aligned LC cell in the SmC$_x$ phase between crossed polarizers (a) without electric field, (b) with an AC field of 16 V/μm, 80 Hz, and (c) after turning off the field, showing an irreversible field-induced transformation.

shows the temporal profile of the applied voltage across the sample and current response at 408 K. The in-phase ohmic current was found to contribute substantially to the current response of our sample, and no polarization reversal current peak was observed in the SmC_x phase. This current peak was not observed even at an applied electric field as high as 20 V/μm at various frequencies. But careful observations showed a broad hump in the current response in excess to the ohmic current (see figure 5.11). This broad hump was found to persist even in the isotropic phase and therefore is not associated with the polarization of the sample. This broad current peak perhaps arises due to the space charge effect in the sample.

Interestingly, despite the absence of polarization reversal current peak in the mesophase, a field-induced textural transformation was observed at a sufficiently high field, as depicted in figure 5.10. The inhomogeneous grainy texture at zero field starts to change to a clear fan texture above a field of 10 V/μm at lower frequencies ($<$ 100 Hz), which increases at higher frequencies. The fan becomes increasingly smoother at higher fields, as shown in figure 5.10(b). The extinction brushes in the

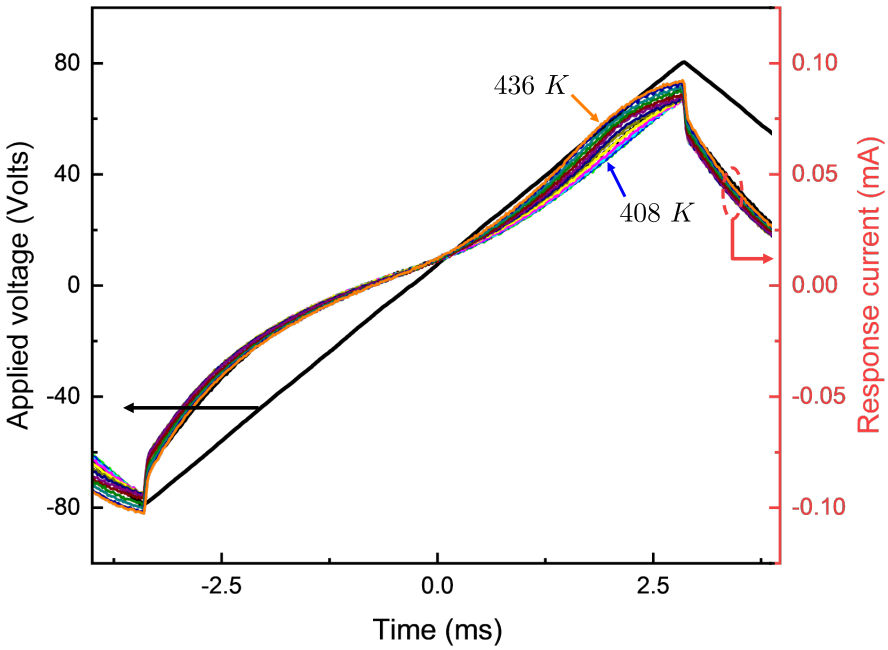

Fig. 5.11: The current response of a 5 μm thick planar aligned sample under the application of a triangular wave AC voltage (80 V, 80 Hz) at different temperatures (from 408 K to 436 K in steps of 2 K). Two broad humps in each half cycle of the applied voltage were observed, which persist even in the isotropic phase. Moreover, the observed broad humps are found to be more prominent at lower frequencies of the applied field and gradually reduce with increasing frequency. These observations confirm that the observed broad peaks are not associated with the polarization of the sample but arise due to the space charge effect of the sample. The ohmic part of the sample's current response is relatively larger compared to the capacitive or polarization reversal part of the response, which perhaps masks any polarization response of the sample, as discussed in the main text.

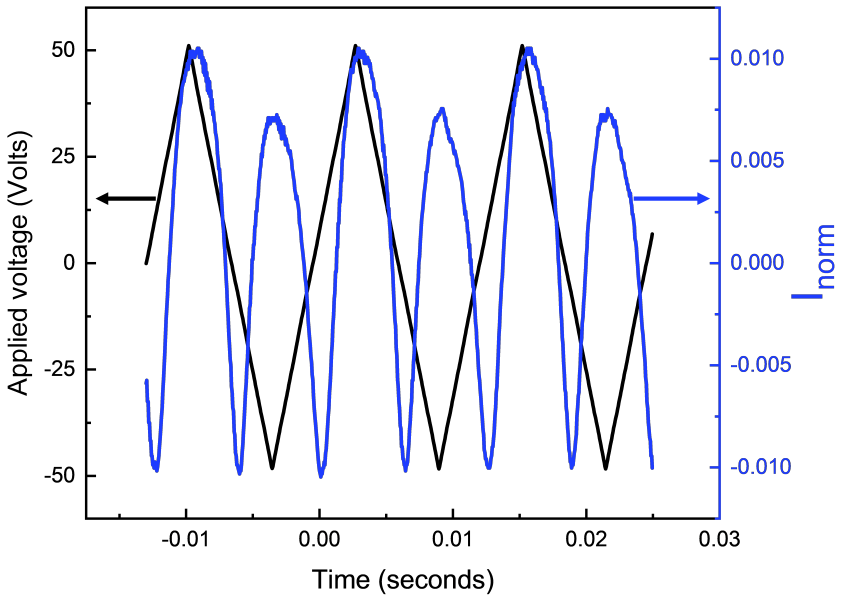

Fig. 5.12: Temporal profile of the optical transmittance of the sample in 5 μm LC cell between crossed polarizers and the corresponding applied triangular wave AC voltage.

smoother fans align at an angle of about 43° from the polarizer direction, suggesting an interlayer *synclinic* molecular organization in the field-induced state. It is found that the texture does not revert completely to the original zero-field texture after turning off the field, as shown in figure 5.10(c). Additionally, once the texture acquires the field-induced fan texture, it can be switched between figure 5.10(b) and 5.10(c) on the application of a field as low as 1 V/μm. It is also found that with the application of a very low-frequency field, the zero field texture (figure 5.10(c)) switches to the field-induced texture (figure 5.10(b)) symmetrically for both the positive and negative field. This observation indicates that the positive and negative field-induced states of the sample are optically equivalent.

We also measured the time evolution of optical transmittance through a planar aligned sample of thickness 5 μm between crossed polarizers under the application of a triangular wave voltage. A He-Ne laser was employed as the source, and the transmitted intensity was recorded using a low-noise high gain photodiode connected to a mixed signal oscilloscope (Agilent Technologies MSO6012A). To normalize the intensity, we used $I_{norm} = (I - \bar{I})/\bar{I}$, where I is the measured transmitted intensity passing through the sample, and $\bar{I}$ is the mean value of the transmitted intensity. The optical transmittance, along with the applied electric field, is shown in figure 5.12. The transmitted intensity is maximum at both the highest positive and negative field and is minimum at the zero field. The slight asymmetry in the transmitted intensity corresponding to the positive and negative applied field is perhaps due to the alignment of the sample with respect to the

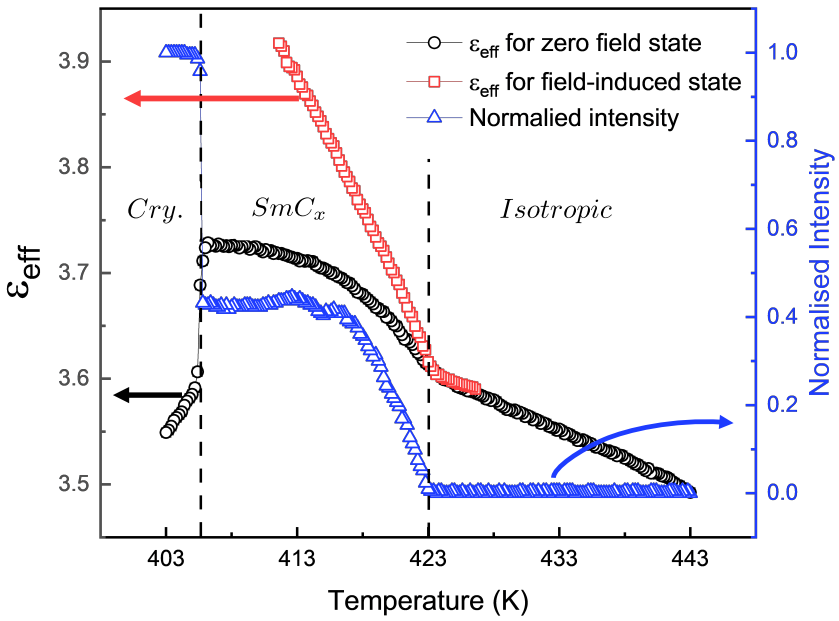

Fig. 5.13: The temperature variation in the effective dielectric constant (ϵ_{eff}) and the optical transmittance through a 5 μm thick planar aligned sample kept between crossed polarizers. The open circle and open triangular symbols show the variation of ϵ_{eff} and normalized transmitted intensity, respectively, while cooling the sample from the isotropic phase. The red rectangular symbols show the variation of ϵ_{eff} on heating the sample from the field-induced state of the SmC$_x$ phase.

crossed polarizers. This observation again confirms that the field-induced states corresponding to the positive and negative applied fields are optically equivalent, and the optical transmittance varies at twice the frequency of the applied field.

The variation of the effective dielectric constant of the sample was studied as a function of temperature using a custom-made setup. A sinusoidal AC voltage of rms amplitude 0.5 Volts and frequency 5641 Hz was applied to the series combination of the sample cell and a resistance of 1 kΩ. A lock-in amplifier (Stanford Research SR830) was utilized to measure the amplitude and phase of the voltage drop across the 1 kΩ resistance. The capacitance of the LC cell with and without the sample can be determined using impedance analysis. The ratio of these measured capacitances gives the effective dielectric constant of the sample. The temperature of the sample was monitored by a microscope hot stage equipped with a temperature controller (Instec Inc.) with a temperature stability of 0.1 K. A customized LabVIEW program was used to control the measurements and data acquisition. Additionally, in this setup, we can simultaneously measure the optical transmittance through the sample kept between crossed polarizers using a He-Ne laser as a source.

Figure 5.13 shows the temperature variation of the effective dielectric constant and optical transmittance of a 5 μm thick planar aligned sample on cooling from its isotropic phase. The monotonic increase of the dielectric constant with decreasing

temperature in the isotropic phase can perhaps be attributed to the increase in the density of the sample. The slope change in both curves at about 423.4 K indicates the transition from the isotropic to SmC$_x$ phase, which is consistent with the DSC measurements. In the SmC$_x$ phase, the dielectric constant increases with decreasing temperature and saturates to a value of about 3.72. The discontinuous jump in both curves at about 405.8 K indicates the transition from the SmC$_x$ to the crystal phase.

In figure 5.13, we also show the variation of the ϵ_{eff} carried out on the field-induced state of the SmC$_x$ phase (open square symbols) on heating the sample. For this measurement, the sample was first cooled to the desired temperature in the SmC$_x$ phase and switched to a field-induced state under a high field. Subsequently, the field was removed, and the dielectric measurements were performed with an applied voltage of 0.5 V and 5641 Hz while heating the sample. The ϵ_{eff} value for the field-induced state of the SmC$_x$ phase was found to be higher than that of the zero field state as expected, which decreases on increasing the temperature and tends to merge with zero-field values close to the SmC$_x$ to isotropic transition temperature.

5.2.6 Nucleation and growth of SmC$_x$ phase

The smectic phases usually nucleate and grow as batônnet while cooling from their isotropic phase [91]. This batônnet growth of smectic phases is energetically favored due to their layered structure and to minimize the interfacial energy. However, it was found that the nucleation and growth of the SmC$_x$ phase of the compound DIBO12 shows a fractal structure when quenched from its isotropic phase, as shown in figure 5.14(a). Such fractal structure is usually unexpected because it allows the formation of a relatively large interface between the mesophase and the isotropic phase, which is energetically costly. Only a few compounds comprised of calamatic [92] as well as BC molecules [93, 94] are found to exhibit such fractal growth of their smectic phases on cooling from the isotropic phase.

The nucleation and growth studies were carried out on a 5 μm thick sample in a planar aligned LC cell using a polarizing optical microscope. The sample was quenched from its isotropic phase, and time-lapsed images of the growing structures were recorded. Figure 5.14(a) shows a snapshot of the growing SmC$_x$ phase in the isotropic phase between crossed polarizers. The SmC$_x$ phase nucleates at some random points, which subsequently grow as highly irregular domains with large interfaces. This unusual growth of SmCx domains leads to macroscopic quasi-2-dimensional fractal structures. One way to quantify the growth is by calculating the

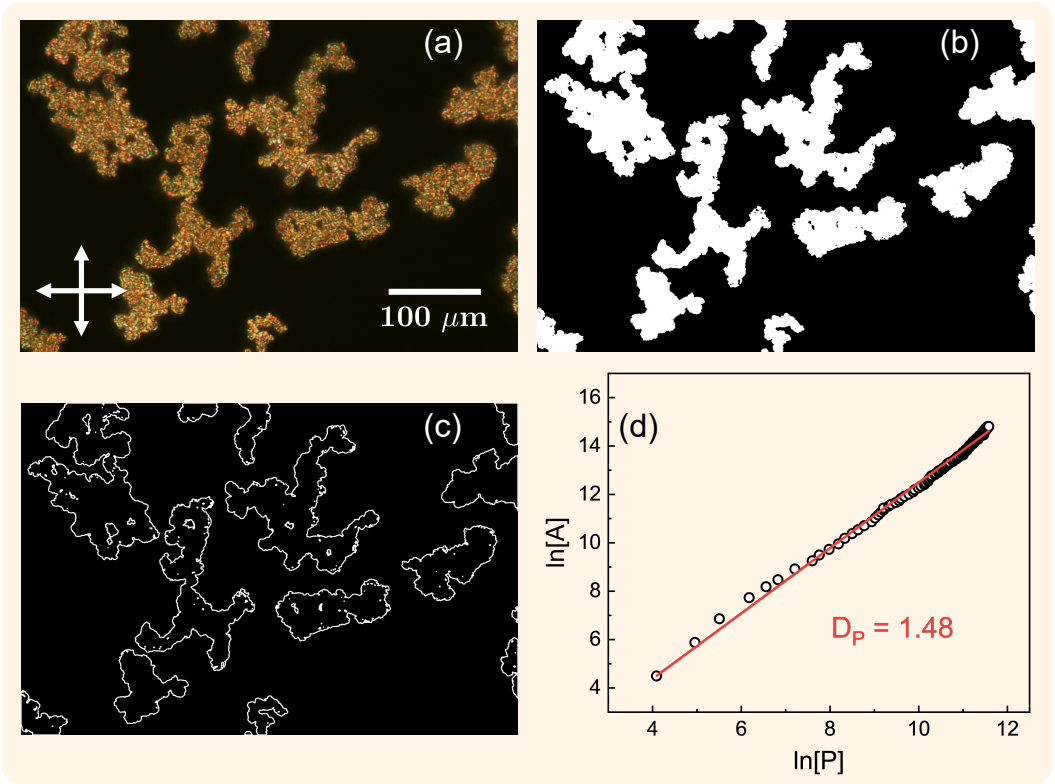

Fig. 5.14: (a) The POM texture of the SmC_x phase for a 5 μm thick sample in planar aligned LC cell when quenched from its isotropic phase. (b) A binary image obtained after thresholding the image shown in (a). (c) The perimeter of the growing SmC_x domains, and (d) A log-log plot of the area vs perimeter of the growing domains. A linear fit to the data gives the area-perimeter dimension $D_p = 1.48$.

fractal dimension of these domains. We used **area-perimeter method**, proposed by Mandelbrot [103], to find out the so-called area-perimeter dimension (D_p) of the growing domains. In order to calculate the D_p value of a 2-dimensional geometrical object, Mandelbrot [97, 103] proposed the relation between area and perimeter as,

$$A \propto (P)^{2/D_p} \tag{5.1}$$

where A and P are the area and perimeter of the object, respectively. For a 2-dimensional Euclidean surface, the D_p value should be 1, whereas $D_p > 1$ indicates the fractal nature of the surface.

In our experiments, the sample was quenched from its isotropic phase to a temperature below the clearing temperature with a sufficiently high quench rate, and the SmC_x domains were allowed to grow with time. The captured time-lapsed images were converted to binary form (figure 5.14(b)) using MATLAB by thresholding the pixel intensity based on its histogram. The number of white pixels in the binary image provides a measure of the area of the domains. The perimeter of these domains can be calculated from the number of white pixels that have at least one

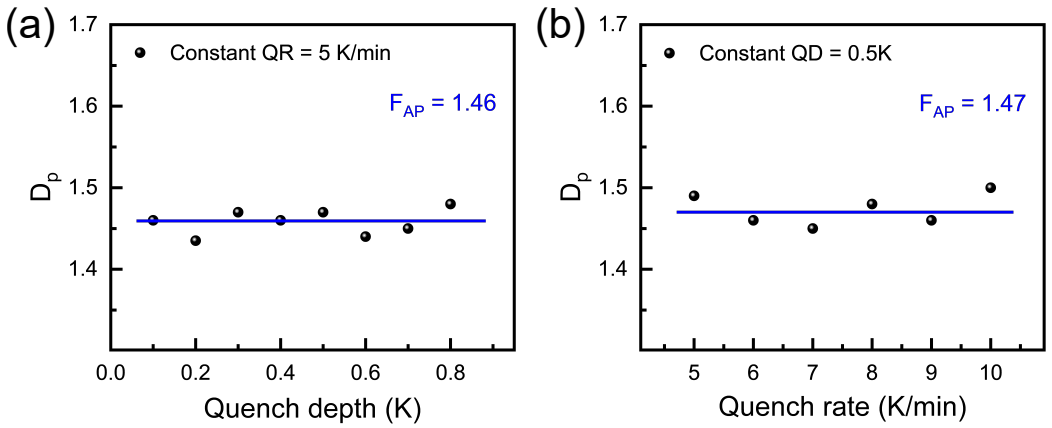

Fig. 5.15: The area-perimeter fractal dimension of the growing SmC_x domains of the sample as a function of (a) quench rate for a constant quench depth 0.5 K and (b) quench depth for a constant quench rate of 5 K/min.

neighboring dark pixel (see figure 5.14(c)). The time evolution of area and perimeter were computed, and the D_p value of the growing domains was obtained from the slope of the log-log plot of area vs. perimeter, as shown in figure 5.14(d). The D_p value of the SmC_x domains was found to be about 1.48, confirming their fractal nature. It can be noted that the D_p value obtained for the individual domains is the same as that, taking into account all the domains in the field of view. We studied the variation of D_p value as a function of quench rate (at a constant quench depth) and quench depth (at a constant quench rate). The D_p was found to be almost constant with different quench rates as well as with different quench depths as shown in figure 5.15. This indicates that the fractal nature of the growing SmC_x domains is independent of the quench rate and depth.

The fractal analysis was also performed for POM texture obtained from a thin sample between a clean glass plate and a coverslip, when quenched from the higher temperature isotropic phase. In this configuration, the coexistence of two types of textures was observed, as discussed earlier. One of these textures is similar to that observed for the planar-aligned sample, the growth of which also results in a fractal structure, as shown in the inset of figure 5.16. We performed area-perimeter fractal analysis on one of the growing domains enclosed by a circle shown in the inset of figure 5.16. The quench rate and quench depth for this experiment were chosen to be 5 K/min and 1.0 K, respectively. The resulting log-log plot of area vs. perimeter (figure 5.16) indicates an area-perimeter dimension $D_p = 1.43$, which is similar to that obtained for the sample filled in the planar-aligned LC cell of thickness 5 μ. This observation indicates that the D_p value for our sample is independent of the thickness of the sample. These findings are consistent with the earlier results reported on different liquid crystalline compounds [93].

5.3 Discussion

The XRD and POM studies on the compound DIBO12 clearly indicate the tilted lamellar molecular organization in the SmC_x phase. The zero-field texture in the SmC_x phase resembles the grainy texture of the B2 phase reported for some other compounds [160, 161]. However, these compounds exhibiting the B2 phase clearly showed large polarization reversal current peaks under the application of triangular wave voltage. For our compound, on the other hand, the absence of polarization reversal current response and the low value of the dielectric constant, even in the field-induced state of the SmC_x phase, rule out the possibility of a conventional B2 phase [21]. Moreover, the absence of satellite peaks in the small angle region of the XRD profile and no evidence of chirality in the POM studies rule out the possibility of the B7 phase [44]. Furthermore, the possibility of other B-phases [23] does not conform to our experimental observations.

We, therefore, propose a polarization-modulated structure for the SmC_x phase, which can account for our experimental results. In this model, the constituent BC molecules are uniformly tilted within the layers, and the ordering of the arrow direction of the molecules gives rise to a small local layer polarization perpendicular to the director. The orientation of this local polarization modulates in a direction

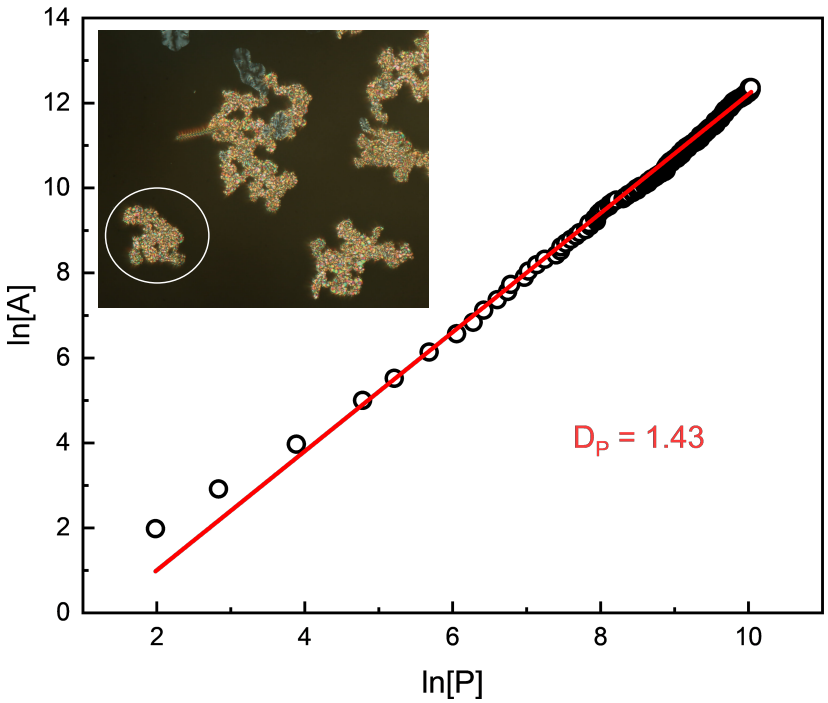

Fig. 5.16: A log-log plot of the area versus perimeter of a growing domain of the SmC_x phase shown enclosed by a circle in the inset. A linear fit to the data gives the area-perimeter dimension $D_p = 1.43$.

along the layers by rotating about the director (see figure 5.17(a)), giving rise to the polarization-modulated structure of the observed SmC_x phase. This polarization modulation also gives rise to the undulation of the layers in the SmC_x phase [37]. The undulation periodicity in the SmC_x phase was found to be about 5 μm from the POM studies (see figure 5.4(c)) as well as from cryo-FESEM observations. With this molecular organization, the layers in the SmC_x phase have essentially $SmCP_G$ structure with alternating SmTP and SmCP regions along the layers. This mesophase can be denoted as $SmCP_G$[U] to indicate the tilted smectic phase with a general orientation of layer polarization and undulated layer structure.

The leaning configuration of the molecules in the $SmCP_G$[U] layers can be attributed to the asymmetric structure of the constituent BC molecules [151, 162] and low dipole moment [152]. The large tilt angle obtained from the XRD studies, in combination with the leaning configuration of the molecules in the layers, gives rise to a strong longitudinal asymmetry as one of the arms is tilted larger than the other. This asymmetry gives rise to the spontaneous bending tendency of the layers, as observed in the POM studies. The leaning configuration of the molecules in the layers is known to produce bending and, hence, undulated layer structures [37, 151, 162].

The layers in the planar-aligned LC cell tend to orient orthogonal to the bounding substrates. They have local biaxial order with three different principle refractive indices with the corresponding principle axes along the director, the polarization direction, and perpendicular to them. Therefore, in this geometry, the polarization modulation gives rise to a variation of the effective birefringence along layers, as observed in the POM studies (see figure 5.4(a)).

This model can also account for the field-induced transformation of the $SmCP_G$[U] phase observed in the electro-optic studies. On the application of an electric field above a threshold, the molecules reorient with their bent axes aligning parallel to the field. Thus, the $SmCP_G$[U] phase transforms to a B2-like phase on the application of a sufficiently high electric field (see figure 5.17(b)). The undulation of the layers in the field-induced state of the $SmCP_G$[U] phase is eliminated, giving rise to a smooth fan-like texture as observed in POM studies (see figure 5.10(b)).

The dipole moment, calculated from the energy-minimized structure of the molecules, was found to be about 1.8 Debye, pointing essentially towards the long axis of the molecule. The transverse component of the molecular dipole moment is low, which mainly contributes to the experimentally observed polarization reversal current. The absence of the polarization reversal current peak in the $SmCP_G$[U] phase is perhaps due to the low transverse components of the dipole moment of

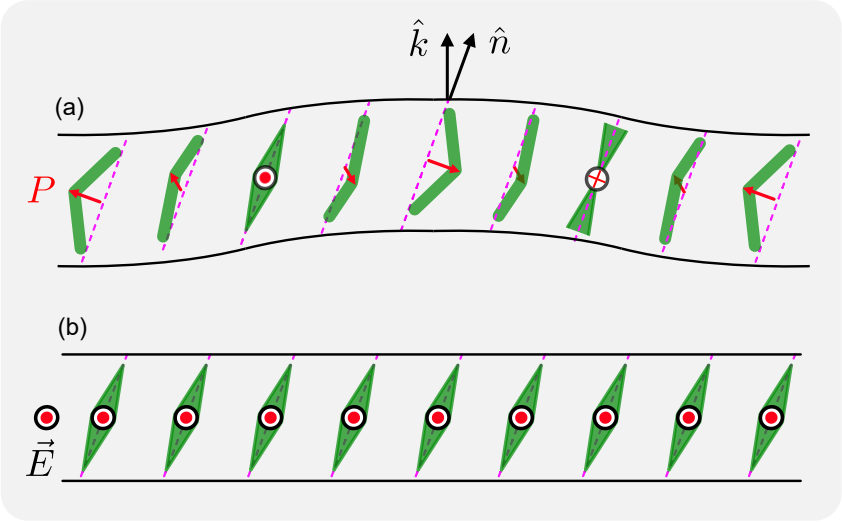

Fig. 5.17: Schematic representation of molecular organization within a layer of the $SmCP_G[U]$ phase in (a) the absence of the field and (b) the field-induced state. The director $\hat{n}$ remains uniformly tilted with respect to the layer normal. In the absence of the field, the local polar order rotates about the director as one goes along the layers with a long-wavelength undulation of the layers. The applied field aligns the polarization along itself, giving rise to an irreversible field-induced state and expelling the layer undulations.

the molecules and the relatively high ohmic current observed in our sample, which masks the polarization response.

The smectic phases are usually found to grow as batônnet structures from their isotropic melt on cooling due to the anisotropic properties of the system. The growth along the layer normal direction is more preferred than along the layers, i.e., the addition of smectic layers is favored over the growth of individual layers. This gives rise to an anisotropic batônnet shape of the growing domains [91]. However, the domains still tend to grow, keeping a compact shape with minimum interfacial energy. The nucleation and growth of the $SmCP_G[U]$ domains in its isotropic melt were found to have a fractal structure with large interfaces, in contrast to the conventional smectic phase. We attribute this fractal nature of the $SmCP_G[U]$ domains to the unique type of growth observed in the POM studies. The POM studies revealed that a bud-like structure grows randomly from the interface with a spontaneous bending tendency. This observation also indicates that the growth along the layers of the $SmCP_G[U]$ phase is favored over that along the layer normal. This can be attributed to the strong intermolecular interactions between the BC molecules within the layers [92]. Moreover, the highly ordered lamellar structure of the $SmCP_G[U]$ phase gives rise to some rigidity to the $SmCP_G[U]$ domains. Due to this rigidity, the growing domains are not able to reorganize to minimize their interfacial energy. Rather, they retain their fractal shape.

As observed in the POM studies, the BC molecules in the $SmCP_G[U]$ phase tend to align homeotropically in some regions when kept between a glass plate and a cover slip. These regions did not show fractal growth; rather, they nucleated and grew as compact domains. This observation further supports the argument that growth along the layers is more dominant, and their spontaneous bending tendency gives rise to the observed fractal growth for samples in the planar aligned cells. However, more detailed studies are required to confirm the mechanism of this fractal growth.

5.4 Conclusion

The liquid crystalline phase of a compound consisting of asymmetric BC molecules has been investigated experimentally. The DSC thermogram of the sample clearly detects one liquid crystalline phase. The XRD and POM studies establish that the mesophase is a tilted smectic phase with an undulated layer structure. Based on our experimental results, we proposed a layer undulated tilted smectic phase with in-plane modulation of the polar order. This novel structure of the mesophase perhaps arises due to the asymmetry between the two arms of the constituent BC molecules. We also studied the nucleation and growth of the $SmCP_G[U]$ domains on quenching from its higher-temperature isotropic phase. A fractal growth pattern was observed in contrast to the usual batônnet structure. The measured area-perimeter fractal dimension of the domains was found to be independent of the quench rate and quench depth.

6 Conclusion and future outlook

This thesis provides a comprehensive investigation into the mesomorphic behavior of three distinct compounds consisting of bent-core molecules using a range of experimental techniques. The observed liquid crystalline phases of these compounds have unique self-organized structures. The phase behavior and the physical properties of these mesophases are of fundamental significance and can also be exploited for potential applications. In this chapter, we conclude with the important findings from these studies and potential avenues for future research.

Chapter 3 presents the experimental studies on the phase behavior of a homologous series of compounds *8OBFn* with asymmetric bent-core banana shaped molecules. The compounds exhibit a layer undulated SmC_{LU} phase with a 2D rectangular lattice structure, which is different from the previously discovered layer undulated phase known as the B7 phase. In the usual B7 phases of BC liquid crystals, large polarization is the driving force for the splay in polar order and, hence, the layer undulated structure. In contrast, the SmC_{LU} phase exhibits a layer undulated structure despite showing no polarization reversal current response. We propose that, in the SmC_{LU} phase, the BC molecules acquire a leaning configuration because of the strongly asymmetric shape of the molecules. The layer undulation in the SmC_{LU} phase can be attributed to the leaning configuration of the molecules in the layers. This model structure can be utilized to account for layer undulation in other systems in the absence of strong polarization.

The study presented in chapter 3 is mainly based on the XRD measurements. It is well established that the XRD intensity profile is comprised of *structure factor* and *form factor*. The former provides the structural information about how the constituents are organized in space (information about lattice), whereas the latter arises due to scattering from the constituents themselves (information about the basis). Our studies presented in chapter 3 only explore the details of the structure of the lattice. Further analysis by measuring the relative amplitude of the XRD intensity profile will provide the details about the basis, which will enable one to construct a detailed electron-density map for the structure of the SmC_{LU} phase.

In chapter 4, we report the experimental investigations on a compound comprised of achiral thiophene-based bent-core molecules, which exhibits the following

enantiotropic liquid crystalline phases on cooling: *Isotropic* $\rightarrow$ *Nematic* $\rightarrow$ *dSmA* $\rightarrow$ *SmC* $\rightarrow$ *Glass of Smectic*. The studies revealed two key findings: (i) The higher temperature smectic phase is found to be the *de Vries SmA* phase, which transits to the SmC phase on decreasing temperature with practically no layer contraction. De Vries SmA phases in BC liquid crystals are extremely rare. (ii) Both the smectic phases show a dielectric relaxation mode whose relaxation frequency decreases sharply when temperature is lowered, suggesting a glassy behavior. The calorimetric studies further confirmed the glass transition at a temperature of about 271 K, which is consistent with the dielectric studies. We proposed a model for the observed dielectric mode in the de Vries SmA phase to account for experimental results. This is the first report of a BC liquid crystal exhibiting a de Vries SmA phase and showing glassy behavior.

A few possible future directions to explore such compounds are as follows.

- The functionalized thiophenes-based compounds are one of the most often utilized families of molecules for application in optoelectronic as well as optophotonic materials. The liquid crystals built with π-conjugated cores provide better organization and show excellent charge carrier mobility. Thus, it would be interesting to explore the electronic and electro-optical properties of the compound.

- A detailed dielectric spectroscopy study in the lower temperature range (near glass transition) will provide better insight into the pre-transitional behavior of the compound.

- Two possible mechanisms have been proposed for the observed dielectric relaxation mode M_1 in the mesophases of the compound BTCN8. Further dielectric studies with bias voltage can be performed to determine the origin of the relaxation mode M_1.

In chapter 5, a liquid crystalline phase of a compound consisting of asymmetric BC molecules has been investigated experimentally. The studies reveal a tilted smectic phase with an undulated layer structure, which is denoted as *SmCP$_G$[U]*. The layers in the SmCP$_G$[U] phase exhibit in-plane modulation of the polar order. This novel mesophase structure perhaps arises due to the asymmetry between the two arms of the constituent BC molecules. The nucleation and growth studies of the SmCP$_G$[U] domains on quenching from its higher-temperature isotropic phase reveal a fractal growth pattern. The measured area-perimeter fractal dimension of the domains was found to be independent of experimental parameters such as quench rate, depth, and thickness of the sample.

The structure of the $SmCP_G[U]$ phase was proposed based on the POM and SEM observations. Further investigations using small-angle X-ray studies (SAXS) and other techniques can be performed to confirm the proposed structure. Our studies suggest that the favored growth of the $SmCP_G[U]$ domains along the layer direction, in combination with intralayer leaning molecular configuration, gives rise to the fractal-type growth. However, further investigations are required to confirm the exact mechanism leading to such fractal growth. The nucleation and growth of liquid crystal phases is an interesting aspect of the phase ordering process, which has not been explored rigorously and presents an important direction for future research.

Bibliography

[1] P. M. Chaikin, T. C. Lubensky, and T. A. Witten, *Principles of condensed matter physics*, Vol. 10 (Cambridge university press, 1995).

[2] S. Chandrasekhar, *Liquid crystals*, 2nd ed. (Cambridge University Press, 1992).

[3] F. Reinitzer, "Beiträge zur kenntniss des cholesterins", Monatsh. Chem. **9**, 421 (1888).

[4] O. Lehmann, "Über fliessende krystalle", Z. Phys. Chem. **4**, 462 (1889).

[5] D. Vorländer, "Krystallinisch-flüssige substanzen", Ber. Dtsch. Chem. Ges. **39**, 803–810 (1906).

[6] G. Friedel, "Les états mésomorphes de la matiere", Ann. Physique **18**, 273 (1922).

[7] P. G. de Gennes, *The physics of liquid crystals* (Clarendon Press, Oxford, 1975).

[8] T.-H. Lin, Y.-J. Chen, C.-H. Wu, et al., "Cholesteric liquid crystal laser with wide tuning capability", Applied Physics Letters **86**, 10.1063/1.1897439 (2005).

[9] S. Diele, P. Brand, and H. Sackmann, "X-ray Diffraction and Polymorphism of Smectic Liquid Crystals 1. A-, B- and C-modifications", Molecular Crystals and Liquid Crystals **16**, 105–116 (1972).

[10] J. Doucet, A. M. Levelut, and M. Lambert, "Long and short range order in the crystalline and smectic b phases of terephthal-bis-butylaniline (tbba)", Molecular Crystals and Liquid Crystals **24**, 317–329 (1973).

[11] A. De Vries, "Experimental Evidence Concerning Two Different Kinds of Smectic C to Smectic A Transitions", Molecular Crystals and Liquid Crystals **41**, 27–31 (1977).

[12] R. Bartolino, J. Doucet, and G. Durand, "Molecular tilt in the smectic C phase : a zigzag model", Annales de Physique **3**, 389–395 (1978).

[13] J. P. F. Lagerwall and F. Giesselmann, "Current Topics in Smectic Liquid Crystal Research", ChemPhysChem **7**, 20–45 (2006).

[14] A. De Vries, A. Ekachai, and N. Spielberg, "Why the Molecules are Tilted in all Smectic A Phases, and How the Layer Thickness Can be Used to Measure Orientational Disorder*", Mol. Cryst. Liq. Cryst. **49**, 143–152 (1979).

[15] A. de Vries, “The description of the smectic A and C phases and the smectic A–C phase transition of TCOOB with a diffuse-cone model”, J. Chem. Phys. **71**, 25–31 (1979).

[16] T. P. Rieker, N. A. Clark, G. S. Smith, et al., ““chevron" local layer structure in surface-stabilized ferroelectric smectic-C cells”, Phys. Rev. Lett. **59**, 2658–2661 (1987).

[17] R. B. Meyer, L. Liebert, L. Strzelecki, and P. Keller, “Ferroelectric liquid crystals”, Journal de Physique Lettres **36**, 69–71 (1975).

[18] S. Chandrasekhar, B. Sadashiva, and K. Suresh, “Liquid crystals of disc-like molecules”, pramana **9**, 471–480 (1977).

[19] T. Wöhrle, I. Wurzbach, J. Kirres, et al., “Discotic Liquid Crystals”, Chemical Reviews **116**, 1139–1241 (2016).

[20] T. Niori, T. Sekine, J. Watanabe, T. Furukawa, and H. Takezoe, “Distinct ferroelectric smectic liquid crystals consisting of banana shaped achiral molecules”, J. Mater. Chem. **6**, 1231–1233 (1996).

[21] D. R. Link, G. Natale, R. Shao, et al., “Spontaneous Formation of Macroscopic Chiral Domains in a Fluid Smectic Phase of Achiral Molecules”, Science **278**, 1924–1927 (1997).

[22] D. Vorländer, “Die richtung der kohlen-stoff-valenzen in benzolabkommlingen”, Ber. Dtsch. Chem. Ges. **65**, 1101–1109 (1932).

[23] H. Takezoe and A. Eremin, *Bent-Shaped Liquid Crystals: Structures and Physical Properties* (CRC Press, Boca Raton, 2017).

[24] A. Jákli, O. D. Lavrentovich, and J. V. Selinger, “Physics of liquid crystals of bent-shaped molecules”, Rev. Mod. Phys. **90**, 045004 (2018).

[25] R. Pratibha, N. V. Madhusudana, and B. K. Sadashiva, “An Orientational Transition of Bent-Core Molecules in an Anisotropic Matrix | Science”, Science, 2184–2187 (2000).

[26] T. Sekine, Y. Takanishi, T. Niori, J. Watanabe, and H. Takezoe, “Ferroelectric properties in banana-shaped achiral liquid crystalline molecular systems”, Jpn. J. Appl. Phys. **36**, L1201–L1203 (1997).

[27] R. A. Reddy, C. Zhu, R. Shao, et al., “Spontaneous ferroelectric order in a bent-core smectic liquid crystal of fluid orthorhombic layers”, Science **332**, 72–77 (2011).

[28] A. Eremin, S. Diele, G. Pelzl, et al., “Experimental evidence for an achiral orthogonal biaxial smectic phase without in-plane order exhibiting antiferroelectric switching behavior”, Phys. Rev. E **64**, 051707 (2001).

[29] D. Pociecha, M. Čepi č, E. Gorecka, and J. Mieczkowski, “Ferroelectric mesophase with randomized interlayer structure”, Phys. Rev. Lett. **91**, 185501 (2003).

[30] Y. Shimbo, E. Gorecka, D. Pociecha, et al., “Electric-field-induced polar biaxial order in a nontilted smectic phase of an asymmetric bent-core liquid crystal”, Phys. Rev. Lett. **97**, 113901 (2006).

[31] M. Gupta, S. Datta, S. Radhika, B. K. Sadashiva, and A. Roy, "Randomly polarised smectic a phase exhibited by bent-core molecules: experimental and theoretical studies", Soft Matter **7**, 4735–4741 (2011).

[32] J. V. Selinger, "Chiral and antichiral order in bent-core liquid crystals", Phys. Rev. Lett. **90**, 165501 (2003).

[33] K. Miyasato, S. Abe, H. Takezoe, A. Fukuda, and E. Kuze, "Direct method with triangular waves for measuring spontaneous polarization in ferroelectric liquid crystals", Jpn. J. Appl. Phy. **22**, L661 (1983).

[34] A. V. Emelyanenko and M. A. Osipov, "Origin of spontaneous polarization, tilt, and chiral structure of smectic liquid-crystal phases composed of bent-core molecules: a molecular model", Phys. Rev. E **70**, 021704 (2004).

[35] C. Zhang, N. Diorio, S. Radhika, et al., "Two distinct modulated layer structures of an asymmetric bent-shape smectic liquid crystal", Liq. Cryst. **39**, 1149–1157 (2012).

[36] N. Chattham, M.-G. Tamba, R. Stannarius, et al., "Leaning-type polar smectic-C phase in a freely suspended bent-core liquid crystal film", Phys. Rev. E **91**, 030502 (2015).

[37] V. D. Mishra, H. T. Srinivasa, and A. Roy, "Leaning induced layer undulated tilted smectic phase of asymmetric bent-core liquid crystals", J. Chem. Phys. **158**, 074906 (2023).

[38] C. Bailey and A. Jákli, "Role of molecular shape on bent-core liquid-crystal structures", Phys. Rev. Lett. **99**, 207801 (2007).

[39] N. Chattham, E. Korblova, R. Shao, et al., "De Gennes' triclinic smectics – not so far-fetched after all", Liquid Crystals **36**, 1309–1317 (2009).

[40] N. Chattham, E. Korblova, R. Shao, et al., "Triclinic fluid order", Phys. Rev. Lett. **104**, 067801 (2010).

[41] A. Jákli, D. Krüerke, H. Sawade, and G. Heppke, "Evidence for triclinic symmetry in smectic liquid crystals of bent-shape molecules", Phys. Rev. Lett. **86**, 5715–5718 (2001).

[42] N. Vaupoti č, M. Čopi č, E. Gorecka, and D. Pociecha, "Modulated structures in bent-core liquid crystals: two faces of one phase", Phys. Rev. Lett. **98**, 247802 (2007).

[43] D. Pociecha, N. Vaupotič, E. Gorecka, J. Mieczkowski, and K. Gomola, "2-d density-modulated structures in asymmetric bent-core liquid crystals", J. Mater. Chem. **18**, 881–885 (2008).

[44] D. Coleman, J. Fernsler, N. Chattham, et al., "Polarization-modulated smectic liquid crystal phases", Science **301**, 1204–1211 (2003).

[45] M. Nakata, D. R. Link, Y. Takanishi, et al., "Electric-field-induced transition between the polarization-modulated and ferroelectric smectic-$C_S P_F^*$ liquid crystalline states studied using microbeam x-ray diffraction", Phys. Rev. E **71**, 011705 (2005).

[46] D. A. Coleman, C. D. Jones, M. Nakata, et al., "Polarization splay as the origin of modulation in the $B1$ and $B7$ smectic phases of bent-core molecules", Phys. Rev. E **77**, 021703 (2008).

[47] H. Takezoe and Y. Takanishi, "Bent-core liquid crystals: their mysterious and attractive world", Jpn. J. Appl. Phys. **45**, 597–625 (2006).

[48] A. Eremin, S. Diele, G. Pelzl, H. Nádasi, and W. Weissflog, "Experimental evidence for $\mathrm{Sm}{-}C_G \rightarrow \mathrm{Sm} - CP$ polymorphism in fluorinated bent-shaped mesogens", Phys. Rev. E **67**, 021702 (2003).

[49] J. Szydlowska, J. Mieczkowski, J. Matraszek, et al., "Bent-core liquid crystals forming two- and three-dimensional modulated structures", Phys. Rev. E **67**, 031702 (2003).

[50] G. Pelzl, M. W. Schröder, U. Dunemann, et al., "The first bent-core mesogens exhibiting a dimorphism $B_7{}^{\smile}SmCP_A$", J. Mater. Chem. **14**, 2492–2498 (2004).

[51] A. Roy and N. V. Madhusudana, "A frustrated packing model for the B6-B1-SmAPA sequence of phases in banana shaped molecules", The European Physical Journal E **18**, 253–258 (2005).

[52] Y. Takanishi, T. Izumi, J. Watanabe, et al., "Field-induced molecular reorientation keeping a frustrated structure in an achiral bent-shaped liquid crystal", J. Mater. Chem. **9**, 2771–2774 (1999).

[53] E. Gorecka, N. Vaupoti č, D. Pociecha, M. Cepic, and J. Mieczkowski, "Switching mechanism in polar columnar mesophases made of bent-core molecules", J. Chem. Phys. Chem. **6**, 1087–1093 (2004).

[54] C. L. Folcia, J. Etxebarria, J. Ortega, and M. B. Ros, "Structure of mesogens possessing $B7$ textures: the case of the bent-core mesogen $8{-}\mathrm{OPIMB}{-}\mathrm{NO}_2$", Phys. Rev. E **72**, 041709 (2005).

[55] R. Amaranatha Reddy, U. Baumeister, C. Keith, et al., "Influence of the core structure on the development of polar order and superstructural chirality in liquid crystalline phases formed by silylated bent-core molecules: lateral substituents", Soft Matter **3**, 558–570 (2007).

[56] C. J. Klok, "BIOLOGICAL GLASS: A STRATEGY TO SURVIVE DESICCATION AND HEAT", Journal of Experimental Biology **213**, iv–iv (2010).

[57] F. B. Wadsworth, M. J. Heap, D. E. Damby, et al., "Local geology controlled the feasibility of vitrifying Iron Age buildings", Scientific Reports **7**, 40028 (2017).

[58] J. Pagacz, P. Stach, L. Natkaniec-Nowak, B. Naglik, and P. Drzewicz, "Preliminary thermal characterization of natural resins from different botanical sources and geological environments", Journal of Thermal Analysis and Calorimetry **138**, 4279–4288 (2019).

[59] M. Petters and S. Kasparoglu, "Predicting the influence of particle size on the glass transition temperature and viscosity of secondary organic material", Scientific Reports **10**, 15170 (2020).

[60] N. R. Jadhav, V. L. Gaikwad, K. J. Nair, and H. M. Kadam, "Glass transition temperature: Basics and application in pharmaceutical sector", en, Asian Journal of Pharmaceutics (AJP) **3**, 10.22377/ajp.v3i2.246 (2009).

[61] Y. H. Roos, "Glass Transition Temperature and Its Relevance in Food Processing", Annual Review of Food Science and Technology **1**, 469–496 (2010).

[62] H. T. H. Nguyen, P. Qi, M. Rostagno, A. Feteha, and S. A. Miller, "The quest for high glass transition temperature bioplastics", Journal of Materials Chemistry A **6**, 9298–9331 (2018).

[63] J. H. Crowe, J. F. Carpenter, and L. M. Crowe, "The role of vitrification in anhydrobiosis", Annual Review of Physiology **60**, 73–103 (1998).

[64] J. M. V. Blanshard and P. Lillford, *The glassy state in foods* (Nottingham Univ. Press, Loughborough, England, 1993).

[65] A. L. Greer, "Metallic Glasses", Science **267**, 1947–1953 (1995).

[66] P. G. Debenedetti and F. H. Stillinger, "Supercooled liquids and the glass transition", Nature **410**, 259–267 (2001).

[67] F. Kremer and A. Schönhals, eds., *Broadband dielectric spectroscopy* (Springer, 2003).

[68] K. Ngai, *Relaxation and Diffusion in Complex Systems*, Partially Ordered Systems (Springer, New York, NY, 2011).

[69] C. A. Angell, "Formation of Glasses from Liquids and Biopolymers", Science **267**, 1924–1935 (1995).

[70] J. C. Dyre, "Colloquium: the glass transition and elastic models of glass-forming liquids", Rev. Mod. Phys. **78**, 953–972 (2006).

[71] R. Elschner, R. Macdonald, H. J. Eichler, S. Hess, and A. M. Sonnet, "Molecular reorientation of a nematic glass by laser-induced heat flow", Phys. Rev. E **60**, 1792–1798 (1999).

[72] I. Dierking, "Experimental investigations of a chiral smectic glass-forming liquid crystal", Liquid Crystals **35**, 1015–1022 (2008).

[73] H. R. Zeller, "Dielectric relaxation and the glass transition in nematic liquid crystals", Phys. Rev. Lett. **48**, 334–337 (1982).

[74] S. J. Rzoska, M. Paluch, S. Pawlus, et al., "Complex dielectric relaxation in supercooling and superpressing liquid-crystalline chiral isopentylcyanobiphenyl", Phys. Rev. E **68**, 031705 (2003).

[75] J. Wu, T. Usui, and J.-i. Hanna, "Synthesis of a novel smectic liquid crystalline glass and characterization of its charge carrier transport properties", J. Mater. Chem. **21**, 8045 (2011).

[76] M. Tarnacka, K. Adrjanowicz, E. Kaminska, et al., "Molecular dynamics of itraconazole at ambient and high pressure", Phys. Chem. Chem. Phy. **15**, 20742–20752 (2013).

[77] M. Jasiurkowska-Delaporte, S. Napolitano, J. Leys, et al., "Glass Transition Dynamics and Crystallization Kinetics in the Smectic Liquid Crystal 4-n-Butyloxybenzylidene-$4'$-n'-octylaniline (BBOA)", J. Phys. Chem. B **120**, 12160–12167 (2016).

[78] A. Deptuch, S. Lalik, M. Jasiurkowska-Delaporte, et al., "Comparative study of electrooptic, dielectric, and structural properties of two glassforming antiferroelectric mixtures with a high tilt angle", Phys. Rev. E **105**, 024705 (2022).

[79] S. Rauch, C. Selbmann, P. Bault, et al., "Glass forming banana-shaped compounds: vitrified liquid crystal states", Phys. Rev. E **69**, 021707 (2004).

[80] R. Teerakapibal, C. Huang, A. Gujral, M. D. Ediger, and L. Yu, "Organic glasses with tunable liquid-crystalline order", Phys. Rev. Lett. **120**, 055502 (2018).

[81] Z. Chen, J. Yu, R. Teerakapibal, et al., "Organic glasses with tunable liquid-crystalline order through kinetic arrest of end-over-end rotation: the case of saperconazole", Soft Matter **16**, 2025–2030 (2020).

[82] C. A. Angell, L. Monnerie, and L. M. Torell, "Strong and Fragile Behavior in Liquid Polymers", MRS Online Proceedings Library **215**, 3–9 (1990).

[83] S. Rzoska, M. Paluch, A. Drozd-Rzoska, et al., "Glassy and fluidlike behavior of the isotropic phase of n-cyanobiphenyls in broad-band dielectric relaxation studies", The European Physical Journal E **7**, 387–392 (2002).

[84] A. Drozd-Rzoska, "Universal behavior of the apparent fragility in ultraslow glass forming systems", Scientific Reports **9**, 6816 (2019).

[85] A. Drozd-Rzoska, S. J. Rzoska, and S. Starzonek, "New scaling paradigm for dynamics in glass-forming systems", Progress in Materials Science **134**, 101074 (2023).

[86] W. Gotze and L. Sjogren, "Relaxation processes in supercooled liquids", Reports on Progress in Physics **55**, 241 (1992).

[87] A. Schönhals, F. Kremer, A. Hofmann, E. W. Fischer, and E. Schlosser, "Anomalies in the scaling of the dielectric \ensuremath{\alpha}-relaxation", Physical Review Letters **70**, 3459–3462 (1993).

[88] L. Ratke and P. W. Voorhees, *Growth and coarsening: ostwald ripening in material processing* (Springer Science & Business Media, 2002).

[89] P. Meakin, *Fractals, scaling and growth far from equilibrium* (Cambridge University Press, 2011).

[90] M. Kleman and O. D. Lavrentovich, *Soft matter physics: an introduction* (Springer, New York, 2003).

[91] I. Dierking and C. Russell, "Universal scaling laws for the anisotropic growth of SmA liquid crystal bâtonnets", Physica B: Condensed Matter **325**, 281–286 (2003).

[92] I. Dierking, H. Chan, F. Culfaz, and S. McQuire, "Fractal growth of a conventional calamitic liquid crystal", Phys. Rev. E **70**, 051701 (2004).

[93] I. Dierking, "Fractal growth of the liquid crystalline B2 phase of a bent-core mesogen", J. Phy.: Condens. Matter **13**, 1353–1360 (2001).

[94] I. Dierking, H. Sawade, and G. Heppke, "Phase ordering of the liquid crystalline 'b7' phase by analysis of fractal growth patterns", Liq. Crys. **28**, 1767–1773 (2001).

[95] H. E. Stanley, "Application of fractal concepts to polymer statistics and to anomalous transport in randomly porous media", J. Stat. Phys. **36**, 843–860 (1984).

[96] D. W. Schaefer, J. E. Martin, P. Wiltzius, and D. S. Cannell, "Fractal Geometry of Colloidal Aggregates", Phys. Rev. Lett. **52**, 2371–2374 (1984).

[97] B. B. Mandelbrot and J. W. Van Ness, "Fractional Brownian Motions, Fractional Noises and Applications", SIAM Review **10**, 422–437 (1968).

[98] E. Bullmore and O. Sporns, "The economy of brain network organization", Nature Reviews Neuroscience **13**, 336–349 (2012).

[99] S. M. Hashemi, U. Jagodič, M. R. Mozaffari, et al., "Fractal nematic colloids", Nature Communications **8**, 14026 (2017).

[100] I. Dierking, "Fractal Growth Patterns in Liquid Crystals", ChemPhysChem **2**, 59–62 (2001).

[101] Y. M. Huang and B.-G. Zhai, "Fractal Features of Growing Aggregates from Isotropic Melt of a Chiral Bent-Core Liquid Crystal", Mol. Crys. Liq. Crys. **511**, 337/[1807]–347/[1817] (2009).

[102] S. Dietrich and A. Aharony, *Introduction To Percolation Theory: Second Edition*, 2nd ed. (Taylor & Francis, London, 2017).

[103] B. B. Mandelbrot, *The fractal geometry of nature*, Vol. 173 (WH freeman New York, 1983).

[104] W. H. Bragg, "X-Rays and Crystals", Nature **90**, 360–361 (1912).

[105] D. Malkar, *Investigation on molecular organization and physical studies on asymmetric bent-core liquid crystals*, Ph.D. Thesis, Jawaharlal Nehru University, New Delhi (Raman Research Institute, Bangalore, 2020).

[106] "Michel-Levy Birefringence Chart", Olympus-lifescience.com, source: Olympus (2024).

[107] R. A. Soref and M. J. Rafuse, "Electrically Controlled Birefringence of Thin Nematic Films", J. Appl. Phys. **43**, 2029–2037 (1972).

[108] W. Haase and D. Pötzsch, "Light Transmission Experiments with Nematic Liquid Crystals Showing Positive and Negative Dielectric Anisotropy", Mol. Crys. Liq. Crys. **38**, 77–85 (1977).

[109] V. Fréedericksz and V. Zolina, "Forces causing the orientation of an anisotropic liquid", Transactions of the Faraday Society **29**, 919–930 (1933).

[110] S. Umadevi, A. Jákli, and B. K. Sadashiva, "Bistable linear electro-optical switching in the b7' phase of novel bent-core molecules", Soft Matter **2**, 215–222 (2006).

[111] N. Vaupoti č and M. Čopi č, "Polarization modulation instability in liquid crystals with spontaneous chiral symmetry breaking", Phys. Rev. E **72**, 031701 (2005).

[112] N. Vaupotič, "Landau-de gennes theory of the polarization modulated and layer undulated structure in liquid crystals made of bent-core molecules", Ferroelectrics **344**, 151–159 (2006).

[113] N. V. Madhusudana, "A two-state model for the modulated b_7 liquid crystalline phase exhibited by bent-core molecules", J. Phys.: Condens. Matter **32**, 234003 (2020).

[114] C. Zhang, B. Sadashiva, O. Lavrentovich, and A. Jákli, "Cryo-tem studies of two smectic phases of an asymmetric bent-core material", Liquid Crystals **40**, 1636–1645 (2013).

[115] C. Zhang, S. M. Salili, N. Diorio, W. Weissflog, and A. Jákli, "Nanoscale structures of polarisation-modulated bent-core materials in thin films", Liquid Crystals **42**, 1621–1626 (2015).

[116] M. A. Handschy, N. A. Clark, and S. T. Lagerwall, "Field-induced first-order orientation transitions in ferroelectric liquid crystals", Phys. Rev. Lett. **51**, 471–474 (1983).

[117] J. Watanabe, T. Niori, T. Sekine, and H. Tekezoe, "Frustrated structure induced on ferroelectric smectic phases in banana-shaped molecular system", Jpn. J. Appl. Phys. **37**, L139 (1998).

[118] K. Pelz, W. Weissflog, U. Baumeister, and S. Diele, "Various columnar phases formed by bent-core mesogens", Liquid Crystals **30**, 1151–1158 (2003).

[119] C. L. Folcia, J. Etxebarria, J. Ortega, and M. B. Ros, "Structural study of a bent-core liquid crystal showing the B_1-B_2 transition", Phys. Rev. E **74**, 031702 (2006).

[120] E. Gorecka, D. Pociecha, N. Vaupotič, et al., "Modulated general tilt structures in bent-core liquid crystals", J. Mater. Chem. **18**, 3044–3049 (2008).

[121] E. Gorecka, N. Vaupotič, and D. Pociecha, *Smectic phases of bent-core liquid crystals* (John Wiley & Sons, Ltd, 2014) Chap. 13, pp. 1–33.

[122] N. V. Madhusudana, "Some geometrical aspects of packing of bent-core molecules in the triclinic smectic-C_g liquid crystals and simple models of the modulated $\mathrm{Sm}C_{gmod}$ phase", Phys. Rev. E **103**, 022704 (2021).

[123] L. Limat and J. Prost, "A model for the chevron structure obtained by cooling a smectic A liquid crystal in a cell of finite thickness", Liquid Crystals **13**, 101–113 (1993).

[124] N. A. Clark and S. T. Lagerwall, "Submicrosecond bistable electro-optic switching in liquid crystals", Appl. Phys. Lett. **36**, 899–901 (1980).

[125] S. K. Prasad, D. S. S. Rao, S. Sridevi, et al., "Unusual dielectric and electrical switching behavior in the de vries smectic A phase of two organosiloxane derivatives", Phys. Rev. Lett. **102**, 147802 (2009).

[126] J. C. Roberts, N. Kapernaum, Q. Song, et al., "Design of Liquid Crystals with "de Vries-like" Properties: Frustration between SmA- and SmC-Promoting Elements", J. Am. Chem. Soc. **132**, 364–370 (2010).

[127] H. Yoon, D. M. Agra-Kooijman, K. Ayub, R. P. Lemieux, and S. Kumar, "Direct observation of diffuse cone behavior in de vries smectic-A and -C phases of organosiloxane mesogens", Phys. Rev. Lett. **106**, 087801 (2011).

[128] C. P. J. Schubert, C. Müller, A. Bogner, F. Giesselmann, and R. P. Lemieux, "Design of liquid crystals with 'de Vries-like' properties: structural variants of carbosilane-terminated 5-phenylpyrimidine mesogens", Soft Matter **13**, 3307–3313 (2017).

[129] H. Ocak, B. Bilgin-Eran, M. Prehm, et al., "Effects of chain branching and chirality on liquid crystalline phases of bent-core molecules: blue phases, de Vries transitions and switching of diastereomeric states", Soft Matter **7**, 8266–8280 (2011).

[130] S. P. Sreenilayam, Y. P. Panarin, J. K. Vij, et al., "Spontaneous helix formation in non-chiral bent-core liquid crystals with fast linear electro-optic effect", Nat. Comm. **7**, 11369 (2016).

[131] A. A. S. Green, M. R. Tuchband, R. Shao, et al., "Chiral incommensurate helical phase in a smectic of achiral bent-core mesogens", Phys. Rev. Lett. **122**, 107801 (2019).

[132] Y. P. Panarin, S. P. Sreenilayam, V. Swaminathan, C. Tschierske, and J. K. Vij, "Observation of an anomalous sma-smc-sma phase sequence in a bent-core liquid crystal derived from 4-cyanoresorcinol", Phys. Rev. Res. **2**, 013118 (2020).

[133] S. Kaur, A. Barthakur, G. Mohiuddin, et al., "Observation of "de vries-like" properties in bent-core molecules", Chem. Sci. **13**, 2249–2257 (2022).

[134] G. Pratap, D. Malkar, E. Varathan, et al., "3-cyano thiophene-based π-conjugated mesogens: xrd and 13c nmr investigations", Liquid Crystals **46**, 680–693 (2019).

[135] A. S. Govind and N. V. Madhusudana, "A simple molecular theory of smectic-C liquid crystals", Europhysics Letters **55**, 505 (2001).

[136] Q. Song, D. Nonnenmacher, F. Giesselmann, and R. P. Lemieux, "Tuning 'de Vries-like' properties in siloxane - and carbosilane-terminated smectic liquid crystals", J. Mater. Chem. C **1**, 343–350 (2013).

[137] H. Kumar Singh, S. Kumar Singh, R. Nandi, et al., "Observation of exceptional 'de Vries-like' properties in a conventional aroylhydrazone based liquid crystal", RSC Advances **6**, 57799–57802 (2016).

[138] S. Havriliak and S. Negami, "A complex plane analysis of α-dispersions in some polymer systems", Journal of Polymer Science Part C: Polymer Symposia **14**, 99–117 (1966).

[139] S. Havriliak and S. Negami, "A complex plane representation of dielectric and mechanical relaxation processes in some polymers", Polymer **8**, 161–210 (1967).

[140] D. W. Davidson and R. H. Cole, "Dielectric Relaxation in Glycerol, Propylene Glycol, and n-Propanol", J. Chem. Phys. **19**, 1484–1490 (1951).

[141] K. S. Cole and R. H. Cole, "Dispersion and Absorption in Dielectrics I. Alternating Current Characteristics", J. Chem. Phys. **9**, 341–351 (1941).

[142] A. Drozd-Rzoska and S. J. Rzoska, "Derivative-based analysis for temperature and pressure evolution of dielectric relaxation times in vitrifying liquids", Physical Review E **73**, 041502 (2006).

[143] F. Stickel, E. W. Fischer, and R. Richert, "Dynamics of glass-forming liquids. II. Detailed comparison of dielectric relaxation, dc-conductivity, and viscosity data", The Journal of Chemical Physics **104**, 2043–2055 (1996).

[144] J. Souletie, "The glass transition: dynamic and static scaling approach", Journal de Physique **51**, 883–898 (1990).

[145] P. Salamon, N. Éber, Á. Buka, et al., "Dielectric properties of mixtures of a bent-core and a calamitic liquid crystal", Phys. Rev. E **81**, 031711 (2010).

[146] L. Marino, A. T. Ionescu, S. Marino, and N. Scaramuzza, "Dielectric investigations on a bent-core liquid crystal", Journal of Applied Physics **112**, 114113 (2012).

[147] H. R. Brand, P. Cladis, and H. Pleiner, "Macroscopic properties of smectic liquid crystals", Eur. J. Phys. (B) **6**, 347–353 (1998).

[148] A. Roy, N. V. Madhusudana, P. Tolédano, and A. M. Figueiredo Neto, "Longitudinal spontaneous polarization and longitudinal electroclinic effect in achiral smectic phases with bent-shaped molecules", Phys. Rev. Lett. **82**, 1466–1469 (1999).

[149] L. Guo, E. Gorecka, D. Pociecha, et al., "Ferroelectric behavior of orthogonal smectic phase made of bent-core molecules", Phys. Rev. E **84**, 031706 (2011).

[150] E. D. Korblova, E. Guzman, J. E. Maclennan, et al., "New smap$_F$ mesogens designed for analog electrooptics applications", Materials **10**, 10.3390/ma10111284 (2017).

[151] N. Chattham, M.-G. Tamba, R. Stannarius, et al., "Leaning-type polar smectic-C phase in a freely suspended bent-core liquid crystal film", Phys. Rev. E **91**, 030502 (2015).

[152] A. V. Emelyanenko and M. A. Osipov, "Origin of spontaneous polarization, tilt, and chiral structure of smectic liquid-crystal phases composed of bent-core molecules: a molecular model", Phys. Rev. E **70**, 021704 (2004).

[153] D. Patra and A. Roy, "Spontaneous breaking of chiral symmetry in achiral bent-core liquid crystals: excluded volume effect", Phys. Rev. E **107**, 034704 (2023).

[154] N. Vaupotič, D. Pociecha, M. Čepič, et al., "Evidence for general tilt columnar liquid crystalline phase", Soft Matter **5**, 2281–2285 (2009).

[155] A. Eremin, S. Diele, G. Pelzl, H. Nádasi, and W. Weissflog, "Experimental evidence for $\mathrm{Sm}{-}C_G \rightarrow \mathrm{Sm} - CP$ polymorphism in fluorinated bent-shaped mesogens", Phys. Rev. E **67**, 021702 (2003).

[156] N. Chattham, E. Korblova, R. Shao, et al., "De Gennes' triclinic smectics – not so far-fetched after all", Liq. Crys. **36**, 1309–1317 (2009).

[157] P. G. De Gennes and J. Prost, *The physics of liquid crystals* (Clarendon Press, Oxford, 1995).

[158] G. Pelzl, S. Diele, and W. Weissflog, “Banana-shaped compounds—a new field of liquid crystals”, Adv. Mat. **11**, 707–724 (1999).

[159] R. M. Haralick, K. Shanmugam, and I. Dinstein, “Textural features for image classification”, IEEE Transactions on Systems, Man, and Cybernetics **SMC-3**, 610–621 (1973).

[160] J. C. Rouillon, J. P. Marcerou, M. Laguerre, H. T. Nguyen, and M. F. Achard, “New banana-shaped thiobenzoate liquid crystals with B6, B1 and B2 phases”, Journal of Materials Chemistry **11**, 2946–2950 (2001).

[161] W. Weissflog, H. Nádasi, U. Dunemann, et al., “Influence of lateral substituents on the mesophase behaviour of banana-shaped mesogens”, Journal of Materials Chemistry **11**, 2748–2758 (2001).

[162] N. V. Madhusudana, “Some geometrical aspects of packing of bent-core molecules in the triclinic smectic-C_g liquid crystals and simple models of the modulated $\mathrm{Sm}C_{gmod}$ phase”, Phys. Rev. E **103**, 022704 (2021).

List of Figures

1.1 Schematic organization of anisotropic rod-like molecules in different phases of thermotropic liquid crystals. 2

1.2 (a) Schematic representation of the molecular organization in the nematic phase. The arrow indicates the mean orientation of molecular long axes and is denoted by director $\hat{n}$. (b) The molecular structures of typical rod-like molecules 5CB and 8OCB, which follow the phase sequence $Isotropic \rightarrow Nematic \rightarrow Crystal$ and $Isotropic \rightarrow Nematic \rightarrow SmA \rightarrow Crystal$, respectively. 4

1.3 The orientational distribution function $f(\theta)$ of rod-like molecules in the nematic phase. For rod-like molecules, the distribution $f(\theta)$ generally attains a minimum value at $\theta = \pi/2$ and maximum values at $\theta = 0$ and π. 5

1.4 Schematic representation of splay, twist, and bend deformations in the nematic phase. 7

1.5 Schematic representation of molecular organization in the cholesteric phase consisting of chiral molecules. The director $\hat{n}$ remains in the xy-plane but rotates about the z-axis, giving rise to a helical structure having pitch p. Note that the spatial periodicity of the structure is $p/2$ because of $\hat{n} \leftrightarrow -\hat{n}$ symmetry. 8

1.6 Schematic representation of the molecular organization in fluid lamellar structure in the SmA and SmC phases. The director $\hat{n}$ orient parallel to the layer normal in the case of the SmA phase, whereas it tilts away from the layer normal in the case of the SmC phase. 10

1.7 Schematic representation of the molecular arrangement in conventional SmA, SmC, and de-Vries SmA phases comprised of calamitic molecules. In the de Vries SmA phase, the molecules are oriented with a large tilt angle with respect to layer normal having long axes randomly distributed on a cone according to the diffuse cone model proposed by Adrian de Vries. During the transition from the SmA to the SmC phase, a significant layer contraction is observed. In contrast, the dSmA to SmC transition is accompanied by practically no layer contraction. . . . 12

1.8 (a) A 'bookshelf geometry' of the homogeneously planar aligned SmA phase with layers perpendicular to the bounding plates. (b) A chevron configuration giving rise to zig-zag defects. It arises due to the buckling of the layers while transitioning from the SmA to the SmC phase. . . . 14

1.9 (a) A typical molecular structure of bent-core banana shaped liquid crystal. (b) Schematic representation of a bent-core molecule when viewed from three different directions. The cross and dot symbols represent the arrow axis pointing downward and upward, respectively. 16
1.10 A schematic representation of the arrangement of bent-core molecules in different orthogonal smectic phases. 18
1.11 (a) Schematic representation of tilted molecular configuration in a layer. The layer normal ($\hat{k}$), tilt direction ($\hat{c}$), and polar order ($\vec{P}$) are orthogonal to each other, giving rise to a particular handedness of the layers. (b) Schematic representation of the arrangement of bent-core molecules in different tilted smectic phases (B2 phase). Yellow and blue colors represent left-handed and right-handed layer chirality, respectively. The notations used have the following meaning: $C_A \rightarrow$ anticlinic tilt, $C_S \rightarrow$ synclinic tilt, $P_A \rightarrow$ antiferroelectric polar order, and $P_F \rightarrow$ ferroelectric polar order. 19
1.12 Schematic diagram of the molecular configuration in four possible structures for **leaning phase**. Here, the molecular long axes are leaned (tilted) with respect to the layer normal in a way that the polar order remains in the tilt plane. These structures are achiral in nature. 21
1.13 (a) Schematic representation of SmCP layers having uniform polar order. For large polarization, the splay of polar order takes place, resulting in stripes separated by defects (b). To incorporate these defects, the layers undulate at the edges of the stripes and form $SmCP_{mod}$ phase (c). a and b are the lattice parameters corresponding to the rectangular lattice structure. 22
1.14 Schematic representation of columnar phase where stripes slide halfway through the layers to exhibit two-dimensional ordering. Along the columns, the molecules have a fluid-like order. 24

2.1 The typical DSC thermogram of a compound 8OBF12 (discussed in chapter 3) while heating and cooling the sample at a rate of 5 K/min. The peaks correspond to various phase transitions. 30
2.2 A typical XRD intensity profile characteristic of a smectic phase. 31
2.3 Schematic representation of homeotropic (left) and homogeneous planar (right) alignment of director $\hat{n}$. 33
2.4 The typical POM texture of a thin sample in the nematic phase in (a) homeotropic alignment and (b) homogeneous planar alignment. Crossed arrows represent the orientation of crossed polarizers. The double arrow in (b) shows the orientation of the director, which is similar to the rubbing direction of the LC cell. Scale bar: 50 μm. 34
2.5 Schematic representation of optical components in a polarizing microscope. 35

2.6 The variation of effective birefringence as a function of temperature for the compound BTCN8 discussed in chapter 4. 38
2.7 The temporal variation of the steady state optical transmittance along with the applied field for compound BTCN8 discussed in chapter 4. . . 39
2.8 Schematic diagram of electro-optical setup 40
2.9 Schematic diagram of the electrical circuit of RC equivalent of LC cell used in the dielectric measurements. 40
2.10 (a) Schematic diagram of the experimental setup for polarization reversal current measurements. (b) Schematics of the corresponding electrical circuit with the RC equivalent of LC cell. 43
2.11 Typical signal showing a polarization reversal current response under the application of a triangular wave voltage. 44
2.12 Schematic representation of components in a scanning electron microscope. 45

3.1 (a) Molecular structure of the homologous series of compounds 8OBFn with varying chain length **n** attached to one end of the BC molecule. (b) DSC thermograms of the compound 8OBF12 with a heating and cooling rate of 5 K/min. Only one enantiotropic liquid crystalline phase was observed below the isotropic phase. All other transitions correspond to crystal to crystal transitions. 49
3.2 Cooling scan transition temperatures as a function of alkyl chain length **n** attached to one end of the molecule. All the homologs exhibit one enantiotropic liquid crystal phase without any odd-even effect. 50
3.3 The POM texture of a 5 μm thick planar aligned sample of the compound 8OBF12 between crossed polarizers at 413 K while cooling the sample from the isotropic phase at a rate of (a) 0.01 K/min, and (b) 3 K/min. 52
3.4 The POM textures of the compound 8OBF12 in a planar aligned LC cell of sample thickness 5 μm between the crossed polarisers at 413 K with (a) no applied field, (b) ac field of 15 V/μm, (c) ac field of 20 V/μm, and (d) after turning off the field. The changes in the birefringence color show the irreversible field-induced transition from the SmC_{LU} phase as a consequence of the dielectric anisotropy. 52
3.5 The switching current response of the compound 8OFB12 for a planar aligned sample of thickness 5 μm under the application of a triangular wave voltage. No peak corresponding to polarization reversal was observed, indicating the apolar nature of the SmC_{LU} phase. The inset shows the current response under the application of a square wave voltage. A single exponentially dropping peak was observed associated with the capacitive response of the LC cell, confirming the absence of layer polarization in the SmC_{LU} phase. 53

3.6 The switching current response of the compound 8OFB12 for a planar aligned sample of thickness 5 μm under the application of a triangular wave voltage at a lower frequency. No peak corresponding to polarization reversal was observed, indicating the apolar nature of the SmC_{LU} phase. The inset shows the current response under the application of a square wave voltage. A single exponentially dropping peak was observed associated with the capacitive response of the LC cell, confirming the absence of layer polarization in the SmC_{LU} phase. 54

3.7 The POM texture of (a) a homeotropically aligned sample of thickness 9 μm, and (b) a thin sample sandwiched between a clean glass plate and a cover slip placed between crossed polarizers. 54

3.8 The optical response of a planar aligned sample of thickness 5 μm in the SmC_{LU} phase under the application of a triangular wave voltage. The $2f$ response in the optical signal indicates a quadratic coupling between the electric field and the dielectric anisotropy of the sample. . 55

3.9 The POM textures of 5 μm thick sample kept between crossed polarizers of the compounds (a) 8OBF16 and (c) 8OBF8 at a temperature of 408 K in the SmCLU phase. The corresponding field-induced textures of compounds (b) 8OBF16 and (d) 8OBF8. The field required to obtain the complete transformation of the SmCLU phase for the compounds 8OBF16 and 8OBF8 was about 20 V/μm and 30 V/μm, respectively. . . 57

3.10 The variation of the effective dielectric constant of the compound 8OBF12 in a planar aligned LC cell of sample thickness 5 μm as a function of temperature. The filled circle symbols show the variation of the dielectric constant on cooling the sample from its isotropic phase, clearly detecting the range of stability of the SmC_{LU} phase. The open triangular symbols show the variation of the dielectric constant on heating the sample from the field-induced state of the SmC_{LU} phase. . 57

3.11 The XRD intensity profile of the compound 8OBF12 at 417 K as a function of wave vector q in the SmC_{LU} phase. The sharp peaks in the small angle region indicate the lamellar order of the molecules in this phase. The broad diffused peak in the wide-angle region indicates a liquid-like order along the layers. 59

3.12 A high-resolution XRD measurement of the compound 8OBF12 focused only in the small angle region shows several weak satellite peaks corresponding to undulation perpendicular to the layer normal, which can be fitted to a 2D rectangular lattice with lattice parameters d and a depicted in the inset. The ordered pairs in the square bracket indicate the Miller indices corresponding to these peaks. Some of the peaks associated with these Miller indices overlap due to a relatively large value of a ($\approx$ 600 Å) and can not be resolved experimentally. 61

3.13 A high-resolution XRD intensity profile measured in the small angle region for the homologs 8OBFn as denoted in each figure. The numbers represent the scattering vector associated with each peak. All the presented XRD profiles were taken at a temperature of 408 K. Strong sharp peaks corresponding to the layer spacing are consistent for the homologs. In addition, numerous weak satellite peaks associated with the layer undulation along the layer were observed. All the peaks can be well-fitted with a 2D rectangular lattice. The XRD profile of the compound 8OBF8 is slightly different from others as the observed satellite peaks were relatively prominent. See the text for a detailed discussion. 62

3.14 The variation of the layer undulation wavelength a with temperature for the compound 8OBF13. The dashed line shows the linear fit to the data. 63

3.15 The tilt angle θ as a function of chain length n attached to one end of the molecule for the homologs 8OBFn; n = 8 to 16. 63

3.16 The variation of the lattice parameters d and a as a function of chain length n at temperature 408 K for the homologs 8OBFn; n = 8 to 16. . 64

3.17 The cryo-FESEM texture of the SmC_{LU} phase for the compound 8OBF15 showing the periodic stripes having periodicity consistent with the XRD measurements. 65

3.18 (a) Illustration of undulated layer structure having double tilted organization of BC molecules in the SmC_{LU} phase. The defect walls are shown as gray regions in the layers. Two different colors have been used to indicate the molecular asymmetry. (b) The field-induced metastable state of the structure shown in (a) with the local reorientation of the molecules in the layers, which accounts for the irreversible field-induced transition observed experimentally. The stacking of these undulated layers produces a 2D rectangular lattice with no net polarization. . . . 67

4.1 Schematic representation of the molecular arrangement in conventional SmA, SmC, and de Vries SmA phases comprised of calamitic molecules. In the dSmA phase, the molecules are, on average, tilted away from the layer normal by a significantly large angle with their long axes randomly distributed on a cone according to the diffuse cone model proposed by Adriaan de Vries [15]. 72

4.2 (a) The molecular structure of the compound BTCN8. (b) DSC thermogram of the compound BTCN8 with heating and cooling rate of 5 K/min. The inset demonstrates the existence of a small range nematic phase. The sample does not crystallize on cooling till room temperature. The mesomorphic properties of the sample were retained for several weeks, and the melting transition was observed only on the first heating. (c) The temperature variation of the optical transmittance through a planar aligned sample of thickness 5 μm kept between crossed polarizers while cooling from the isotropic phase. The optical transmittance clearly detects the following phase transition sequence: Isotropic (523.5 K) N (521.5 K) dSmA (402 K) SmC. The inset reveals the existence of a nematic phase with a small range of temperature. All the observed phases are enantiotropic. 74

4.3 (a) The XRD intensity profile for the compound BTCN8 in dSmA and SmC phases at temperatures 473 K and 393 K, respectively. (b) The temperature variation of the ratio d/d_{AC} and tilt angle θ were obtained from the XRD data and estimated molecular length. The layer thickness remains almost unchanged across the dSmA-SmC transition, showing the de Vries nature of the SmA phase. The vertical dotted line indicates the dSmA to the SmC transition temperature. Across the transition depicted by the pink-shaded region, the layer contraction is only about 0.17%. The error bars are smaller than the size of the symbols. 76

4.4 POM texture of homeotropically aligned thin sample kept between a clean glass plate and a cover slip at (a) 522 K, (b) 518 K, and (c) 388 K; and that of the planar aligned sample of thickness 5 μm at (d) 522 K, (e) 508 K, and (f) 333 K. The POM textures were taken under crossed polarizers conditions while cooling the samples from their isotropic phase. ***R*** indicates the rubbing direction, and the crossed arrows denote the positions of the polarizers. The scale bar represents a length of 50 μm. 78

4.5 The POM textures of a planar aligned sample of compound BTCN8 in the SmC phase at 373 K for three orientations (a) -11°, (b) 0°, and (c) 11° of rubbing direction of the sample cell with respect to the analyzer. Two oppositely tilted domains indicated by i and ii were observed which appears identical at 0°. The brightness of the domains i and ii interchange on rotating the sample clockwise and counterclockwise. (d) The variation of the normalized intensity of the domain i and domain ii as a function of the rotation angle θ of the rubbing direction of the LC cell with respect to the analyzer. The minima at $\mp 11\circ$ corresponds to the optical tilt angle in the domain i and ii, respectively. 79

4.6 (a) The variation of optical tilt angle θ_{opt} as a function of $(T_{AC} - T)$ in the SmC phase. The solid line shows the fit to the experimental data using eqn. 4.1. The inset of (a) shows the oppositely tilted domains in the SmC phase with the layer normal denoted by unit vector $\hat{k}$. In both the domains, $\hat{k}$ are parallel, but the optic axes are tilted on the opposite side of $\hat{k}$, giving rise to the optical contrast between crossed polarizers. The white and red arrows represent the direction of the layer normal $\hat{k}$ and the optic axis, respectively, in the two domains. (b) Temperature variation of the effective birefringence (Δn) of a planar aligned sample while cooling from the isotropic phase. The inset of (b) shows the magnified view of the data in the short temperature range of the nematic phase. 81

4.7 Time evolution of current response when the sample was subjected to a triangular AC voltage of amplitude 50 V and frequency 40 Hz for planar alignment in (a) dSmA and (b) SmC phase, and homeotropic alignment in (c) dSmA and (d) SmC phase, respectively. The absence of a current peak due to polarization reversal indicates that both the smectic phases are apolar in nature. 83

4.8 The field induced changes in the POM textures of a planar aligned sample in the SmC phase at 360 K between crossed polarizers. The texture (a) at initial zero fields, (b) with a triangular field of amplitude 2 V/μm and frequency f, and (c) after removing the field. The length of the bar shows a scale of 50 μm. 84

4.9 The normalized optical transmittance along with the applied AC voltage as a function of time through a planar aligned sample of thickness 5 μm kept between crossed polarizers at 393 K. 84

4.10 The variation of the effective dielectric constant (ϵ_{eff}) of the compound BTCN8 in a planar aligned LC cell of sample thickness 5 μm as a function of temperature. The data clearly detects the various phase transitions and is in agreement with the DSC and POM observations. The dielectric constant's low value indicates the absence of spontaneous polarization in the sample. The inset shows the magnified view of the marked region. 86

4.11 The variation of the imaginary part of the dielectric constant (ϵ'') as a function of frequency at different temperatures. (a) In high temperature range from 423 K to 395 K with a temperature step of 4 K. (b) In the low temperature range from 393 K to 303 K with a temperature step of 10 K. The peaks in the data represent various dielectric relaxation processes. 87

4.12 The variation of the real part of the dielectric constant (ϵ') as a function of frequency at various temperatures. (a) In high temperature range from 423 K to 395 K with a temperature step of 4 K. (b) In the lower temperature range from 393 K to 303 K with a temperature step of 10 K. The step change in the data represent various dielectric relaxation processes. 88

4.13 Frequency dependence of the real part of dielectric constant ϵ' for (a) planar aligned sample and (b) homeotropically aligned sample at different temperatures. The noisy data in the lower frequency domain is due to experimental artifacts. The temperature depicted in the legend applies to both graphs. A slight change in the data enclosed by the dotted rectangle is not a sample property. Rather, it occurs due to the LC cell, as it was found to exist in the measurements with empty cells, too. 89

4.14 The POM texture of the sample in a homeotropic LC cell of thickness 9 μm under crossed polarizers in (a) the dSmA phase and (b) the SmC phase. The scale bar indicates 100 μm. 89

4.15 (a) Frequency variation of ϵ'' at 333 K along with fitted curve (solid line) using eqn. 4.4. The deviation of the fitted curve in the higher frequency region is due to the overlap of the relaxation peak in the MHz range associated with ITO coating. (b) Relaxation frequency of mode M_1 as a function of inverse temperature. The solid curve represents the fit to the experimental data using VFT eqn. 4.5, indicating the non-Arrhenius behavior of the liquid. 92

4.16 The linear variation of $T\ [d(\ln\tau)/d(1/T)]^{-1/2}$ as a function of temperature showing two dynamical regimes separated by the crossover temperature $T_B = 370\ K$. The slope and ordinate of the linear fit in the lower (higher) temperature region are 0.028 and -6.51 (0.123 and -41.65), respectively. 93

4.17 The DSC thermogram of the compound BTCN8 at different rates while cooling from the isotropic phase and subsequent heating. A step change in the curve at a temperature of 271 K is indicative of glass transition. The sample does not crystallize over a few weeks. 94

4.18 Schematic representation for the arrangement of bent-core molecules in a layer of the dSmA phase (a) without electric field, and (b) in the presence of the field applied parallel to the smectic layer. The change in the molecular distribution on the application of field gives rise to collective mode M_1 observed in our sample. 95

5.1 Schematic representation of molecular organization in a layer for different possible smectic phases of BC molecules. The vector P indicates the direction of layer polarization. The unit vectors $\hat{k}$, $\hat{n}$, and $\hat{c}$ show the orientation of layer normal, the director, and projection of $\hat{n}$ on the layer plane, respectively. 98

5.2 (a) Molecular structure of the compound DIBO12 with asymmetric arms and identical aliphatic chains attached to each end of the BC molecule. (b) DSC thermograms of the sample with a heating and cooling rate of 3 K/min showing the presence of only one mesophase of the compound. 99

5.3 The XRD intensity profile of the compound DIBO12 at 421 K as a function of wave vector q in the SmC_x phase. The sharp peaks in the small angle region reveal the lamellar molecular order in this phase. A diffuse peak in the wide angle region indicates a liquid-like order along the layers. 101

5.4 The POM texture of the compound DIBO12 between crossed polarizers kept (a) in a planar aligned LC cell of thickness 5 μm, and (b) between a glass plate and cover slip. The texture in (b) exhibits both planar and homeotropic domains coexisting in the field of view. The schlieren texture in the homeotropic region of the sample showed a periodic undulation. (c) The intensity profile along the white arrow drawn on the undulated texture, which is shown in the inset. Scale bar = 40 μm. 102

5.5 (a) The POM textures containing circular domains of the SmC_x phase for the compound DIBO12 between crossed polarizers. These rarely observed circular domains have extinction brushes oriented at an angle of about 43° in some of them (image at top) and parallel to the crossed polarizers in others (image at bottom). This observation indicates the existence of synclinic as well as anticlinic interlayer molecular configuration. The synclinic structures appear significantly more often than the anticlinic ones. (b) The POM texture of a 5 μm thick planar aligned sample in the SmC_x phase after removing one of the polarizers from the light path while cooling the sample at a rate of 0.1 K/min from its isotropic phase. This enables the visualization of the numerous defects lines in the texture more clearly. The curved defect lines demonstrate the spontaneous bending of the layers, as discussed in detail in the main text. 103

5.6 A grayscale image of the POM texture shown in figure 5.5(b) featuring numerous curved defect lines. These curved defect lines are fitted with red circles to calculate the corresponding radii of the curvature within the computational error. The curved defect lines were treated as part of circles, and the radius of curvature for each curved line was computed using the circular Hough transform technique in MATLAB. 104

5.7 (a) Histogram of preferred radii of curvature of defect lines observed in POM texture after removing one of the polarizers from the light path. (b) The log-log plot of intensity-intensity correlation $C(r)$ as a function of distance r calculated from a POM texture of a 5 μm thick planar aligned sample. 105

5.8 The cryo-FESEM texture of the SmC$_x$ phase showing (a) the undulated layers and (b) the layers forming circular domains. 106

5.9 The current response for a planar aligned sample of thickness 5 μm in the SmC$_x$ phase at 408 K under the application of a triangular wave voltage (50 V, 1 kHz). 107

5.10 The POM textures of a 5 μm thick sample in planar aligned LC cell in the SmC$_x$ phase between crossed polarizers (a) without electric field, (b) with an AC field of 16 V/μm, 80 Hz, and (c) after turning off the field, showing an irreversible field-induced transformation. 107

5.11 The current response of a 5 μm thick planar aligned sample under the application of a triangular wave AC voltage (80 V, 80 Hz) at different temperatures (from 408 K to 436 K in steps of 2 K). Two broad humps in each half cycle of the applied voltage were observed, which persist even in the isotropic phase. Moreover, the observed broad humps are found to be more prominent at lower frequencies of the applied field and gradually reduce with increasing frequency. These observations confirm that the observed broad peaks are not associated with the polarization of the sample but arise due to the space charge effect of the sample. The ohmic part of the sample's current response is relatively larger compared to the capacitive or polarization reversal part of the response, which perhaps masks any polarization response of the sample, as discussed in the main text. 108

5.12 Temporal profile of the optical transmittance of the sample in 5 μm LC cell between crossed polarizers and the corresponding applied triangular wave AC voltage. 109

5.13 The temperature variation in the effective dielectric constant (ϵ_{eff}) and the optical transmittance through a 5 μm thick planar aligned sample kept between crossed polarizers. The open circle and open triangular symbols show the variation of ϵ_{eff} and normalized transmitted intensity, respectively, while cooling the sample from the isotropic phase. The red rectangular symbols show the variation of ϵ_{eff} on heating the sample from the field-induced state of the SmC$_x$ phase. 110

5.14 (a) The POM texture of the SmC$_x$ phase for a 5 μm thick sample in planar aligned LC cell when quenched from its isotropic phase. (b) A binary image obtained after thresholding the image shown in (a). (c) The perimeter of the growing SmC$_x$ domains, and (d) A log-log plot of the area vs perimeter of the growing domains. A linear fit to the data gives the area-perimeter dimension $D_p = 1.48$. 112
5.15 The area-perimeter fractal dimension of the growing SmC$_x$ domains of the sample as a function of (a) quench rate for a constant quench depth 0.5 K and (b) quench depth for a constant quench rate of 5 K/min. . . 113
5.16 A log-log plot of the area versus perimeter of a growing domain of the SmC$_x$ phase shown enclosed by a circle in the inset. A linear fit to the data gives the area-perimeter dimension D_p = 1.43. 114
5.17 Schematic representation of molecular organization within a layer of the SmCP$_G$[U] phase in (a) the absence of the field and (b) the field-induced state. The director $\hat{n}$ remains uniformly tilted with respect to the layer normal. In the absence of the field, the local polar order rotates about the director as one goes along the layers with a long-wavelength undulation of the layers. The applied field aligns the polarization along itself, giving rise to an irreversible field-induced state and expelling the layer undulations. 116

List of Tables

3.1 Transition temperatures and the phase sequence along with the associated changes in enthalpy across the transitions while heating and cooling the sample at a rate of 5 K/min for the homologs 8OBFn; n = 8-16 obtained from the DSC studies. The transition temperatures are in K, and the corresponding enthalpy changes in J/g are shown in the brackets. 51

3.2 XRD results and the lattice parameters for the homologous series of compounds 8OBFn. The calculated scattering vectors were found to be in excellent agreement with that of the experimentally observed values. Due to the relatively large value of lattice parameter a, some of the satellite peaks are too close to be resolved experimentally. 60

4.1 The shape parameters α and β, and dielectric strength $\Delta\epsilon$ value obtained from fitting the experimental data with eqn. 4.4 at different temperatures. 91